Delft University of Technology

Super-resolution microscopy in tissue through illumination engineering and aberration correction

Hung, S.

Important note
To cite this publication, please use the final published version (if applicable).
Please check the document version above.

SUPER-RESOLUTION MICROSCOPY IN TISSUE THROUGH ILLUMINATION ENGINEERING AND ABERRATION CORRECTION

Super-resolution microscopy in tissue through illumination engineering and aberration correction

Proefschrift

ter verkrijging van de graad van doctor aan de
Technische UniversiteitDelft,
op gezag van de Rector Magnificus Prof.dr.ir. T.H.J.J. van der Hagen,
voorzitter van het College voor Promoties,
in het openbaar te verdedigen op
woensdag 2 oktober 2024 om 15:00 uur

door

Shih-Te HUNG

Master of Science in Photonics, Friedrich Schiller University, Jena, Germany
geboren te Tainan, Taiwan

Dit proefschrift is goedgekeurd door de promotoren.

Samenstelling promotiecommissie bestaat uit:

Rector Magnificus,	voorzitter
Prof. dr. ir. M. H. G. Verhagen	Technische Universiteit Delft, promotor
Dr. ir. C.S. Smith	Technische Universiteit Delft, copromotor

Onafhankelijke leden:

Prof. dr. N. H. Dekker	Technische Universiteit Delft
Prof. dr. ir. S. J. T. van Noort	Leiden Universiteit
Dr. A. Gustavsson	Rice University, United States of America
Dr. ir. S. F. Pereira	Technische Universiteit Delft
Dr. W. Vandenberg	Katholieke Universiteit Leuven, België
Prof. dr. S. Stallinga	Technische Universiteit Delft, reservelid

An electronic version of this dissertation is available at
http://repository.tudelft.nl/.

CONTENTS

LIST OF ACRONYMS

A.U. Airy Unit

AO Adaptive Optics

APD Avalanche Photodetector

CRLB Cramér-Rao Lower Bound

cspline cubic spline

DM Deformable Mirror

DMD Digital Micromirror Device

dSTORM Direct Stochastic Optical Reconstruction Microscopy

FFT Fast Fourier Transform

FOV Field of View

FWHM Full Width Half Maximum

FRC Fourier Ring Correlation

HILO Highly Inclined and Laminated Optical Sheet Microscopy

HIST Highly Inclined Swept Tile Microscopy

INSPR In Situ Point Spread Function Retrieval

ISM Image Scanning Microscopy

LITE Lateral Interference Tilted Excitation Microscopy

MLE Maximum Likelihood Estimation

MINFLUX Minimum Flux

NA Numerical Aperture

NLLS Non-Linear Least Squares

OPM Oblique Plane Microscopy

OTF Optical Transfer Function

PE-SMLM Pattern-Enhanced Single Molecule Localization Microscopy

PMT Photomultiplier Tube

PSF Point Spread Function

SIM Structured Illumination Microscopy

SLM Spatial Light Modulator

SMLM Single Molecule Localization Microscopy

SNR Signal-to-Noise Ratio

soSPIM Single Objective Light-Sheet Microscopy

STED Stimulated Emission Depletion Microscopy

TILT Tilted Light-Sheet Microscopy

TIRF Total Internal Reflection Fluorescence Microscopy

WF Widefield Microscopy

SUMMARY

Super-resolution microscopy has been demonstrated to surpass the diffraction limit, delivering high-resolution images. State-of-the-art super-resolution research continually strives to improve imaging resolution using existing super-resolution technology. This thesis aims to enhance super-resolution microscopy resolution through engineered illumination and establish a solid theoretical foundation to support resolution improvements.

In Chapter 2, I discuss the enhancement of resolution in single molecule localization microscopy for thick sample imaging. In thick samples, the issue of high background noise can degrade the localization precision of single molecule localization. We introduce Single Objective Lens Lightsheet Microscopy (SOLEIL) as a solution to mitigate the high background photon issue, thereby improving the resolution of single molecule localization microscopy. Compared to conventional lightsheet microscopy, SOLEIL employs only one objective lens throughout the system, significantly simplifying system complexity and making it more user-friendly. We demonstrate that the theoretical localization precision of SOLEIL surpasses that of widefield microscopy and highly inclined and laminated optical sheet (HILO) microscopy in 10 μm thick samples.

In Chapter 3, I propose an imaging solution to address the high background issue and sample-induced aberration in thick sample imaging. In thick sample imaging, sample-induced aberrations can distort the Point Spread Function (PSF), leading to systematic localization bias and reduced localization precision. In this chapter, I suggest combining SOLEIL microscopy with a sensorless Adaptive Optics (AO) method to address these issues. The sensorless AO method corrects sample-induced aberrations, while SOLEIL microscopy reduces high background noise in thick samples. By combining AO and SOLEIL, we demonstrate a twofold improvement in axial localization precision compared to widefield microscopy with AO correction or SOLEIL microscopy without AO correction.

In Chapter 4, I propose a comprehensive PSF model theory for Image Scanning Microscopy (ISM) that fully considers vectorial effects, aberrations, Stokes shifts, and Fresnel coefficients at media interfaces. This approach allows for the accurate modeling of excitation and emission PSFs, providing precise references for selecting hardware parameters and assessing image quality. Many studies have emphasized the importance of considering vectorial effects in high numerical aperture microscopy. Based on the proposed theory, I discovered that the width of the ISM Point Spread Function predicted by the proposed theory can deviate by 30% from that predicted by scalar ISM theory. Additionally, I found that the size of the pinhole can affect resolution improvement in the presence of aberrations. According to my simulation results, a 1 Airy unit pinhole is opti-

mal for balancing resolution and emission efficiency. I also applied the proposed theory to explore multi-photon ISM. The results suggest that the optimal sweep factor for multi-photon ISM is not 2, as predicted by 1-photon scalar theory. Instead, for 2-photon ISM, the optimal sweep factor is 1.22, and for three-photon ISM, the optimal sweep factor is 1.17. These findings can assist users in selecting optimal hardware parameters for their microscopy setups and improving image quality.

SAMENVATTING

Super-resolutiemicroscopie heeft aangetoond de diffractielimiet te overtreffen en levert hoogwaardige beelden met hoge resolutie op. State-of-the-art super-resolutieonderzoek streeft voortdurend naar verbetering van de beeldresolutie met behulp van bestaande super-resolutietechnologie. Deze scriptie heeft tot doel de resolutie van super-resolutiemicroscopie te verbeteren door middel van geëngineerde verlichting en een solide theoretische basis te leggen om resolutieverbeteringen te ondersteunen.

In Hoofdstuk 2 bespreek ik de verbetering van de resolutie in single molecule localization microscopy voor het beeldvormen van dikke monsters. Bij dikke monsters kan het probleem van hoge achtergrondruis de precisie van de lokalisatie van single molecule localization aantasten. We introduceren Single Objective Lens Lightsheet Microscopy (SOLEIL) als oplossing om het probleem van hoge achtergrondfotonen te verminderen en daarmee de resolutie van single molecule localization microscopy te verbeteren. In vergelijking met conventionele lightsheet-microscopie maakt SOLEIL alleen gebruik van één objectieflens in het hele systeem, wat de systeemcomplexiteit aanzienlijk vereenvoudigt en het gebruiksvriendelijker maakt. We tonen aan dat de theoretische precisie van lokalisatie van SOLEIL die van widefield-microscopie en highly inclined and laminated optical sheet (HILO) microscopie overtreft bij monsters van 10 μm dik.

In Hoofdstuk 3 stel ik een beeldvormingsoplossing voor om het probleem van hoge achtergrondruis en monster-geïnduceerde aberraties bij het beeldvormen van dikke monsters aan te pakken. Bij het beeldvormen van dikke monsters kunnen monster-geïnduceerde aberraties de Point Spread Function (PSF) vervormen, wat leidt tot systematische lokalisatiebias en verminderde lokalisatieprecisie. In dit hoofdstuk stel ik voor om SOLEIL-microscopie te combineren met een sensorloze Adaptive Optics (AO) methode om deze problemen aan te pakken. De sensorloze AO-methode corrigeert monster-geïnduceerde aberraties, terwijl SOLEIL-microscopie hoge achtergrondruis in dikke monsters vermindert. Door AO en SOLEIL te combineren, tonen we een tweevoudige verbetering in axiale lokalisatieprecisie in vergelijking met widefield-microscopie met AO-correctie of SOLEIL-microscopie zonder AO-correctie.

In Hoofdstuk 4 stel ik een uitgebreide PSF-modeltheorie voor Image Scanning Microscopy (ISM) voor die volledig rekening houdt met vectoriële effecten, aberraties, Stokes-verschuivingen en Fresnel-coëfficiënten bij media-interface. Deze aanpak maakt een nauwkeurige modellering van excitatie- en emissie-PSF's mogelijk, wat precieze referenties biedt voor het selecteren van hardwareparameters en het beoordelen van beeldkwaliteit. Veel studies hebben benadrukt hoe belangrijk het is om vectoriële effecten in hoge numerieke apertuurmicroscopie te overwegen. Op basis van de voorgestelde theorie ontdekte ik dat de breedte van de ISM Point Spread Function voorspeld door de voorgestelde theorie met 30% kan afwijken van die voorspeld door scalar ISM-theorie. Bovendien ontdekte ik dat de grootte van de pinhole van invloed kan zijn op de resolutieverbetering in aanwezigheid van aberraties. Volgens mijn simulatieresultaten is

een pinhole van 1 Airy-eenheid optimaal voor het balanceren van resolutie en emissie-efficiëntie. Ik paste de voorgestelde theorie ook toe om multi-photon ISM te verkennen. De resultaten suggereren dat de optimale sweepfactor voor multi-photon ISM niet 2 is, zoals voorspeld door 1-foton scalar-theorie. In plaats daarvan is de optimale sweepfactor voor 2-foton ISM 1.22, en voor 3-foton ISM is de optimale sweepfactor 1.17. Deze bevindingen kunnen gebruikers helpen bij het selecteren van optimale hardwareparameters voor hun microscopiesetups en het verbeteren van de beeldkwaliteit.

1

INTRODUCTION

Super-resolution techniques have effectively overcome the limited resolution in fluorescence microscopy. In this section, I provide background information on conventional fluorescence microscopy, including state-of-the-art hardware and its resolution limitations. Furthermore, I explain the principles of super-resolution fluorescence microscopy. Building upon modern super-resolution technology, I address several practical challenges that limit the resolution in single-molecule localization microscopy by adopting illumination modalities incorporating adaptive optics to mitigate resolution degradation in single-molecule localization microscopy. Additionally, I will explore a structured illumination microscopy approach to enhance resolution. To establish a robust theoretical foundation, I develop a vectorial physical optical theory to simulate the point spread function in image scanning microscopy. Furthermore, I integrate pattern-enhanced single-molecule localization microscopy with machine learning to achieve high-density images, potentially increasing the image speed of single-molecule localization microscopy.

1.1. FLUORESCENCE MICROSCOPY

Fluorescence microscopy has been an essential tool in bioimaging to visualize the microstructure of the biology sample. Fluorescence microscopy acquires the fluorescence emission signal from the fluorescent molecule attached to the target structure, by which fluorescence microscopy is able to image with high sensitivity and specificity [1, 2]. To achieve this sensitivity and specificity of fluorescence microscopy, the design of fluorescence microscopy takes advantage of the physical property of the fluorescence effect.

The fluorescence effect is an optical phenomenon that occurs widely in nature, such as the fluorescence of jellyfish [3] and butterfly [4]. From the aspect of quantum physics, the Jablonski diagram describes the mechanism of fluorescence as follows [5, 6] (1) an electron in the ground state is excited by a photon and the electron absorbs the energy from the photon, (2) the excited electron jumps to the excitation state, (3) the excited electron drops back to the ground state and emits a photon. In step (3), the excited electron can experience a couple of nonradiative states and loses some energy, so the photon emitted at step (3) contains less energy than the photon excited by the electron at step (1) (Fig. 1 (a)). Because of this, the wavelengths of excitation and emission light deviate, and we call the shift between excitation and emission spectrum the Stokes shift [7] (Fig. 1 (b)).
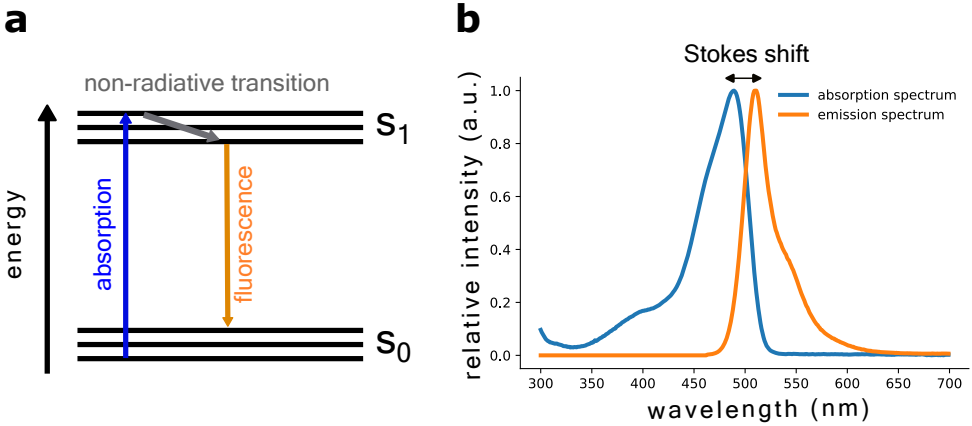
Figure 1: Figure of Jablonski diagram and fluorescence spectrum. (a)Jablonski diagram figure. S_0 stands for ground state and S_0 stands for excitation state. The arrow direction of the energy line stands for higher energy. (b) fluorescent molecule absorption and emission spectrum. The blue line stands for absorption spectrum, and the orange line stands for emission spectrum. The spectrum is plotted based on the spectrum data of EGFP from FPbase, and the data mainly comes from several works [8–10].

This stokes shift gives a clear way to optimize the sensitivity by separating the excitation and fluorescence emission light spectrally so that the image only contains the signal from the fluorescent molecule on the target structure and minimizes the light from the excitation light. A dichroic mirror is used to achieve this separation. The dichroic mirror is a coated mirror, which creates a wavelength-dependent reflectivity to separate the excitation and fluorescence signal. The basic structure of fluorescence microscopy con-

sists of excitation light, an objective lens, a tube lens, a dichroic mirror, and a filter [1] (Fig. 2 (a)). The excitation light works as the external source to pump the electrons on the fluorescent molecule to the excitation state and then emits the fluorescence signal. Combining an objective lens and tube lens can magnify the structure to visualize the microstructure on the sample. The emission filter is placed at the emission path to further filter out the excitation light from the emission light. The excitation filter is placed at the excitation path to limit the excitation spectrum. Combining an excitation and emission filter ensures the excitation light cannot leak into the emission path. A digital camera is located after the tube lens to acquire the image of the emission.
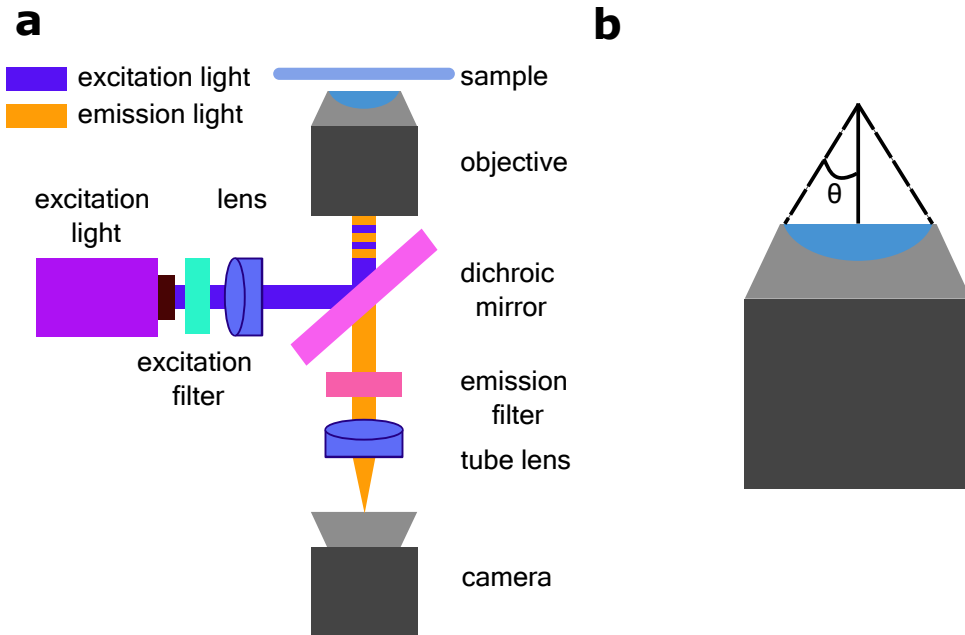
Figure 2: Basic design of widefield fluorescence microscopy and the spectrum of dichroic mirror, filter, and fluorescent molecule. (a) Basic widefield fluorescence microscopy. (b) A schematic figure for the collection angle of the objective lens (θ)

1.2. STATE-OF-ART OF FLUORESCENCE MICROSCOPY

In this section, I will introduce the state-of-the-art fluorescence microscopy hardware and explain the benefits and drawbacks of each microscopy module.

1.2.1. WIDEFIELD EPI-ILLUMINATION AND TIRF MICROSCOPY

The design of widefield epi-illumination microscopy adopts a plane wave illumination, which is achieved by focusing an excitation light on the objective's back focal plane. Widefield microscopy features a simple optical layout and adjustable field of view (FOV) size. However, as the illumination of widefield microscopy is a plane wave, the whole

sample is excited, which adds a background signal to the resulting images proportional to the thickness of the sample. Widefield microscopy is unsuitable for thick sample imaging because of the poor optical sectioning. Optical sectioning means that the illumination of microscopy only excites a thin layer of sample to avoid the high image background from an out-of-focus region. The poor optical sectioning delivers high signal-to-noise images and results in low image quality.

To address this high background issue, total internal reflection fluorescence microscopy (TIRF) is developed [11–13]. TIRF adopts an evanescent wave illumination by total internal reflection effect due to index mismatch between coverslip and sample media, where the refractive index of coverslip is typically around 1.52 and sample media is around 1.33 ~ 1.4. TIRF can achieve around 200 nm thickness in optical sectioning. The amount of optical sectioning is determined by the thickness of illumination of the sample. However, a pitfall of TIRF microscopy is that the imaging depth of TIRF is limited to circa 200 nanometres from the coverslip because it adopts a total internal reflection effect [14, 15].

1.2.2. HILO AND HIST MICROSCOPY

To alleviate the drawback of poor optical sectioning of widefield epi-illumination microscopy and maintain the possibility to image samples deeper than the TIRF region, highly inclined and laminated optical sheet (HILO) microscopy is developed [16]. HILO microscopy adopts an inclined narrow plane-wave illumination, and the thickness of optical sectioning can achieve sub-10 μm [16]. As HILO microscopy improves the optical sectioning by adopting a narrow illumination beam, the FOV of HILO microscopy is rather small, ranging around 10 ~ 50 μm in diameter.

To address the minor FOV issue, Highly inclined swept tile (HIST) microscopy is developed [17]. HIST microscopy employs a thin sheet of plane wave illumination, dynamically synchronized with the active pixels on the camera. This innovative approach enables HIST microscopy to preserve a thin optical sectioning thickness while expanding the FOV.

1.2.3. CONFOCAL AND SPINNING DISK MICROSCOPY

Confocal microscopy is developed to improve the optical sectioning of fluorescence microscopy. Confocal microscopy is an imaging method that utilizes a focused point illumination and a spatial pinhole to increase the performance of optical sectioning [18, 19]. The illumination is a focused laser spot, and the fluorescence signal is acquired by a light sensor such as a Photomultiplier Module (PMT) or an Avalanche Photodetector (APD). The intensity data for each scanning point reconstruct the image. As confocal microscopy adopts the focused laser spot as illumination, the thickness of optical sectioning can reach around 500 ~ 1000 nm, also known as the axial resolution of confocal microscopy. Although the point scanning method alleviates the background issue, the point scanning method slows down the imaging speed.

An improved modality of confocal microscopy is spinning disk microscopy [20, 21]. In spinning disk microscopy, excitation light is focused through a microlens array to achieve multiple-focus illumination, accelerating the imaging speed. The fluorescence signal of spinning disk microscopy is not acquired by a point detector but by using a digital camera.

1.2.4. LIGHT-SHEET MICROSCOPY

Light-sheet microscopy is developed to reduce the phototoxicity and reach narrow optical sectioning using a thin sheet illumination, resulting in a low imaging background [22]. Conventional light-sheet microscopy consists of two objective lenses, which are an illumination objective lens and a detection objective lens. The illumination objective lens launches the illumination shaped like a thin sheet, and the detection objective lens collects the fluorescence signal from the sample. The illumination and detection objectives are assigned in an orthogonal structure in conventional light sheet microscopy. In addition, to avoid the collision of two objective lenses, a long working distance of the detection objective is required, which limits the usage of a high NA objective lens. Tilted light sheet microscopy (TILT3D) and lateral interference tilted excitation microscope (LITE) address the low detection NA problem by adopting a tilted light-sheet illumination [23, 24]. The dual-objective lens structure of light-sheet microscopy also increases the complexity of light-sheet microscopy as it is more challenging to construct and maintain the light-sheet microscopy compared with other single-objective lens systems such as TIRF, confocal, and spin disk microscopy.

To address the complexity of light-sheet microscopy, single objective light-sheet microscopes (soSPIM) are developed [25–27]. In soSPIM, the light-sheet illumination is launched vertically from the detection objective lens, and soSPIM methods adopt a special sample holder to rotate the light-sheet illumination so that the illumination plane is aligned with the imaging plane. However, the customized sample holder significantly increases the difficulty of the experiment, and it is difficult for non-experts to adopt these methods.

To address these issues, oblique plane microscopy (OPM) is developed. The OPM adopts the tilted light-sheet illumination and two additional objective lenses in the emission path, where the final objective lenses at the emission path are rotated with an angle to rotate the imaging plane such that the ultimate imaging plane is aligned with the light-sheet illumination. OPM requires no customized sample holder or dual objective lens structure, simplifying the experiment. In addition, the rotation of the final objective lens can also reduce the effective NA of emission. To address this issue, the water-immersed and glass-tipped objective lenses are used in OPM and achieve 1.27 effective NA in emission path [28, 29]. Besides, because of the usage of the remote focusing method in OPM, the design of OPM needs to fulfill the sine and Herschel conditions [29]. Violating these two conditions causes additional aberration in the imaging [30]. To achieve both conditions, the magnification between the first and second objective lenses has to be equal to the ratio of the refractive index of the sample medium and the working environment of the second objective lens. This requirement limits the application on different samples as the refractive index of different samples could differ. Nevertheless, using multiple objective lenses at the emission path can decrease the intensity of emission light because of the transmission spectrum of the objective lens.

1.2.5. ADAPTIVE OPTICS MICROSCOPY

Adaptive optics (AO) for microscopy is developed to compensate for aberrations present in the imaging system. Examples of AO elements are the spatial light modulator (SLM) [31] and the deformable mirror (DM) [32]. The SLM is a pixel-wise phase correction

element based on liquid crystals, and a deformable mirror is a thin membrane with several actuators on the backside to deform the membrane. However, using an SLM at the emission path causes additional loss of fluorescence signal because the SLM can only respond to a specific polarization direction while the fluorescence emission is usually unpolarized.

Adaptive optical (AO) microscopy has two different ways to measure the aberrations. The first is called direct sensing AO [33–35]. The direct sensing AO uses a wavefront sensor to measure the aberration, and the adaptive element corrects the aberration based on the measurement. The pitfall of the direct sensing AO is the complexity of the system. An additional wavefront sensor and a relay system are required to measure the aberration. In addition, since a different optical path measures the aberrations, the measured aberrations can differ from the actual aberrations in the imaging path. This is called as a non-common path error [36, 37]. The second is indirect sensing AO, also called sensorless adaptive optics AO [33]. This method corrects the aberration only based on the quality of the image, such as sharpness, maximum intensity, or metric of the optical transfer function. Nevertheless, the sensorless AO method corrects aberration by the image quality, not by the wavefront sensor. Hence, it cannot ensure the corrected aberration is the actual aberration in the imaging path [38].

1.3. RESOLUTION LIMITATION OF FLUORESCENCE MICROSCOPY AND POINT SPREAD FUNCTION

The resolution of fluorescence microscopy is limited, so some microscopy images are blurred[39, 40]. The physical reason for the resolution limitation of microscopy is the diffraction limit of the wave nature of light. PSF is an optical diffraction phenomenon, which is the microscopy image when imaging an infinitely small point source [41]. Therefore, the image of the microscope can be considered as a summation of PSF from each point source. Thus, the imaging formation equation of microscopy can be written as follows [42–44]:

$$I(x, y, z) = O(x, y, z) \otimes PSF(x, y, z), \tag{1.1}$$

where $\otimes$ is convolution operator, x, y, z is the spatial position on imaging plane, I is the microscopy image, O is the object to be imaged, and PSF is point spread function. The above equation suggests that the microscopy image does not represent the original object, but the image is blurred by the PSF through the convolution operator. Hence, PSF determines the resolution in conventional microscopy image.

To understand the physical context of the PSF, we can start with the microscopy system's numerical aperture (NA). The mathematical definition of NA is:

$$NA = n \cdot \sin\theta, \tag{1.2}$$

where n is the refractive index of immersion media and θ is the maximum light collection angle of the objective lens Fig. 2 (b).

A high NA system means that the microscope can collect light that enters the system at a highly inclined angle, and low NA microscopy can only collect light with a low incoming angle. From Fourier optics theory, a high NA system means that the microscopy

system can deliver higher spatial frequency information, and the pupil function (P) of microscopy is wider. The Fourier optics interpret PSF as an autocorrelation of the pupil function. The Fourier transform of a wider pupil function leads to a narrower PSF. Thus, high NA microscopy delivers a high-resolution image.

A theoretical estimation of the full-width half maximum (FWHM) of PSF (w_{PSF}) of given NA is

$$w_{PSF} = \frac{\lambda}{2NA},\tag{1.3}$$

where λ is the wavelength of light.

The w_{PSF} is called the diffraction limit or the Abbe limitation. w_{PSF} is the highest resolution that fluorescence microscopy can achieve for a given NA. Considering the eq. 1.1, any two point sources whose distance below w_{PSF} cannot be resolved by the microscopy system.

To surpass the resolution, several important super-resolution microscopes have been developed, such as Stimulated Emission Depletion microscopy (STED) [45, 46], Structured Illumination Microscopy (SIM) [47, 48], Single-Molecule Localization Microscopy (SMLM) [49, 50], and Image Scanning Microscopy (ISM) [51, 52]. STED adopts a donut shape beam to deplete the fluorescence emission, resulting in a sub-diffraction effective excitation PSF. SIM adopts the interference of light to shift the high spatial frequency information to the low spatial frequency region and reconstructs the image, resulting in a wider OTF in the imaging system. In this thesis, I mainly focused on the latter two methods, which are SMLM and ISM. A more detailed discussion regarding these two methods is in the latter part of this thesis.

1.4. SINGLE-MOLECULE LOCALIZATION MICROSCOPY

Single-molecule localization microscopy (SMLM) is a type of super-resolution imaging technology. This section introduces the SMLM method and discusses the technology used to realize it.

1.4.1. INTRODUCTION OF SINGLE-MOLECULE LOCALIZATION MICROSCOPY

Single-molecule localization microscopy (SMLM) is a super-resolution technology that can surpass the diffraction limit by localizing the position of single-molecules with a precision higher than the diffraction limit[53]. In SMLM imaging, a special fluorescence dye, imaging buffer, or fluorophore binding and unbinding effect creates the necessary stochastic blinking of single-molecules. Examples are photoactivation [54], direct stochastic optical reconstruction microscopy (dSTORM) buffer [55–57], or DNA-PAINT sample [58, 59]. In SMLM imaging, it is usual to acquire at least several thousand frames of images to accumulate enough single-molecule data. Afterward, the localization algorithm can localize the position of each molecule with sub-10 nm precision under ideal imaging conditions, which breaks the diffraction limits. After sufficient molecules have been localized the reconstruction algorithm can render a high-resolution SMLM image.

A typical flowchart of localization algorithm is spot detection, localization, filtering, and drift correction [60].

The spot detection algorithm picks up the possible single-molecule spots from the

noised SMLM images. Some common algorithms are the Gaussian filter, a difference of the Gaussian filter, and the wavelet filter [61, 62]. These filters help the spot detection algorithm to overcome the Poisson noise in camera images. The localization algorithm estimates the position of single-molecule based on the given PSF model with sub-diffraction limit precision. Filtering discards unwanted localizations such as low photon intensity or high background noise data to improve the quality of localization imaging. The drift correction algorithm corrects the image drift from frame to frame, improving the ultimate image resolution.

1.4.2. CRAMÉR-RAO LOWER BOUND

The localization precision of SMLM determines the ultimate resolution limits of SMLM images. Based on the mathematical rule, the localization precision of the MLE algorithm is Cramér-Rao lower bound (CRLB) [60], which means that the localization algorithm cannot estimate the position of single-molecule with a better precision than CRLB. Therefore, CRLB is a crucial parameter in evaluating the quality of SMLM imaging. CRLB is shown to be sensitive to image conditions, such as image intensity and background [60]. The low-intensity or high background can deteriorate the CRLB and deliver low-resolution SMLM images. Designing proper microscopy to reduce the imaging background and choosing proper imaging parameters, such as the excitation laser's power and the camera's exposure time, are critical in SMLM.

1.4.3. LOCALIZATION ALGORITHM OF SMLM

The SMLM algorithm estimates the position of a single-molecule by fitting a known PSF model to an experiment single-molecule image. This procedure can be achieved by using the nonlinear least-squares (NLLS) [63] or maximum likelihood estimation (MLE) [60]. It is shown that in most cases, the MLE is more precise than NLLS [60] and nowadays, it is a standard method for the SMLM algorithm. NLLS methods are still widely used due to low computation cost.

In the MLE algorithm, the noise model of the image is assumed to be Poisson noise because of the physical nature of the photon [64]. Nevertheless, the camera image is rescaled by the conversion gain and offset of the camera, which breaks the Poisson noise model [65, 66]. To reconstruct the Poisson noise, the camera's conversion gain and offset need to be measured.

The relationship between the raw image frame ($x_{\mathrm{raw},i}$) and the calibrated frame ($x_{\mathrm{cal},i}$) is following:

$$x_{\mathrm{cal},i} = g \cdot \left(x_{\mathrm{raw},i} - o \right), \tag{1.4}$$

where g is the camera conversion gain and the o is camera offset.

The localization of the SMLM data-set relies on a complex algorithm. The main principle of SMLM localization algorithm is to estimate the position of single-molecule by fitting the PSF model to the single-molecule image data. Thus, using a proper PSF model is crucial as a wrong PSF model can lead to a biased localization result. In the following, I will introduce two-dimensional and three-dimensional SMLM algorithms.

TWO-DIMENSIONAL SMLM

For 2D SMLM, the Gaussian model is widely used, and the robustness is well-proved, although the ground-truth PSF model is not a Gaussian function. The estimates are $\hat{\theta} = (\theta_x, \theta_y, \theta_I, \theta_{bg})$, where θ_x, θ_y are the position of single-molecule, θ_I is the intensity of single-molecule, and θ_{bg} is the background of single-molecule per pixel. It is shown that if the aberration of PSF is lower than 72 $m\lambda$, the experimental localization precision matches the CRLB of the Gaussian PSF model, and the Gaussian PSF model is still a valid model[67].

THREE-DIMENSIONAL SMLM

For the 3D SMLM, many algorithms are proposed for different modalities. For astigmatism-based PSF, a commonly used method to determine the axial position of a single-molecule relies on analyzing the x and y-axis widths of the astigmatism PSF [53, 60]. For a general PSF model such as double-helix or tetrapod PSF, aberration PSF estimator such as ZOLA3D [68], vectorFitter [69], and VIPR [70] can deliver high precision localization. The aberration PSF model builds the PSF based on the pupil phase aberration, which can theoretically simulate an arbitrary PSF model. However, it relies on a comprehensive physical model to simulate the high NA PSF. To address this issue, a pure experiential PSF model, the cubic spline (cspline) model, is developed [71, 72]. Nevertheless, all of the above methods rely on a pre-calibrated PSF model for localization. In practice, the sample-induced aberration can distort the PSF, causing the localization bias [73] and can deteriorate the axial CRLB of the PSF model. The in situ PSF retrieval (INSPR) PSF model can retrieve the PSF model by the blinking data directly, which can avoid the mismatch between the imaging PSF and calibrated PSF model [74]. However, the INSPR cannot restore the loss of axial CRLB out of the index-mismatching aberration.

1.5. STRUCTURED ILLUMINATION MICROSCOPY AND IMAGE SCANNING MICROSCOPY

Structured Illumination Microscopy (SIM) [47] and Image Scanning Microscopy (ISM) [75] are both super-resolution microscopy techniques employing patterned illumination. However, it is crucial to distinguish their unique attributes. SIM harnesses a spatially modulated excitation intensity distribution, achieved through the interference of two plane waves, yielding a periodic sinusoidal function. This distinctive illumination allows the optical system to capture spatial frequencies beyond the numerical aperture's constraints. To reconstruct high-resolution SIM images, it necessitates multiple illumination patterns with varying phases and orientations. Typically, SIM delivers a twofold enhancement in resolution compared to conventional widefield microscopy [47, 48].

In contrast, ISM adopts a point-scanning approach, utilizing single or multiple focused spots as its illumination pattern [52, 75, 76]. ISM's hardware closely resembles that of confocal microscopy, but it deviates from its use of an image sensor for capture and subsequent image reconstruction via pixel reassignment. A preliminary

estimate suggests that ISM can achieve a $\sqrt{2}$ resolution improvement over widefield microscopy. Furthermore, ISM benefits from Fourier re-weighting [52], an ISM-specific deconvolution technique, enabling it to enhance twofold resolution. Nevertheless, ISM microscopy lacks a comprehensive physical model that considers the polarization effect, aberration, and the Stokes shift, which limits the user from determining the optimal hardware parameters and accessing the quality of microscopy images.

1.6. Pattern-enhanced single-molecule localization microscopy

The resolution of Single-Molecule Localization Microscopy (SMLM) is inherently constrained by the Cramér-Rao Lower Bound (CRLB), primarily when Poisson noise characterizes the noise model. The CRLB's limitations are influenced by various factors, including the photon count emitted by the molecule, the background photon level, and the Point Spread Function's (PSF) width. Notably, under ideal imaging conditions, the positional CRLB (Δx_{SMLM}) exhibits an approximate proportionality to the PSF width (σ) divided by the square root of the photon count from the emitter (N) [77]:

$$\Delta x_{\text{SMLM}} = \frac{\sigma}{\sqrt{N}} \tag{1.5}$$

The photon count signifies the information available to determine the position of a single emitter. To mitigate this limitation, pattern-enhanced single-molecule localization microscopy (PE-SMLM) has been introduced. The fundamental concept behind PE-SMLM involves encoding molecule position information through intensity data. This additional information aids the estimator in accurately determining the position of a single molecule.

The pioneering PE-SMLM technique, known as MINFLUX [78, 79], employs a donut-shaped excitation beam inspired by STED microscopy. When a molecule resides in different regions of the donut-shaped beam, its fluorescence intensity varies. MINFLUX adopts triangulation within an interval size (L) to pinpoint the precise location of a single-molecule. With this modulation, the CRLB of MINFLUX ($\Delta x_{\text{MINFLUX}}$) is determined by the interval size divided by the square root of the photon count from the emitter:

$$\Delta x_{\text{MINFLUX}} = \frac{L}{\sqrt{N}} \tag{1.6}$$

Remarkably, the scanning range of the donut-shaped beam is approximately 10 nm, a significant enhancement compared to the width of the PSF (approximately 200 nm).

An iterative MINFLUX approach has been developed to further enhance the resolution of MINFLUX. Iterative MINFLUX gradually reduces the scanning range of the donut-shaped beam in successive iterations, ultimately achieving a resolution of 1-3 nm based on published research [78, 79]. However, it's important to note that in both MINFLUX and iterative MINFLUX, only one emitter can be imaged in each iteration. Since reconstructing an SMLM image typically requires approximately one million localizations, and

each localization takes 30 ms in MINFLUX [80], this presents a challenge regarding imaging speed.

To address this challenge, SIMFLUX was introduced [81]. SIMFLUX utilizes a structured illumination pattern along the x- and y-axes and shifts the pattern through three phases for each axis. Single-molecule position information is encoded in the variation of single-molecule intensity across the six illumination patterns. Unlike MINFLUX, SIMFLUX's illumination approach is broader, enabling the detection of multiple molecules in each frame. In summary, SIMFLUX achieves a twofold improvement in resolution compared to conventional SMLM. It balances imaging speed and resolution enhancement, offering a practical solution to maintain both imaging speed and resolution quality.

1.7. THESIS MOTIVATION

In this section, I elucidate three critical factors that have the potential to degrade the quality of super-resolution imaging or expose inadequacies in current SMLM and ISM super-resolution methods. These factors serve as the the motivation for this thesis.

HIGH IMAGING BACKGROUND
The CRLB of localization determines the ultimate resolution of SMLM images. As reported in a previous paper [60], a high imaging background can deteriorate the CRLB, which leads to poor resolution. In tissue imaging, the out-of-focus fluorescence and auto-fluorescence can cause a high background in the SMLM imaging. In state-of-the-art research, the light-sheet methods are widely used to alleviate the problem [24, 25]. However, these methods rely on multiple objectives for light-sheet illumination [24] or customized nano-fabrication sample holders for single objective light-sheet imaging [25]. Besides, the size of the FOV of these methods is limited by the Rayleigh length of the light sheet, which originates from the physics of the Gaussian beam.

SAMPLE-INDUCED ABERRATION
The localization algorithm of SMLM relies on the PSF model for accurate localization, the distortion of PSF caused by the sample-induced aberration can cause a systematic localization bias and the deterioration on CRLB [73]. In addition, the index-mismatch aberration can further deteriorate the axial localization CRLB, reducing the axial imaging resolution.
Some algorithms claim to address the localization bias caused by the sample aberration. The depth-dependent PSF model conducts a post-correction on the axial localization bias by a pre-calibrated lookup table [73]. The INSPR algorithm can alleviate the bias by directly calibrating the PSF model based on blinking data. However, the above methods cannot address the loss of the axial CRLB caused by the sample-induced aberration.

INSUFFICIENT PHYSICAL MODEL IN ISM PSF
To correctly model the PSF in the microscopy system, the polarization effect, Fresnel coefficient at the different interfaces, Stokes shifts, and aberration must be considered

in the PSF modeling. Some previous research has worked on modeling ISM PSF, but none of them are comprehensive physical models for ISM PSF. While some studies have contributed to the scalar PSF model with aberration-free modeling [52, 82], the Stokes shift effect [83], vectorial effects for PSF-engineered ISM [84], and multiphoton excitation ISM [85–88], the previous ISM PSF modeling are insufficient because they didn't fully consider all physical effect in the microscopy system.

1.8. OUTLINE

In this section, I list the contents of the upcoming chapters and elucidate their interconnection with the motivation behind the thesis, demonstrating how they address the issues highlighted in the thesis motivation section.

CHAPTER 2

Chapter 2 describes a novel single-objective light-sheet microscopy, SOLEIL: Single-objective lens inclined light sheet localization microscopy, which aims to address the high background issue in tissue imaging. SOLEIL adopts an inclined light-sheet illumination to achieve optical sectioning and a stepping illumination method based on a galvo mirror. An optimization scheme is proposed in Chapter 2 to achieve optimal optical sectioning. Compared with the soSPIM method, SOLEIL adopts a conventional microscopy mounting and doesn't rely on the complex customized sample holder. In addition, SOLEIL doesn't adopt a multiple objective lens structure in the emission path to avoid the loss of emission photons and aberration caused by lens stack in the emission path. SOLEIL demonstrates an improvement in intensity to background ratio and, thus, the improvement in CRLB in different samples. In the thick sample imaging, we observe a 374% higher intensity to background ratio compared to widefield epi-illumination microscopy.

This chapter is based on the following publication:

Shih-Te Hung, Jelmer Cnossen, Daniel Fan, Marijn Siemons, Daphne Jurriens, Kristin Grußmayer, Oleg Soloviev, Lukas C. Kapitein, and Carlas S. Smith, "SOLEIL: single-objective lens inclined light sheet localization microscopy," Biomed. Opt. Express 13, 3275-3294

CHAPTER 3

The sample-induced aberration is another problematic issue in tissue imaging. In Chapter 3, I proposed a synergistic solution, AO-SOLEIL, to address the high background problem and sample-induced aberration in tissue imaging. AO-SOLEIL adopts the SOLEIL microscopy illumination to mitigate the high background problem, uses the sensorless AO method to correct the sample-induced aberration, and uses the In Situ Point Spread Function Retrieval (INSPR) algorithm to calibrate an accurate PSF model to avoid a localization bias. In Chapter 3, it is proved that the index mismatch aberration can deteriorate the axial CRLB. Although adopting the INSPR algorithm can prevent the localization bias caused by sample-induced aberration, the loss of CRLB cannot be mitigated by the INSPR. Therefore, AO-SOLEIL combines the sensorless AO method to

correct the sample-induced aberration and adopts the INSPR algorithm to calibrate the PSF. The reason for adopting INSPR is that we realize that the sensorless AO algorithm cannot correct all aberrations, especially in high background situations. Thus, adopting INSPR to calibrate the PSF can avoid residual aberration. In addition, the SOLEIL illumination improves image quality and improves the localization of CRLB. We verify AO-SOLEIL in several thick samples, including adult Drosophila brains, and it shows a twofold improvement in axial CRLB.

This chapter is based on the following publication:

Shih-Te Hung, Arnau Llobet Rosell, Daphne Jurriens, Marijn Siemons, Oleg Soloviev, Lukas C. Kapitein, Kristin Grußmayer, Lukas J. Neukomm, Michel Verhaegen, Carlas Smith, "Adaptive Optics in Single Objective Inclined Light Sheet Microscopy Enables Three-Dimensional Localization Microscopy in Adult Drosophila Brains." Frontiers in Neuroscience, vol. 16, 6 Oct. 2022

Chapter 4

In Chapter 4, I propose a comprehensive physical model for the PSF of image scanning microscopy. Compared with the previous research, this model considers the polarization effect, supports variant excitation and emission wavelength, and aberration effect. In Chapter 4, it is proved that in a high NA situation, the polarization effect can affect the PSF model significantly. Chapter 4 also describes how the system aberration can deteriorate the ISM PSF and, thus, the imaging resolution. A finding in the simulation proves that a small pinhole can mitigate the PSF deterioration, and a 1 Airy unit of the pinhole is the optimal trade-off between the PSF and emission efficiency. Because of the support for variant excitation and emission wavelength, I also use the proposed model to simulate the multiphoton excitation ISM, and it shows that the multiphoton excitation can decrease the improvement factor of ISM over widefield microscopy. An important finding on multiphoton ISM is that the optimal sweep factor is not two, predicted by scalar 1-photon theory, but 1.22 for 2-photon ISM and 1.17 for 3-photon ISM. With this model, a more comprehensive and detailed physics of ISM PSF is described.

This chapter is based on the following publication:

Shih-Te Hung, Dylan Kalisvaart, and Carlas Smith, "Image scanning microscopy: a vectorial physical optics analysis," Opt. Express 32, 2024

BIBLIOGRAPHY

1. Lichtman, J. W. & Conchello, J.-A. Fluorescence microscopy. *Nature Methods* **2,** 910–919. https://www.nature.com/articles/nmeth817 (Nov. 2005).

2. Sanderson, M. J., Smith, I., Parker, I. & Bootman, M. D. Fluorescence Microscopy. *Cold Spring Harbor Protocols* **2014,** pdb.top071795–pdb.top071795. https://www.ncbi.nlm.nih.gov/pmc/articles/PMC4711767/ (Oct. 2014).

3. Tsien, R. Y. The green fluorescent protein. *Annual Review of Biochemistry* **67,** 509–544. https://www.annualreviews.org/doi/10.1146/annurev.biochem.67.1.509 (June 1998).

4. Vukusic, P. & Hooper, I. Directionally Controlled Fluorescence Emission in Butterflies. *Science* **310,** 1151–1151. https://www.science.org/doi/10.1126/science.1116612 (Nov. 2005).

5. Jablonski, A. Efficiency of Anti-Stokes Fluorescence in Dyes. *Nature* **131,** 839–840. https://www.nature.com/articles/131839b0 (June 1933).

6. Atkins, P. W. & Paula, J. D. *Physical chemistry* (W.H. Freeman, 2006).

7. Lakowicz, J. R. *Principles of Fluorescence Spectroscopy* (Springer Us, 2006).

8. Cormack, B. P., Valdivia, R. H. & Falkow, S. FACS-optimized mutants of the green fluorescent protein (GFP). *Gene* **173,** 33–38. https://www.sciencedirect.com/science/article/pii/0378111995006850 (Jan. 1996).

9. Myšková, J. *et al.* Directionality of light absorption and emission in representative fluorescent proteins. *Proceedings of the National Academy of Sciences* **117,** 32395–32401. https://www.pnas.org/doi/10.1073/pnas.2017379117 (Dec. 2020).

10. Sarkisyan, K. S. *et al.* Green Fluorescent Protein with Anionic Tryptophan-Based Chromophore and Long Fluorescence Lifetime. *Biophysical Journal* **109,** 380–389. https://www.cell.com/biophysj/fulltext/S0006-3495(15)00600-1 (July 2015).

11. Fish, K. N. Total Internal Reflection Fluorescence (TIRF) Microscopy. *Current Protocols in Cytometry.* https://currentprotocols.onlinelibrary.wiley.com/doi/10.1002/0471142956.cy1218s50 (Oct. 2009).

12. Axelrod, D. Cell-substrate contacts illuminated by total internal reflection fluorescence. *The Journal of Cell Biology* **89,** 141–145. https://rupress.org/jcb/article/89/1/141/59168/Cell-substrate-contacts-illuminated-by-total (Apr. 1981).

13. Mattheyses, A. L. & Axelrod, D. Direct measurement of the evanescent field profile produced by objective-based total internal reflection fluorescence. *Journal of Biomedical Optics* **11,** 014006. https://doi.org/10.1117/1.2161018 (2006).

1

14. Axelrod, D. Total Internal Reflection Fluorescence Microscopy in Cell Biology. *Traffic* **2,** 764–774. https://onlinelibrary.wiley.com/doi/abs/10.1034/j.1600-0854.2001.21104.x (2001).

15. Schneckenburger, H. Total internal reflection fluorescence microscopy: technical innovations and novel applications. *Current Opinion in Biotechnology* **16.** Analytical biotechnology, 13–18. ISSN: 0958-1669. https://www.sciencedirect.com/science/article/pii/S0958166904001697 (2005).

16. Tokunaga, M., Imamoto, N. & Sakata-Sogawa, K. Highly inclined thin illumination enables clear single-molecule imaging in cells. *Nature Methods* **5,** 159–161. https://www.nature.com/articles/nmeth1171 (Jan. 2008).

17. Tang, J. & Han, K. Y. Extended field-of-view single-molecule imaging by highly inclined swept illumination. *Optica* **5,** 1063–1069. https://opg.optica.org/optica/abstract.cfm?URI=optica-5-9-1063 (Sept. 2018).

18. Bates, M., Huang, B. & Zhuang, X. Super-resolution microscopy by nanoscale localization of photo-switchable fluorescent probes. *Current Opinion in Chemical Biology* **12,** 505–514. https://www.sciencedirect.com/science/article/abs/pii/S1367593108001233 (Oct. 2008).

19. Jerome, (& Price, R. L. *Basic Confocal Microscopy* (Springer, Oct. 2018).

20. lchihara, A. *et al.* High-Speed Confocal Fluorescence Microscopy Using a Nipkow Scanner with Microlenses for 3-D Imaging of Single Fluorescent Molecule in Real Time. *bioimages* **4,** 57–62. https://www.jstage.jst.go.jp/article/bioimages/4/2/4_57/_article/-char/ja/ (1996).

21. Nakano, A. Spinning-disk Confocal Microscopy — A Cutting-Edge Tool for Imaging of Membrane Traffic. *Cell Structure and Function* **27,** 349–355. https://www.jstage.jst.go.jp/article/csf/27/5/27_5_349/_pdf/-char/en (2002).

22. Power, R. M. & Huisken, J. A guide to light-sheet fluorescence microscopy for multiscale imaging. *Nature Methods* **14,** 360–373 (Apr. 2017).

23. Fadero, T. C. *et al.* LITE microscopy: Tilted light-sheet excitation of model organisms offers high resolution and low photobleaching. *Journal of Cell Biology* **217,** 1869–1882. ISSN: 0021-9525. eprint: https://rupress.org/jcb/article-pdf/217/5/1869/1378296/jcb_201710087.pdf. https://doi.org/10.1083/jcb.201710087 (Feb. 2018).

24. Gustavsson, A.-K., Petrov, P. N., Lee, M. Y., Shechtman, Y. & Moerner, W. E. 3D single-molecule super-resolution microscopy with a tilted light sheet. *Nature Communications* **9** (Jan. 2018).

25. Meddens, M. B. M. *et al.* Single objective light-sheet microscopy for high-speed whole-cell 3D super-resolution. *Biomed. Opt. Express* **7,** 2219–2236. https://opg.optica.org/boe/abstract.cfm?URI=boe-7-6-2219 (June 2016).

26. Galland, R. *et al.* 3D high- and super-resolution imaging using single-objective SPIM. *Nature Methods* **12,** 641–644 (May 2015).

27. Zagato, E. *et al.* Microfabricated devices for single objective single plane illumination microscopy (SoSPIM). *Opt. Express* **25,** 1732–1745. https://opg.optica.org/oe/abstract.cfm?URI=oe-25-3-1732 (Feb. 2017).

28. Sapoznik, E., Chang, B.-J. & Huh, J. A versatile oblique plane microscope for large-scale and high-resolution imaging of subcellular dynamics. *eLife* **9** (eds Lakadamyali, M., Akhmanova, A. & Power, R.) e57681. ISSN: 2050-084X. https://doi.org/10.7554/eLife.57681 (Nov. 2020).

29. Yang, B. *et al.* Epi-illumination SPIM for volumetric imaging with high spatial-temporal resolution. *Nature Methods* **16,** 501–504. https://www.nature.com/articles/s41592-019-0401-3 (June 2019).

30. Botcherby, E. J., Juškaitis, R., Booth, M. J. & Wilson, T. An optical technique for remote focusing in microscopy. *Optics Communications* **281,** 880–887. https://www.sciencedirect.com/science/article/pii/S003040180701005X (Feb. 2008).

31. Maurer, C., Jesacher, A., Bernet, S. & Ritsch-Marte, M. What spatial light modulators can do for optical microscopy. *Laser* & *Photonics Reviews* **5,** 81–101. https://onlinelibrary.wiley.com/doi/abs/10.1002/lpor.200900047 (Dec. 2010).

32. Bifano, T. MEMS deformable mirrors. *Nature Photonics* **5,** 21–23. https://www.nature.com/articles/nphoton.2010.297 (Jan. 2011).

33. Booth, M. J. Adaptive optical microscopy: the ongoing quest for a perfect image. *Light: Science* & *Applications* **3,** e165–e165. https://www.nature.com/articles/lsa201446 (Apr. 2014).

34. Ji, N. Adaptive optical fluorescence microscopy. *Nature Methods* **14,** 374–380. https://www.nature.com/articles/nmeth.4218.pdf (Apr. 2017).

35. Azucena, O. *et al.* Wavefront aberration measurements and corrections through thick tissue using fluorescent microsphere reference beacons. *Opt. Express* **18,** 17521–17532. https://opg.optica.org/oe/abstract.cfm?URI=oe-18-16-17521 (Aug. 2010).

36. Ren, D., Dong, B., Zhu, Y. & Christian, D. J. Correction of Non–Common-Path Error for Extreme Adaptive Optics. *Publications of the Astronomical Society of the Pacific* **124,** 247–253. https://iopscience.iop.org/article/10.1086/664947 (Mar. 2012).

37. Fusco, T. *et al.* Design of the extreme AO system for SPHERE, the planet finder instrument of the VLT. *Proceedings of SPIE* **6272.** https://www.spiedigitallibrary.org/conference-proceedings-of-spie/6272/1/Design-of-the-extreme-AO-system-for-SPHERE-the-planet/10.1117/12.670794.short (June 2006).

38. Hu, Q. *et al.* A universal framework for microscope sensorless adaptive optics: Generalized aberration representations. *APL photonics* **5.** https://pubs.aip.org/aip/app/article/5/10/100801/238210/A-universal-framework-for-microscope-sensorless (Oct. 2020).

39. Rayleigh. XXXI. Investigations in optics, with special reference to the spectroscope. *The London, Edinburgh, and Dublin Philosophical Magazine and Journal of Science* **8,** 261–274. `https://adsabs.harvard.edu/full/1880MNRAS..40..254R` (Oct. 1879).

40. Rayleigh, L. V. Investigations in optics, with special reference to the spectroscope. *The London, Edinburgh, and Dublin Philosophical Magazine and Journal of Science* **9,** 40–55. `https://www.tandfonline.com/doi/abs/10.1080/14786448008626795` (Jan. 1880).

41. Born, M., Wolf, E. & Bhatia, A. B. *Principles of optics electromagnetic theory of propagation, interference and diffraction of light* `https://www.cambridge.org/core/books/principles-of-optics/D12868B8AE26B83D6D3C2193E94FFC32` (Cambridge Cambridge Univ. Press, 2016).

42. Lal, A., Shan, C. & Xi, P. Structured Illumination Microscopy Image Reconstruction Algorithm. *IEEE Journal of Selected Topics in Quantum Electronics* **22,** 50–63. `https://ieeexplore.ieee.org/abstract/document/7400963` (July 2016).

43. Sarder, P. & Nehorai, A. Deconvolution methods for 3-D fluorescence microscopy images. *IEEE Signal Processing Magazine* **23,** 32–45 (May 2006).

44. Agard, D. A., Hiraoka, Y., Shaw, P. & Sedat, J. W. *Chapter 13 Fluorescence Microscopy in Three Dimensions* (eds Taylor, D. L. & Wang, Y.-L.) ScienceDirect, Jan. 1989. `https://www.sciencedirect.com/science/article/abs/pii/S0091679X08609863?via%3Dihub`.

45. Willig, K. I., Harke, B., Medda, R. & Hell, S. W. STED microscopy with continuous wave beams. *Nature Methods* **4,** 915–918. (2022) (Oct. 2007).

46. Vicidomini, G., Bianchini, P. & Diaspro, A. STED super-resolved microscopy. *Nature Methods* **15,** 173–182 (Jan. 2018).

47. Gustafsson, M. G. L. Surpassing the lateral resolution limit by a factor of two using structured illumination microscopy. *Journal of Microscopy* **198,** 82–87. `https://onlinelibrary.wiley.com/doi/10.1046/j.1365-2818.2000.00710.x` (May 2000).

48. Smith, C. S. *et al.* Structured illumination microscopy with noise-controlled image reconstructions. *Nature Methods* **18,** 821–828. `https://www.nature.com/articles/s41592-021-01167-7` (June 2021).

49. Rust, M. J., Bates, M. & Zhuang, X. Sub-diffraction-limit imaging by stochastic optical reconstruction microscopy (STORM). *Nature Methods* **3,** 793–796 (Aug. 2006).

50. Smith, C. S., Joseph, N., Rieger, B. & Lidke, K. A. Fast, single-molecule localization that achieves theoretically minimum uncertainty. *Nature Methods* **7,** 373–375. `https://www.nature.com/articles/nmeth.1449` (2022) (May 2010).

51. Müller, C. B. & Enderlein, J. Image Scanning Microscopy. *Physical Review Letters* **104** (May 2010).

52. Schulz, O. *et al.* Resolution doubling in fluorescence microscopy with confocal spinning-disk image scanning microscopy. *Proceedings of the National Academy of Sciences* **110,** 21000–21005. https://www.pnas.org/doi/full/10.1073/pnas.1315858110 (Dec. 2013).

53. Huang, B., Wang, W., Bates, M. & Zhuang, X. Three-dimensional Super-resolution Imaging by Stochastic Optical Reconstruction Microscopy. *Science (New York, N.Y.)* **319,** 810–813. https://www.ncbi.nlm.nih.gov/pmc/articles/PMC2633023/ (Feb. 2008).

54. Betzig, E. *et al.* Imaging Intracellular Fluorescent Proteins at Nanometer Resolution. *Science* **313,** 1642–1645. https://www.science.org/doi/10.1126/science.1127344 (Sept. 2006).

55. Van de Linde, S. *et al.* Direct stochastic optical reconstruction microscopy with standard fluorescent probes. *Nature Protocols* **6,** 991–1009. https://www.nature.com/articles/nprot.2011.336 (June 2011).

56. Heilemann, M. *et al.* Subdiffraction-Resolution Fluorescence Imaging with Conventional Fluorescent Probes. *Angewandte Chemie* **47,** 6172–6176. https://onlinelibrary.wiley.com/doi/10.1002/anie.200802376 (Aug. 2008).

57. Heilemann, M., van de Linde, S., Mukherjee, A. & Sauer, M. Super-Resolution Imaging with Small Organic Fluorophores. *Angewandte Chemie International Edition* **48,** 6903–6908. https://onlinelibrary.wiley.com/doi/10.1002/anie.200902073 (Sept. 2009).

58. Schnitzbauer, J., Strauss, M. T., Schlichthaerle, T., Schueder, F. & Jungmann, R. Super-resolution microscopy with DNA-PAINT. *Nature Protocols* **12,** 1198–1228. https://www.nature.com/articles/nprot.2017.024 (May 2017).

59. Dai, M., Jungmann, R. & Yin, P. Optical imaging of individual biomolecules in densely packed clusters. *Nature Nanotechnology* **11,** 798–807. https://www.nature.com/articles/nnano.2016.95 (July 2016).

60. Smith, C. S., Joseph, N., Rieger, B. & Lidke, K. A. Fast, single-molecule localization that achieves theoretically minimum uncertainty. *Nature Methods* **7,** 373–375. https://www.nature.com/articles/nmeth.1449 (May 2010).

61. Ovesný, M., Křížek, P., Borkovec, J., Švindrych, Z. & Hagen, G. M. ThunderSTORM: a comprehensive ImageJ plug-in for PALM and STORM data analysis and super-resolution imaging. *Bioinformatics* **30,** 2389–2390. https://academic.oup.com/bioinformatics/article/30/16/2389/2748167 (May 2014).

62. Ries, J. SMAP: a modular super-resolution microscopy analysis platform for SMLM data. *Nature Methods* **17,** 870–872 (Aug. 2020).

63. Thompson, R. E., Larson, D. R. & Webb, W. W. Precise Nanometer Localization Analysis for Individual Fluorescent Probes. *Biophysical Journal* **82,** 2775–2783. https://www.sciencedirect.com/science/article/pii/S000634950275618X (May 2002).

1

64. Hasinoff, S. W. Photon, Poisson Noise. *Computer Vision,* 608–610. `https://link.springer.com/referenceworkentry/10.1007/978-0-387-31439-6_482` (2014).

65. Mullikin, J. C., van Vliet, L. J., Netten, H., Boddeke, F. R. & Young, I. S. Methods for CCD camera characterization. *Image Acquisition and Scientific Imaging Systems* **2173.** `https://www.spiedigitallibrary.org/conference-proceedings-of-spie/2173/1/Methods-for-CCD-camera-characterization/10.1117/12.175165.short` (May 1994).

66. Heintzmann, R., Relich, P. K., Nieuwenhuizen, R. P. J., Lidke, K. A. & Rieger, B. *Calibrating photon counts from a single image* arXiv.org, Mar. 2018. `https://arxiv.org/abs/1611.05654`.

67. Stallinga, S. & Rieger, B. Accuracy of the Gaussian Point Spread Function model in 2D localization microscopy. *Opt. Express* **18,** 24461–24476. `https://opg.optica.org/oe/abstract.cfm?URI=oe-18-24-24461` (Nov. 2010).

68. Aristov, A., Lelandais, B., Rensen, E. & Zimmer, C. ZOLA-3D allows flexible 3D localization microscopy over an adjustable axial range. *Nature Communications* **9,** 2409. `https://www.nature.com/articles/s41467-018-04709-4` (June 2018).

69. Siemons, M., Hulleman, C. N., Thorsen, R. Ø., Smith, C. S. & Stallinga, S. High precision wavefront control in point spread function engineering for single emitter localization. *Optics Express* **26,** 8397–8416. `https://opg.optica.org/oe/fulltext.cfm?uri=oe-26-7-8397&id=383954` (Apr. 2018).

70. Ferdman, B. *et al.* VIPR: vectorial implementation of phase retrieval for fast and accurate microscopic pixel-wise pupil estimation. *Optics Express* **28,** 10179–10179. `https://opg.optica.org/oe/fulltext.cfm?uri=oe-28-7-10179&id=429442` (Mar. 2020).

71. Babcock, H. P. & Zhuang, X. Analyzing Single Molecule Localization Microscopy Data Using Cubic Splines. *Scientific Reports* **7.** `https://www.nature.com/articles/s41598-017-00622-w` (Apr. 2017).

72. Li, Y. *et al.* Real-time 3D single-molecule localization using experimental point spread functions. *Nature Methods* **15,** 367–369. `https://www.nature.com/articles/nmeth.4661` (May 2018).

73. Li, Y., Wu, Y.-L., Hoess, P., Mund, M. & Ries, J. Depth-dependent PSF calibration and aberration correction for 3D single-molecule localization. *Biomedical Optics Express* **10,** 2708–2718. `https://opg.optica.org/boe/fulltext.cfm?uri=boe-10-6-2708&id=412042` (June 2019).

74. Xu, F. *et al.* Three-dimensional nanoscopy of whole cells and tissues with in situ point spread function retrieval. *Nature Methods* **17,** 531–540. `https://www.nature.com/articles/s41592-020-0816-x` (May 2020).

75. Müller, C. B. & Enderlein, J. Image Scanning Microscopy. *Physical Review Letters* **104.** `https://journals.aps.org/prl/abstract/10.1103/PhysRevLett.104.198101` (May 2010).

76. York, A. *et al.* Instant super-resolution imaging in live cells and embryos via analog image processing. *Nature Methods* **10,** 1122–1126. https://www.nature.com/articles/nmeth.2687 (Nov. 2013).

77. Hess, S. T., Girirajan, T. P. & Mason, M. D. Ultra-High Resolution Imaging by Fluorescence Photoactivation Localization Microscopy. *Biophysical Journal* **91,** 4258–4272. https://www.cell.com/biophysj/fulltext/S0006-3495(06)72140-3?_returnURL=https%3A%2F%2Flinkinghub.elsevier.com%2Fretrieve%2Fpii%2FS0006349506721403%3Fshowall%3Dtrue (Dec. 2006).

78. Gwosch, K. C. *et al.* MINFLUX nanoscopy delivers 3D multicolor nanometer resolution in cells. *Nature Methods* **17,** 217–224. https://www.nature.com/articles/s41592-019-0688-0 (Jan. 2020).

79. Balzarotti, F. *et al.* Nanometer resolution imaging and tracking of fluorescent molecules with minimal photon fluxes. *Science* **355,** 606–612. https://www.science.org/doi/10.1126/science.aak9913 (Dec. 2016).

80. Schmidt, R. *et al.* MINFLUX nanometer-scale 3D imaging and microsecond-range tracking on a common fluorescence microscope. *Nature Communications* **12.** https://www.nature.com/articles/s41467-021-21652-z (Mar. 2021).

81. Cnossen, J. *et al.* Localization microscopy at doubled precision with patterned illumination. *Nature Methods* **17,** 59–63. https://www.nature.com/articles/s41592-019-0657-7 (Jan. 2020).

82. Luca, G. M. D. *et al.* Re-scan confocal microscopy: scanning twice for better resolution. *Biomed. Opt. Express* **4,** 2644–2656. http://opg.optica.org/boe/abstract.cfm?URI=boe-4-11-2644 (Nov. 2013).

83. Sheppard, C. J. R., Mehta, S. B. & Heintzmann, R. Superresolution by image scanning microscopy using pixel reassignment. *Opt. Lett.* **38,** 2889–2892. https://opg.optica.org/ol/abstract.cfm?URI=ol-38-15-2889 (Aug. 2013).

84. Wang, W. *et al.* Image scanning microscopy with a long depth of focus generated by an annular radially polarized beam. *Opt. Express* **28,** 39288–39298. https://opg.optica.org/oe/abstract.cfm?URI=oe-28-26-39288 (Dec. 2020).

85. Gregor, I. *et al.* Rapid nonlinear image scanning microscopy. *Nature Methods* **14,** 1087–1089. https://www.nature.com/articles/nmeth.4467 (Nov. 2017).

86. Tzang, O., Feldkhun, D., Agrawal, A., Jesacher, A. & Piestun, R. Two-photon PSF-engineered image scanning microscopy. *Optics Letters* **44,** 895. https://opg.optica.org/ol/abstract.cfm?uri=ol-44-4-895 (Feb. 2019).

87. Koho, S. V. *et al.* Two-photon image-scanning microscopy with SPAD array and blind image reconstruction. *Biomedical Optics Express* **11,** 2905. https://opg.optica.org/boe/fulltext.cfm?uri=boe-11-6-2905&id=431589 (May 2020).

88. Sheppard, C. J. R. *et al.* Image scanning microscopy with multiphoton excitation or Bessel beam illumination. *Journal of the Optical Society of America A* **37,** 1639. https://opg.optica.org/josaa/abstract.cfm?uri=josaa-37-10-1639 (Sept. 2020).

2

SOLEIL: SINGLE OBJECTIVE LENS LIGHTSHEET MICROSCOPY

High-NA light sheet illumination can improve the resolution of single-molecule localization microscopy (SMLM) by reducing the background fluorescence. These approaches currently require custom-made sample holders or additional specialized objectives, which makes the sample mounting or the optical system complex and therefore reduces the usability of these approaches. Here, we developed a single-objective lens-inclined light sheet microscope (SOLEIL) that is capable of 2D and 3D SMLM in thick samples. SOLEIL combines oblique illumination with point spread function PSF engineering to enable dSTORM imaging in a wide variety of samples. SOLEIL is compatible with standard sample holders and off-the-shelve optics and standard high NA objectives. To accomplish optimal optical sectioning we show that there is an ideal oblique angle and sheet thickness. Furthermore, to show what optical sectioning delivers for SMLM we benchmark SOLEIL against widefield and HILO microscopy with several biological samples. SOLEIL delivers in 15 μm thick Caco2-BBE cells a 374% higher intensity to background ratio and a 54% improvement in the estimated CRLB compared to widefield illumination, and a 184% higher intensity to background ratio and a 20% improvement in the estimated CRLB compared to HILO illumination.

2.1. INTRODUCTION

Single-molecule localization microscopy (SMLM) has been shown to surpass the diffraction limit and has become an important imaging technology for biological research [1–6]. SMLM overcomes the diffraction limit by localizing sparsely activated single molecules. The ultimate resolution of an SMLM reconstruction is limited not by the optical resolution, but by the localization uncertainty and the localization density of the single molecules [7]. The theoretical minimum localization uncertainty can be calculated using the Cramér-Rao lower bound (CRLB) [6, 8]. The CRLB predicts that an increase in background photon counts increases the localization uncertainty [6]. An increase in localization uncertainty leads to a decrease in the theoretical maximum detection efficiency [9]. The reduction in detection efficiency reduces the number of detected molecules and therefore the localization density. Therefore, an increase in background photon counts leads to a deterioration of the ultimate resolution in localization microscopy.

In biological samples, the main sources of background fluorescence are autofluorescence and fluorescence from excited out-of-focus dyes [10–17]. A common strategy to reduce background fluorescence is increasing the optical sectioning capabilities of the microscope. For example, total internal reflection microscopy (TIRF) increases the optical sectioning by illuminating the coverslip with a super-critical angle and the sample with an evanescent field. This evanescent field (e^{-1} at $\approx$ 200 nm) limits the axial excitation range above the coverslip and therefore reduces background fluorescence [18, 19].

Highly inclined and laminated optical sheet (HILO) microscopy and variable-angle epifluorescence (VAEM) microscopy extend the axial excitation range, by illuminating the coverslip at a sub-critical angle and the sample with a tilted beam [20, 21]. Similar to TIRF microscopy this approach typically requires a total internal reflection–compatible objective lens (NA$\geq$ 1.45) to achieve optimal performance. The optical sectioning of HILO and VAEM is proportional to the field of view (FOV). HILO microscopy has been demonstrated on SMLM with DNA-PAINT [22]. To accomplish sufficient background-reduction, the field of view (FOV) in both dimensions is usually limited to 5 to 10 μm. Furthermore, HILO is typically limited to thin specimens due to aberration, originating from the index-mismatch between oil and the sample of interest [23]. The trade-off between the size of the field of view and the thickness of optical sectioning has been abated by highly inclined swept tile (HIST) microscopy [24]. HIST microscopy sweeps an elongated HILO beam and synchronizes the excitation area with the active pixel of the camera to extend the FOV while maintaining the optical sectioning capabilities of HILO.

A way to further optimize optical sectioning is by the use of light sheet microscopy. Light sheet microscopy is also called selective plane illumination microscopy (SPIM). Light sheet microscopy is typically accomplished using an objective for the detection of the fluorescence signal and an additional objective for illuminating the sample with a thin sheet of light [25, 26]. The orthogonal dual objective lens configuration hinders the use of high NA detection objectives. To extend the FOV beyond the size predicted by Gaussian beam optics, axially swept light sheet microscopy (ASLM) sweeps the light sheet axially and synchronizes the light sheet excitation with the camera readout [27, 28].

While this approach allows for a larger FOV size, the drawback is that a lot of signal is lost, as only a thin line on the detector is read out. However, the acquisition speed of ASLM is slower than with a static light sheet because of the nature of the scanning/sweeping strategy. Tilted light sheet microscopy (TILT3D) and lateral interference tilted excitation microscope (LITE) successfully addressed the problem of a low detection NA by use of a tilted (non-orthogonal) illumination configuration [29, 30]. At the cost of detection NA, this can be further extended to dual tilted illumination [31]. TILT3D employs PSF engineering making it suitable for 3D SMLM [29]. The major disadvantages of these multi-objective approaches are that the microscope alignment and assembly are complex and that it often requires a custom-made sample holder.

Single objective light sheet microscopes (soSPIM) have been developed in an attempt to reduce the complexity of multi-objective light sheet microscopes [32–34]. soSPIMs makes use of special sample holders to rotate the light sheet by 90°. This operation aligns the light sheet with the focal plane and thereby creates an in-focus light sheet without the use of additional objectives. These custom sample holders are made with special nano-fabrication techniques. The complexity of the fabrication, sample mounting, and alignment of these customized sample holders significantly increases the experiment complexity.

To alleviate the disadvantage of both the sample mounting and low detection and illumination NA, oblique plane microscopes (OPM) have been developed [35–40]. OPM is related to HILO and VAEM as they all utilize inclined illumination. However, to optimize the FOV and the optical sectioning OPM uses a significantly different illumination scheme that makes use of the principles from light sheet microscopy [24, 41]. The combination of oblique illumination and detection avoids, in principle, the use of custom-made sample holders. OPM has fewer constraints in terms of sample preparation, and its development followed that of conventional two-objective light sheet microscopy, with extensions such as multi-color [42], multi-view imaging [43], and also has the benefits of remote lateral [37, 44, 45] and axial scanning [46] of the light sheet and detection planes. The oblique detection is often made possible through the use of two additional objective lenses that are placed downstream in the emission path. These two objectives make it possible to re-position the focal plane to match the oblique light sheet illumination. A disadvantage of these approaches was a truncated detection NA [40], which deteriorated the resolution and the quality of the point spread function (PSF). This weak point has recently been addressed with custom-made objective lenses making it possible to use them close to the maximum detection NA (1.27) and improve the quality of the PSF [39, 47]. However, the use of two additional objectives significantly increases the complexity of the system and more importantly decreases the photon throughput. Objective lenses have a transmission of about 80% (see specifications), which results in 35% reduction of photon throughput.

Here, we present SOLEIL (Single-Objective Lens Inclined light sheet), a platform that combines principles of PSF engineering and oblique plane microscopy to provide an alternative solution to alleviate the previously discussed disadvantages of existing HILO and high-NA light sheet approaches for SMLM. We show that oblique plane microscopy has an optimal illumination angle and sheet thickness to achieve the best possible optical sectioning. We have determined the NA and inclined angle for the best optical sec-

tioning using OPM, which results in a light sheet width of 0.645 μm and length of 66 μm on the camera. To acquire large FOVs the light sheet needs to be translated (Fig. 2.1 (d)). To experimentally compare the performance of optical sectioning of SOLEIL with widefield and HILO microscopy, we designed a microscope that can switch between the different illumination schemes (widefield, HILO, and SOLEIL). To quantify the difference in optical sectioning performance between widefield, HILO, and SOLEIL microscopy we imaged fluorescent beads embedded in agarose gel (see section 2.2.10) and measured the signal-to-background ratio Fig. 2.1 (e-g). To demonstrate the impact of SOLEIL for SMLM we benchmarked it against widefield and HILO microscopy on dSTORM samples. We show that in several biological samples SOLEIL achieves a significant improvement in the estimated CRLB.

2.2. METHOD

2.2.1. OPTICAL SYSTEM

An overview of the SOLEIL microscope is shown in Fig. 2.1(i). The sample was placed on a stick-slip piezo stage (Smartact; x,y an SLC1730; z an SLC1720). The light sheet was generated using a doublet achromatic cylindrical lens (CL, Thorlabs, ACY254-250-B). One achromatic doublet lens (L1, Thorlabs, AC254-300-A-ML) was assembled with the CL as a 4f-telescope. A galvo mirror (Scanlab, dynAXIS 20 mm) was placed at the pupil plane of the scan lens (SL, TTL200MP, Thorlabs) forming a scanning module for translating the light sheet. The doublet achromatic lens (L2, Thorlabs, AC254-200-A-ML) and the reflective mirror (M, Thorlabs, BB1-E02) were mounted on a translation stage (TS, Thorlabs, XR25P/M) to shift the spot at the pupil plane generating the excitation light sheet. The dichroic mirror (Semrock, Di03-R405/488/561/635-t1-25x36) was used to separate the excitation and emission path. The 180 mm focal length tube lens (Olympus, SWTLU-C) is combined with a 60 times objective lens (Olympus, UPlanSAPO 60x Oil NA 1.35). In the emission path, an achromatic lens (L3, AC254-200-A-ML) was assembled as a 4f-telescope with the TL, which conjugated the back focal plane of the objective lens to the deformable mirror (Alpao DM69-15). The deformable mirror is used to modify the pupil phase in the emission path, to enable PSF engineering needed for 3D SMLM (Fig. 2.1(j)). The deformable mirror was rotated by approximately 15° to reflect the emission light to the sCMOS camera (Andor Zyla 4.2). An emission filter (AHF, FF01-446/510/581/703-25) was used to block the back-reflected excitation laser. The achromatic lens (L4, AC254-200-A-ML) images the pupil plane at the deformable mirror to the sCMOS camera. A flip mirror was used to switch the emission path to bypass the deformable mirror, which was used for 2D localization microscopy. The sCMOS camera and galvo mirror were synchronized using an Arduino micro-controller. The sCMOS camera acquired an image at each galvo mirror step.

To achieve widefield and HILO illumination, we used a flip mirror to bypass the optical path that generates the light sheet. To adjust the HILO illumination an iris and a translation stage (TS) were used to adjust the spot size and the HILO angle (see Fig. 2.1 (i)).
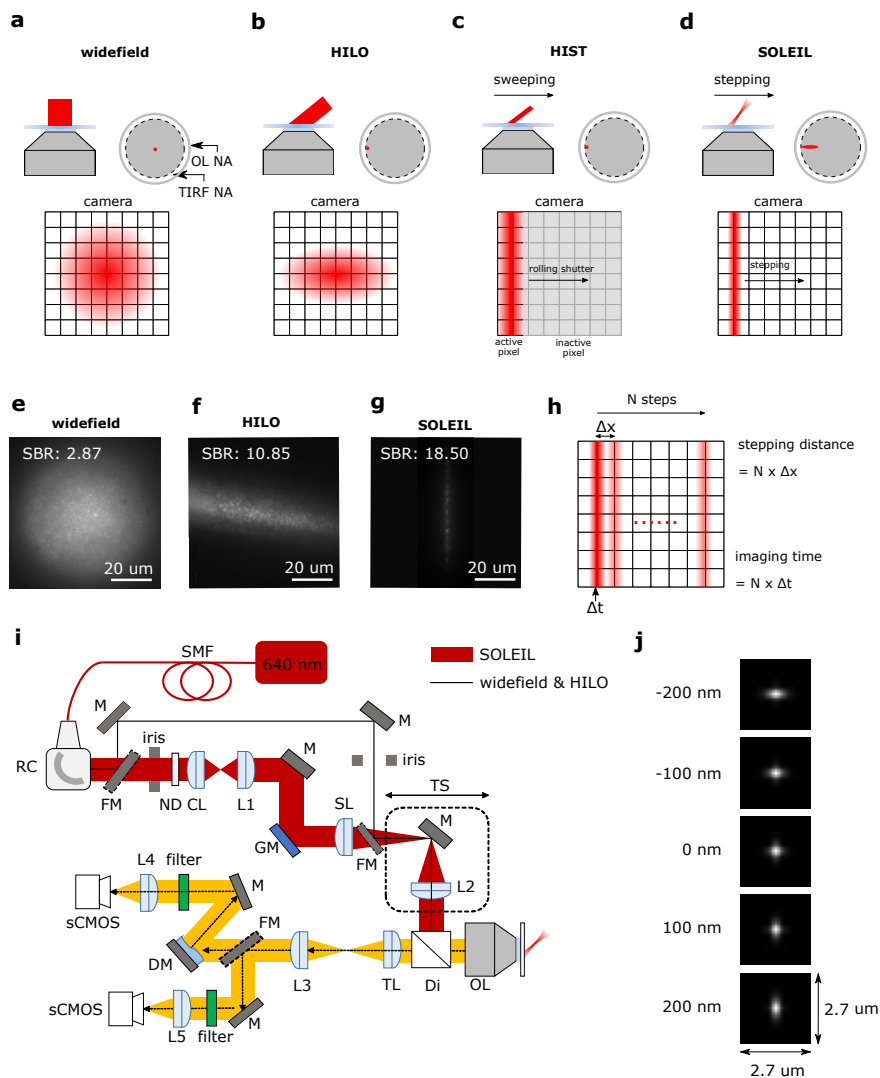
Figure 2.1: Introduction of SOLEIL and the benchmark between the different illumination modalities in terms of the signal-to-background-ratio (SBR). (a-d) upper row: Illumination profile of the different illumination schemes (widefield, HILO, HIST, and proposed method SOLEIL) and corresponding back focal planes (red). lower row: camera view of each illumination scheme. The details about HILO, HIST, SOLEIL are in section 2.3. (e-g) the raw images acquired from 23 nm fluorescence beads embedded in 1 % agarose gel (see section 2.2.10) with corresponding SBR (see section 2.2.6). (h) stepping procedure, where the total stepped distance is the step size (Δx) times the number of steps (N). The imaging time for the whole FOV is the exposure time per step (Δt) times the number of steps. (i) Schematic representation of the optical system of SOLEIL. SMF, single-mode fiber; RC, reflective collimator; ND, neutral density filter; CL, cylindrical lens; L, lens; GM, galvo mirror; SL, scan lens; TS, translation stage; Di, dichroic mirror; TL, tube lens; OL, objective lens; DM, deformable mirror; filter, emission filter; FM, flip mirror; M, reflective mirror. Details of the optical elements are presented in the method section. (j) Simulation of the astigmatism aberration engineered PSF.

2.2.2. OPTIMIZED OPTICAL SECTIONING FOR SOLEIL MICROSCOPY

To find the configuration that can achieve the optimal optical sectioning with SOLEIL microscopy, we simulated the excitation profile with varying NA and determined the resulting optical sectioning from the simulated data. We modelled the excitation (λ = 640 nm) profile as an inclined Gaussian beam (supplementary section 4.S1). The waist of Gaussian beam w_0 and the inclined angle of the Gaussian beam (θ_{inc}) were corrected for the refraction from the layer between the coverslip/immersion oil ($n = 1.52$) and the dSTORM buffer ($n = 1.33$). The simulation window ranged from -5 to 5 μm along the optical axis (z) from the imaging plane and across the FOV (x) (Fig.2.S1).

We defined the optical sectioning as the (projected) thickness of the beam at which the intensity drops to e^{-1} along the optical axis (Fig. 2.2), which matches with the definition of the penetration depth of TIRF illumination [48, 49]. To determine the thickness of the optical sectioning, we extracted the intensity profile of simulated Gaussian beam along the z-axis (white dashed line in Fig. 2.2 (a)) and fitted it to a Gaussian function with the parameters of amplitude, center, and width of Gaussian function (σ) by minimizing the mean square error Fig. 2.2 (b). The $2\sqrt{2}$ times of estimated σ of Gaussian function was the thickness of optical sectioning.

We found that a higher illumination NA generates a thinner Gaussian beam at the cost of reducing the (maximum) possible inclined angle (θ_{inc}) Fig. 2.2 (c). Both the illumination NA and the inclined angle have an impact on the optical sectioning Fig. 2.2 (c,d). The best optical sectioning of SOLEIL microscopy is achieved with an illumination NA of 0.66 and an inclined angle of 38° from the optical axis of the objective lens Fig. 2.2(e). At this optimal NA, the width is 0.645 μm and the length of 66 μm. The stepping speed is limited, because the microscope can only acquire photons from the single-molecule when the single-molecule is in its fluorescent on-state and it is illuminated.

2.2.3. COMPARATIVE ANALYSIS BETWEEN HILO, HIST, AND SOLEIL MICROSCOPY

To achieve optical sectioning in HILO, HIST, and SOLEIL microscopy different optical configurations are used. In the Fig. 2.3 (a-c), we show a schematic of HILO, HIST, and SOLEIL microscopy. HILO microscopy (Fig. 2.3 (a)) adopts an inclined (collimated) excitation beam to generate the optical sectioning. The excitation beam illuminated the sample under an angle and therefore a projected beam width is observed on the camera ($R_{1,HILO} > R_{2,HILO}$). In HILO microscopy, increasing the excitation area increases the thickness of optical sectioning (see supplementary section 2.S3). This typically limits the usability of HILO microscopy. HIST microscopy is an improved version of HILO microscopy, and it adopts a pair of cylindrical lenses to elongate the beam in one dimension ($R_{1,HIST} < R_{2,HIST}$) (Fig. 2.3 (b)). Furthermore, the excitation area is swept over the sample by a galvo mirror and the pixel readout of camera is synchronized with the excitation area (i.e. the area that is illuminated at a single galvo position). With the above two modifications, HIST microscopy acquires a larger FOV (i.e. the area acquired from multiple galvo positions) compared to HILO microscopy without increasing the thickness of optical sectioning. With SOLEIL, we adopt an inclined light sheet to generate the optical sectioning (Fig. 2.3 (c)), which is different from HILO and HIST microscopy. This

2

a

b

c

d

e
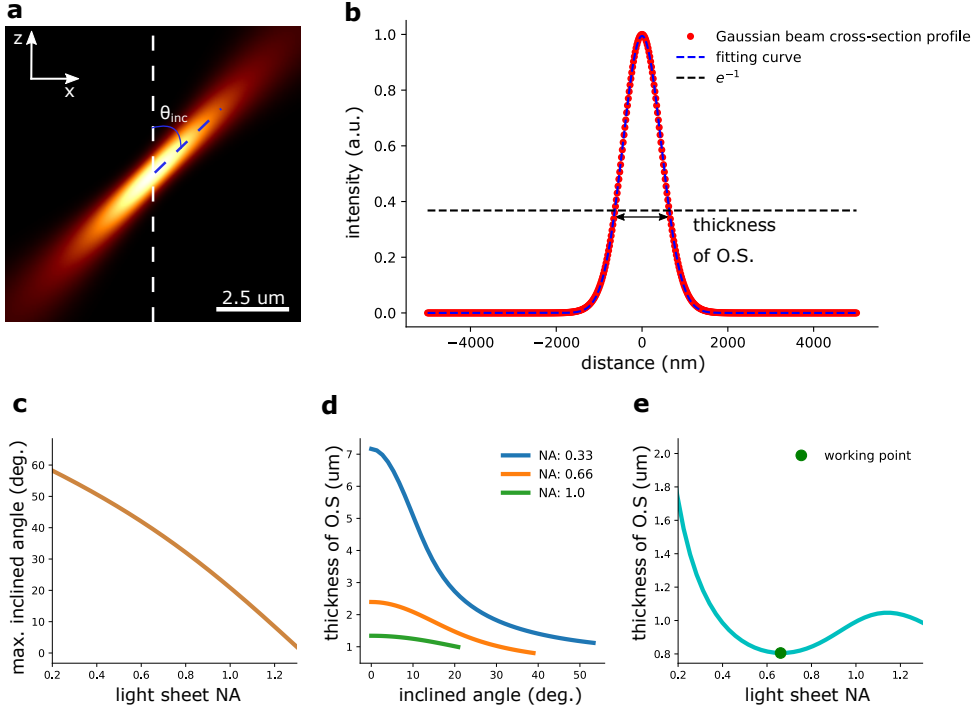
Figure 2.2: Investigation of the system parameters versus the optical sectioning (O.S.) achieved by SOLEIL. (a) a simulated inclined Gaussian beam with 1 mm beam radius at the back focal plane and 45° inclined angle (θ_{inc}) from the optical axis of the objective lens (z-axis). We use the intensity profile along the white dashed line in (a) to determine the thickness of optical sectioning in (b). The O.S. thickness is determined at the position where the intensity drops down to e^{-1} (black dashed line). The red dots are the intensity values of the Gaussian beam along the white dash line in (a) and the blue dashed line is the fitting curve. (c) The SOLEIL light sheet NA versus the maximum inclined angle. (d) The optical sectioning versus the inclined angle (the angle between the beam and the optical axis). (e) The best optical sectioning for Gaussian beams with different NA. (c; green dot) The optimal optical sectioning is achieved at an NA of 0.66.

is accomplished by moving a lens to place the beam at the edge of the back focal plane of the objective to generate the light sheet at an inclined angle. With SOLEIL, similar to HIST, the light sheet is stepped over the sample by a galvo mirror to image the desired FOV (Fig.2.1 (d)). The light sheet is not scanned but is kept at a fixed position during the exposure time before it is moved to the next position (Fig.2.1 (h)). This increased exposure time will increase the acquired photons from the single-molecule until the molecule turns off, which improves the CRLB (supplementary section 2.S6). The I/bg ratio decreases after a molecule has turned off, which deteriorates the estimated CRLB, which is shown in supplementary section 2.S4. We observed that moving the light sheet slower than 20 ms will significantly decrease the I/bg ratio making it hard to process the data. In contrast to HIST microscopy, SOLEIL reads out whole camera frames. To distinguish this difference, we termed the lateral displacement in HIST microscopy as sweeping and that of SOLEIL as stepping in Fig. 2.1 (c,d). The width of the SOLEIL light sheet (w) is determined by the beam radius (r_{ex}) at the back focal plane and the inclination angle from the optical axis of the objective lens Fig. 2.3 (c). The length of the SOLEIL light sheet (L) is determined by the beam radius at the conjugated imaging plane before the objective $L = 2r_L \cdot 3$ mm/200 mm, where 200 mm is the focal length of lens in Fig. 2.3 (c) and 3 mm is the focal length of the objective lens. If no additional beam shaping is applied in the excitation path, $r_L = r_{ex}$.

In HILO, HIST, and SOLEIL microscopy, the size of the excitation area is coupled to the thickness of optical sectioning. In Fig. 2.3 (d), we show the trade-off curve between the beam radius ($R_{1,HILO}, R_{2,HILO}$) and the thickness of optical sectioning of HILO and HIST microscopy. The inclined angle of HILO used for this simulation was chosen to be the same as the inclined angle of HILO setup used in our HILO system (74.5°). The HILO angle in the previously published paper was 77 °, which was close to the angle in our setup. For HIST microscopy, we refer to the experiment parameters from the HIST paper [24]. The inclined angle of HIST is 69.7°, which is given by the inverse tangent of the ratio between the HIST beam width ($R_{1,HIST} = 10$ μm) and the HIST beam thickness (dz=3.7 μm). The relationship of beam width and beam thickness of HIST microscopy are the same as for HILO microscopy (see supplementary section 2.S3). In the simulation, a constant inclined angle of HIST microscopy was chosen. In practice however, this angle changes over the FOV, which generates an in-homogeneous thickness of optical sectioning over the FOV [24].

In Fig. 2.3 (e), we show the trade-off curve of the SOLEIL between the width (w), length (L), and the thickness of optical sectioning (O.S.). With the data from Fig. 2.3 (d,e), we can evaluate the relationship between the excitation area and the thickness of the optical sectioning obtained by HILO, HIST and SOLEIL microscopy (Fig. 2.3 (f)). The HILO excitation area A_{HILO} was approximated as an ellipse and the area was calculated as $A_{HILO} = \pi R_{1,HILO} \cdot R_{2,HILO}/4$. The HIST excitation area A_{HIST} was calculated as $A_{HIST} = R_{1,HIST} \cdot R_{2,HIST}$. The SOLEIL excitation area A_{SOLEIL} was calculated as $A_{SOLEIL} = L \cdot w$ (see the coordinate in Fig.2.3 (a-c)).

The excitation area is a critical parameter that affects the total acquisition time of a SMLM acquisition. The total acquisition time is

$$T_{SMLM} = \frac{A_{de}}{A_{ex}} \cdot T_{exp} \cdot n_{iter}, \tag{2.1}$$

where A_{de} is the area of desired FOV, A_{ex} is the excitation area, T_{exp} is the exposure time per frame typically ranging from 10 ms ∼ 50 ms, and n_{iter} is the number of iteration for the SMLM imaging typically larger than 1000 iteration. From the above formula, we know that a larger A_{ex} leads to faster SMLM imaging.

From the Fig. 2.3 (f), HILO microscopy delivers the largest excitation area compared to SOLEIL and HIST. SOLEIL microscopy offers the best optical sectioning at the cost of sacrificing the imaging speed. HIST microscopy has medium optical sectioning and a medium size of FOV. For the HILO and HIST microscopy, we want to note that the thickness of optical sectioning and excitation area vary depending on the inclined angle and input beam size. The data points in Fig. 2.3 (f) come from our system and previous published research [20, 24].

2.2.4. CHARACTERIZATION OF SOLEIL EXCITATION PROFILE

To measure the excitation profile of our light sheet, we scanned a single fluorescence bead (23 nm) embedded in 1% agarose gel in x and z axis. We estimated the light sheet profile by summing the signal acquired by the camera per scan position (see Fig.2.S2). The acquired signal from the bead was proportional to the excitation intensity and therefore gave an estimate of the light sheet profile. The light sheet profile was characterized by fitting the excitation intensities to an inclined Gaussian beam, by minimizing the mean squared error (MSE), resulting in a Gaussian beam waist (w_0) and Rayleigh length (z_r). The MSE was minimized using the Nelder-Mead algorithm [50]. The width and Rayleigh length of the Gaussian beam was estimated to be 0.627 μm and 1.929 μm, respectively (Fig.2.S3). The inclined angle was measured to be 30° from the optical axis of the objective lens in the environment with a refractive index of $n = 1.33$.

2.2.5. CHARACTERIZATION OF THE HILO EXCITATION PROFILE

To characterize the HILO illumination, we acquired 200 frames images of fluorescent beads homogeneously embedded in 1% agarose gel (see section 2.2.10) at different FOVs. We used Super-resolution Microscopy Analysis Platform (SMAP, EMBL Heidelberg) [51] to localize the bead images to acquire the beads' position and intensity (Fig.2.S4). With this information, we built inertia matrix M and $R_{1,HILO}$, $R_{2,HILO}$ were obtained from the the eigenvalue of inertia matrix M (supplementary section 2.S3). The HILO angle was the inverse cosine of the ratio between $R_{1,HILO}$ and $R_{2,HILO}$. The beam thickness of HILO was estimated based on the $R_{1,HILO}$ and the HILO angle.

2.2.6. COMPUTING THE SIGNAL-TO-BACKGROUND RATIO (SBR) OF AGAROSE BEAD IMAGING

To benchmark the difference in optical sectioning performance, we imaged 23 nm fluorescent beads embedded in 1 % agarose gel (see section 2.2.10) (>50 μm) with widefield, HILO, and SOLEIL microscopy Fig. 2.1 (e-g). To obtain enough localizations to characterize the excitation profile we scanned the sample over the FOV. The SBR ratio was computed from the ratio between the estimated intensity and the estimated background of each bead. The estimation of intensity and background of beads was done by fitting the PSF with the Gaussian function, which is performed by using the SMAP platform.

The reported SBR (WF: 2.87; HILO: 10.85; SOLEIL: 18.50) in Fig. 2.1 (e-g) for widefield,

2
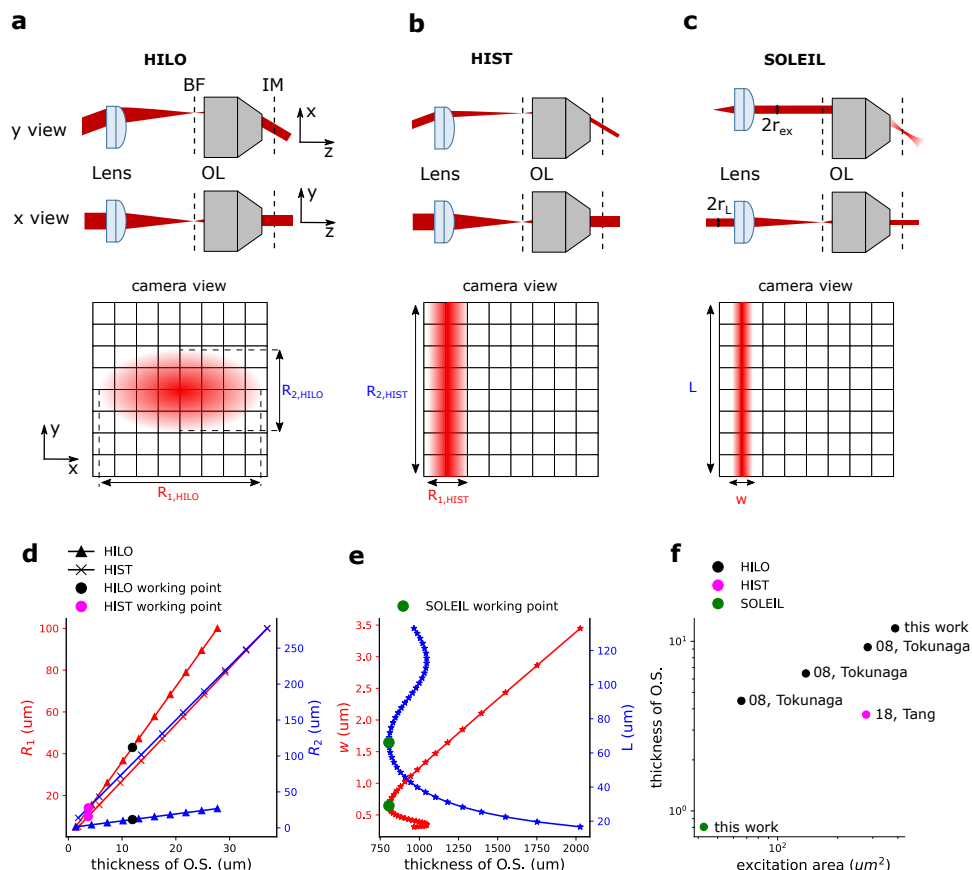
Figure 2.3: Benchmark between HILO, HIST, and SOLEIL microscopy. (a)BF: back focal plane; IM: imaging plane; OL: objective lens. upper row: the schematic figure of HILO microscopy from x and y view. The z-axis stands for the optical axis of the objective lens. Lower row: camera view of HILO excitation profile at imaging plane. $R_{1,\text{HILO}}$ the beamwidth of HILO at the imaging plane. $R_{2,\text{HILO}}$ the original width of the HILO beam, which is not elongated by the inclination projection. (b) upper row: the schematic figure of HIST microscopy from x and y view. Lower row: camera view of HIST excitation profile at imaging plane. (c) upper row: the schematic figure of SOLEIL microscopy from x and y view. Lower row: camera view of the SOLEIL excitation profile at the imaging plane. L: length of SOLEIL light sheet, r_{ex}: the beam radius at the back focal plane of the objective lens, which determines the NA of Gaussian beam. r_L: the beam radius at the plane conjugated to the imaging plane, which can determine the length of SOLEIL profile (L). (d) the beam radius of HILO and HIST (R_1, R_2) microscopy versus thickness of optical sectioning. (e) The beam dimension of SOLEIL versus the thickness of optical sectioning. The working point is the same as the working point in sub-figure Fig. 2.2 (c). (f) The benchmark of excitation area and thickness of optical sectioning between HILO, HIST, and SOLEIL. The data of HILO microscopy is from our HILO microscopy. The data of HIST microscopy is from the previous HIST paper [24]. The data of SOLEIL is from the working point in Fig. 2.2 (e).

HILO and SOLEIL were the median SBR obtained from 402 beads, 37078 beads, and 1054 beads, respectively. These were obtained by imaging multiple FOVs.

2.2.7. Data acquisition

For all excitation modes, the sample was pre-bleached to reduce the density of molecules in the on-state. The pre-bleaching was done with widefield illumination for 30 to 60 seconds. For SOLEIL a simple data acquisition sequence was defined to acquire one full image at each light sheet step (i.e. we do not use a rolling shutter). The camera was used in external trigger mode and the camera and galvo mirror were synchronized by an Arduino micro-controller. All SOLEIL samples were imaged with a step size of 0.375 μm, 36.3 - 44.43 frames per second, and with 20 - 25 ms exposure time per frame. These settings ensured that typically the full on-time of the molecule was captured before moving the light sheet. The impact of the exposure time on the signal to background ratio is shown in Fig.2.S5. The dSTORM data consists of 3000 ~ 10000 frames per step. Each sample was imaged with a specific number of steps, resulting in a different total stepped distance (2D/3D COS7: 25 μm, HEK-293T: 35 μm, Caco2-BBE: 27 μm) and size of the imaging FOV.

2.2.8. DSTORM data analysis

Super-resolution Microscopy Analysis Platform (SMAP, EMBL Heidelberg) was used for the 2D and 3D localization of single molecules[51]. In the 2D case, the width of the Gaussian PSF σ is taken as an additional parameter that needs to be estimated. The initial estimate of the width is set to $\sigma = 1.6$ pixel, corresponding to 175 nm. We filtered out the localizations with an intensity lower than 200 photons and larger than 10000 photons and σ larger than 1.61 pixel. For the 3D localization, we calibrated a cubic-spline PSF model (supplementary section 2.S7) with an experimentally obtained z-stack with 10 nm step size of fluorescence beads with 23 nm radius (Thermo Fisher Scientific, Tetraspeck). The drift correction was done by using the redundant cross-correlation method in SMAP [51, 52].

2.2.9. Deformable mirror calibration using interferometric wavefront sensing

We used a Michelson interferometer to calibrate the deformable mirror (DM) [53]. The optical configuration of the interferometer is shown in Fig.2.S6 (a). The influence matrix was obtained by measuring the change in Zernike coefficients of the DM phase created with a push-pull cycle, with each actuator at 80% of the stroke range [54]. The interferometric DM calibration software from dmlib was used [55]. The phase information on the DM was captured within the interferogram fringes Fig.2.S6 (b). To extract the phase information from the interferogram fringe, the recorded interferogram fringe was transformed by fast Fourier transform (FFT), and three peaks were presented in the spatial frequencies domain Fig.2.S6 (c). Then, the software cropped the spatial frequencies around the first-order peak and shifted back to zero spatial frequency position. After that, the inverse FFT was used to transform the cropped spatial frequencies and the phase information was the angle of the complex number. With the phase information, we constructed the control matrix of DM.

To flatten the DM and to correct for system aberrations, we minimized the width of the PSF by minimizing the second moment of the PSF [56]:

$$M_{sec} = \sum_{i=0}^{N} \sum_{j=0}^{N} I(i,j) \cdot \left[(i - c_x)^2 + (j - c_y)^2 \right], \tag{2.2}$$

where $I(i,j)$ is the pixel value at row i and column j of a camera image of a single fluorescence bead, c_x and c_y are the center of mass of $I(i,j)$, and N is both the width and height of the camera image. We minimized the second moment of the PSF using the random walk algorithm [57] by imaging a single 23 nm fluorescence bead (Thermo Fisher Scientific, Tetraspeck). First, the control signal of the DM was perturbed by a random vector X, where each element X_k was drawn from a uniform distribution $X_k \sim U(-0.025 S_{max}, 0.025 S_{max})$ with S_{max} as the maximum stroke of the DM. Subsequently, the second momentum of the PSF was measured, and if this input reduced the second moment, this new DM control signal was chosen as the new optimum. We repeated these steps until the algorithm converged to a stable point, typically after 500 iterations. This procedure was repeated two more times, and each time the stroke range was reduced by a factor of 2.

2.2.10. SAMPLE PREPARATION

SAMPLE PREPARATION FLUORESCENCE BEADS EMBEDDED IN AGAROSE GEL

Agarose solution (1% w/v) was prepared in a glass bottle by adding 45 mg of Agarose powder (BP160-100, Thermo Fisher Scientific, Waltham MA, U.S.A.) to 4.5 mL of deionized (DI) water followed by 20 minutes stirring with a magnetic stirrer at 100 °C. Polystyrene 40 nm diameter microspheres labeled with a red fluorescent dye (633 nm excitation / 720 nm emission, Invitrogen TransFluoSphere T8870, Thermo Fisher Scientific) at 2% solid concentration was first lightly ultra-sonicated to achieve a distributed dispersion of microspheres and aliquoted at 1:500 dilution with DI water. Then, 0.5 mL of this aliquot was added to the agarose solution and stirred for a further 10 minutes at 70 °C, giving a final concentration of 0.0004% solid microspheres by weight in agarose solution. Next, a standard microscope glass slide (25 mm x 75 mm x 1 mm, Thermo Fisher Scientific) and borosilicate glass coverslip (22 mm x 22 mm, #1.5 thickness, Merck KGaA, Darmstadt, Germany) were cleaned with ultra-sonication in acetone (5 minutes, Merck KGaA), DI water (5 minutes), isopropanol (5 minutes, Merck KGaA), DI water (5 minutes), and blow-dry with a compressed air gun. A few droplets of the agarose solution were placed on the glass slide using a plastic pipette, and the coverslip was immediately dropped on top. The specimen was left to cool for 10 minutes resulting in a solid agarose gel with embedded labeled microspheres. The coverslip was then sealed to the glass slide with nail polish.

CACO2-BBE CELLS

Caco2-BBE cells (a gift from S.C.D. van IJzendoorn, University Medical Center Groningen, the Netherlands) were maintained in DMEM supplemented with 9% FBS (fetal bovine serum), 50 μg/μl penicillin/streptomycin and 2 mM L-glutamine at 37 °C and 5% CO_2. Cells were seeded on 18 mm coverslips at a density of $1 \cdot 10^5$/cm^2 and cultured for 10

to 12 days to allow for spontaneous polarization and brush border formation. Cells were fixed with 4% paraformaldehyde (PFA) in phosphate-buffered saline (PBS) for 10 minutes, washed with PBS (3 × 5 minutes), permeabilized with 0.5% Triton X-100 in Milli-Q water for 15 minutes, washed with PBS (3 × 5 minutes) and blocked with 3% BSA in PBS for at least 1 hour. Cells were incubated overnight at 4 °C with a primary antibody against ezrin (mouse, BD Biosciences, 610602, dilution 1:500). After washing in PBS (3 × 5 minutes), the cells were incubated with secondary antibody (goat, anti-Mouse IgG (H+L), Alexa Fluor 647 (Life Technologies, dilution 1:500) for 1 hour at room temperature (RT) and washed with PBS.

COS-7 CELLS

COS-7 cells (a gift from Anna Akhmanova, Utrecht University, the Netherlands) were cultured at 37 °C and 5% CO_2 in DMEM, supplemented with 9% FBS and 1% penicillin/streptomycin. 24 hours after seeding them onto 18 mm #1.0 coverslips, cells were pre-extracted with 0.1% glutaraldehyde and 0.3% Triton-X100 in PEM80 (80 mM Pipes, 1mM EGTA, 4 mM MgCl2, pH 6.8) for 1 minute. The cells were subsequently fixed with 4% PFA and 4% sucrose in PEM80 for 10 minutes. After washing in PBS (3 × 5 minutes), cells were permeabilized in 0.25% Triton-X100 in PEM80 for 15 minutes. After washing (3 × 5 minutes), blocking was performed in 3% BSA in PEM80 for 1 hour, and cells were incubated overnight at 4 °C with a primary antibody against α-tubulin (mouse IgG1, Sigma-Aldrich, B-5-1-2, dilution 1:1000 in blocking buffer). The cells were again washed with PBS (3 × 5 minutes) and incubated with a secondary antibody (goat, anti-Mouse IgG (H+L), Alexa Fluor 647 (Life Technologies, dilution 1:500 in blocking buffer) for 1 hour at RT and washed with PBS.

HEK-293T CELLS

Human Embryonic Kidney cells (HEK-293T, DSMZ no. ACC 635) were cultured at 37 °C and 5% CO_2 in DMEM without phenol red supplemented with 4.5g/l glucose (Gibco, Thermo Fisher Scientific), 4 mM L-gluthamine (Gibco, Thermo Fisher Scientific), 10% fetal bovine serum (Gibco, Thermo Fisher Scientific) and 1× penicillin-streptomycin (Gibco, Thermo Fisher Scientific). Cells were seeded on plasma treated 25 mm high-precision #1.5 borosilicate coverslips (Marienfeld) in 6-well plates (Thermo Fisher Scientific) 1 to 2 days before fixation.

The cells were washed twice in prewarmed DMEM without phenol red and then incubated for 90 seconds in prewarmed extraction buffer (MTSB2, 80 mM PIPES, 7 mM $MgCl_2$, 1 mM EGTA, 150 mM NaCl, 5 mM D-glucose, KOH for tuning the pH to 6.8) with freshly added 0.3% Triton X-100 and 0.25% glutaraldehyde. Subsequently, cells were fixed in prewarmed 4% PFA in MTSB2 for 10 minutes and washed with PBS (3 × 5 minutes). Then, cells were incubated with a freshly prepared solution PBS with 10 mM $NaBH_4$ for 7 minutes followed by washing in PBS (1× quick, 2 × 10 minutes). Afterwards, cells were permeabilized in PBS with 0.25% Triton X-100 for 7 minutes and then blocked with blocking buffer (BB, 2% (w/v) BSA, 10 mM glycine, 50 mM NH_4Cl in PBS pH 7.40 for 60 minutes at room temperature or overnight at 4°C. Blocked samples were incubated with anti-tubulin antibody (clone B-5-1-2 ascites fluid 1:200 dilution in BB, Sigma-Aldrich) at RT for 1 hour. Then, cells were washed with BB (3 × 5 minutes),

2

followed by incubation with donkey anti-mouse Alexa Fluor 647 antibody (donkey anti-mouse (H+L) highly cross-adsorbed at 0.005 mg/ml in BB, Life Technologies) in the dark at RT for 1 hour. After washing with BB (3 × 5 minutes), samples were post-fixed by incubation with 2% PFA in 1× PBS for 10 minutes, followed by washing with 1× PBS (3 × 5 minutes).

DSTORM BUFFER

For the dSTORM buffer, 84 μl of 20 mM Tris (pH 8.0, Sigma-Aldrich) were freshly mixed with 10 μl of 1M MEA (Sigma-Aldrich), 5 μl of 50% w/v Glucose stock, and 1 μl of Glucose Oxygen Scavenging buffer (70 mg/ml glucose oxidase (Sigma-Aldrich) and 4 mg/ml catalase (Sigma-Aldrich) in Milli-Q water [58]. The coverslip with cells was mounted on a cavity microscope slide with a 25 mm dent (Sigma-Aldrich, BR475505). 75 μl dSTORM buffer was deposited in the microscope slide dent. The surplus of dSTORM buffer was removed using lens tissue. Next, we carefully sealed the coverslip with silicone-glue Twinsil (Picodent, Wipperfürth). When applying the silicone gel around the coverslip, no liquid should be present around the coverslip, otherwise, it is more difficult to harden the silicone gel. After 20 minutes, the silicone gel was dry and the sample was ready for measuring.

2.3. RESULTS

2.3.1. COS-7 TUBULIN DSTORM IMAGING

We benchmarked SOLEIL against widefield excitation by imaging COS-7 cells labeled with Alexa Fluor 647. For the 2D and 3D imaging with SOLEIL of COS-7 cells the light sheet has an incline angle of 30°. The exposure time of widefield and SOLEIL were both 25 ms. In the SOLEIL experiment, the laser intensity was adjusted to make the single-molecule intensity match the intensity obtained from widefield mode. The total stepped distance and FOV of SOLEIL were 25 μm and 25 μm × 45 μm, respectively. For the benchmark, we did not use a CRLB filter to warrant an unbiased estimate of the intensity to background ratio (I/bg). Using the SOLEIL improved the median value of the I/bg ratio from 10.03 to 84.22 compared with widefield illumination (Fig. 2.4 (g)). In widefield microscopy, the median value of localization intensity was 585 photons and in SOLEIL the median value of localization intensity was 468 photons (Fig. 2.4 (i)). The median background of widefield microscopy was 58.30 photons/pixel and the median background of SOLEIL was 5.71 photons/pixel (Fig. 2.4 (h)). We performed a simulation to demonstrate that optimization of the I/bg ratio can improve the CRLB by 72.5% when the intensities are the same (Fig.2.S7 (a,b)). In Fig. 2.4 (d), the estimated CRLB improvement was 57% because the localizations of the SOLEIL data had lower photon counts on average than for the widefield data. For the widefield data, the median value of localization intensity was 585 photons, whereas for SOLEIL data it was 468 photons (Fig. 2.4 (i)). The total number of localizations acquired was $\approx 1.3 \cdot 10^6$ and $\approx 7.5 \cdot 10^5$ for widefield and SOLEIL microscopy, resp., which corresponds to $\approx 3.0 \cdot 10^5$ localizations/min in widefield microscopy and $\approx 9.5 \cdot 10^3$ localizations/min in SOLEIL microscopy. Fig. 2.4 (k,l) is the I/bg over the imaging time.

To enable 3D SMLM, we used the deformable mirror to introduce an astigmatic aberration, of which the resulting PSF and CRLB curve are shown in Fig.2.S8. In this case,

the background fluorescence for SOLEIL was lower than the background for widefield illumination, which results in an improved estimated CRLB. Based on the measured localizations, we found that the median I/bg ratio was improved from 22 to 230 (Fig. 2.5 (g)). Using SOLEIL the average lateral and axial CRLB improved 200% compared with widefield illumination (Fig. 2.5 (j,k)). The median value of localization intensity was 1416 photons and 737 photons, for widefield and SOLEIL illumination, resp. (Fig. 2.5 (i)), whereas the median background was 65 photons/pixel and 2.59 photons/pixel (Fig. 2.5 (h)). The footprint of an astigmatic PSF is larger than that of a Gaussian PSF, and therefore spots needed a higher intensity to pass the spot detection threshold. For this reason, we performed a longer experiment to accumulate enough high-intensity spots, as the low-intensity spots were not detected by the spot detection algorithm. The total number of localizations acquired was $\approx 3.9 \cdot 10^5$ and $\approx 3.7 \cdot 10^5$ for widefield and SOLEIL illumination, resp. This corresponds to $\approx 3.1 \cdot 10^4$ localizations/min in widefield microscopy and $\approx 2.1 \cdot 10^3$ localizations/min in SOLEIL microscopy. Fig. 2.5 (l,m) is the I/bg ratio over imaging time.
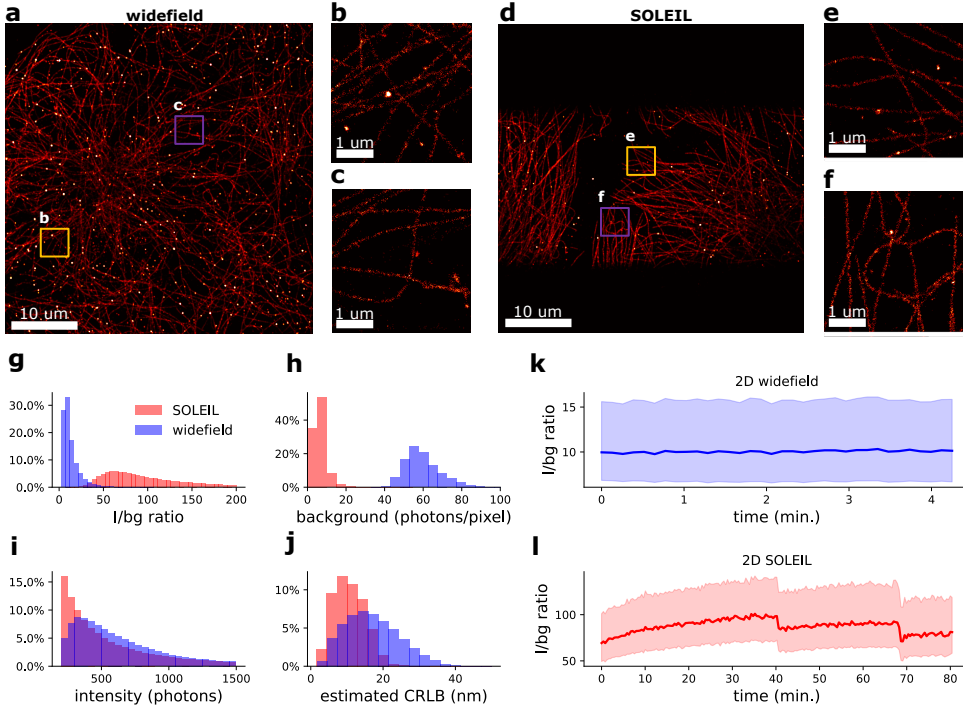
Figure 2.4: 2D super-resolution image of a COS-7 tubulin. The imaging depth was <1 μm for (a,d). (a) 2D super-resolution image with the microscope in widefield mode. (b,c) Zoom-in of (a). (d) 2D localization image with the microscope in SOLEIL mode, with 25 μm total stepped distance. (e,f) Zoom in image of (d). (g-j) Benchmark of intensity to background ratio, background, intensity, and estimated CRLB between widefield and SOLEIL. (k,l) I/bg ratios of widefield mode and SOLEIL mode over experiment time. The opaque colored region represents the first quartile to the third quartile.

2
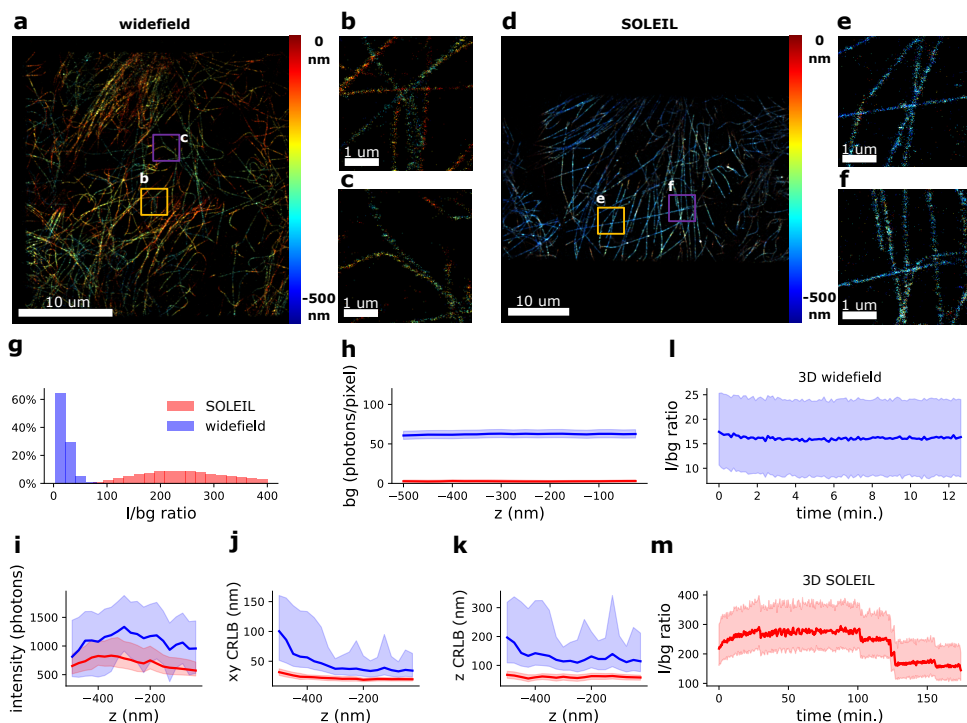
Figure 2.5: 3D super-resolution image of COS-7 tubulin. The imaging depth was <1 μm for (a,d). (a) 3D super-resolution image with the microscope in widefield mode. (b,c) Zoom-in of (a). (d) 3D super-resolution image with with the microscope in SOLEIL mode, with 25 μm total stepped distance. (e,f) Zoom-in of (d). (g-k) Benchmark of I/bg ratio, background, intensity, and estimated CRLB between widefield mode and SOLEIL mode. The opaque color region represents the first quartile to the third quartile. (l,m) I/bg ratios of widefield mode and SOLEIL mode over experiment time. The opaque color region represents the first quartile to the third quartile.

2.3.2. HEK-293T TUBULIN AND CACO-2-BBE EZRIN DSTORM IMAGING

We chose HEK-293T and Caco-2-BBE cells to demonstrate the capacity to image thick samples. The thickness of cells are ≈ 9 μm and ≈ 15 μm [59], respectively. For HEK-293T and Caco2-BBE cells, we used SOLEIL microscopy that had an incline angle of 30° from the optical axis of the objective lens. The angle of HILO we used in HEK-293T and Caco2-BBE sample imaging was 74.5° and the HILO beam width ($R_{1,\text{HILO}}$) was 43 μm. In the HEK-293T sample, the exposure time of widefield, HILO, and SOLEIL were both 25 ms. In Caco2-BBE cells imaging, the angle for SOLEIL microscopy was the same as the SOLEIL angle we used for HEK-293T cells imaging. The exposure times were 20 ms, 25 ms, and 25 ms for widefield, HILO and SOLEIL illumination resp. The total stepped distance and FOV were 35 μm and 35 μm × 35 μm, respectively. For the HEK-293T sample, the median I/bg ratio acquired by widefield microscopy was 7.50, the median I/bg ratio acquired by HILO microscopy was 13.06, and the median I/bg ratio acquired by SOLEIL microscopy was 31.39 (Fig. 2.6 (j)). The median estimated CRLB acquired by widefield microscopy was 18.88 nm, the median estimated CRLB acquired by HILO microscopy was 15.90 nm, and the median estimated CRLB acquired by SOLEIL microscopy was 12.20 nm (Fig. 2.6 (m)). We observed a 400% higher I/bg ratio and 54% improvement of estimated CRLB in the benchmark between SOLEIL and widefield microscopy and a 240% higher I/bg ratio and 30% improvement of estimated CRLB in the benchmark between SOLEIL and HILO microscopy(Fig. 2.6 (j,m)). In the widefield microscopy, the median value of localization intensity was 507 photons, in HILO was 608 photons and in SOLEIL was 508 photons (Fig. 2.6 (l)). The median background of widefield microscopy was 69 photons/pixel, the median background of HILO was 48 photons/pixel and the median background of SOLEIL was 17 photons/pixel (Fig. 2.6 (k)). The total number of localization acquired by widefield microscopy was $\approx 3.1 \cdot 10^5$, the total number of localization acquired by HILO microscopy was $\approx 1.6 \cdot 10^5$ and the total number of localization acquired by SOLEIL microscopy was $\approx 6.4 \cdot 10^5$, which corresponds to $\approx 1.8 \cdot 10^5$ localizations/min in widefield microscopy, $\approx 3.0 \cdot 10^4$ localizations/min in HILO microscopy and $\approx 9.4 \cdot 10^3$ localizations/min in SOLEIL microscopy.

For the Caco-2-BBE sample, the median I/bg ratio acquired by widefield microscopy was 13.06, the median I/bg ratio acquired by HILO microscopy was 26.48, and the median I/bg ratio acquired by SOLEIL microscopy was 48.86 (Fig. 2.7 (j)). The median estimated CRLB acquired by widefield microscopy was 21.93 nm, the median estimated CRLB acquired by HILO microscopy was 17.12 nm, and the median estimated CRLB acquired by SOLEIL microscopy was 14.26 nm (Fig. 2.7 (m)). We observed a 374% higher I/bg ratio and 54% improvement of estimated CRLB in the benchmark between SOLEIL and widefield microscopy and a 184% higher I/bg ratio and 20% improvement of estimated CRLB in the benchmark between SOLEIL and HILO microscopy (Fig. 2.7 (j,m)). The median value of the estimated intensity was with widefield microscopy 303 photons, with HILO microscopy 325 photons, and with SOLEIL microscopy 345 photons (Fig. 2.7 (l)). The median value of the estimated background was with widefield microscopy 23 photons/pixel, with HILO microscopy 12.7 photons/pixel, and with SOLEIL 7 photons/pixel (Fig. 2.7 (k)). The total number of localization acquired with widefield microscopy was $\approx 1.1 \cdot 10^5$, with HILO microscopy $\approx 1.0 \cdot 10^5$, and with SOLEIL microscopy $\approx 1.4 \cdot 10^5$. This corresponds to $\approx 3.2 \cdot 10^4$ localizations/min with widefield microscopy, $\approx 3.0 \cdot 10^4$

localizations/min with HILO microscopy and $\approx 5.6 \cdot 10^3$ localizations/min with SOLEIL microscopy.
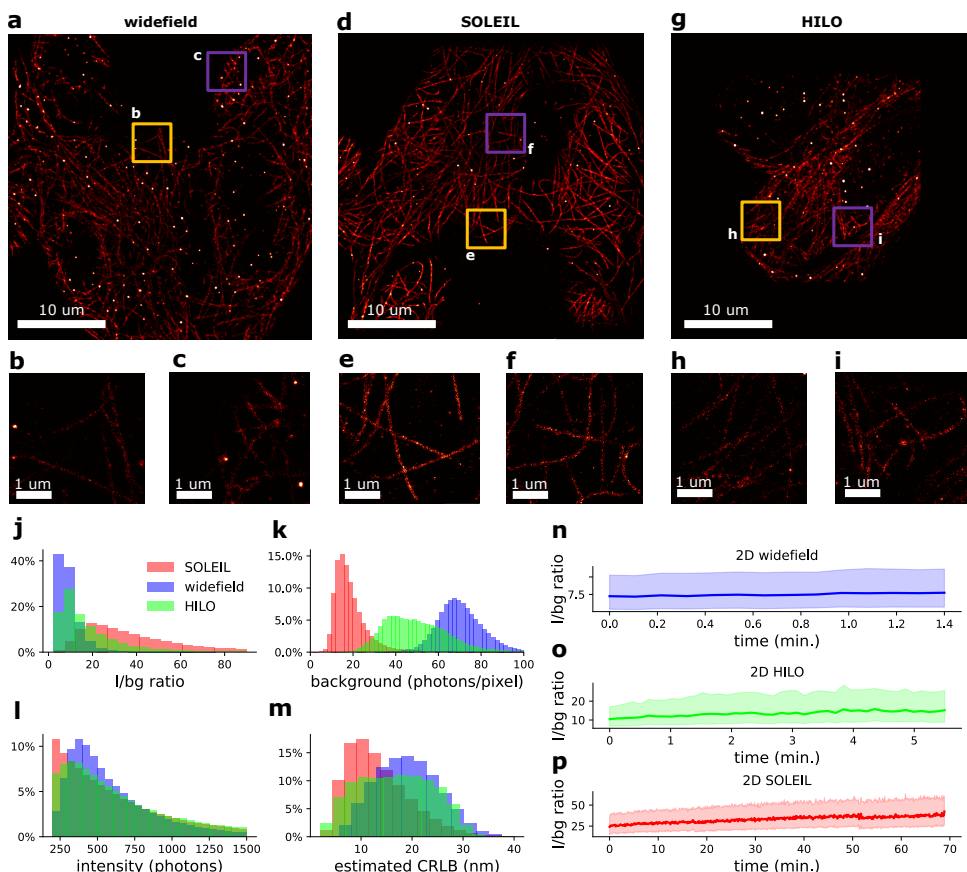
Figure 2.6: 2D super-resolution image of HEK-293T tubulin. The imaging depth was approximately 5 μm for (a,d,g). (a) 2D super-resolution reconstruction from widefield imaging data. (b,c) Zoom-in of (a). (d) 2D localization reconstruction from SOLEIL imaging data, with a 35 μm total stepped distance. (e,f) Zoom-in image of (d). (g) 2D localization reconstruction from HILO imaging data. (h,i) Zoom-in image of (g). (j-m) Benchmark of I/bg ratio, background, intensity, and estimated CRLB between widefield, HILO, and SOLEIL microscopy. (n-p) I/bg ratios for widefield, HILO, and SOLEIL microscopy over experiment time. The opaque color region represents the first quartile to the third quartile.

2.4. DISCUSSION AND CONCLUSION

To achieve a better SMLM resolution in thick samples, it is essential to minimize background fluorescence. Minimizing background fluorescence can improve CRLB in SMLM (Fig.2.S7 (a)). TIRF microscopy shows excellent background rejection capabilities, but the short illumination depth limits its applicability to thin samples. HILO and HIST microscopy achieve optical sectioning with a single objective structure. However, the performance of optical sectioning of these methods are typically worse than light sheet
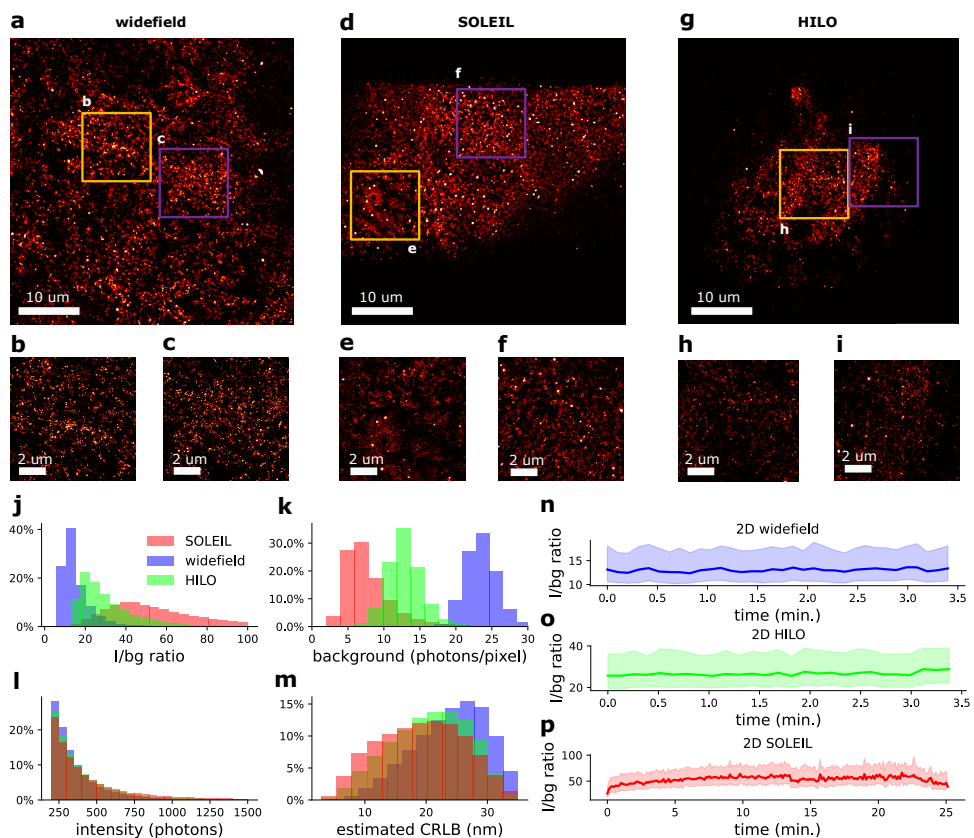
Figure 2.7: 2D super-resolution reconstruction of Caco2-BBE ezrin. The imaging depth was approximately 8 - 10 μm for (a,d,g) (a) 2D super-resolution reconstruction from widefield imaging data. (b,c) Zoom-in of (a). (d) 2D super-resolution reconstruction from SOLEIL imaging data, with a 27 μm total stepped distance. (e,f) Zoom-in image of (d). (g) 2D super-resolution reconstruction from HILO imaging data. (h,i) Zoom-in image of (g). (j-m) Benchmark of I/bg ratio, background, intensity, and estimated CRLB for widefield, HILO, and SOLEIL microscopy. (n-p) I/bg ratios of for widefield, HILO, and SOLEIL microscopy over experiment time. The opaque colored region represents the first quartile to the third quartile.

	m.v. of intensity (phot.)	m.v. of I/bg ratio	m.v. of CRLB
2D COS-7 WF	585	10.03	16.43 nm
2D COS-7 SOLEIL	468	84.22	10.43 nm
3D COS-7 WF	1416	22	xy: 31.59 nm
			z: 99.41 nm
3D COS-7 SOLEIL	737	230	xy: 20.98 nm
			z: 59.43 nm
2D HEK-293T WF	507	7.5	18.88 nm
2D HEK-293T HILO	508	13.06	15.90 nm
2D HEK-293T SOLEIL	533	31.39	12.20 nm
2D Caco-2 BBE WF	303	13.06	21.93 nm
2D Caco-2 BBE HILO	325	26.48	17.12 nm
2D Caco-2 BBE SOLEIL	345	48.86	14.26 nm

Table 2.1: Benchmarking the SMLM performance between WF and SOLEIL. m.v. stands for median value and phot. stands for photons.

microscopy. SPIM and soSPIM approaches have a limited detection and/or illumination NA and require custom-made sample holders. To avoid these drawbacks, we developed a novel single objective lens inclined light sheet platform, SOLEIL. SOLEIL has no constraints for sample mounting and avoids the restriction on the NA. We demonstrated this on HEK-293T and Caco-2-BBE cells with a thickness of ≈9 μm and ≈15 μm, respectively.

Our simulations showed that the optimal optical sectioning of SOLEIL is at 0.66 excitation NA and can reach 0.8 μm optical sectioning, which is around four times larger than the thickness of optical sectioning of TIRF microscopy (≈200 nm). We experimentally measured the excitation profile of our microscope. The measured width of an inclined Gaussian beam is 0.627 μm while the theoretical width is 0.346 μm. We hypothesize that the difference between the measured and theoretical spot sizes is caused by multiple laser modes and aberrations in the system, which enlarges the inclined Gaussian beam width. The laser can be cleaned using a pinhole or a single-mode fiber, and aberrations can be minimized by selecting optimal lenses using sophisticated optical software such as Zemax. This could lead to a performance that is closer to the theoretical value, but this has not been investigated in the current study since most of the information about the objective lens is proprietary information.

We have demonstrated that SOLEIL performs effective optical sectioning in thick samples with a FOV that is comparable to soSPIM; as previously reported: 19 μm× 37 μm [32], 10.8 μm× 25.7 μm [33], and 10 μm× 19 μm [34]. To demonstrate this, we have imaged COS-7 samples in 2D and 3D with an FOV of 25 μm × 45 μm.

We experimentally investigated the difference of optical sectioning between SOLEIL, widefield, and HILO microscopy. The experimental benchmark was done with 23 nm fluorescent beads embedded in 1% agarose gel. We showed that the SBR ratio of SOLEIL improved 80% over HILO microscopy and improved 540% over widefield microscopy. The benefits of SOLEIL over the other illumination schemes (widefield and HILO) have also been demonstrated with several dSTORM samples. With the dSTORM experiments, we showed that the I/bg ratio and the estimated CRLB were significantly improved when us-

ing SOLEIL instead of widefield and HILO illumination. We found that the use of SOLEIL significantly improved the distribution of the I/bg ratio and SOLEIL does not suffer in the same way from the trade-off between FOV and optical sectioning like HILO, SPIM, and soSPIM. The I/bg ratio of SOLEIL was 3.5 to 8.5 times better than that of the widefield illumination (Fig. 2.4, 2.5 (g), Fig. 2.6, 2.7 (j)). This observation was reproducible in all SOLEIL SMLM imaging (Fig. 2.S9, 2.S10). We observed that the labeling density and labeled protein of dSTORM sample can affect background fluorescence. We observed that this effect can be more significant than increasing the sample thickness. For example, we obtained a median I/bg ratio of 10.03 in the 2D COS-7 sample with widefield microscopy and a median I/bg ratio of 13.06 in the 2D Caco2-BBE sample with widefield microscopy. In some SOLEIL experiments, we observed that the I/bg ratio was not a smooth curve, but that the I/bg ratio drops at some arbitrary moments in time (Fig. 2.4 (l), 2.5 (m)). One potential explanation for this is the stability of the stage (supplementary section 2.S9). When the imaging plane is close to the coverslip and the sample drifts away from the objective lens, the sample is excited by a part of the light sheet further away from the center, where the beam width is larger. This changes the excitation condition and can change I/bg ratio. We experimentally validated our assumption by purposely drifting the sample away from the objective lens, and indeed we observed a drop in the I/bg ratio curve (Fig. 2.S11).

In Fig. 2.S5, we performed dSTORM imaging by using SOLEIL microscopy with different exposure times to investigate how exposure time affects the I/bg ratio and the estimated CRLB. We observed that long exposure time deteriorates the I/bg ratio, which can result in a worse CRLB. A possible reason is that the exposure time is longer than the average on-time of the molecule and therefore only background photons are acquired once the molecule has turned off.

Fig. 2.3 (d,f) shows the trade-off between the size of FOV and the optical sectioning of HILO microscopy, similar to previous work [20]. We benchmarked the performance of optical sectioning for HILO with a small and large FOV by use of dSTORM imaging with Caco2-BBE cell (Fig. 2.S12). We observed that the I/bg ratio of large FOV HILO was lower than that of small FOV HILO (Fig. 2.S12 (c)). This illustrates the trade-off relationship between FOV and optical sectioning of HILO in dSTORM sample.

SOLEIL can be extended with more advanced features to increase the acquisition speed and FOV. For example, scanning with multiple parallel light sheets will massively increase the acquisition speed and FOV. These parallel light sheets can be created by diffraction of optical elements [60]. Furthermore, we envision that the DM can be used for adaptive optics (AO) to correct system aberrations when imaging thick samples and that the average fluorescence intensity and blinking rate can be optimized through real-time adaptive control of the light sheet intensity. We believe that SOLEIL will become an important approach for SMLM samples where optical sectioning and aberration correction is essential.

DATA AVAILABILITY

The original image data is available upon reasonable request.

2

DISCLOSURES
The authors declare no conflicts of interest.

SUPPLEMENTAL DOCUMENT
See Supplement 1 for supporting content.

FUNDING

ACKNOWLEDGMENTS

BIBLIOGRAPHY

1. Hess, S. T., Girirajan, T. P. & Mason, M. D. Ultra-High Resolution Imaging by Fluorescence Photoactivation Localization Microscopy. *Biophysical Journal* **91,** 4258–4272. ISSN: 0006-3495. http://www.sciencedirect.com/science/article/pii/S0006349506721403 (2006).

2. Manley S. Gillette J. Patterson, G. High-density mapping of single-molecule trajectories with photoactivated localization microscopy. *Nat. Methods* **5,** 155–157 (2008).

3. Betzig, E. *et al.* Imaging Intracellular Fluorescent Proteins at Nanometer Resolution. *Science* **313,** 1642–1645. ISSN: 0036-8075. eprint: https://science.sciencemag.org/content/313/5793/1642.full.pdf. https://science.sciencemag.org/content/313/5793/1642 (2006).

4. Egner, A. *et al.* Fluorescence Nanoscopy in Whole Cells by Asynchronous Localization of Photoswitching Emitters. *Biophysical Journal* **93,** 3285–3290. https://www.cell.com/biophysj/fulltext/S0006-3495(07)71582-5 (2022) (Nov. 2007).

5. Lidke, K. A., Rieger, B., Jovin, T. M. & Heintzmann, R. Superresolution by localization of quantum dots using blinking statistics. *Opt. Express* **13,** 7052–7062. http://www.opticsexpress.org/abstract.cfm?URI=oe-13-18-7052 (Sept. 2005).

6. Smith, C. & Joseph N. Rieger, B. Fast, single-molecule localization that achieves theoretically minimum uncertainty. *Nat. Methods* **7,** 373–375 (2010).

7. Nieuwenhuizen, R. P. J. *et al.* Measuring image resolution in optical nanoscopy. *Nature Methods* **10,** 557–562 (2013).

8. Ober, R. J., Ram, S. & Ward, E. S. Localization Accuracy in Single-Molecule Microscopy. *Biophysical Journal* **86,** 1185–1200. https://www.cell.com/biophysj/fulltext/S0006-3495(04)74193-4 (2004).

9. Smith, C. S., Stallinga, S., Lidke, K. A., Rieger, B. & Grunwald, D. Probability-based particle detection that enables threshold-free and robust in vivo single-molecule tracking. *Molecular Biology of the Cell* **26,** 4057–4062 (2015).

10. Smith, C. S. *et al.* An automated Bayesian pipeline for rapid analysis of single-molecule binding data. *Nature Communications* **10.** https://www.nature.com/articles/s41467-018-08045-5 (2019).

11. Cowen, T., Haven, A. J. & Burnstock, G. Pontamine sky blue: A counterstain for background autofluorescence in fluorescence and immunofluorescence histochemistry. *Histochemistry* **82,** 205–208 (1985).

12. Bierwagen, J. *et al.* Far-Field Autofluorescence Nanoscopy. *Nano Letters* **10,** 4249–4252 (2010).

13. Clancy, B. & Cauller, L. Reduction of background autofluorescence in brain sections following immersion in sodium borohydride. *Journal of Neuroscience Methods* **83,** 97–102. ISSN: 0165-0270. https://www.sciencedirect.com/science/article/pii/S0165027098000661 (1998).

14. Mansfield, J. R., Gossage, K. W., Hoyt, C. C. & M.D., R. M. L. Autofluorescence removal, multiplexing, and automated analysis methods for in-vivo fluorescence imaging. *Journal of Biomedical Optics* **10,** 1–9. https://doi.org/10.1117/1.2032458 (2005).

15. MURRAY, J. M., APPLETON, P. L., SWEDLOW, J. R. & WATERS, J. C. Evaluating performance in three-dimensional fluorescence microscopy. *Journal of Microscopy* **228,** 390–405. https://onlinelibrary.wiley.com/doi/abs/10.1111/j.1365-2818.2007.01861.x (2007).

16. Mertz, J. & Kim, J. Scanning light-sheet microscopy in the whole mouse brain with HiLo background rejection. *Journal of Biomedical Optics* **15,** 1–7. https://doi.org/10.1117/1.3324890 (2010).

17. White, J. G., Amos, W. B. & Fordham, M. An evaluation of confocal versus conventional imaging of biological structures by fluorescence light microscopy. *Journal of Cell Biology* **105,** 41–48. ISSN: 0021-9525. https://doi.org/10.1083/jcb.105.1.41 (July 1987).

18. Axelrod, D. Total Internal Reflection Fluorescence Microscopy in Cell Biology. *Traffic* **2,** 764–774. https://onlinelibrary.wiley.com/doi/abs/10.1034/j.1600-0854.2001.21104.x (2001).

19. Schneckenburger, H. Total internal reflection fluorescence microscopy: technical innovations and novel applications. *Current Opinion in Biotechnology* **16.** Analytical biotechnology, 13–18. ISSN: 0958-1669. https://www.sciencedirect.com/science/article/pii/S0958166904001697 (2005).

20. Tokunaga, M., Imamoto, N. & Sakata-Sogawa, K. Highly inclined thin illumination enables clear single-molecule imaging in cells. *"Nat. Methods"* **5,** 159–161. (2021) (Jan. 2008).

21. Konopka, C. A. & Bednarek, S. Y. Variable-angle epifluorescence microscopy: a new way to look at protein dynamics in the plant cell cortex. *The Plant Journal* **53,** 186–196 (2008).

22. Jungmann, R. *et al.* Multiplexed 3D cellular super-resolution imaging with DNA-PAINT and Exchange-PAINT. *Nature Methods* **11,** 313–318. https://www.ncbi.nlm.nih.gov/pmc/articles/PMC4153392/ (Feb. 2014).

23. Liu, S., Huh, H., Lee, S.-H. & Huang, F. Three-Dimensional Single-Molecule Localization Microscopy in Whole-Cell and Tissue Specimens. *Annual Review of Biomedical Engineering* **22,** 155–184. https://www.annualreviews.org/doi/abs/10.1146/annurev-bioeng-060418-052203 (June 2020).

24. Tang, J. & Han, K. Y. Extended field-of-view single-molecule imaging by highly inclined swept illumination. *Optica* **5,** 1063–1069. https://opg.optica.org/optica/abstract.cfm?URI=optica-5-9-1063 (Sept. 2018).

25. Ahrens, M., Orger, M. & Robson, D. e. a. Whole-brain functional imaging at cellular resolution using light-sheet microscopy. *Nat. Methods* **10,** 413–420 (2013).

26. Lu, C., Tang, W. & Liu, Y. e. a. Lightsheet localization microscopy enables fast, large-scale, and three-dimensional super-resolution imaging. *Commun Biol* **2** (2019).

27. Dean, K. M., Roudot, P., Welf, E. S., Danuser, G. & Fiolka, R. Deconvolution-free Subcellular Imaging with Axially Swept Light Sheet Microscopy. *Biophysical Journal* **108,** 2807–2815. https://www.sciencedirect.com/science/article/pii/S0006349515004981 (June 2015).

28. Gustavsson, A.-K., Petrov, P. N. & Moerner, W. E. Light sheet approaches for improved precision in 3D localization-based super-resolution imaging in mammalian cells. *Opt. Express* **26,** 13122–13147. http://www.opticsexpress.org/abstract.cfm?URI=oe-26-10-13122 (May 2018).

29. Gustavsson, A., Petrov, P. & Lee, M. e. a. 3D single-molecule super-resolution microscopy with a tilted light sheet. *Nat Commun* **9.** https://www.nature.com/articles/s41467-017-02563-4 (Jan. 2018).

30. Fadero, T. C. *et al.* LITE microscopy: Tilted light-sheet excitation of model organisms offers high resolution and low photobleaching. *Journal of Cell Biology* **217,** 1869–1882. ISSN: 0021-9525. eprint: https://rupress.org/jcb/article-pdf/217/5/1869/1378296/jcb_201710087.pdf. https://doi.org/10.1083/jcb.201710087 (Feb. 2018).

31. Migliori, B. *et al.* Light sheet theta microscopy for rapid high-resolution imaging of large biological samples. *BMC Biology* **16.** https://bmcbiol.biomedcentral.com/articles/10.1186/s12915-018-0521-8 (2021) (May 2018).

32. Meddens, M. B. M. *et al.* Single objective light-sheet microscopy for high-speed whole-cell 3D super-resolution. *Biomed. Opt. Express* **7,** 2219–2236. http://www.osapublishing.org/boe/abstract.cfm?URI=boe-7-6-2219 (June 2016).

33. Galland, R. *et al.* 3D high- and super-resolution imaging using single-objective SPIM. *Nat Methods* **12,** 641–644. https://www.nature.com/articles/nmeth.3402 (July 2015).

34. Zagato, E. *et al.* Microfabricated devices for single objective single plane illumination microscopy (SoSPIM). *Opt. Express* **25,** 1732–1745. http://www.osapublishing.org/oe/abstract.cfm?URI=oe-25-3-1732 (Feb. 2017).

35. Kumar, M. & Kozorovitskiy, Y. Tilt-invariant scanned oblique plane illumination microscopy for large-scale volumetric imaging. *Opt. Lett.* **4,** 1706–1709 (2019).

36. Kumar, M. & Kozorovitskiy, Y. Tilt (in)variant lateral scan in oblique plane microscopy: a geometrical optics approach. *Biomed. Opt. Express* **11,** 3346–3359 (June 2020).

37. An, S. *et al.* Axial plane single-molecule super-resolution microscopy of whole cells. *Biomed. Opt. Express* **11,** 461–479. http://www.osapublishing.org/boe/abstract.cfm?URI=boe-11-1-461 (Jan. 2020).

38. An, S. *et al.* Axial plane single-molecule super-resolution microscopy of whole cells. *Biomed. Opt. Express* **11,** 461–479. http://www.osapublishing.org/boe/abstract.cfm?URI=boe-11-1-461 (Jan. 2020).

39. Yang, B. *et al.* Epi-illumination SPIM for volumetric imaging with high spatial-temporal resolution. *Nature Methods* **16,** 501–504. https://www.nature.com/articles/s41592-019-0401-3 (June 2019).

40. Dunsby, C. Optically sectioned imaging by oblique plane microscopy. *Optics Express* **16,** 20306 (Nov. 2008).

41. Tang, J. & Han, K. Y. Low-photobleaching line-scanning confocal microscopy using dual inclined beams. *Journal of Biophotonics* **12,** e201900075. https://onlinelibrary.wiley.com/doi/abs/10.1002/jbio.201900075 (2019).

42. Sikkel, M. B. *et al.* High speed sCMOS-based oblique plane microscopy applied to the study of calcium dynamics in cardiac myocytes. *Journal of Biophotonics* **9,** 311–323 (Oct. 2015).

43. Sparks, H. *et al.* Dual-view oblique plane microscopy (dOPM). *Biomed. Opt. Express* **11,** 7204–7220. http://www.osapublishing.org/boe/abstract.cfm?URI=boe-11-12-7204 (Dec. 2020).

44. Bouchard, M. B. *et al.* Swept confocally-aligned planar excitation (SCAPE) microscopy for high-speed volumetric imaging of behaving organisms. *Nature Photonics* **9,** 113–119. https://www.nature.com/articles/nphoton.2014.323#Sec6 (Feb. 2015).

45. Kumar, M., Kishore, S., Nasenbeny, J., McLean, D. L. & Kozorovitskiy, Y. Integrated one- and two-photon scanned oblique plane illumination (SOPi) microscopy for rapid volumetric imaging. *Optics Express* **26,** 13027–13041. https://www.osapublishing.org/oe/fulltext.cfm?uri=oe-26-10-13027&id=386184 (May 2018).

46. Kumar, S. *et al.* High-speed 2D and 3D fluorescence microscopy of cardiac myocytes. *Opt. Express* **19,** 13839–13847. http://www.osapublishing.org/oe/abstract.cfm?URI=oe-19-15-13839 (July 2011).

47. Sapoznik, E., Chang, B.-J. & Huh, J. A versatile oblique plane microscope for large-scale and high-resolution imaging of subcellular dynamics. *eLife* **9** (eds Lakadamyali, M., Akhmanova, A. & Power, R.) e57681. ISSN: 2050-084X. https://doi.org/10.7554/eLife.57681 (Nov. 2020).

48. Fish, K. N. Total Internal Reflection Fluorescence (TIRF) Microscopy. *Current Protocols in Cytometry.* https://currentprotocols.onlinelibrary.wiley.com/doi/10.1002/0471142956.cy1218s50 (Oct. 2009).

49. Axelrod, D. Cell-substrate contacts illuminated by total internal reflection fluorescence. *The Journal of Cell Biology* **89,** 141–145. https://rupress.org/jcb/article/89/1/141/59168/Cell-substrate-contacts-illuminated-by-total (Apr. 1981).

50. Gao, F. & Han, L. Implementing the Nelder-Mead simplex algorithm with adaptive parameters. *Computational Optimization and Applications* **51,** 259–277. https://link.springer.com/article/10.1007/s10589-010-9329-3 (2010).

51. Ries, J. SMAP: a modular super-resolution microscopy analysis platform for SMLM data. *Nature Methods* **17,** 870–872 (Aug. 2020).

52. Wang, Y. *et al.* Localization events-based sample drift correction for localization microscopy with redundant cross-correlation algorithm. *Optics Express* **22,** 15982 (June 2014).

53. Booth, M., Wilson, T., Sun, H.-B., Ota, T. & Kawata, S. Methods for the characterization of deformable membrane mirrors. *Appl. Opt.* **44,** 5131–5139. http://www.osapublishing.org/ao/abstract.cfm?URI=ao-44-24-5131 (Aug. 2005).

54. Pozzi, P. *et al.* Anisoplanatic adaptive optics in parallelized laser scanning microscopy. *Opt. Express* **28,** 14222–14236. http://www.osapublishing.org/oe/abstract.cfm?URI=oe-28-10-14222 (May 2020).

55. Antonello, J., Wang, J., He, C., Phillips, M. & Booth, M. Interferometric calibration of a deformable mirror. *Zenodo.* https://zenodo.org/record/3714951#.YUtw7PkzZPY (Mar. 2020).

56. Patlan, V., Soloviev, O. & Vdovin, G. V. Optimal diffraction-limited focusing through static aberrations. *Proc. of SPIE* **9194,** 54–62. https://doi.org/10.1117/12.2063373 (2014).

57. Bertsimas, D. & Vempala, S. Solving convex programs by random walks. *J. ACM* **51,** 540–556. https://doi.org/10.1117/12.2063373 (July 2004).

58. Marijn E. Siemons, N. A. K. H., Kole, M. H. P. & Kapitein, L. C. Robust adaptive optics for localization microscopy deep in complex tissue. *Nat. Commun.* **12.** https://www.nature.com/articles/s41467-021-23647-2 (2021).

59. Siemons, M. *et al.* Comparing strategies for deep astigmatism-based single-molecule localization microscopy. *Biomed. Opt. Express* **11,** 735–751. http://www.osapublishing.org/boe/abstract.cfm?URI=boe-11-2-735 (Feb. 2020).

60. Weng, C. H., Tang, J. & Han, K. Y. Optimizing the performance of multiline-scanning confocal microscopy. *J Phys D Appl Phys* **54,** 105401. https://doi.org/10.1088/1361-6463/abc84b (Dec. 2020).

SUPPLEMENTAL INFORMATION:

SINGLE-OBJECTIVE LENS INCLINED LIGHT SHEET LOCALIZATION MICROSCOPY

2

2.S1. EXCITATION PROFILE OF SOLEIL INCLINED LIGHT-SHEET

We used an inclined Gaussian beam to model the excitation profile of SOLEIL and corrected the inclined angle for the refraction index mismatch. The inclined light sheet profile is dependent on the beam radius (r_{ex}), the beam displacement (d) at the back focal plane of the objective, the excitation wavelength (λ_{ex}), and the refractive index of the sample medium (n_{medium}) [1]. The optical axis of the Gaussian beam (z_{Gau}) was obtained through a coordinate transformation from the optical axis of the objective lens (z) and light sheet inclined direction (x) Fig. 2.S1:

$$\begin{bmatrix} r_{Gau} \\ z_{Gau} \end{bmatrix} = \begin{bmatrix} \cos\theta_{inc} & -\sin\theta_{inc} \\ \sin\theta_{inc} & \cos\theta_{inc} \end{bmatrix} \begin{bmatrix} x \\ z \end{bmatrix}, \tag{2.S1}$$

where θ_{inc} is the angle of inclined light sheet in the sample medium (see Fig. 2.S1). The inclined angle θ_{inc}, taking into account the reflective index at the sample medium and coverslip interface, becomes:

$$\theta_{oil} = \arctan(d/f_{ob})$$
$$\theta_{inc} = \arcsin(n_{oil} \cdot \sin(\theta_{oil})/n_{medium}) \tag{2.S2}$$

where n_{oil} and n_{medium} are the refractive indices of immersion oil and the sample medium, respectively, and d is the beam displacement from the optical axis at the back focal plane of the objective. In the above formula, we assume that the refractive index of the coverslip is the same as the immersion oil, and the inclined angle remains the same in immersion oil and the coverslip. We did dSTORM imaging in this research, so the refractive index of sample media (n_{medium}) is same as water (n=1.33).

The intensity profile of the Gaussian beam is as follows:

$$I(r_{Gau}, z_{Gau}) = I_0 \left(\frac{w_0}{w(z)} \right)^2 \exp \left(\frac{-2r_{Gau}^2}{w(z)^2} \right) \tag{2.S3}$$

with the radius of the Gaussian beam waist as [2][3].

$$w_0 = \frac{\lambda_{ex}}{\pi \cdot \arctan\left(\frac{r_{ex}}{f_{ob}} \right)}$$
$$w(z) = w_0 \sqrt{1 + \left(\frac{z}{z_R} \right)^2}, \tag{2.S4}$$

where r_{ex} is the beam radius in the back focal plane, λ_{ex} is the wavelength of the excitation laser, z_R is the Rayleigh length of the Gaussian beam, and f_{ob} is the focal length of the objective lens.

The beam radius and the maximum beam displacement, d, are limited by the NA at which total internal reflection fluorescence (TIRF) occurs. In a water-immersed sample, the NA at which this happens is 1.33. Illumination at higher NA will result in an increased background. The size of the back focal plane (pupil plane) is $2.66 \cdot f_{ob}$ (i.e. $2NAf_{ob}$). Therefore, the maximum beam shift d is $1.33 \cdot f_{ob} - r_{ex}$.
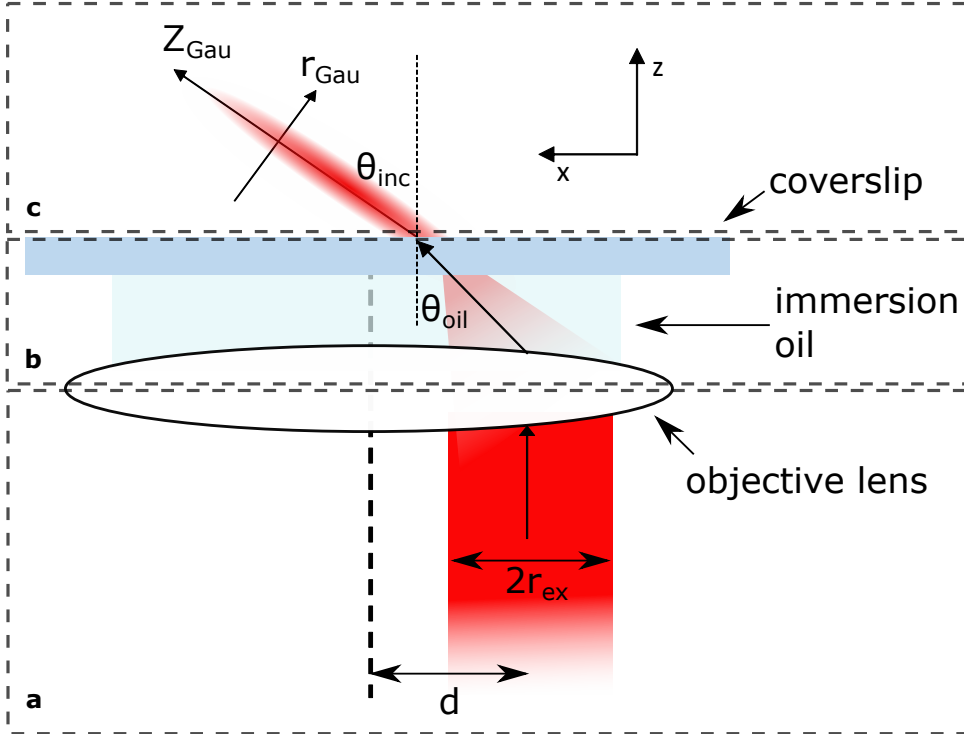
Figure 2.S1: Gaussian beam model of SOLEIL. (a) The excitation beam is shifted by d, which generates the inclined angle. The beam radius r_{ex} determines the size of the Gaussian beam waist and the excitation numerical aperture. (b) The Gaussian beam is launched from the objective at an incline of θ_{oil} from the optical axis because of the beam shift d at the back focal plane. (c) The tilted angle in the sample follows Snell's law and becomes θ_{inc}.

2.S2. CHARACTERIZATION OF SOLEIL LIGHT SHEET PROFILE

To measure the light-sheet profile, we used a 23 nm fluorescence bead (Thermo Fisher, Tetraspeck) embedded in agarose gel (n=1.33) to scan the SOLEIL light sheet profile. Given the total emission intensity in the acquired image is proportional to the excitation intensity, the light sheet profile can be measured by summarizing the photon counts in the acquired camera image. Fig. 2.S2 (a) shows the schematic of bead scanning over the light sheet profile. In practice, we used a piezo stage (Smaract, SMC2) to move a fluorescence bead through light sheet. Fig. 2.S2 (b) shows the camera images we acquired at different x/z position. To characterize the light sheet profile, we fitted the measured light sheet profile (Fig. 2.S3 (a)) with an inclined Gaussian beam, using the Nelder-Mead algorithm and the mean square error as cost function. Fig. 2.S3 (b) is the fitted result. The waist of light sheet (w_0) is 0.627 μm and the Rayleigh length is 1.929 μm. The angle of the light sheet (θ_{inc}) is 30° from the optical axis of the objective lens (z-axis).

a

b
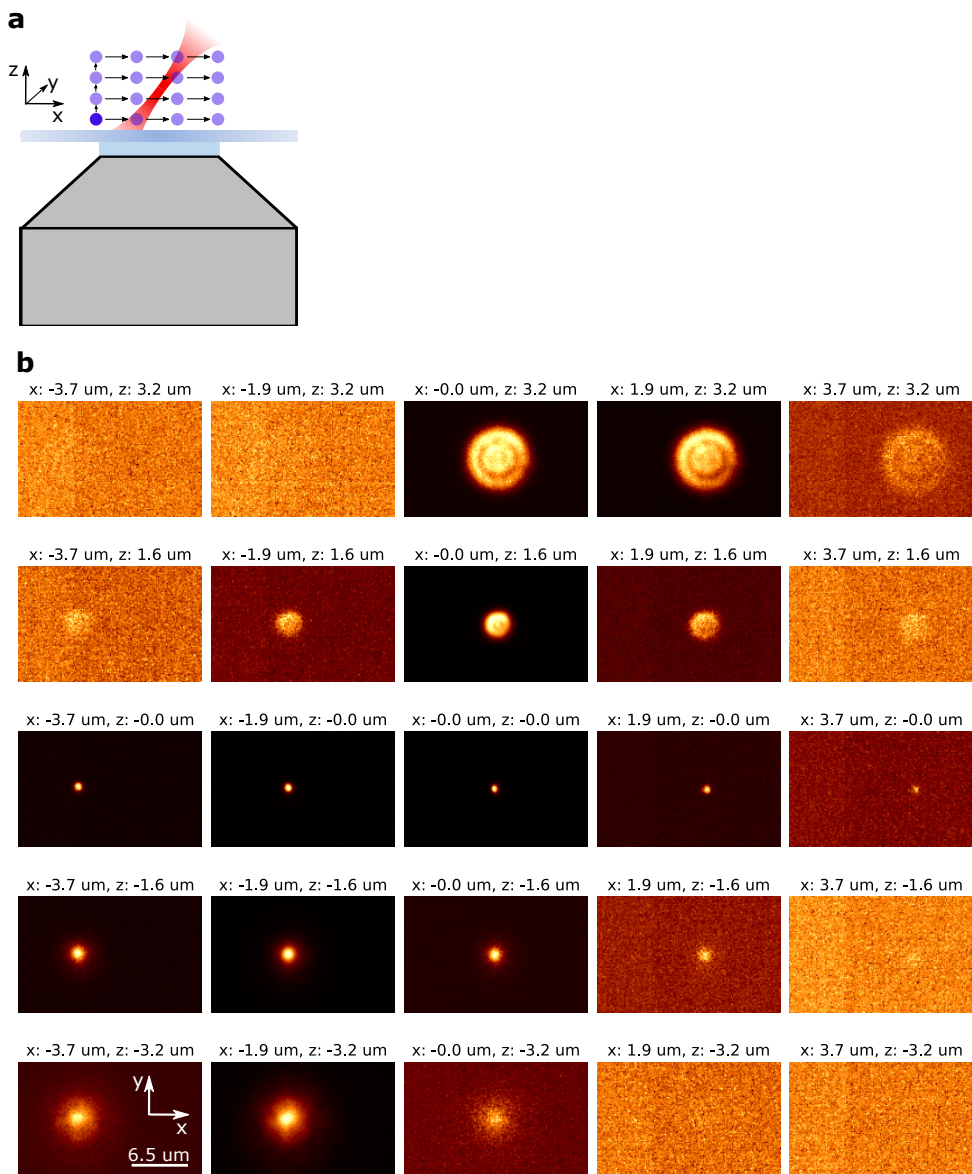
Figure 2.S2: Bead scanning experiment to characterize the light sheet profile. (a) Schematic of bead scanning experiment. The blue dot is a fluorescent bead used to scan the light sheet profile. (b) The acquired images when the piezo stage is moved to different x/z positions.
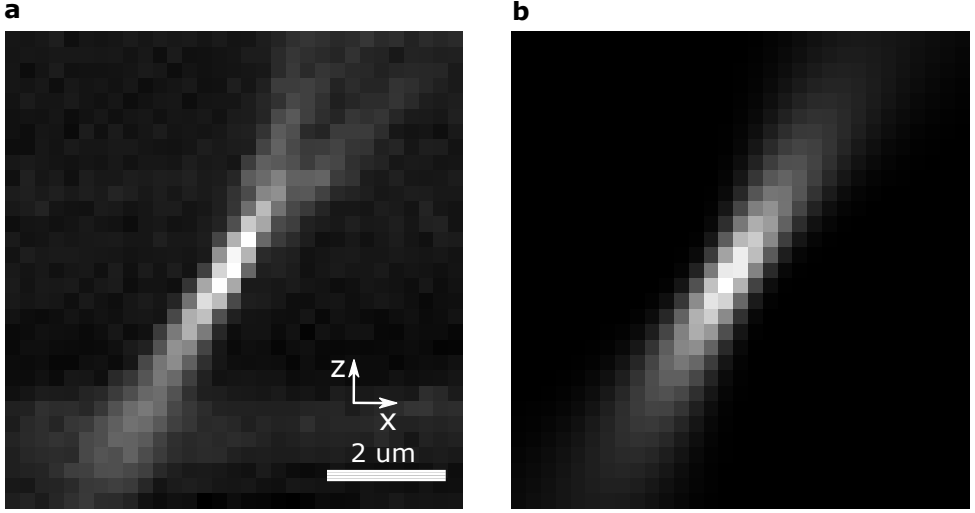
Figure 2.S3: Inclined light-sheet illumination profile. (a) Measured inclined light-sheet excitation profile with a scanned bead. Scale bar is 2 μm. (b) Estimated inclined Gaussian beam model.

2.S3. CHARACTERIZATION OF HILO MICROSCOPY

The profile of highly inclined widefield illumination is fully parameterized by two radii: i) that of the beam width (R_2) and ii) that of the projected beamwidth (R_1) (Fig. 2.S4 (a)). The beamwidth R_2 projects onto the focal plane (FP) and becomes an ellipse, where R_1 is the long axis and R_2 is the short axis.

$$\frac{R_2}{R_1} = \cos\theta. \tag{2.S5}$$

The optical sectioning achieved by HILO (dz) follows from the geometric relationship between the HILO beam width (R_1) and the inclined angle (θ) from the optical axis of objective lens [4]:

$$dz = \frac{R_1}{\tan\theta}. \tag{2.S6}$$

To measure the two radii we imaged 200 frames of fluorescent beads embedded in agarose gel (Fig. 2.S4 (b)). For every frame, the stage was moved to obtain a different set of beads. To measure the illumination profile independent of the background the position, intensities, and background were estimated for each bead using maximum likelihood estimation with a Gaussian model. The reconstruction was a superposition of 37078 bead positions and intensities (Fig. 2.S4 (c)). From these localizations, we calculated the moment of inertia matrix M:

$$M = \begin{bmatrix} M_{xx} & M_{xy} \\ M_{yx} & M_{yy} \end{bmatrix}, \tag{2.S7}$$

with

$$M_{xx} = \sum_{i=0}^{N} I_i x_i^2 / I_{sum},$$

$$M_{yy} = \sum_{i=0}^{N} I_i y_i^2 / I_{sum},$$

$$M_{xy} = M_{yx} = \sum_{i=0}^{N} I_i x_i \cdot y_i / I_{sum}, \qquad (2.S8)$$

$$I_{sum} = \sum_{i=0}^{N} I_i,$$

where N is the number of localizations, x_i, y_i is the position, and I_i is the intensity of ith localization.

The principal axes of M are the best estimates of R_1 and R_2:

$$M = Q\Lambda Q^T \qquad (2.S9)$$

with

$$Q = \begin{bmatrix} v_1 & v_2 \end{bmatrix},$$

$$\Lambda = \begin{bmatrix} \lambda_1 & 0 \\ 0 & \lambda_2 \end{bmatrix}, \lambda_1 > \lambda_2 \qquad (2.S10)$$

where v_1 and v_2 are the eigenvectors (principal axes), and λ_1 and λ_2 are the eigenvalues (these are computed using NumPy linear algebra functions "eig").

The angle (θ) is obtained from the ratio of the two eigenvalues of M:

$$\theta = \cos^{-1} \sqrt{\frac{\lambda_2}{\lambda_1}} \qquad . \qquad (2.S11)$$

The HILO beam width R_2 is obtained from the eigenvalue of matrix M:

$$R_1 = 2\sqrt{\lambda_1}$$
$$R_2 = 2\sqrt{\lambda_2} \qquad (2.S12)$$

The measured angle of the HILO profile is 74.5° from the optical axis of the objective lens, the HILO beam width R_1 is 43 μm (which is close to the previously published result [4]) and the corresponding beam thickness (dz) is 11.94 μm.
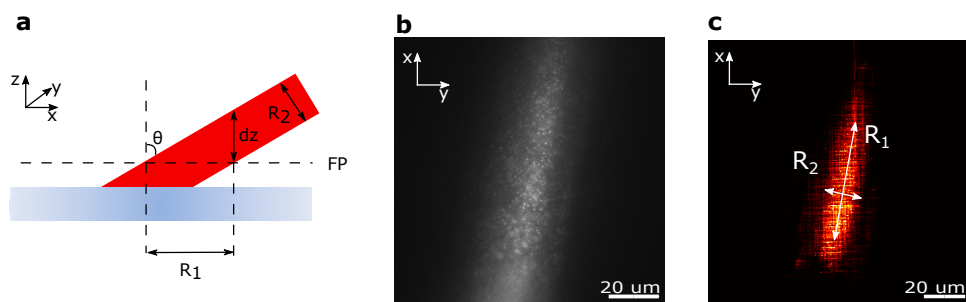
Figure 2.S4: Characterization of HILO microscopy. (a) HILO profile and definition of the parameters. θ is the HILO beam angle and FP indicates the focal plane. dz is the HILO beam thickness. The R_1, R_2 are consistent with the parameters in Eq.2.S5. (b) 3D agarose bead image with HILO microscope. (c) localization result of 200 frames of 3D agarose bead imaging. Here, we assume the laser beam is a perfect circle, so the beam radius along the beam direction R_2 in (a) is the same as the laser beam width on the focal plane R_2 in (c).

2.S4. CAMERA EXPOSURE TIME AFFECTS THE INTENSITY-TO-BACKGROUND RATIO AND ESTIMATED CRLB

Here, we investigated the influence of exposure time on estimated CRLB and I/bg ratio in SOLEIL microscopy. In dSTORM imaging, the fluorescence molecules randomly enter a fluorescent (on) state for several milliseconds and then turn off, by bleaching or entering a dark state. Increasing the camera exposure time beyond the molecule on-state duration only acquires more background photons, and does not add any additional information about the molecule position. Thus, increasing camera exposure time does not always improve the estimated CRLB. We use the HEK-293T sample for this demonstration. In Fig. 2.S5 (e), we show that long exposure time can decrease the I/bg ratio, which ultimately deteriorates the estimated CRLB Fig. 2.S5 (e). We think that an exposure time lower than 20 ms would not affect the I/bg ratio too much, but would decrease the localization intensity deteriorating the estimated CRLB.
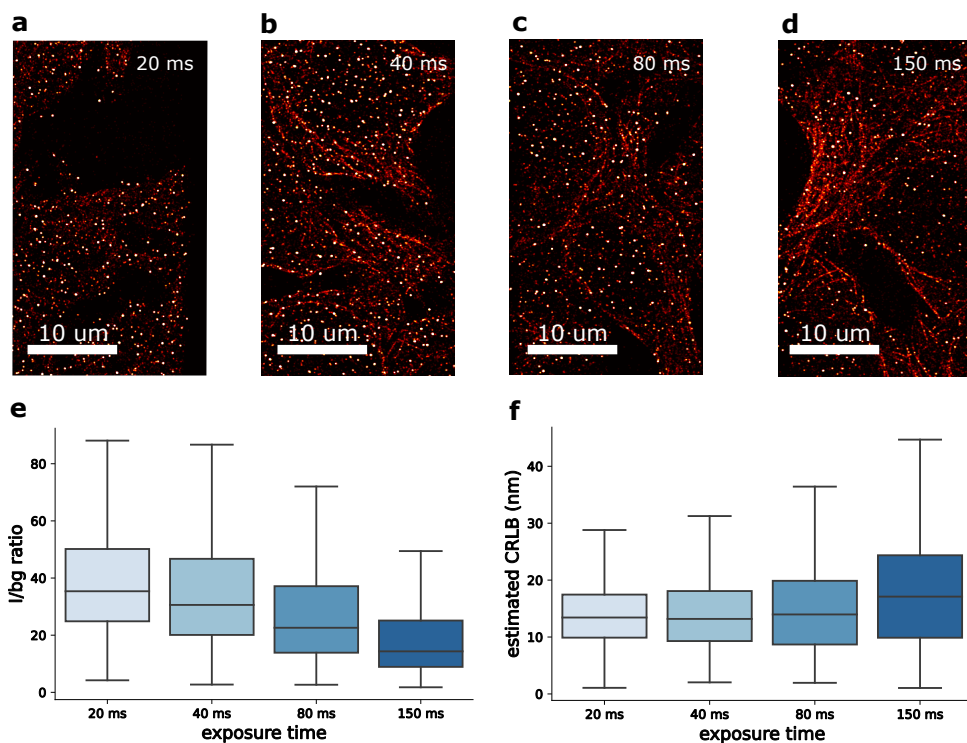
Figure 2.S5: The experimental I/bg ratio and estimated CRLB under different exposure time in SOLEIL microscopy with HEK-293T dSTORM sample. The laser intensity is 5.46 kWcm^{-2}. (a-d) imaging HEK-293T dSTORM sample with SOLEIL microscopy with different exposure time (20,40,80,150 ms). (e,f) I/bg ratio and estimated CRLB versus exposure time.

2.S5. OPTICAL SETUP FOR INTERFEROMETRIC WAVEFRONT SENSING

We measured the phase introduced by the deformable mirror (DM) with a Michelson interferometric (Fig. 2.S6 (a)). The light reflected by the DM interfered with the light reflected from the flat reference mirror. The interferogram is shown in Fig. 2.S6 (b) contains the information about the phase on the DM. The reference mirror was tilted, which created high-frequency stripes in the interferogram. The discrete Fourier transform (DFT) computed using the fast Fourier transform (FFT) of the interferogram shows three peaks (Fig. 2.S6 (c)), originating from the stripes in the interferogram. The DM phase information was contained in the ±1 order peak. By cropping the first-order peak and performing an inverse FFT we acquired the wrapped phase. After unwrapping the phase, we obtained an estimate for the phase introduced by the DM. More detailed information can be found in [5, 6].

A coherent 532 nm laser diode (Thorlabs, CPS532) was collimated and expanded five times through a telescope (f1,2, Thorlabs, AC254-100-A-ML; Thorlabs, AC254-500-A-ML). An iris (iris, Thorlabs, SM1D12D) was used to control the beam diameter and to match the width of the laser beam with the DM size. A 50:50 non-polarization beam splitter (BS, Thorlabs, BS013) was used to split the beam and to recombine the reference beam with the one from the DM. The relay systems f3,4 (Thorlabs, AC254-300-A-ML) and f5,6 (Thorlabs, AC254-250-A-ML; Thorlabs, AC254-100-A-ML) were used to image the DM plane on the camera. The reference mirror was a broadband dielectric mirror (reference mirror, Thorlabs, BB1-E02). The tilted angle of the reference mirror was adjusted with a kinetic mount (reference mirror, Thorlabs, KM100). A CMOS camera (Thorlabs, DCC 1545M-GL) was used to image the interferogram (Thorlabs, DCC1545-M GL).
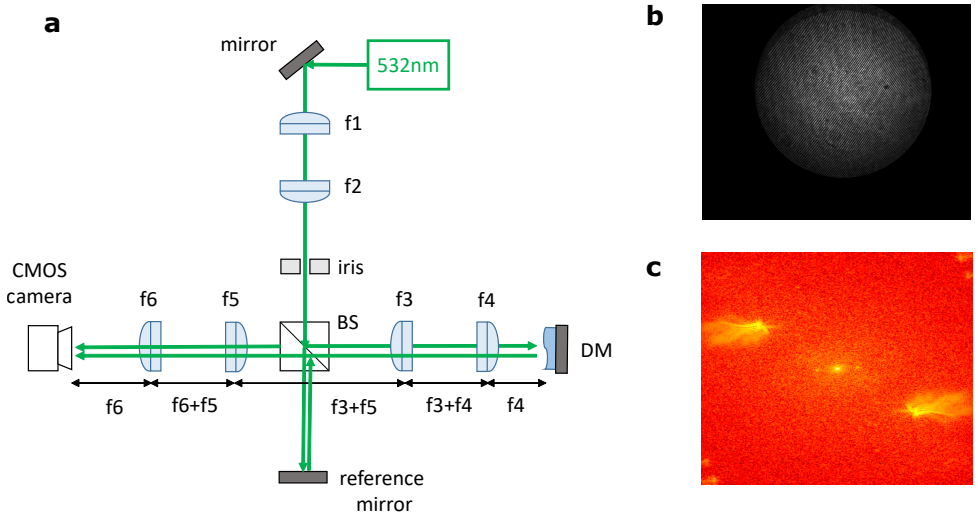
Figure 2.S6: Overview of interferometric wavefront sensing. (a) A schematic overview of the optical setup. (b) The interferogram of the interference between the light from the reference mirror and the light from the deformable mirror measured with the CMOS camera. (c) The Fourier transform of the interferogram in (b).

2.S6. THE CRLB OF SOLEIL VERSUS WIDEFIELD ILLUMINATION

In Fig. 2.S7 (a), we show the CRLB under different intensity and background counts. We observed a significant reduction in background and improvement of the CRLB of SOLEIL over widefield illumination.

We simulated the CRLB with a Gaussian PSF model to demonstrate the CRLB improvement Fig. 2.S7 (b) at these different I/bg ratios. The median intensity and background ratio (I/bg ratio) of the 2D COS-7 cells (Fig.2.4 (g)) imaged with widefield and SOLEIL illumination are 10.03 and 84.22, respectively. The CRLB of SOLEIL is improved by IF = 72.5% compared to widefield illumination,

$$\text{IF} = \frac{\text{CRLB}_{\text{WF}}}{\text{CRLB}_{\text{SOLEIL}}}, \tag{2.S13}$$

where $\text{CRLB}_{\text{SOLEIL}}$ is the CRLB with the SOLEIL and CRLB_{WF} is CRLB with widefield illumination.
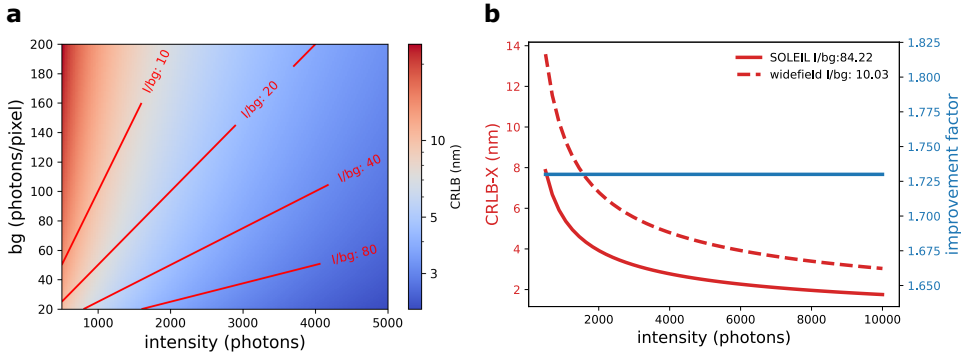
Figure 2.S7: The impact of the intensity and background ratio on the CRLB. (a) The CRLB at different intensities and background counts. The red solid line is the contour line of an I/bg ratio. (b) Red line: Theoretical CRLB with experimental I/bg ratio from 2D COS-7 STORM measurement (Fig. 2.4 (g)). Blue line: improvement ratio. In the simulation, the Gaussian model width σ is chosen as $\frac{\lambda}{4NA}$.

2.S7. CRLB CURVE OF ASTIGMATISM PSF

Here, we show the CRLB curve of an astigmatic PSF. The PSF model was estimated using the cubic spline method from the SMAP software [7]. We imaged fluorescent beads with 23 nm radius embedded in 1% w/v agarose gel to measure the experimental PSF. The z step size is 10 nm.
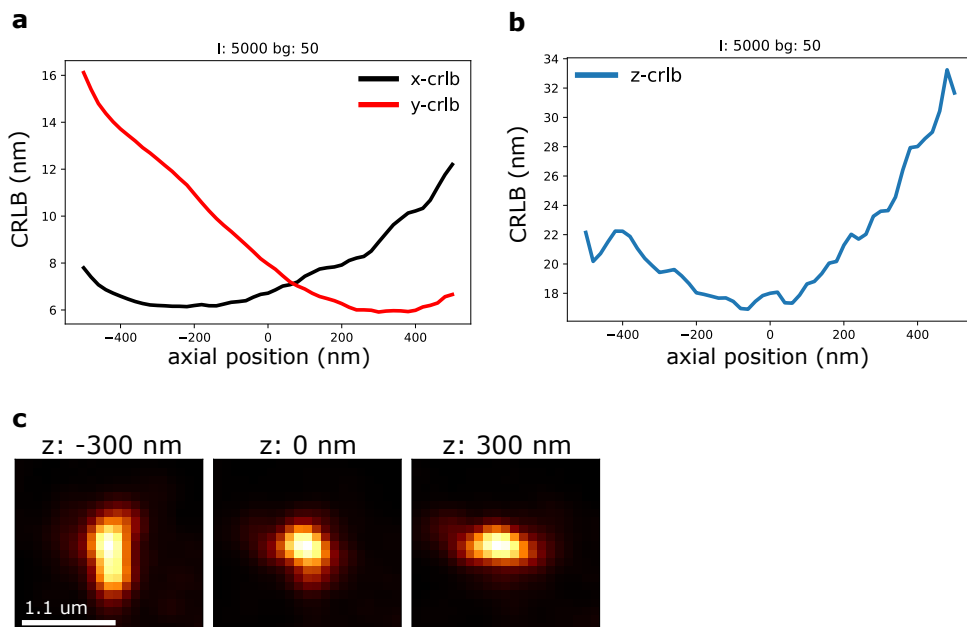
Figure 2.S8: CRLB curve of the astigmatic PSF. I indicates the photon count of the localization and bg stands for the background (photons/pixel).(a) x,y-CRLB curve of the astigmatic PSF. (b) z-CRLB of the astigmatic PSF. (c) cubic spline model of the astigmatic PSF.

2.S8. 2D AND 3D SUPER-RESOLUTION RECONSTRUCTION OF A COS-7 CELL

In this section, we imaged COS-7 cells with an 8 μm total stepped distance. In 2D COS-7 cell imaging, without the astigmatic PSF, we observed that the I/bg ratio significantly improved. In widefield microscopy, the median value of localizations intensity was 692 photons and in SOLEIL was 641 photons. The median background of widefield microscopy was 110 photons/pixel and the median background of SOLEIL was 26 photons/pixel. In widefield microscopy, the median value of estimated CRLB was 16.3 nm and in SOLEIL microscopy was 12.2 nm.

In 3D COS-7 cell imaging, with the astigmatic PSF, we can observe a 120% improvement of the lateral estimated CRLB and 106% improvement of the axial CRLB improves. In widefield microscopy, the median value of localizations intensity was 1256 photons and in SOLEIL was 1183 photons. The median background for widefield microscopy was 59 photons/pixel and the median background for SOLEIL was 5 photons/pixel. (Fig. 2.S10 (e,h,i)).
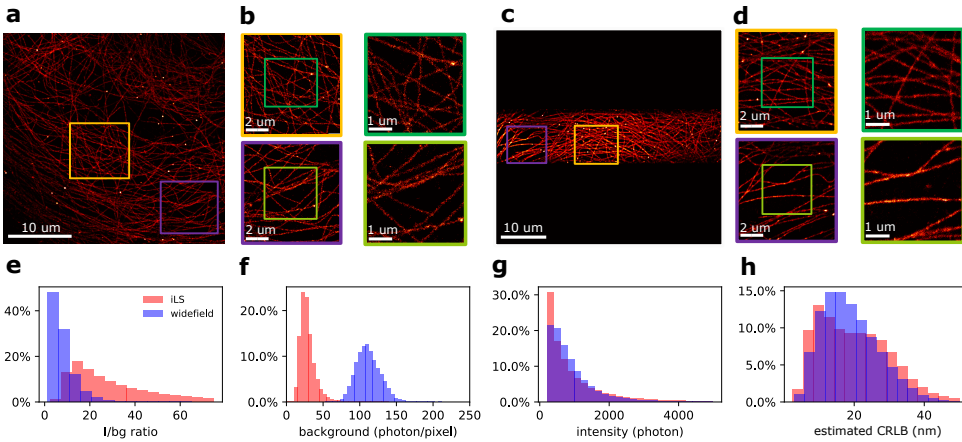
Figure 2.S9: The 2D super-resolution reconstruction of a COS-7 cell. (a) 2D super-resolution reconstruction with widefield illumination. (b) Zoom-in of (a). (c) 2D localization reconstruction from SOLEIL with an $8\mu m$ scanning distance. (d) Zoom-in image of (c). (e-h) Comparison of intensity to background ratio, background, intensity, and precision between widefield and SOLEIL.

2
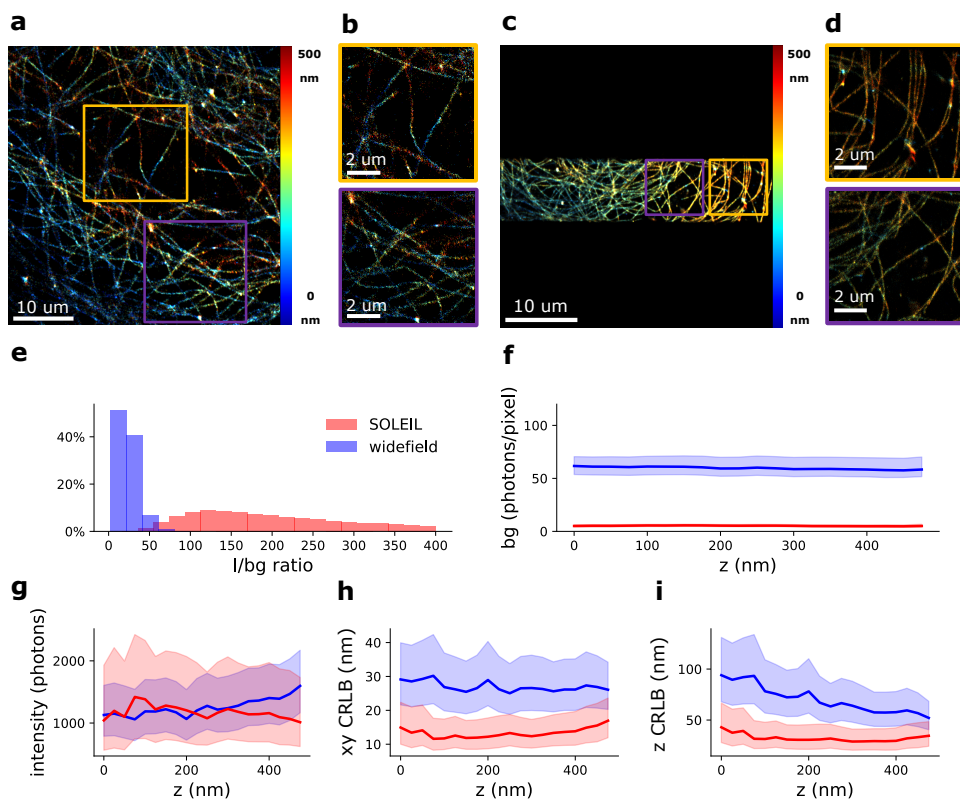
Figure 2.S10: 3D super-resolution reconstruction of a COS-7 cell with an astigmatic PSF. (a) 3D super-resolution reconstruction with widefield illumination. (b) Zoom-in of (a). (c) 3D super-resolution reconstruction from SOLEIL (8 μm scanning distance). (d) Zoom-in of (c). (e-i) Benchmark of I/bg ratio, background, intensity, and precision between SOLEIL and widefield illumination. The opaque color region represents the first quartile to the third quartile.

2.S9. STABILITY TEST OF SOLEIL

To investigate the reason for the sudden decrease of the I/bg ratio in SOLEIL microscopy, we performed a stability test with a HEK-293T sample. First, we imaged the sample at the regions close to the coverslip Fig. 2.S11 (a). Then we manually shifted the sample 500 nm away from the objective lens Fig. 2.S11 (b). In the Fig. 2.S11 (c), we can observe a sudden decrease in I/bg ratio. We considered this as one possible reason for the sudden decrease of I/bg in the COS-7 sample imaging.
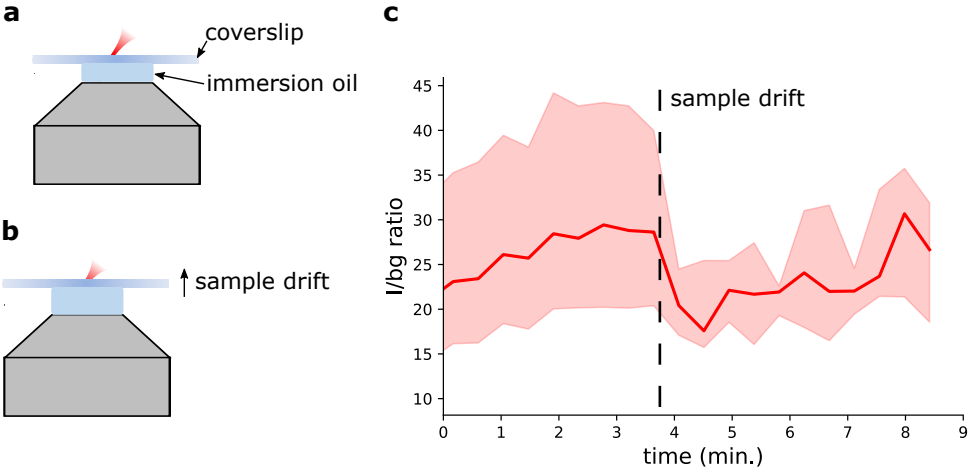
Figure 2.S11: The stability test of SOLEIL microscopy. (a) imaging the region closed to the coverslip. (b) shift the stage away from the objective lens. (c) I/bg ratio curve versus the experiment time.

2.S10. FOV AFFECTS THE OPTICAL SECTIONING IN HILO MICROSCOPY

To investigate how the FOV of HILO microscopy affects the optical sectioning, we performed SMLM imaging with a large and a small FOV using HILO microscopy with a dSTORM Caco2-BBE sample. The FOV of for HILO was controlled by the iris in the excitation path of the system. The beam width (R_1) of the small FOV HILO measurement was 43 μm, with a HILO angle of 74.5° degrees (the same as the HILO microscopy we used for benchmarking with SOLEIL and widefield (Fig. 2.6,2.7)). The beam width of the large FOV HILO measurement was approximately twice as large, limited by the laser beam width itself. Then, we estimated that the thickness of optical sectioning of the large FOV HILO measurement was two times smaller than for the small FOV HILO measurement. We observed that the I/bg ratio of small FOV HILO was 160% higher than for the small FOV HILO measurement, and resulted in a 20% improvement on the estimated CRLB Fig. 2.S12 (c,f).

2.S11. THE IMPACT OF THE INTENSITY AND BACKGROUND RATIO ON THE FALSE DETECTION RATE AND THE TRUE DETECTION RATE

The final localization microscopy reconstruction relies on the spot detection algorithm. We investigated the impact of the I/bg ratio on the spot detection efficiency. We quantified the true detection using the true positive (correctly detected) detection probability ($P_{detected}$) and the false detection probability (P_f):

$$P_{detected} = \frac{n_{detected}}{n_{GT}},$$
$$P_f = \frac{n_{non}}{n_{GT}}, \quad (2.S14)$$

where $n_{detected}$ is the number of correctly detected emitters, n_{non} is the number of incorrectly detected emitters, and n_{GT} is the total number of (ground truth) emitters. We used Photonpy [8] (https://pypi.org/project/photonpy/) to generate Gaussian PSFs with different intensities and I/bg ratios and added Poisson noise to simulate real detection situations on camera. We used SMAP platform for spot detection with a Difference of Gaussian (DoG) filter (σ = 1.2 pixel). DoG is spot detection algorithm that works by subtracting one Gaussian-blurred version of an image from a less blurred version of the same image. Based on this in-silico experiment, we observed that the I/bg ratio was an important parameter for the true detection probability. An increased I/bg ratio resulted in an increased detection probability. We also found that a higher spot detection threshold factor (dynamic factor) decreased the detection probability of low I/bg ratio spots. We can address this issue by using a lower dynamic factor but with the risk of increasing the false detection probability. This simulation delivers a hint that low I/bg ratio can result in low detected localizations, but this effect cannot be addressed by reducing the dynamic factor as it could lead to a high false detection probability.
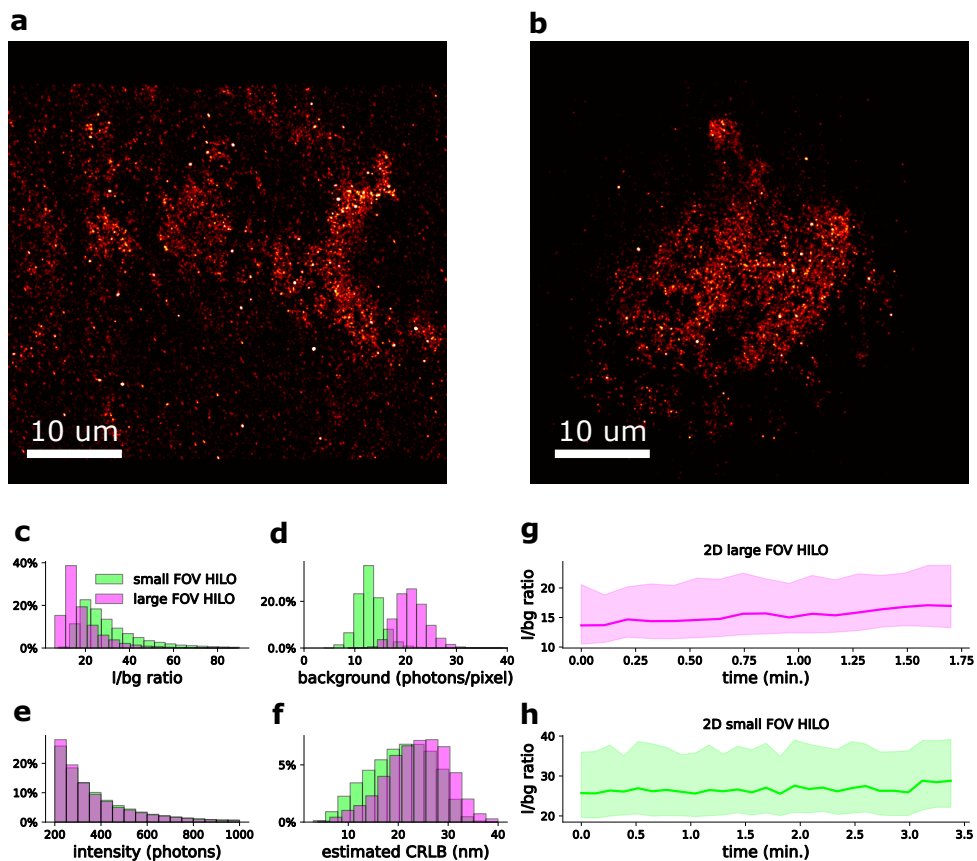
Figure 2.S12: The benchmark between large FOV HILO and small FOV HILO (a) 2D super-resolution image of Caco2-BBE sample with large FOV HILO. The diameter of FOV is 50 μm. (b) 2D super-resolution image of Caco2-BBE sample with small FOV HILO. The diameter of FOV is 30 μm. (c-f) Benchmark of intensity to background ratio, background, intensity, and estimated CRLB between widefield and SOLEIL. (g,h) I/bg ratios of large and small FOV HILO over experiment time. The opaque colored region represents the first quartile to the third quartile.

2
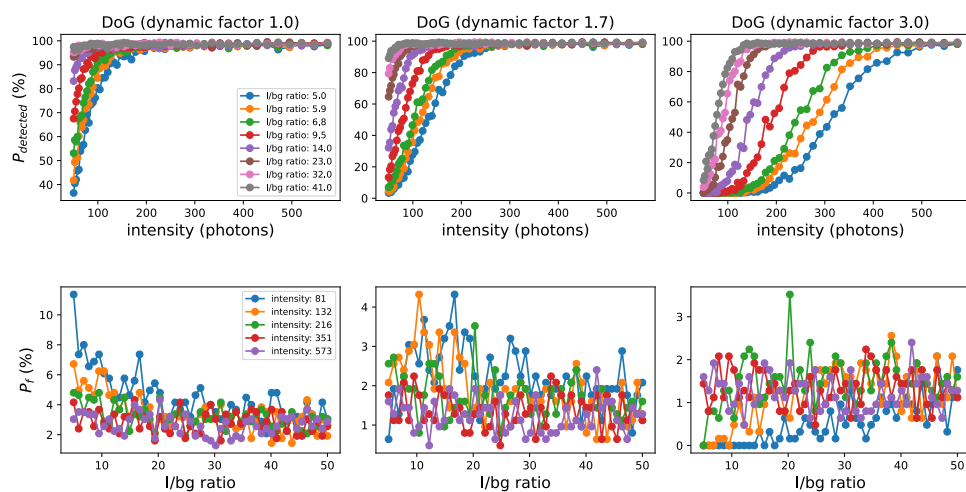
Figure 2.S13: Spot detection test on simulated images with different I/bg ratio (5.0-41.0) and DoF dynamic factor (1.0, 1.7 and 3.0). In the figures, we show the impacts of dynamic factor and I/gb ratio on detection probability (P_{detected}) and false detection probability (P_{f}). In this simulation, I simulate the single-molecule image with different I/bg ratio and perform localization with different DoF dynamic factor. As it is done on a simulated dataset, we know the ground truth of image (number and position of simulated single-molecule). We compare the localization result and the ground truth information and then we can calculate the P_{detected} and P_{f}.

BIBLIOGRAPHY

1. Vogel, M. Principles of Lasers, 5th edn., by O. Svelto. *Contemporary Physics* **53,** 173–173. https://doi.org/10.1080/00107514.2011.647714 (2012).

2. Gustavsson, A.-K., Petrov, P. N. & Moerner, W. E. Light sheet approaches for improved precision in 3D localization-based super-resolution imaging in mammalian cells. *Opt. Express* **26,** 13122–13147. http : / / www . opticsexpress . org / abstract.cfm?URI=oe-26-10-13122 (May 2018).

3. Gustavsson, A., Petrov, P. & Lee, M. e. a. 3D single-molecule super-resolution microscopy with a tilted light sheet. *Nat Commun* **9.** https://www.nature.com/articles/s41467-017-02563-4 (Jan. 2018).

4. Tokunaga, M., Imamoto, N. & Sakata-Sogawa, K. Highly inclined thin illumination enables clear single-molecule imaging in cells. *"Nat. Methods"* **5,** 159–161. (2021) (Jan. 2008).

5. Antonello, J., Wang, J., He, C., Phillips, M. & Booth, M. Interferometric calibration of a deformable mirror. *Zenodo.* https : / / zenodo . org / record / 3714951 # .YUtw7PkzZPY (Mar. 2020).

6. Booth, M., Wilson, T., Sun, H.-B., Ota, T. & Kawata, S. Methods for the characterization of deformable membrane mirrors. *Appl. Opt.* **44,** 5131–5139. http://www.osapublishing.org/ao/abstract.cfm?URI=ao-44-24-5131 (Aug. 2005).

7. Ries, J. SMAP: a modular super-resolution microscopy analysis platform for SMLM data. *Nature Methods* **17,** 870–872 (Aug. 2020).

8. Cnossen, J., Cui, T. J., Joo, C. & Smith, C. Drift correction in localization microscopy using entropy minimization. *Opt. Express* **29,** 27961–27974. http://www.opticsexpress.org/abstract.cfm?URI=oe-29-18-27961 (Aug. 2021).

3

ADAPTIVE OPTICS SINGLE OBJECTIVE INCLINED LIGHT SHEET LOCALIZATION MICROSCOPY

Single-molecule localization microscopy (SMLM) enables the high-resolution visualization of organelle structures and the precise localization of individual proteins. However, the expected resolution is not achieved in tissue as the imaging conditions deteriorate. Sample-induced aberrations distort the point spread function (PSF), and high background fluorescence decreases the localization precision. Here, we synergistically combine sensorless adaptive optics (AO), in-situ 3D-PSF calibration, and a single-objective lens inclined light sheet microscope (SOLEIL), termed (AO-SOLEIL), to mitigate deep tissue-induced deteriorations. We apply AO-SOLEIL on several dSTORM samples including brains of adult Drosophila. We observed a 2x improvement in the estimated axial localization precision with respect to widefield without aberration correction while we used synergistic solution. AO-SOLEIL enhances the overall imaging resolution and further facilitates the visualization of sub-cellular structures in tissue.

3.1. INTRODUCTION

Single-molecule localization microscopy (SMLM) routinely surpasses the diffraction limit in thin samples [1–5]. This is achieved by estimating the position of the isolated fluorescent molecules with higher precision than the diffraction limit [6]. For example, SMLM revealed the periodic structure of actin filaments in axons [7], and the distribution of βII spectrin in dendrites [8] in cultured neurons. While these approaches uncover substantial cell-intrinsic details, the effects of extracellular components, such as the extracellular matrix (ECM), cannot be studied in-vitro [9]. The absence of the ECM can affect cellular morphology and gene/protein expression [10], revealing the limitations of imaging cultured cells. However, the application of SMLM inside ex-vivo tissue is also limited due to sample-induced aberrations and high fluorescent background. The refractive index mismatch between the immersion media and tissue induces (high-order) spherical aberrations [11]. This is particularly problematic for SMLM due to the use of a high NA oil immersion objective lens to optimize the emission fluorescence efficiency. Sample-induced aberrations distort the point spread function (PSF), which can result in artifact-containing reconstructions. Furthermore, imaging in tissue often increases background fluorescence, which results in a decrease in the localization precision [6], and thus a decrease in the theoretical maximum spot detection efficiency [12]. A decrease in the localization precision and the localization density ultimately results in a lower reconstruction resolution [13]. Thus, increased background fluorescence leads to a lower reconstruction resolution.

To decrease the background fluorescence, several optical sectioning methods were established, including highly inclined and laminated optical sheet (HILO) microscopy [14], and variable-angle epi-fluorescence (VAEM) microscopy [15] that adopt an inclined widefield illumination profile to achieve optical sectioning at a sub-10μm level. However, the size of the field of view (FOV) is around tens of μm in HILO microscopy, which limits the application of HILO microscopy. Alternatively, selective plane illumination microscopy (SPIM) is widely used to achieve optical sectioning. SPIM relies on two orthogonal objectives, where one illuminates the sample while the other one collects the fluorescence [16, 17]. Tilted light-sheet microscopy (TILT3D) successfully utilizes a high detection NA objective by illuminating the sample with a tilted light sheet [18] in combination with PSF engineering. However, the sample mounting is challenging with dual objective lens configurations because of the need for customized sample holders. Oblique plane microscopy (OPM) alleviates this drawback by the use of the same objective for illumination and detection. Optical sectioning is achieved by illuminating the sample with an inclined light sheet. However, OPM requires multiple objective lenses downstream in the emission path to rotate the focal plane matching the inclined light-sheet illumination [19–24]. Single objective lens inclined light sheet (SOLEIL) microscopy is based on an oblique light-sheet with optimal optical sectioning [25]. The focal plane is not re-positioned by additional objectives; a deformable mirror (DM) is used for PSF engineering instead. SOLEIL is therefore also compatible with 3D SMLM.

To avoid artifacts in SMLM reconstructions an accurate point spread function model (PSF) is needed [26–28]. To mitigate the effects from sample-induced aberrations both numerical [29] and pre-calibration [30–32] approaches have been used for modeling depth-dependent PSFs. Both approaches neglect sample-induced aberrations originat-

ing from biological variability. To accommodate for this higher order sample-induced aberrations, the PSF should be retrieved from in-situ data. The state-of-the-art for in-situ PSF calibration is In situ PSF retrieval (INSPR) [33].

Sample-induced aberrations deteriorate the localization precision [34]. Therefore, in 3D SMLM, in-situ PSF calibration should be combined with active aberration correction. To accomplish sample-induced aberration correction, two distinct approaches have been adopted: the first is based on a wave-front sensor to measure sample-induced aberrations and a DM to compensate for the measured aberration [35]; the second on a sensorless approach [34, 36–38], where the aberrations are minimized by maximizing a metric for the image quality. Both algorithm and metric function should be tailored to an application to avoid non-convergent aberration corrections [38] due to the non-convex dependency of the aberrations [39, 40].

To alleviate the difficulties of 3D SMLM in tissue we propose AO-SOLEIL, which combines adaptive optics, in-situ PSF calibration, and three-dimensional SOLEIL microscopy (Fig. 3.1). We experimentally show the need for AO-SOLEIL as sample-induced aberrations deteriorate the axial localization precision and thereby prevent three-dimensional localization microscopy. To correct for sample-induced aberrations and enable 3D SMLM in tissue, we implemented sensorless adaptive optics combined with in-situ PSF calibration. We demonstrate the feasibility of AO-SOLEIL with several samples, including mitochondria in Caco2-BBE cells, and single neurons in the adult *Drosophila* brain. The results show that AO-SOLEIL facilitates the visualization of subcellular structures in tissue.

3.2. AO-SOLEIL

3.2.1. PRINCIPLE OF AO-SOLEIL

We proposed a synergistical approach (AO-SOLEIL) to optimize for three-dimensional SMLM in tissue. The AO-SOLEIL consists of two modules, SOLEIL illumination and sensorless AO (Fig.3.1 (a)). AO-SOLEIL adopts single objective lightsheet illumination (SOLEIL) for background rejection [25]. Here we synchronized the camera readout pixel and the SOLEIL illumination to expose the whole FOV on a same image frame (Fig.3.1 (b)). The ability of background rejection is demonstrated by imaging spheroid Caco2-BBE sample, which is a 10 μm thick cell sample (Fig.3.1 (c,d)). From the raw images, we observed that SOLEIL delivers a higher signal to background ratio (Fig.3.1 (c)). Furthermore, the reconstruction image from SOLEIL microscopy shows more details than the reconstruction image from widefield microscopy (Fig.3.1 (c)). We observed that the background rejection delivers a higher detection efficiency and an improved CRLB (Fig.3.1 (d)). To restore the 3D PSF and improve the CRLB, the 7 Zernike modes ($Z_2^{\pm2}$, $Z_3^{\pm1}$, $Z_3^{\pm3}$, Z_4^0) are corrected using the DM (Fig.3.1 (e-g)). To enable unbiased estimation the 3D PSF model is estimated directly from the raw SMLM data (Fig.3.1 (h)). For this in-situ PSF calibration, we estimated up to the fifth radial order of Zernike modes using the INSPR algorithm [33].

To correct for sample induced-aberrations it is important that the sensorless AO algorithm is not susceptible to the high fluorescent background that we observe in tissue. We performed several in-silico experiments to investigate the best possible design for

3
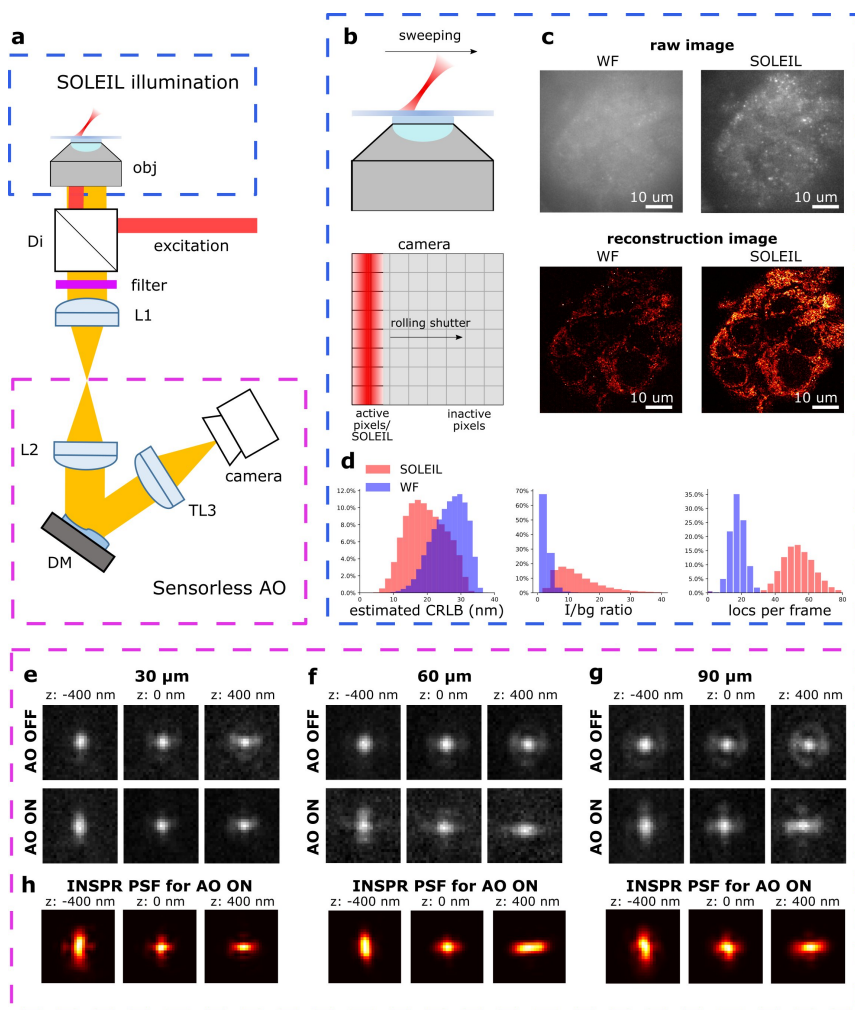
Figure 3.1: (a) Optical setup of AO-SOLEIL microscopy. obj: objective lens, Di: dichroic mirror, filter: emission filter, L1 to L3: achromatic doublet lens, DM: deformable mirror, camera: sCMOS camera. For the details of the system, see supplementary section 3.S1. (b) Working principle of SOLEIL and camera readout. The camera readout is synchronized with the SOLEIL illumination area (red). The SOLEIL illumination is controlled by a galvo mirror. (c) Demonstration of SOLEIL background reduction (dSTORM) on spheroid Caco2-BBE cells (mitochondria). upper row: raw camera image by widefield and SOLEIL microscopy (equal contrast). lower row: SMLM reconstructions. (d) Comparison between WF and SOLEIL of estimated lateral CRLB, I/bg ratio, and number of localization per frame (loc per frame). (e-g) The astigmatism PSF before (AO OFF) and after (AO ON) AO correction at different imaging depths ($30\mu m$, $60\mu m$, $90\mu m$). The PSFs were acquired by imaging 23 nm fluorescence beads (Thermo Fisher Scientific, Tetraspeck) embedded in 1% agarose gel. The emission wavelength is 680 nm. (h) The estimated in-situ PSF models using the INSPR algorithm.

an in-tissue 3D SMLM sensorless AO approach (Fig. 3.9). We analyzed the convergence versus the number of measurement steps (Fig. 3.9 (a)). We observe that with a high background (I/bg is 5), 11 measurement steps are needed for correcting one Zernike mode in contrast with what was previously predicted [39, 41, 42]. Furthermore, we investigated the impact of sparsity in SMLM data. We observed that more than 30 single-molecules per frame are needed to deliver a robust aberration correction (Fig. 3.9 (b)). In practice, the concentration of MEA in the dSTORM buffer is adjusted to achieve this. From the benchmark against other sensorless AO metric functions we found that our novel metric function is less susceptible to a high fluorescent background (Fig. 3.9 (c,d)).

To analyze the synergy between aberration correction and in-situ PSF calibration, we performed in-silico experiments (Fig. 3.4, 3.5, 3.6). First, the accuracy of the in-situ PSF was evaluated. We found the in-situ calibrated PSF model with AO correction (AO ON) has no statistical difference with ground truth PSF up to the intensity of 3000 photons while without AO (AO OFF) the in-situ PSF model was statistically different at the intensity of 1500 photons (Fig. 3.4 (d,e)). We also evaluated the theoretical CRLB with and without AO (Fig. 3.4 (f)). Here, we observed a 200% improvement of the axial CRLB. The combination of aberration correction and in-situ PSF calibration significantly reduces the axial localization bias (Fig. 3.4 (g)). The effects of axial CRLB and axial localization bias are visualized on a simulated dataset of a 3D ring structure (Fig. 3.5). We observed in this experiment that the 3D ring is visible with AO, but not visible without AO.

These findings are in-line with the experiments that we have done on beads embedded in 1% agarose. We observed that we could restore the astigmatism PSF up to 90 μm depth (Fig.3.1 (h), Fig. 3.3). The axial CRLB was significantly improved.

3.2.2. SENSORLESS AO ALGORITHM

In this manuscript, we use a model-based wavefront sensorless approach for aberration correction. Namely, the aberration in the pupil is represented as a linear combination of the first 7 Zernike modes ($Z_2^{\pm 2}$, $Z_3^{\pm 1}$, $Z_3^{\pm 3}$, Z_4^0), and the indirect wavefront sensing is based on the widely accepted (*e.g.* [39, 43]) Fourier annulus image quality metric.

The metric, defined by two radii r_1 and r_2, is given by relative total energy of the image spatial frequencies **m** in the annulus with inner and outer radii given by r_1 and r_2. In practice, for a digital image $I[x, y]$ and its 2D discrete Fourier Transform $\widehat{I}[m, n]$,

$$\widehat{I}[m, n] = \mathscr{F}_2 I[x, y], \tag{3.1}$$

the metric $M(\widehat{I}[m, n]) = M(\widehat{I}[m, n]; r_1, r_2)$ is defined as

$$M(\widehat{I}[m, n]) = \frac{\sum_{m,n} |\widehat{I}[m, n]| \cdot w[m, n]}{\sum_{m,n} |\widehat{I}[m, n]| \cdot u[m, n]}, \tag{3.2}$$

with binary masks w, u defined as

$$w[m, n] = \begin{cases} 1, & r_1 < |\mathbf{m}| < r_2 \\ 0, & \text{else} \end{cases},$$

$$u[m, n] = \begin{cases} 1, & |\mathbf{m}| < R \\ 0, & \text{else} \end{cases}, \tag{3.3}$$

where $|\mathbf{m}| = \sqrt{m^2 + n^2}$, and R is the radius corresponding to the diffraction-limited maximum spatial frequency. (For a camera with pixel size Δx and resolution $L \times L$, $R = \frac{NA}{\lambda} L \Delta x$.)

The idea is to discard the low spatial frequencies (background variations) and the high spatial frequencies (usually attributed to noise). Radii r_1, r_2 are often expressed in multiples of R [34, 38].

In our work, to achieve sensorless AO correction of spherical aberration, we have used the previous published metric function with $r_1 = 0, r_2 = R/2$ [34].

As the image I depends on the aberration, represented by its Zernike coefficients vector $\vec{\alpha}$, the metric $M(\widehat{I}[m, n])$ is also a function of α, $M = M(\vec{\alpha})$, As the higher values of the metric correspond to a sharper image [43], the aberration correction is equivalent to the optimisation problem

$$\hat{\vec{\alpha}} = \arg\max_{\vec{\alpha}} M(\vec{\alpha}). \tag{3.4}$$

The optimisation is performed independently for each of the Zernike modes used to control the DM. To this end, for each of the modes we acquired 11 images with the mode amplitude values varying uniformly in the range $[-\lambda/2, \lambda/2]$ and computing the image metric for each of the images. Previously it has been shown that a minimum of $2N + 1$ of measurements are needed for correcting N Zernike modes with sensorless AO correction [39, 43]. In our experiments a minimum of 11 measurement steps are needed to mitigate a high fluorescence background and sparse images (Fig. 3.9).

The correction point for each mode was determined by fitting the metric value points with a Gaussian function $G(M)$ and taking its central point. Namely, with $G(M)$ defined as

$$G(M) = ae^{\frac{-(M-c)^2}{\sigma^2}} + bg, \tag{3.5}$$

where M is the metric value, a is the amplitude of Gaussian function, σ is the width of Gaussian function, c is the center of Gaussian function, which is the value for aberration correction, and bg is the background of the metric value curve. The optimal value $\hat{\alpha}_i$ for the current mode is c.

We used bounded non-linear least squares to fit the amplitude term a, center c, width σ, and background bg. Based on the design of the metric function, we know the best aberration correction happens at the peak of the metric value curve, so the amplitude term must be positive. The boundary condition of amplitude term is $0 < a < \infty$. The fitting procedure is done by using the *curve fit* function in the Scipy library (version 3.8) [44]. We corrected the spherical aberration first and then we corrected the other first order aberrations. In our samples we mainly observed spherical aberration because of refractive index mismatch. Therefore, first two iterations were performed to correct for the spherical aberration (Z_4^0). Subsequently, to correct for the other aberrations ($Z_2^{\pm2}$, $Z_3^{\pm1}$, $Z_3^{\pm3}$) one iteration were done for each mode. In total, the aberration correction uses 88 frames, which is a small fraction in typical dSTORM imaging (10000 ~ 30000 frames).

3.2.3. DEFOCUS COMPENSATION FOR SPHERICAL ABERRATION CORRECTION

Zernike polynomials, although orthogonal in the phase of the pupil plane, do not guarantee the absence of cross-talk in the optimisation procedure described in the previous subsection. That means that by maximising $M(\vec{\alpha})$ moving along one of the modes, we might move out of the maximum value for the other modes. Different techniques are known to deal with this effect, finding their principles in Gram-Schmidt orthogonalization [39, 40]. In this work, we propose the following simple procedure to establish and to compensate for the major cross-talk effect in our setup, that is between the defocus and spherical aberration terms (Fig. 3.2).

To compensate for the axial defocus that is caused by a DM when correcting for spherical aberrations a calibration is made [34]. To create this calibration the defocus offset was measured by imaging fluorescent beads (23 nm; embedded in 1% agarose) on a 2D surface, which means the fluorescence beads only appear at a certain axial plane. This was done as follows: a certain amount of spherical aberration is introduced on the DM. This shifted the focal plane and we then applied a defocus aberration to re-focus the bead images. To determine the amount of defocus for the re-focusing we used the same metric function as for sensorless AO. This procedure was repeated for a different amounts of spherical aberration. Finally, a linear function was fitted by minimizing the mean square error (Fig.3.2 (b)), which was used as the calibration:

$$\Delta Z_2^0 = \beta \cdot Z_4^0, \tag{3.6}$$

where Z_2^0, Z_4^0 are defocus and spherical Zernike mode respectively, ΔZ_2^0 is the defocus aberration, and β is the *coupling* coefficient, which in our system is 0.00371 $^{\mu m}/_{nm}$.

3.2.4. IMPACT OF AO CORRECTION ON INSPR PSF MODEL AND AXIAL LOCALIZATION PRECISION

To validate the synergy between our sensorless AO algorithm and the INSPR algorithm for improving the axial CRLB, we imaged homogenously embedded beads (23 nm) in 1% agarose (>100 μm). Firstly, we performed AO correction to minimize the sample-induced aberration. We call this procedure AO ON and without this procedure AO OFF. Then, we introduced an astigmatism aberration with the DM to generate an astigmatism-based PSF for 3D localization. To estimate the in-situ PSF, INSPR algorithm needs multiple single-molecules at different axial positions to build a model (Fig. 3.3 (a-c)) [33]. To estimate the in-situ PSF model with the INSPR algorithm, we acquired data by moving the piezo stage in discrete steps (100 nm) along an axial and lateral dimension (2 μm). In (Fig. 3.3 (d-f)), we show the theoretical axial CRLB and in Fig. 3.3 (g-j) we show the axial CRLB estimated from the localizations. We found that this synergetic combination of AO correction and INSPR can improve the axial CRLB. However, this effect is not observed in lateral CRLB (Fig. 3.S2).

3.2.5. VALIDATION OF SENSORLESS AO IN COMBINATION WITH IN-SITU PSF CALIBRATION

We used active aberration correction to correct the first 7 Zernike modes. Subsequently, in-situ PSF calibration (INSPR) was used to calibrate the 3D PSF model (INSPR PSF).

3

a

b

c
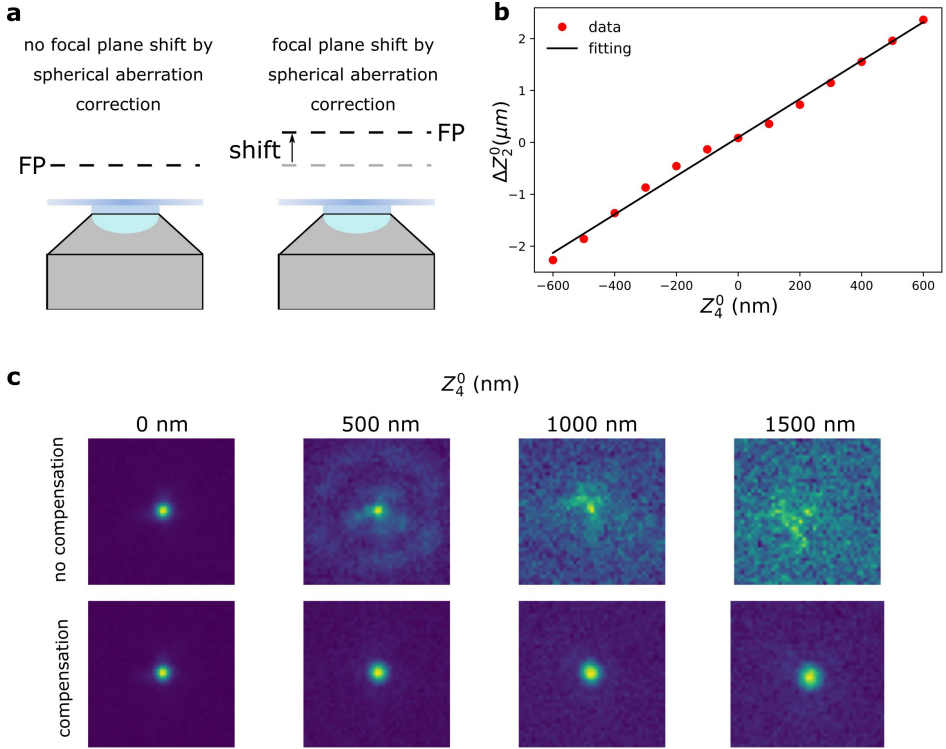
Figure 3.2: Defocus calibration for spherical aberration compensation. (a) Focal plane shift induced by coupling between defocus and spherical aberration. When correcting for the spherical aberration, the coupling between the spherical and the defocus aberration shifts the focal plane (FP). (b) Calibration of the compensation for the defocus introduced by spherical aberration. (c) Raw data with different amount of spherical aberration (Z_4^0: 0, 500, 1000, 1500 nm) without (upper row) and with (lower row) defocus compensation. The calibration was done with spherical aberration in the range of -600 ~ 600 nm.
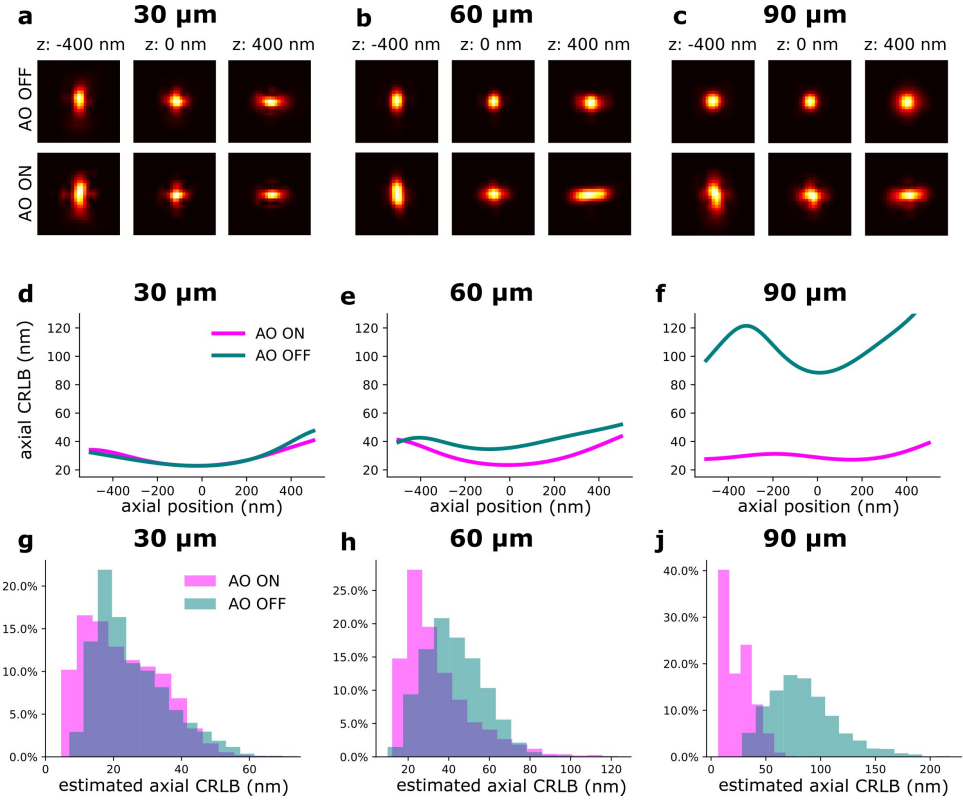
Figure 3.3: The INSPR PSF before and after sensorless AO correction at different imaging depths. The PSF model was calibrated by imaging a fluorescence bead sample. (a-c) Estimated in-situ PSF models using the IN-SPR algorithm with and without AO correction at different depths (30 μm, 60 μm, 90 μm). (d-f) The theoretical axial CRLB based on the estimated PSF model from (a-c) with 3000 photons of intensity and 50 photons/pixel of background. (g-j) The distribution of estimated axial CRLB at different imaging depths.

In this section, we investigated this approach in-silico. We used the SDS simulator (details of SDS simulator is in supplementary section 3.S2) mentioned above to simulate blinking images in the presence of aberrations. To mimic the high aberration situation, we simulated PSFs by randomly assigning 150 mλ Zernike aberrations uniformly distributed over the first 17 Zernike modes ($Z_2^{\pm2}, Z_3^{\pm3,\pm1}, Z_4^{\pm4,\pm2,0}, , Z_5^{\pm5,\pm3,\pm1}$) excluding the piston, tip, tilt, and defocus aberrations. Spherical aberration (220 mλ) was added to mimic the refractive index mismatch between oil immersion and tissue. We term this set of Zernike aberrations as the initial i.e. AO OFF aberration. Then, combining with the SDS, we used the proposed sensorless AO algorithm to correct the 7 Zernike modes ($Z_2^{\pm2}$, $Z_3^{\pm1}, Z_3^{\pm3}, Z_4^0$). In this step, we input the Zernike aberrations into the SDS and generated images with aberrated blinking single-molecules. Based on this, we can investigate the performance of the proposed sensorless AO algorithm in-silico.

To enable the 3D localization of single-molecules an astigmatic PSF was chosen. This PSF was created by adding 100 mλ astigmatism aberration (Z_2^2). To estimate the in-situ PSF, we simulated 1000 frames of blinking images (intensity: 2000 photons, background: 30 photons/pixel) with the initial aberration (AO OFF) and the final aberration after correction (AO ON) Fig.3.4 (a,b). The ground truth PSFs were computed based on the true initial (AO OFF) and final aberration (AO ON) Fig.3.4 (c).

The χ^2 value was used to compare and evaluate the accuracy of the PSF models [45].

$$\chi^2 = \sum_{i=1}^{K} \frac{\left(n_i - u_i(\hat{\theta})\right)^2}{u_i} \tag{3.7}$$

$$u_i(\hat{\theta}) = \hat{\theta}_I \cdot PSF_i\left(\hat{\theta}_x, \hat{\theta}_y, \hat{\theta}_z\right) + \hat{\theta}_{bg} \tag{3.8}$$

, where K is the number of pixels of the region of interest, n_i is the photon count of the data at the ith pixel, u_i is the photon count in ith pixel, $PSF_i\left(\hat{\theta}_x, \theta_y, \hat{\theta}_z\right)$ is the 3D PSF model in ith pixel, $\hat{\theta}$ is the vector with the estimates containing the estimands $\theta_x, \theta_y, \theta_z, \theta_I, \theta_{bg}$. These correspond to the x,y,z position, emitter intensity, and the emitter background, respectively. To calculate $u_i\left(\hat{\theta}\right)$, the $\hat{\theta}$ is obtained using maximum likelihood estimation [6].

For Poissonian distributed measurement the expected χ^2 value ($E\left[\chi^2\right]$) and the variance of χ^2 value ($var\left[\chi^2\right]$) can be expressed as following:

$$E\left[\chi^2\right] = K \tag{3.9}$$

$$var\left[\chi^2\right] = 2K + \sum_{i=1}^{K} \frac{1}{u_i} \tag{3.10}$$

The above equation delivers a statistical way to determine whether the PSF model is accurate and when it's not. The PSF is statistically different (not accurate) from the data when the χ^2 value is larger than the expected χ^2 value plus its standard deviation. The χ^2 was computed based on Eq. 3.8. In Fig.3.4 (d,e), the expected χ^2 value of the estimated PSF models versus intensity are shown. The curve of estimated PSF models are computed by keeping the estimated PSF model constant and generating 51 independent noise realisations (Eq. 3.8). We observed that the χ^2 value increases with increasing

intensity Fig, 3.4 (d,e). We observed that the INSPR PSF estimated model without AO was statistically different at 1500 photons. The INSPR PSF estimated model with AO was statistically different until 3000 photons.

In Fig.3.4 (f), we calculated the theoretical axial CRLB over different axial positions and we observed the improvement of theoretical axial CRLB with AO correction over without AO correction. Furthermore, the impact of a model mismatch between the estimated and the ground truth PSF was analyzed by calculating the estimation bias in the z direction Fig.3.4 (g). To do this we generated the raw SMLM images with 1000 photons and background 30 photons/pixel. The reason for choosing 1000 photons intensity is to make sure the INSPR model is not statistically different from ground truth PSF model and 30 photons/pixel background is to match with the I/bg ratio of 33.33 in χ^2 test (Fig. 3.4). The INSPR PSF model obtained from INSPR was used for the localization. Fig.3.4 (g) shows the estimated axial position versus the ground truth axial position. We observed that the estimated axial position is strongly biased without AO. With AO correction the bias is significantly reduced. The ground z position is within the standard deviation of estimated axial position up to ±400 nm. To visualize the impact of the improvement of the CRLB and reduction of the bias raw SMLM data of a 3D ring was simulated. In the 3D ring test, we simulated the 3D PSF blinking spots along the 3D ring structure with the ground truth PSF models and used INSPR PSF model for localization. The reconstructions are shown in Fig.3.5. We found that in the AO OFF situation the reconstruction has completely failed. This result aligns with the observation in Fig.3.4 (g), which is the strong axial position bias occurs in AO OFF model. This result again justifies our motivation to combine AO correction and INSPR mehtod.

To analyze the use of in-situ PSF calibration and not use the pre-calibrated cubic spline (cspline) PSF [27, 28], we performed an in-silico experiment (Fig. 3.6). In this experiment, we have the PSFs after AO correction in Fig.3.4 (b) and we also have the PSF model calibrated by INSPR. In addition, to mimic a pre-calibrated PSF model from a thin sample with fluorescence beads we simulated astigmatism PSF only with 100 mλ astigmatism aberration (Z_2^2) and without other aberrations and did a cspline calibration with Super-resolution Microscopy Analysis Platform (SMAP, EMBL Heidelberg) [46] (Fig. 3.6 (a)). In Fig. 3.6 (b), we show the axial localization bias using INSPR PSF model and cspline PSF model. We observed a strong axial bias from the cspline PSF model. In Fig. 3.6 (c), we show the χ^2 value of cspline and INSPR model, which suggests that a pre-calibrated cspline method is not accurate in tissue SMLM imaging.

3.3. METHODS

3.3.1. INITIAL ABERRATION CORRECTION OF THE SYSTEM

To compensate for the aberrations introduced by the DM and the static aberrations of the microscope we acquired PSFs by imaging single 23 nm beads embedded in 1% agarose. Here, because our input image is small and contains only a single PSF, we don't need to use the extended image quality metric from the previous section, but can just minimize the mean width of the PSF by adopting a second moment metric function:

$$M_{sec} = \sum_{i=1}^{N} \sum_{j=1}^{N} I(i,j) \cdot \left[(i - c_x)^2 + (j - c_y)^2 \right] / \sum_{i=1}^{N} \sum_{j=1}^{N} I(i,j), \qquad (3.11)$$
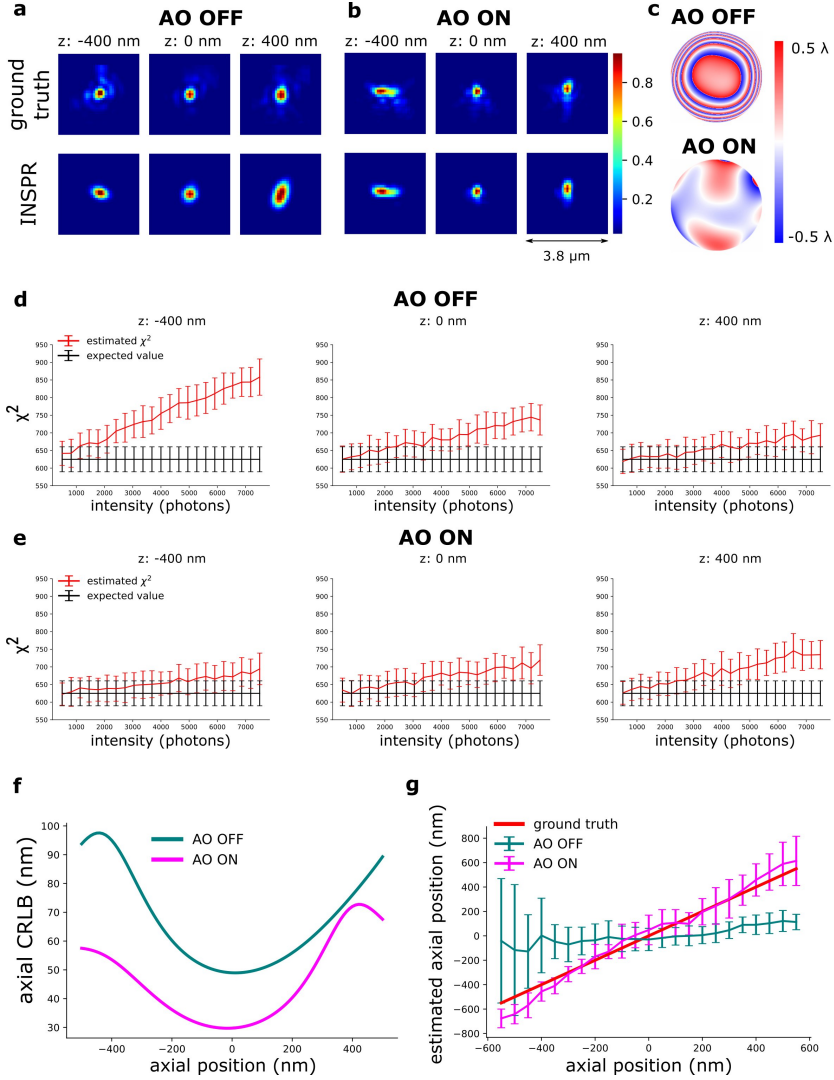
Figure 3.4: Validation of the principle of AO-SOLEIL. (a) PSFs without AO correction.(b) PSFs with AO correction. (c) Pupil phase of ground truth PSF with addition 100 mλ astigmatism for 3D SMLM. (d) χ^2 value of AO OFF PSF at different intensity and depth (-400 nm, 0nm, 400 nm). In this test, we fixed the I/bg ratio to 33. (e) χ^2 value of AO ON PSF at different intensity and depth (-400 nm, 0nm, 400 nm). In this test, we fixed the I/bg ratio to 33. (f) Curve of axial CRLB versus axial position (intensity: 1000 photons, background: 30 photons/pixel). (g) Curve of axial position versus estimated axial position. For each data point, we repeated the localization 51 times. The errorbar is the standard deviation of estimated axial position.
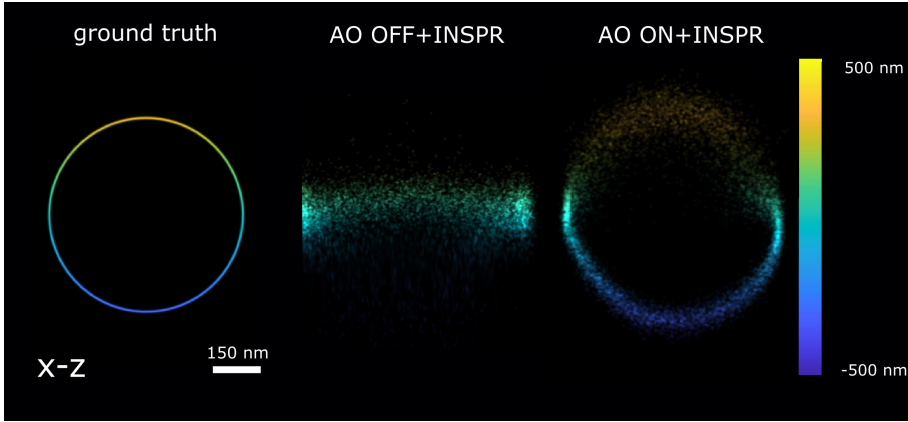
Figure 3.5: Reconstruction x-z cross-section of the 3D ring localized by AO OFF and AO ON INSPR PSF model. ground truth: the x-z view of 3D ring. AO OFF+INSPR: the reconstruction image without AO correction, but in-situ PSF estimated using the INSPR algorithm. AO ON+INSPR: the reconstruction image with AO and the in-situ PSF estimated using the INSPR algorithm.
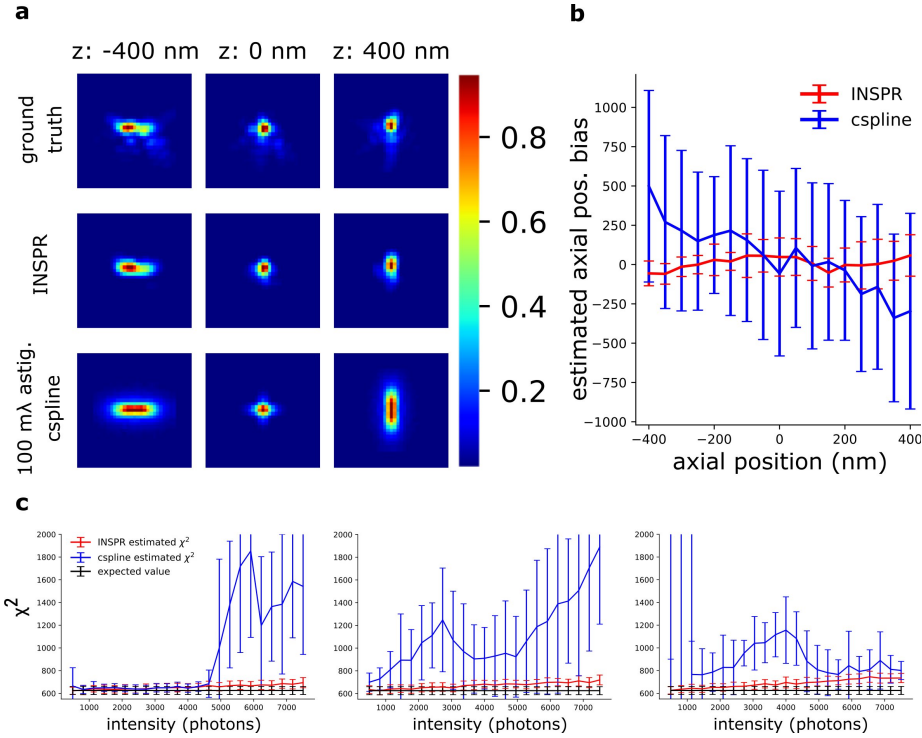
Figure 3.6: Investigation of the synergy between INSPR and AO-SOLEIL. (a) PSFs with AO correction. Ground truth: the PSF simulated using the true Zernike aberrations. INSPR: PSFs calibrated from the raw SMLM data. 100 mλ astig. cspline: cubic spline PSF model calibrated by z-stack PSFs data without sample-induced aberration. (b) the axial position bias ($z_{true} - z_{estimated}$). (c) χ^2 of PSF models estimated using INSPR and cspline calibration.

where M_{sec} is the second moment of single PSF, $I(i, j)$ is the pixel value at row i and column j of the acquired image, c_x and c_y are the center of mass of $I(i, j)$, and N is both the width and height of the camera image in pixels. In our experiment, we chose N as 21 pixels. The metric is minimized by use of the adaptive Nelder-Mead algorithm from the Scipy library (version 1.7.3) for 3000 iterations with 30 ms of exposure time for each frame. This minimization is not performed in the Zernike basis, but in that of the deformable mirror control voltages, because it leads to more robust performance when strong aberration present in the system [38]. In principle, maximum intensity or sharpness metric functions can also be adopted as metric function to minimize the system aberration [47, 48]. However, these metric functions are more susceptible to the photobleaching making they unsuited for our application.

3.3.2. DATA ACQUISITION FOR SENSORLESS AO-SOLEIL MICROSCOPY

To reduce the imaging background the sample was pre-bleached for 30 to 60 seconds. The pre-bleaching was done while moving the piezo stage (Smartact; x,y an SLC1730; z an SLC1720) through the targeted axial area. Sensorless AO was subsequently performed on this desired 3D FOV while illuminating the sample with widefield illumination (integration time 30 ms).

After AO correction, first the widefield SMLM acquisition was finished and subsequently the SOLEIL benchmark. This order may potentially decrease the quality of SOLEIL imaging including the estimated CRLB and number of localizations per frame because of photo-bleaching . However, in all imaging, we still observe the improvement of SOLEIL microscopy over widefield microscopy. The SOLEIL acquisition deviates from the previous published work [25]. In this work, the galvo mirror continuously translated the SOLEIL illumination from the top to the bottom of the FOV. To enable a virtual confocal readout [49, 50] we used a rolling shutter by activating the Andor SOLIS LightScan PLUS function. This allowed us to synchronize the rolling shutter readout of the camera to be synchronized with the light sheet illumination. To synchronize the rolling shutter and SOLEIL illumination, the camera trigger mode was set to external trigger and the camera and galvo mirror were controlled by an Arduino micro-controller.

3.3.3. CELL CULTURE

CACO2-BBE CELLS FOR ARTIFICIAL MULTILAYER SAMPLE

Caco2-BBE cells (a gift from S.C.D. van IJzendoorn, University Medical Center Groningen, the Netherlands) were maintained in DMEM supplemented with 9% FBS (fetal bovine serum), 50 μg/μl penicillin/streptomycin and 2 mM L-glutamine at 37°C and 5% CO_2. Cells were seeded on 18 mm coverslips at a density of $1 \cdot 10^5$/cm^2 and cultured for 10 to 12 days to allow for spontaneous polarization and brush border formation. The monolayer of cells was fixed with 4% paraformaldehyde (PFA) in phosphate-buffered saline (PBS) for 10 minutes, washed with PBS (3×5 minutes), permeabilized with 0.5% Triton X-100 in miliQ water for 15 minutes, washed with PBS (3×5 minutes) and blocked with 3% BSA in PBS for at least 1 hour. Cells were incubated overnight at 4°C with a primary antibody against ezrin (mouse, BD Biosciences, 610602, dilution 1:500) from now referred to as ezrin labeled cells. After washing in PBS (3×5 minutes), the cells were incubated with secondary antibody (goat, anti-Mouse IgG (H+L), Alexa Fluor 647 (Life

Technologies, dilution 1:500)) for 1 hour at room temperature (RT) and washed with PBS.

CACO2-BBE CELLS FOR SPHEROID SAMPLE
To create a more three-dimensional culture a monolayer of Caco2-BBE cells, similar as is mentioned above, was perturbed by forcibly pipetting the culturing medium over the cells. The resulting cell clumps were cultured in suspension for an additional 3 days to allow for the formation of spheroid like structures. Spheroids were fixed with 4% PFA and 4% sucrose in PBS for 15 minutes, washed with PBS (3 × 5 minutes), permeabilized with 0.5% Triton X-100 in miliQ water for 30 minutes, washed with PBS (3 × 5 minutes) and blocked with 3% BSA in PBS for at least 1 hour. Cells were incubated overnight at 4°C with a primary antibody against cytochrome C (mouse, BD Biosciences, 556432, dilution 1:500) from now on referred to as mitochondria labeled cells. After washing in PBS (3 × 5 minutes), the cells were incubated with secondary antibody (goat, anti-Mouse IgG (H+L), Alexa Fluor 647 (Life Technologies, dilution 1:500)) for 3 hours at RT and washed with PBS.

PREPARATION OF *Drosophila* BRAINS
Flies (*Drosophila melanogaster*) were kept on Nutri-Fly Bloomington Formulation with dry yeast at 20°C. Males and females were used as no gender-specific differences were observed. Genotypes used: *10xUAS-IVS-mCD8::GFP / + ; MB077c-Gal4 / +* (control) and *10xUAS-IVS-mCD8::GFP / 10xUAS-myr::4xSNAPf ; MB077c-Gal4 / +* (experiment). Adult flies were aged at 20°C for 5-7 days before performing brain dissection [51]. Brain dissections were performed as described [51]. Briefly, decapitated heads were fixed in 4% formaldehyde (47608-250ML-F, Sigma-Aldrich) in PTX (0.1% Triton X-100 (T9284, Sigma-Aldrich) in PBS) for 20 minutes, and washed 3 × 10 minutes with PTX. Brain dissections were performed in PTX, and dissected brains were fixed in 4% formaldehyde in PTX for 10 minutes, followed by 3 × 10 minute washes with PTX. Brains were incubated with SNAP-Surface Alexa Fluor 647 (Inc. S9136S, New England Biolabs) at a concentration of 0.0625 μM with rotation for 15 minutes at RT. Brains were washed 3 × 10 minutes with PTX, and subsequently PTX was completely removed and 200 μL PBS was added.

3.3.4. SAMPLE PREPARATION AND MOUNTING
PREPARATION OF THE LARGE FLUORESCENCE BEAD SAMPLE
We prepared a glass slide with four strips of double sided tape arranged on the four sides of a rectangle. After that, 1% agarose solution was prepared by adding 100 mg of agarose powder (BP160-100, Thermo Fisher Scientific, Waltham MA, U.S.A.) to 10 mL of PBS buffer followed by 20 min stirring with a magnetic stirrer at 100°C. Then, we prepared a 1:10000 diluted fluorescence bead stock (Tetraspeck, Thermo Fisher Scientific) with 1% agarose solution. We quickly mixed the diluted fluorescence bead stock with the agarose solution and added 200 μL of mixture in the middle of double sided tape. Before the agarose gel became solid, a #1.5 coverslip was mounted on the glass slide attaching the double sided tape. Then, we used nail polish to seal the coverslip. The final thickness of the sample is about 120 μm.

SPHEROID CACO2-BBE CELL DSTORM SAMPLE

Firstly, we put two strips of double sided tape on a glass slide (MS10UW, Thorlabs) as spacer (Fig. 3.7 (c)). The spheroid Cao2-BBE cell was stored in PBS in Eppendorf tube. We picked up the spheroid Caco2-BBE cell from the Eppendorf tube by pipette and put the cell on a #1.5 coverslip (CG00C2, Thorlabs). Then, 20 μl of 1% agarose (BP160-100, Thermo Fisher Scientific, Waltham MA, U.S.A.) diluted by PBS was added to stabilize the cell. Before the agarose became solid, the coverslip with the cell was mounted on a glass slide attached with the double sided tape. Then, we used nail polish to seal the edge between the coverslip and the double sided tape. After the nail polish was dry, we added the dSTORM buffer into the chamber and used two-component gel (Picodent, Wipperfürth) to seal the front and backside of the coverslip (Fig. 3.7 (f)).

ARTIFICIAL CACO2-BBE CELL DSTORM SAMPLE

A coverslip with Caco2-BBE cell adhered on the microscopy glass slides with double sided tape (Fig. 3.7 (a)). Another coverslip was attached to the cell coverslip with 65 μm thick double sided tape (details of sample mounting is in Fig. 3.S5). The thickness of double sided tape was measured by using a homemade setup (Fig. 3.S6). The left and right sides of the coverslip were sealed by using nail polish and the front and backside of the coverslip were sealed by using the two-component gel. Compared with the original sample, the artificial Caco2-BBE sample had an additional 65 μm deep buffer layer, which introduced an additional 0.38 λ spherical aberration estimated based on the equation in [11].

FLUORESCENTLY LABELED SINGLE NEURONS IN *Drosophila* BRAINS FOR DSTORM IMAGING

Drosophila brains were mounted in glass slides as previously described in [52]. The dissected brains were stored in PBS buffer at 4°C in 1.5 mL tubes until ready to be mounted. Then, we glued two #0 coverslips (CG00C2, Thorlabs) on a glass slide (MS10UW, Thorlabs) by using nail polish (Fig. 3.7 (e)). The distance between the two coverslips was around 5 mm. A pipette was used to pick up a brain from Eppendorf tube and put the brain on the glass slide between the two #0 coverslips. Then, the brain was placed in the correct orientation with the help of a 20X magnification stereo microscope (LCAch N 20X, Olympus). Then, we added 10 μl of 1% agarose diluted in PBS on the brain. Before the agarose became solid, a #1.5 coverslip was mounted on the brain and attached to the #1 coverslips. The left and right sides of the coverslip were sealed with nail polish and the front and backside were sealed by using two-component gel (Fig. 3.7 (d)).

PREPARATION OF DSTORM BUFFER

In this research, we used oxygen scavenger buffer (Glox-buffer). We prepared a glucose stock solution (300 mM glucose, 50 mM Tris, 10 mM NaCl dissolved in Milli-Q H_2O) and stored it at 4°. The final concentration of each ingredients are 1.25 mg/ml catalase (Sigma, C40-100MG), 1 mg/ml glucose-oxidase (Sigma, G2133-10KU), and 50~150 mM MEA (Sigma, 30070-10G) diluted in glucose stock. We adjusted the blinking density by adjusting the concentration of MEA.
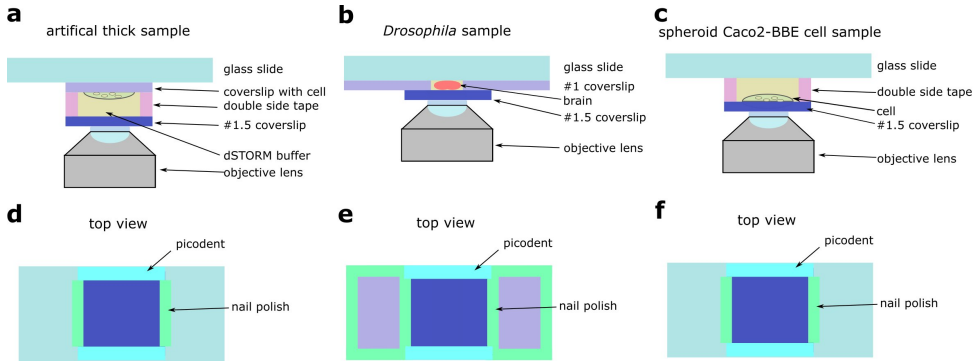
Figure 3.7: schematic of artificial thick and *Drosophila* brain. (a) Side view of artificial thick sample. (b)Side view of *Drosophila* brain. (c) Side view of spheroid Caco2-BBE cell sample. (d) Top view of artificial thick sample. (e) Top view of *Drosophila* brain. (f) Top view of spheroid Caco2-BBE cell sample.

3.3.5. SMLM DATA ANALYSIS

To perform 2D localization, drift correction, filtering, and visualization, we used Super-resolution Microscopy Analysis Platform (SMAP) [46]. We used maximum likelihood estimation (MLE) with a 2D Gaussian PSF model for the estimation. The estimands are the position, intensity, background counts, and the width of the Gaussian PSF model.

To perform 3D PSF calibration, localization, and drift correction, we used the INSPR algorithm [33] to build the PSF and to localize the single molecules. The region of interest (ROI) of the PSF was 27 pixels which correspond to 2.92 μm. To calibrate the PSF with INSPR only the first 36 Zernike basis functions were considered. The 3D reconstruction was made with SMAP.

3.4. RESULTS

3.4.1. IMPACT OF SPHERICAL ABERRATION ON THE THREE-DIMENSIONAL LOCALIZATION PRECISION

To investigate the performance of the INSPR algorithm when spherical aberration presents in the PSF model we performed a set of in-silico experiments. We simulated vectorial PSFs with varying spherical aberrations (0m$\lambda \sim$ 150mλ) (Fig. 3.8 (a)) [53]. The details of the PSF simulation is in supplementary section 3.S2. Then, we used the INSPR algorithm to calibrate the PSF model. The in-situ calibrated PSF model was used for computing the CRLB. We observed that an increased spherical aberration gradually reduces the ellipticity of astigmatism-based PSF, which reduces the ability to localize in three dimensions. This is inline with previous reported observations [54]. We observed in simulation that spherical aberration deteriorates the axial CRLB (Fig. 3.8 (b)), but not the lateral CRLB (Fig. 3.8 (c,d)). This in-silico observation aligns with our experimental observation (Fig. 3.3, Fig. 3.S2). To investigate if this observation is dependent on the algorithm that was used for PSF calibration, we repeated the same simulation using cubic splines (Fig. 3.S3) [27, 28]. We observed a deteriorated axial CRLB when spherical aberration presents in the PSF.
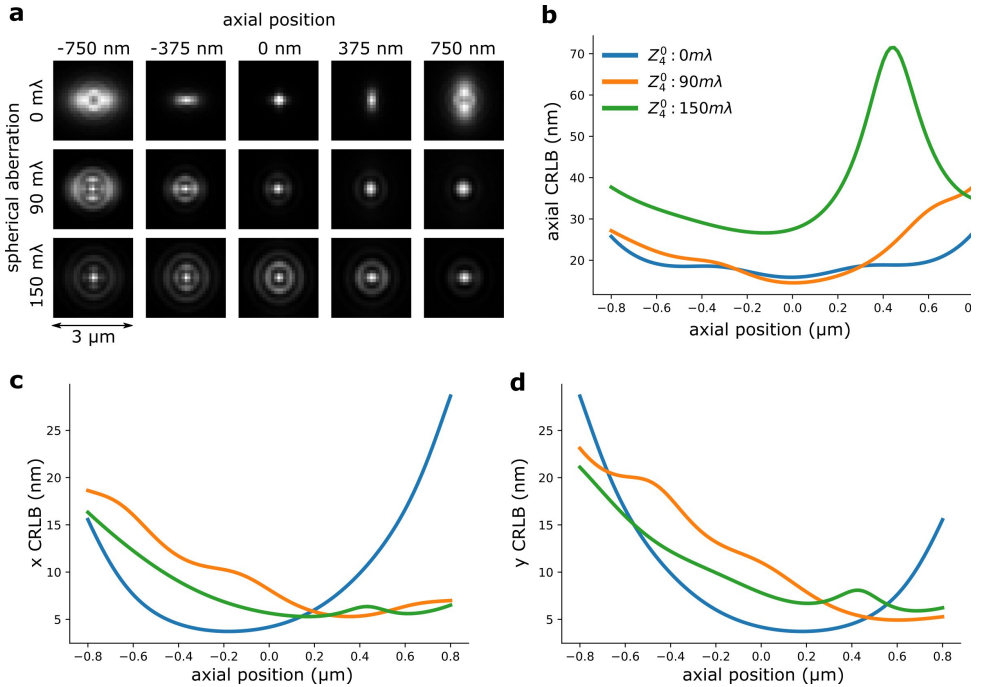
Figure 3.8: Spherical aberration deteriorates axial CRLB of astigmatism-based PSF. (a) PSFs with different amplitude of spherical aberration. (b) Theoretical axial CRLB of INSPR PSF models with different amplitude of spherical aberration. (c,d) Theoretical lateral (x,y) CRLB of INSPR model with different amplitude of spherical aberration.

3.4.2. SENSORLESS AO PERFORMANCE AND BENCHMARK

In this section, we analyze and benchmark the performance of sensorless AO algorithms in-silico based on the SDS simulator (details of the SDS simulator are in supplementary section 3.S2). In the in-silico experiments, we focused on two aspects of sensorless AO algorithm: the number of measurements needed and the sparsity of the acquired images. We found that the number of measurement steps is important for a robust sensorless AO correction. In previous research [39], it was found that in theory 3 measurement steps for correcting a Zernike mode are sufficient. Less measurements can be expected by using more advanced algorithms [42]. However, in Fig. 3.9 (a), we found that 7 measurement steps are the minimal number of measurement steps for stable AO correction in low background situations (I/bg is 10 and 50). We think the reason is that the sparse blinking molecule of localization microscopy images delivers a weak signal in Fourier space, which increases the noise in OTF-based metric functions. For high background situations (I/bg ratio is 5), 11 steps can be more stable than 7 steps. Nevertheless, we didn't observe significant improvement between the results between 11 and 15 measurement steps.

We also observed that the stability of the sensorless AO algorithm depends on the number of blinking single-molecules. In Fig. 3.9 (b), we investigated the sensorless AO algorithm with different number of blinking spots per frame (10, 30, 50). The size of each frame is 30 μm× 30 μm. The pixel size of the camera projected back to the image plane is 108.33 nm, which is the same as our system. In this experiment, we chose the I/bg ratio as 20 and the intensity of each blinking single molecules as 2000 photons. The initial aberrations were uniformly assigned to the 7 Zernike modes, which is the number of modes that we correct in this research. We scaled the initial aberration to be 220 mλ (RMS value). For AO correction we used 11 measurement steps. To investigate the robustness of the approach the experiment was repeated 20 times and we tested low and high background situations corresponding to the I/bg is 20 and 5 respectively. In Fig. 3.9 (b), we observed that when the number of blinking single-molecules is lower than 30 single-molecules/frame, the sensorless AO correction is likely to become unstable. The high background situation can further deteriorate the result (Fig. 3.9 (b)). We didn't observe significant improvement of the result between 30 single-molecules per frame and 50 single-molecules per frame. In the real experiment, we control the concentration of MEA to adjust the number of blinking. However, it should be noted that in SMLM there is a limit to the number of single-molecules that can be on, because the sparsity of single-molecule is used to achieve the resolution improvement in SMLM.

In addition, we also benchmark our metric with other metric functions used in localization microscopy [36, 38] (Fig. 3.9 (c,d)). We found comparing with other metric functions, the proposed metric in this work is more stable in high background situation (I/bg: 5), which suggests it is more stable when performing sensorless AO in tissue imaging (Fig. 3.9 (c)). Nevertheless, in low background situation (I/bg: 20), we didn't observe improvement over REALM [38] (Fig. 3.9 (d)).

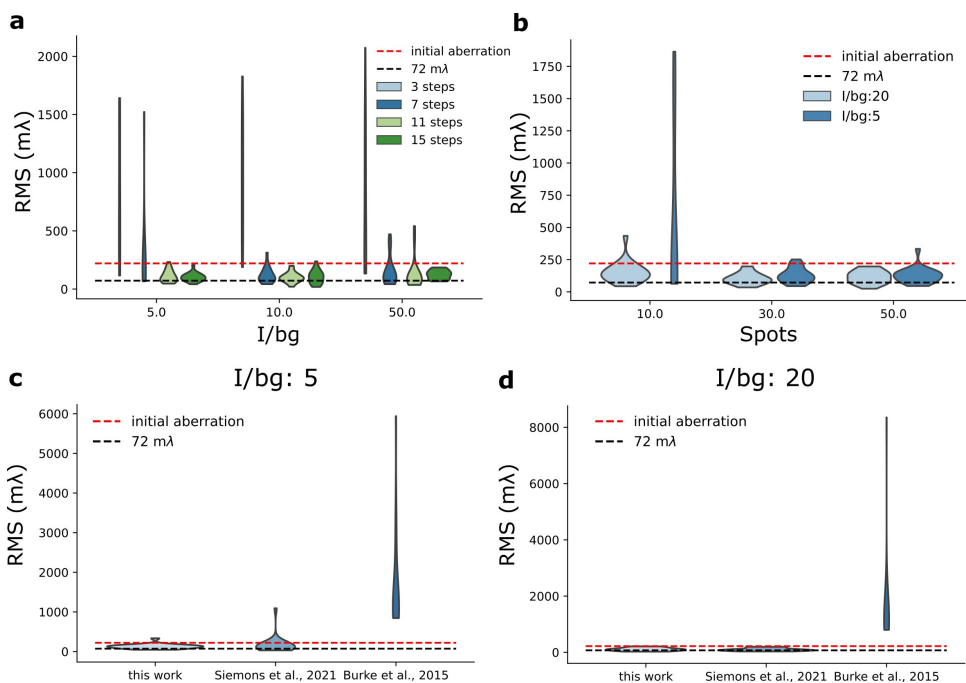Figure 3.9: Simulation test of sensorless AO algorithm. (a) Stability test of sensorless regarding the number of measurement step per frame. (b) Stability test of sensorless regarding the number of blinking single-molecules per frame. For this test, we used 11 measurement steps. (c,d) Benchmark different sensorless AO correction metric functions under different I/bg ratio (I/bg:5 and I/bg: 20).

3.4.3. 2D SMLM OF ERZIN IN AN ARTIFICIAL THICK SAMPLE WITH CACO2-BBE CELLS

To investigate the performance of our AO in a controlled environment we created an artificial thick sample. To create a predominantly spherical aberration we added a 65 μm thick STORM buffer layer to the Caco2-BBE cell. The Caco2-cells with labeled Erzin to perform dSTORM was at the top of the sandwich (Fig. 3.S5). This design introduced an additional 380 mλ spherical aberration. The correction enhances the sharpness of PSF (Fig.3.10 (a,b)) and improves the estimated localization precision estimation (Fig.3.10 (i)) and detection efficiency (Fig.3.10 (j)). The corrected pupil phase, which is computed based on the applied Zernike coefficients on DM, is shown in Fig.3.10 (c). This hypothesis was confirmed by simulation (Fig. 3.S4). The corresponding reconstructions show a better contrast with correction than without correction (Fig. 3.10 (d,e,f)). A quantitative comparison of the localizations shows a three times higher detection efficiency (Fig.3.10 (j)), a 12% improvement in CRLB (Fig.3.10 (i)) and a 45% improvement in Fourier Ring Correlation (FRC) (Fig.3.10 (h)) [13].

3.4.4. 2D SMLM OF MITOCHONDRIA IN SPHEROID CACO2-BBE CELLS

To investigate the performance of the sample-induced aberration correction algorithm we imaged spheroid Caco2-BBE cells at a depth of 17 μm using widefield microscopy (exposure time of 30 ms). For 2D SMLM we observed that the spot detection efficiency was improved by 30% with correction (Fig. 3.11 (e)) and ultimately the FRC resolution [13] was improved by 11% (Fig. 3.11 (c)). The median estimated lateral CRLB is improved by 1 nm with correction (Fig. 3.11 (d)).

3.4.5. 2D SMLM OF A SINGLE NEURON IN AN ADULT *Drosophila* BRAIN

To demonstrate our methodology in deep tissue, we imagined a single neuron in the brain of an adult *Drosophila melanogaster*. We observed that the background in the brain tissue was significantly higher, which demonstrates the importance of the optical sectioning delivered by SOLEIL (Fig. 3.12 (d,e)). The fluorescent signal from the expression of membrane-associated protein (myr-SNAP) under control of MB077c-Gal4 were acquired (Fig. 3.12 (c)) and corresponding SMLM reconstructions were made (Fig. 3.12 (a,b)). The quantitative comparison between SOLEIL and widefield microscopy revealed significant statistical improvements (Fig. 3.12 (f-h)). For SOLEIL microscopy, the median value of estimated CRLB was 21.8 nm and for WF microscopy, the median value of estimated CRLB was 25.8 nm. The median I/bg ratio from WF microscopy was 2.97 and the median I/bg ratio from SOLEIL microscopy was 8.21, which is a 276% improvement. The number of localizations per frame was increased by around 200% when SOLEIL microscopy was used for imaging.

3.4.6. 3D SMLM OF A SINGLE NEURON IN ADULT *Drosophila* BRAINS

To perform 3D SMLM in adult *Drosophila* brains, we combined SOLEIL illumination, sensorless AO correction, and in-situ PSF calibration. SOLEIL microscopy resulted in a significant background reduction (Fig. 3.13 (a,c)). To demonstrate the importance of AO correction and SOLEIL illumination, three different situations were benchmarked: AO correction with SOLEIL microscopy (AO ON+SOLEIL), SOLEIL microscopy alone (AO
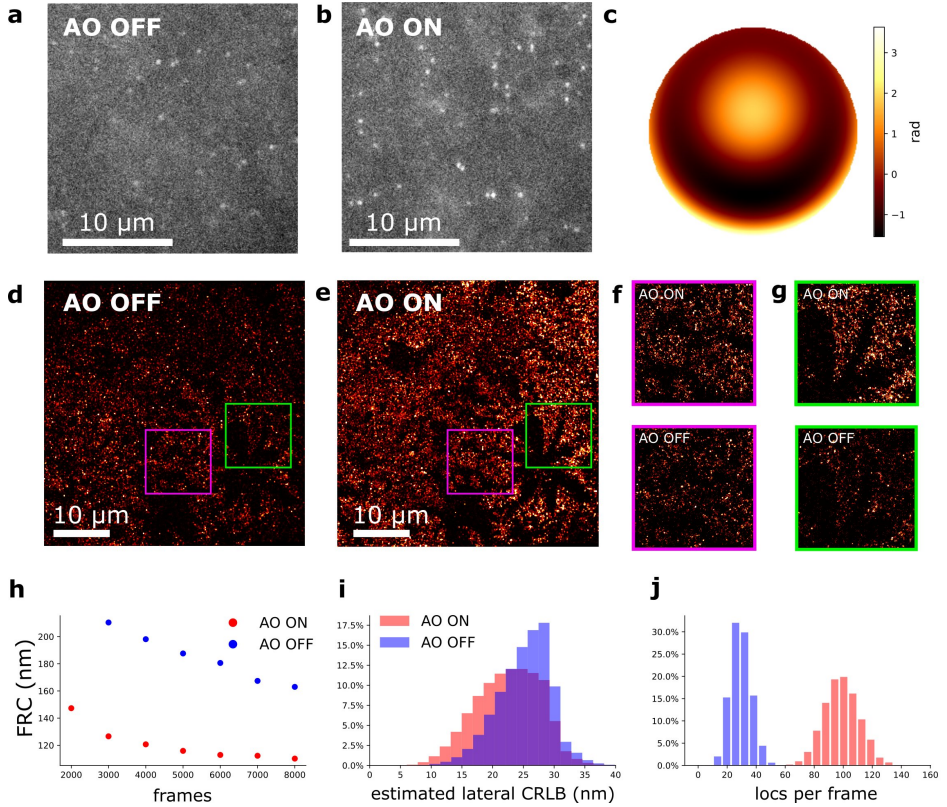
Figure 3.10: Aberration correction on an artificial thick sample with Caco2-BBE cells labeled against Ezrin. (a) Raw camera image of Caco2-BBE STORM sample without aberration correction. (b) Raw camera image of Caco2-BBE STORM data with aberration correction. (c) The pupil phase for aberration correction. (d) Reconstruction image of Caco2-BBE sample without aberration correction. (e) Reconstruction image of Caco2-BBE sample with aberration correction. (d,e) Rendered with the same contrast to visualize the localization density. (f) Zoom-in of (d,e). (h) FRC of (d,e) verse the frame number. (i) Lateral CRLB distribution from the data-set of (d,e). (j) Number of detected localizations per frame from the dataset of (d,e).
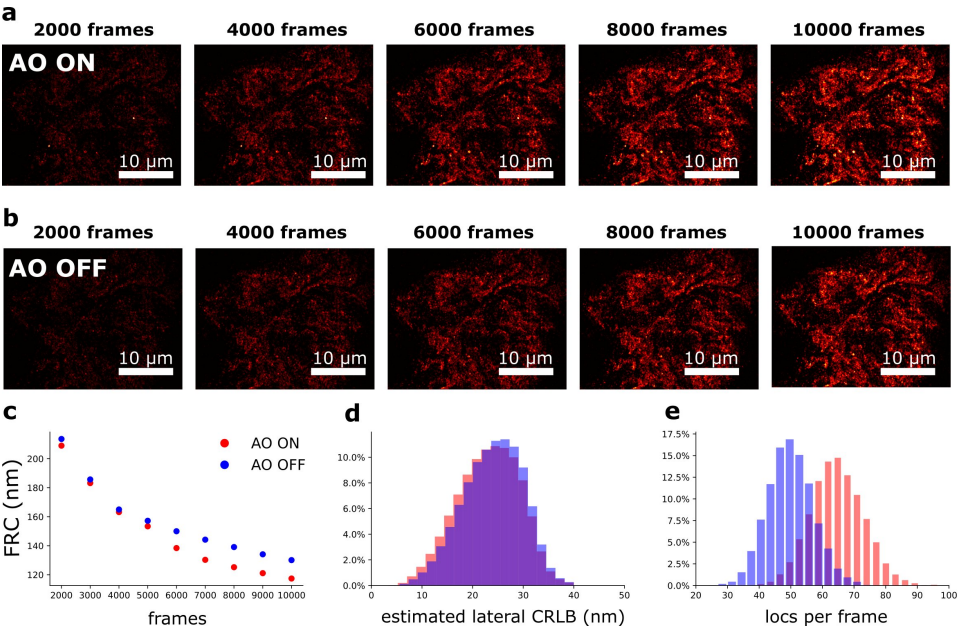
Figure 3.11: Aberration correction on mitochondria of spheroid Caco2-BBE cells (depth is 17 μm). (a) SMLM reconstruction with correction. (b) SMLM reconstruction without correction. (a,b) were rendered with same contrast to visualize the localization density. (c) FRC of (a,b) versus the frame number. (d) Lateral CRLB distribution from the data-set of (a,b). (e) Number of detected localizations per frame from the dataset of (a,b).

3
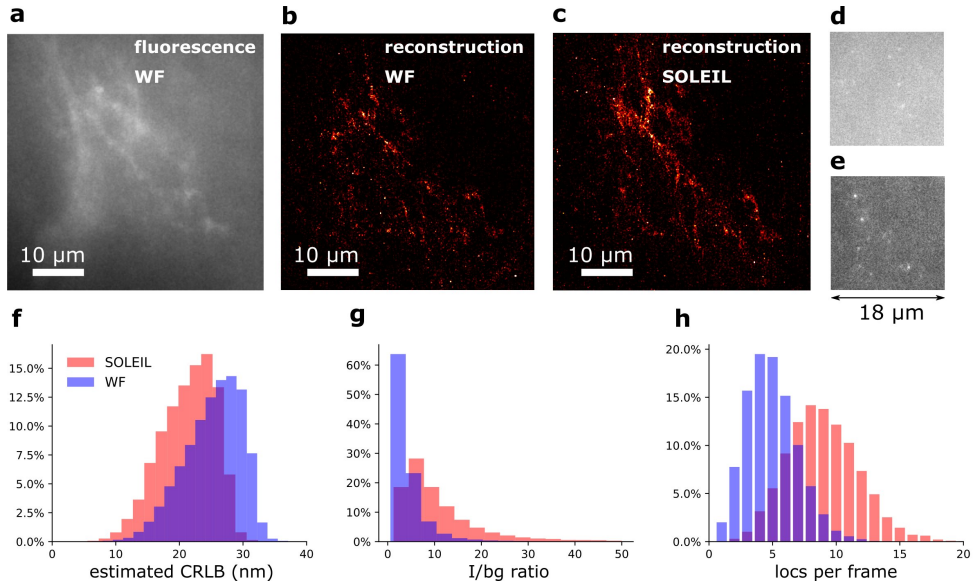
Figure 3.12: 2D SMLM of a single neuron in an whole adult *Drosophila* brain. The imaging depth was 30 μm. (a) Fluorescence images of the same FOV of (b,c) with widefield microscopy. The fluorescence signal was acquired with low laser intensity to avoid blinking. (b) SMLM reconstruction of *Drosophila* brain with widefield microscopy. (c) SMLM reconstruction of *Drosophila* brain with SOLEIL microscopy. (d,e) Raw dSTORM images with widefield and SOLEIL microscopy. The images were plotted in the same contrast to fairly visualize the background reduction. (f,g,h) The estimated CRLB, I/bg ratio, and number of localization per frame (locs per frame) of widefield and SOLEIL microscopy.

OFF+SOLEIL), and AO correction with widefield microscopy (AO ON+WF) (Fig. 3.13 (b), 3.14). The need for AO correction and the use of SOLEIL microscopy was evident from visual inspection of the corresponding reconstructions (Fig. 3.13 (b), 3.14). The quantitative comparison between the three different situations also demonstrated several statistical improvements. The median axial CRLB value was improved by about 200 % (54.5, 115.7 and 114.1 nm; AO ON+SOLEIL, AO OFF+SOLEIL and AO ON+WF, respectively), suggesting that both AO correction and SOLEIL illumination are necessary for acquiring high-resolution 3D reconstruction image in *Drosophila* brains. The median lateral CRLB value was also slightly decreased (23.8, 29.3, and 34.7 nm; AO ON+SOLEIL, AO OFF+SOLEIL, and AO ON+WF, respectively). Lastly, the median value of the I/bg ratios were 22.95, 34.7, and 8.9 (AO ON+SOLEIL, AO OFF+SOLEIL, and AO ON+WF, respectively). These data suggest that AO-SOLEIL delivers an improvement for in tissue SMLM. In (Fig. 3.14), we show the SMLM reconstruction with AO OFF+SOLEIL and AO OFF+WF. In the axial cross-section with AO ON+SOLEIL, we observed more fine structures while in the axial cross-sections with other two imaging conditions this is not visible.
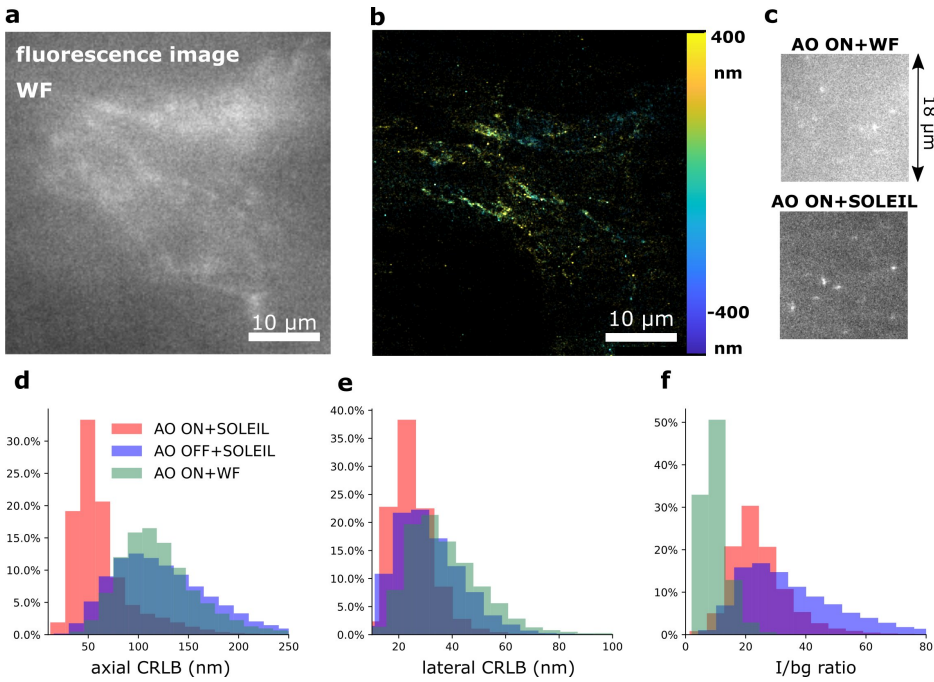
Figure 3.13: 3D SMLM of a single neuron in a whole adult *Drosophila* brain. (a) The fluorescence signal of a part of the dendritic field of the single neuron with widefield microscopy. The data is acquired at a depth of 30 μm. (b) 3D SMLM reconstruction with SOLEIL and AO correction. (c) Raw camera image with widefield microscopy and SOLEIL microscopy. (d-f) Quantitative comparison of the axial CRLB, lateral CRLB, and I/bg ratio. The reconstruction images of AO OFF+SOLEIL and AO ON+WF are in Fig. 3.14

.
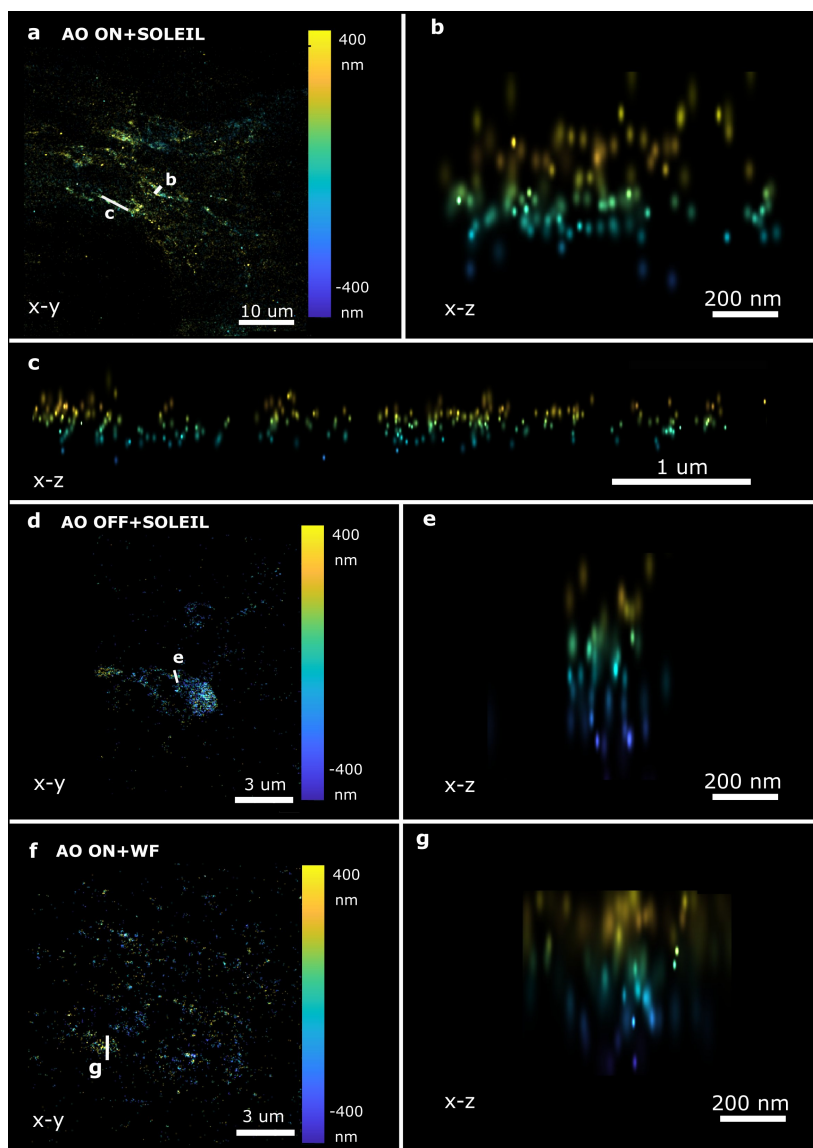
Figure 3.14: Axial SMLM reconstruction cross-section of a single neuron in a whole adult *Drosophila* brain. (a-c) SOLEIL illumination with AO correction. (a) Lateral view and axial cross-section (b,c). (d,e) SOLEIL illumination without AO correction. (d) Lateral view and (e) axial cross-section. (f,g) Widefield illumination with AO correction. (f) Lateral view and (g) axial cross-section.

3.5. Discussion and Conclusion

In this work, to mitigate the sample-induced aberrations and high background effects when imaging thick samples, we synergetically combined sensorless adaptive optics (AO), in-situ 3D-PSF calibration, and a single-objective lens inclined light sheet microscope (SOLEIL) into a new methodology (AO-SOLEIL). We have demonstrated that SOLEIL can reject the out-of-focus fluorescence and thereby increase the I/bg ratio, localization precision, and FRC (Fig. 3.3, S3,4). SOLEIL does not need a customized sample holder and only uses a single objective lens in the whole system thereby it is easier to co-operate adaptive optics element in the emission path. This feature makes the system accessible to non-expert users. We analyzed the benefit of aberration correction for 2D and 3D SMLM. In 2D SMLM, aberration correction can sharpen the PSF, which delivers better FRC resolution and more single-molecules can be detected (Fig. 3.10). In 3D SMLM, we experimentally demonstrated that aberration correction can improve the axial CRLB (Fig. 3.3, 3.13). A pitfall of using sensorless AO on three-dimensional structures is that the focal plane shifts during the correction of spherical aberration. This effect is predominant with the cross-talk between defocus and spherical aberration. To compensate for the induced defocus aberration and minimize the shift of the focal plane during the sensorless AO correction this cross-talk is calibrated (Fig. 3.2).

We experimentally verified the improvement of our sensorless AO approach by imaging thick fluorescence bead sample (Fig. 3.3). We demonstrated that sample-induced aberration can deteriorate the axial CRLB when imaging deep region of sample and aberration correction can restore the astigmatism PSF improving the axial CRLB. Furthermore, we demonstrated our approach is compatible with 2D and 3D SMLM dSTORM imaging. For 2D dSTORM, we found that the improvement in the FRC resolution is less significant in a thin sample (Fig. 3.11) than in a thick sample (Fig. 3.10). In the thin sample (17 μm deep; spheroid Caco2-BBE cells), we observed 11% of improvement in the FRC resolution (Fig. 3.11 (c)) and in the thick samples (65 μm deep; Caco2-BBE cells with artificial layer), we observed 47 % improvement in the FRC resolution (Fig. 3.10 (h)). For the 3D SMLM, we combined SOLEIL and sensorless AO method in *Drosophila* brain imaging to achieve the optimal axial CRLB. We performed the imaging with three different conditions (AO ON+SOLEIL, AO OFF+SOLEIL, and AO ON+WF) and benchmarked the estimated axial CRLB. We found that AO ON+SOLEIL achieves around 200% better estimated axial CRLB than in the other two situations, which suggests that both AO correction and SOLEIL illumination improves the SMLM when imaging tissue samples.

We anticipate that our approach can be used to image the whole adult *Drosophila* brain. We foresee that for imaging deeper in tissue the raw data quality can be improved by using photoactivation as an alternative to dSTORM, because photoactivation does not rely on a specialized buffer to penetrate the tissue [55, 56]. Furthermore, photoactivation is compatible with clearing tissue methods, which will significantly reduce scattering of the illumination and emission light [57].

In our experiments, the imaging time was limited by the stability of the tissue. We hypothesize that the agarose gel gradually heats up during image acquisitions by the excitation laser, which causes thermal expansion and thus sample drifts. Therefore, the brain could be held in place by alternatives, such as by poly-L-lysine treated coverslips. Nevertheless, our synergistic approach enables super-resolution imaging with single color

in sparsely-labeled neurons in adult *Drosophila* brains. To enable relevant 3D SMLM experiments, multi-color imaging would greatly enhance future studies addressing sub-cellular and molecular localizations of candidates of interest.

3

BIBLIOGRAPHY

1. Hess, S. T., Girirajan, T. P. & Mason, M. D. Ultra-High Resolution Imaging by Fluorescence Photoactivation Localization Microscopy. *Biophysical Journal* **91,** 4258–4272. ISSN: 0006-3495. http://www.sciencedirect.com/science/article/pii/S0006349506721403 (2006).

2. Manley S. Gillette J. Patterson, G. High-density mapping of single-molecule trajectories with photoactivated localization microscopy. *Nat. Methods* **5,** 155–157 (2008).

3. Betzig, E. *et al.* Imaging Intracellular Fluorescent Proteins at Nanometer Resolution. *Science* **313,** 1642–1645. ISSN: 0036-8075. eprint: https://science.sciencemag.org/content/313/5793/1642.full.pdf. https://science.sciencemag.org/content/313/5793/1642 (2006).

4. Egner, A. *et al.* Fluorescence Nanoscopy in Whole Cells by Asynchronous Localization of Photoswitching Emitters. *Biophysical Journal* **93,** 3285–3290. https://www.cell.com/biophysj/fulltext/S0006-3495(07)71582-5 (2022) (Nov. 2007).

5. Lidke, K. A., Rieger, B., Jovin, T. M. & Heintzmann, R. Superresolution by localization of quantum dots using blinking statistics. *Opt. Express* **13,** 7052–7062. http://www.opticsexpress.org/abstract.cfm?URI=oe-13-18-7052 (Sept. 2005).

6. Smith, C. & Joseph N. Rieger, B. Fast, single-molecule localization that achieves theoretically minimum uncertainty. *Nat. Methods* **7,** 373–375 (2010).

7. Xu, K., Zhong, G. & Zhuang, X. Actin, Spectrin, and Associated Proteins Form a Periodic Cytoskeletal Structure in Axons. *Science* **339,** 452–456. (2020) (Dec. 2012).

8. Zhong, G. *et al.* Developmental mechanism of the periodic membrane skeleton in axons. *eLife* **3** (ed Singer, R. H.) e04581. ISSN: 2050-084X. https://doi.org/10.7554/eLife.04581 (Dec. 2014).

9. Kapałczyńska, M. *et al.* 2D and 3D cell cultures – a comparison of different types of cancer cell cultures. *Archives of Medical Science* **14** (2016).

10. Sanyal, S. Culture and assay systems used for 3D cell culture. *Corning* **9,** 1–18 (2014).

11. Booth, M. J. & Wilson, T. Refractive-index-mismatch induced aberrations in single-photon and two-photon microscopy and the use of aberration correction. *Journal of Biomedical Optics* **6,** 266 (2001).

12. Smith, C. S., Stallinga, S., Lidke, K. A., Rieger, B. & Grunwald, D. Probability-based particle detection that enables threshold-free and robust in vivo single-molecule tracking. *Molecular Biology of the Cell* **26,** 4057–4062 (2015).

13. Nieuwenhuizen, R. P. J. *et al.* Measuring image resolution in optical nanoscopy. *Nature Methods* **10,** 557–562 (2013).

14. Tokunaga, M., Imamoto, N. & Sakata-Sogawa, K. Highly inclined thin illumination enables clear single-molecule imaging in cells. *"Nat. Methods"* **5,** 159–161. (2021) (Jan. 2008).

15. Konopka, C. A. & Bednarek, S. Y. Variable-angle epifluorescence microscopy: a new way to look at protein dynamics in the plant cell cortex. *The Plant Journal* **53,** 186–196 (2008).

16. Ahrens, M., Orger, M. & Robson, D. e. a. Whole-brain functional imaging at cellular resolution using light-sheet microscopy. *Nat. Methods* **10,** 413–420 (2013).

17. Lu, C., Tang, W. & Liu, Y. e. a. Lightsheet localization microscopy enables fast, large-scale, and three-dimensional super-resolution imaging. *Commun Biol* **2** (2019).

18. Gustavsson, A., Petrov, P. & Lee, M. e. a. 3D single-molecule super-resolution microscopy with a tilted light sheet. *Nat Commun* **9.** https://www.nature.com/articles/s41467-017-02563-4 (Jan. 2018).

19. Kumar, M. & Kozorovitskiy, Y. Tilt-invariant scanned oblique plane illumination microscopy for large-scale volumetric imaging. *Opt. Lett.* **4,** 1706–1709 (2019).

20. Sapoznik, E., Chang, B.-J. & Huh, J. A versatile oblique plane microscope for large-scale and high-resolution imaging of subcellular dynamics. *eLife* **9** (eds Lakadamyali, M., Akhmanova, A. & Power, R.) e57681. ISSN: 2050-084X. https://doi.org/10.7554/eLife.57681 (Nov. 2020).

21. Kumar, M. & Kozorovitskiy, Y. Tilt (in)variant lateral scan in oblique plane microscopy: a geometrical optics approach. *Biomed. Opt. Express* **11,** 3346–3359 (June 2020).

22. An, S. *et al.* Axial plane single-molecule super-resolution microscopy of whole cells. *Biomed. Opt. Express* **11,** 461–479. http://www.osapublishing.org/boe/abstract.cfm?URI=boe-11-1-461 (Jan. 2020).

23. An, S. *et al.* Axial plane single-molecule super-resolution microscopy of whole cells. *Biomed. Opt. Express* **11,** 461–479. http://www.osapublishing.org/boe/abstract.cfm?URI=boe-11-1-461 (Jan. 2020).

24. Yang, B. *et al.* Epi-illumination SPIM for volumetric imaging with high spatial-temporal resolution. *Nature Methods* **16,** 501–504. https://www.nature.com/articles/s41592-019-0401-3 (June 2019).

25. Hung, S.-T. *et al.* SOLEIL: single-objective lens inclined light sheet localization microscopy. *Biomedical Optics Express* **13,** 3275–3294. https://opg.optica.org/boe/fulltext.cfm?uri=boe-13-6-3275&id=472719 (2022) (June 2022).

26. Aristov, A., Lelandais, B., Rensen, E. & Zimmer, C. ZOLA-3D allows flexible 3D localization microscopy over an adjustable axial range. *Nature Communications* **9,** 2409. https://www.nature.com/articles/s41467-018-04709-4 (June 2018).

27. Li, Y. *et al.* Real-time 3D single-molecule localization using experimental point spread functions. *Nature Methods* **15,** 367–369. https://www.nature.com/articles/nmeth.4661 (2022) (May 2018).

28. Li, Y. *et al.* Real-time 3D single-molecule localization using experimental point spread functions. *Nature Methods* **15,** 367–369. https://www.nature.com/articles/nmeth.4661 (May 2018).

29. McGorty, R., Schnitzbauer, J., Zhang, W. & Huang, B. Correction of depth-dependent aberrations in 3D single-molecule localization and super-resolution microscopy. *Optics Letters* **39,** 275–278. https://opg.optica.org/ol/abstract.cfm?uri=ol-39-2-275 (2022) (Jan. 2014).

30. Li, Y., Wu, Y.-L., Hoess, P., Mund, M. & Ries, J. Depth-dependent PSF calibration and aberration correction for 3D single-molecule localization. *Biomedical Optics Express* **10,** 2708–2718. https://opg.optica.org/boe/fulltext.cfm?uri=boe-10-6-2708&id=412042 (2022) (June 2019).

31. Cabriel, C., Bourg, N., Dupuis, G. & Lévêque-Fort, S. Aberration-accounting calibration for 3D single-molecule localization microscopy. *Opt. Lett.* **43,** 174–177. http://opg.optica.org/ol/abstract.cfm?URI=ol-43-2-174 (Jan. 2018).

32. Tafteh, R., Scriven, D. R. L., Moore, E. D. W. & Chou, K. C. Single molecule localization deep within thick cells; a novel super-resolution microscope. *Journal of Biophotonics* **9,** 155–160. (2021) (Aug. 2015).

33. Xu, F. *et al.* Three-dimensional nanoscopy of whole cells and tissues with in situ point spread function retrieval. *Nature Methods* **17,** 531–540. https://www.nature.com/articles/s41592-020-0816-x (May 2020).

34. Mlodzianoski, M. J. *et al.* Active PSF shaping and adaptive optics enable volumetric localization microscopy through brain sections. *Nature Methods* **15,** 583–586. https://www.nature.com/articles/s41592-018-0053-8/ (2021) (Aug. 2018).

35. Park, S. *et al.* Restoring single-molecule localizations with wavefront sensing adaptive optics for deep-tissue super-resolution imaging. *bioRxiv.* eprint: https://www.biorxiv.org/content/early/2021/11/20/2021.11.18.469175.full.pdf. https://www.biorxiv.org/content/early/2021/11/20/2021.11.18.469175 (2021).

36. Burke, D., Patton, B., Huang, F., Bewersdorf, J. & Booth, M. J. Adaptive optics correction of specimen-induced aberrations in single-molecule switching microscopy. *Optica* **2,** 177–185. https://www.osapublishing.org/optica/fulltext.cfm?uri=optica-2-2-177&id=312101 (2021) (Feb. 2015).

37. Tehrani, K. F., Xu, J., Zhang, Y., Shen, P. & Kner, P. Adaptive optics stochastic optical reconstruction microscopy (AO-STORM) using a genetic algorithm. *Optics Express* **23,** 13677. (2020) (May 2015).

38. Siemons, M. E., Hanemaaijer, N. A. K., Kole, M. H. P. & Kapitein, L. C. Robust adaptive optics for localization microscopy deep in complex tissue. *Nature Communications* **12,** 3407. https://www.nature.com/articles/s41467-021-23647-2 (2021) (June 2021).

39. Debarre, D., Booth, M. J. & Wilson, T. Image based adaptive optics through optimisation of low spatial frequencies. *Opt. Express* **15,** 8176. ISSN: 1094-4087. https://www.osapublishing.org/oe/abstract.cfm?uri=oe-15-13-8176 (2007).

40. Soloviev, O. Alias-free basis for modal sensorless adaptive optics using the second moment of intensity. *International Journal of Wavelets, Multiresolution and Information Processing.* https://www.scopus.com/inward/record.uri?eid=2-s2.0-85094130395&doi=10.1142%2fS0219691320400081&partnerID=40&md5=9eb211f54915a24e6bef1cb7d6606f12 (2020).

41. Antonello, J. *et al.* Semidefinite programming for model-based sensorless adaptive optics. *J. Opt. Soc. Am. A* **29,** 2428–2438. http://opg.optica.org/josaa/abstract.cfm?URI=josaa-29-11-2428 (Nov. 2012).

42. Booth, M. J. Wave front sensor-less adaptive optics: a model-based approach using sphere packings. *Opt. Express* **14,** 1339–1352. http://opg.optica.org/oe/abstract.cfm?URI=oe-14-4-1339 (Feb. 2006).

43. Žurauskas, M. *et al.* IsoSense: frequency enhanced sensorless adaptive optics through structured illumination. *Optica* **6,** 370–379. http://www.osapublishing.org/optica/abstract.cfm?URI=optica-6-3-370 (Mar. 2019).

44. . *SciPy documentation — SciPy v1.8.1 Manual* docs.scipy.org. https://docs.scipy.org/doc/scipy/index.html.

45. Siemons, M., Hulleman, C. N., Thorsen, R. Ø., Smith, C. S. & Stallinga, S. High precision wavefront control in point spread function engineering for single emitter localization. *Optics Express* **26,** 8397–8416. https://opg.optica.org/oe/fulltext.cfm?uri=oe-26-7-8397&id=383954 (2022) (Apr. 2018).

46. Ries, J. SMAP: a modular super-resolution microscopy analysis platform for SMLM data. *Nature Methods* **17,** 870–872 (Aug. 2020).

47. Linhai, H. & Rao, C. Wavefront sensorless adaptive optics: a general model-based approach. *Opt. Express* **19,** 371–379. http://opg.optica.org/oe/abstract.cfm?URI=oe-19-1-371 (Jan. 2011).

48. Olivier, N., Débarre, D. & Beaurepaire, E. Dynamic aberration correction for multi-harmonic microscopy. *Opt. Lett.* **34,** 3145–3147. http://opg.optica.org/ol/abstract.cfm?URI=ol-34-20-3145 (Oct. 2009).

49. Chakraborty, T. *et al.* Converting lateral scanning into axial focusing to speed up three-dimensional microscopy. *Light: Science & Applications* **9,** 165. https://www.nature.com/articles/s41377-020-00401-9 (2022) (Sept. 2020).

50. Baumgart, E. & Kubitscheck, U. Scanned light sheet microscopy with confocal slit detection. *Optics Express* **20,** 21805. (2019) (Sept. 2012).

51. Paglione, M., Rosell, A. L., Chatton, J.-Y. & Neukomm, L. J. Morphological and Functional Evaluation of Axons and their Synapses during Axon Death in Drosophila melanogaster. *Journal of Visualized Experiments.* (2021) (Mar. 2020).

52. Kelly, S. M., Elchert, A. & Kahl, M. Dissection and Immunofluorescent Staining of Mushroom Body and Photoreceptor Neurons in Adult Drosophila melanogaster Brains. *Journal of Visualized Experiments.* (2019) (Nov. 2017).

53. Siemons, M., Hulleman, C. N., Thorsen, R. Ø., Smith, C. S. & Stallinga, S. High precision wavefront control in point spread function engineering for single emitter localization. *Optics Express* **26,** 8397–8416. https://opg.optica.org/oe/fulltext.cfm?uri=oe-26-7-8397&id=383954 (Apr. 2018).

54. Siemons, M. *et al.* Comparing strategies for deep astigmatism-based single-molecule localization microscopy. *Biomed. Opt. Express* **11,** 735–751. http://www.osapublishing.org/boe/abstract.cfm?URI=boe-11-2-735 (Feb. 2020).

55. Hess, S. T., Girirajan, T. P. & Mason, M. D. Ultra-high resolution imaging by fluorescence photoactivation localization microscopy. *Biophysical journal* **91,** 4258–4272 (2006).

56. Betzig, E. *et al.* Imaging intracellular fluorescent proteins at nanometer resolution. *science* **313,** 1642–1645 (2006).

57. Lin, H.-Y. *et al.* Imaging through the Whole Brain of Drosophila at $\lambda\backslash 20$ Super-resolution. *iScience* **14,** 164–170. https://www.sciencedirect.com/science/article/pii/S2589004219300914 (2022) (Apr. 2019).

3

SUPPLEMENTAL INFORMATION:

ADAPTIVE OPTICS SINGLE OBJECTIVE INCLINED LIGHT SHEET LOCALIZATION MICROSCOPY

3

3.S1. OPTICAL SYSTEM

The design of SOLEIL microscope is shown in [1]. We used a stick-slip piezo stage as a sample stage (Smartact; x,y an SLC1730; z an SLC1720). The lightsheet was generated by an achromatic doublet cylindrical lens (Thorlabs, ACY254-250-B). Then, an achromatic doublet lens (Thorlabs, AC254-300-A-ML) formed a 4f-telescope with the cylindrical lens. To translate the lightsheet illumination, we placed a galvo mirror (Scanlab, dynAXIS 20 mm) at the pupil plane of the scan lens (TTL200MP, Thorlabs) to work as a scanning module. An achromatic doublet lens (Thorlabs, AC254-200-A-ML) and a reflective mirror (Thorlabs, BB1-E02) were placed on a translation stage (Thorlabs, XR25P/M), which allow us to adjust the angle of inclined lightsheet. A dichroic mirror (Semrock, Di03-R405/488/561/635-t1-25x36) separated the excitation and emission path. A 180 mm focal length tube lens (Olympus, SWTLU-C) was used to form a 60 times imaging system with objective lens (Olympus, UPlanSAPO 60x Oil NA 1.35). In the emission path, an achromatic lens with 200 mm focal length (AC254-200-A-ML) was assembled as a 4f-telescope with the tube lens, which conjugated the back focal plane of the objective lens to the plane of the deformable mirror (Alpao DM69-15). The deformable mirror allowed us to control the pupil phase in the emission path, which enables PSF engineering for 3D SMLM and sensorless AO correction. The deformable mirror was rotated by approximately $15°$ to reflect the emission light so that the emission light wouldn't reflect back to the original path. An emission filter (AHF, FF01-446/510/581/703-25) was used to filter out the back-reflected excitation laser. An achromatic doublet lens (AC254-200-A-ML) imaged the pupil plane at the plane of deformable mirror to the sCMOS camera (Andor Zyla 4.2). The sCMOS camera and galvo mirror were synchronized by using an Arduino micro-controller.

3.S2. IN-SILICO SMLM DATA GENERATION

To test the stability and the performance of the sensorless AO algorithm, we built a SMLM data simulator (SDS) to simulate the blinking images in the presence of (Zernike) aberrations (Fig. 3.S1). The pipeline of SDS consists of several steps. Firstly, we set up a 3D structure of the sample in the SDS (Fig. 3.S1 (a)). In general, the structure can be any shape and in this experiment we set up the structure of the sample as tubulin-like. In the SDS simulator, the algorithm randomly chooses certain number of spots turning them to be the on-state and the others staying in the off-state. Then, SDS simulates the vector PSFs based on the input Zernike aberration, intensity and I/bg ratio (Fig. 3.S1 (b)). The PSF simulation was done with ROI of 25 pixels× 25 pixels, which is 2.5 μm× 2.5 μm.

The high NA aberrated PSF was computed based on the pupil function [2]. The pupil function (Eq. 3.S1) consists a phase aberration ($W(\vec{\rho})$) and an aplantic amplitude factor ($A(\vec{\rho})$) [3]. The pupil function is described by a 91 pixels × 91 pixels array. The electric field (Eq. 3.S2) is described as the Fourier transform of the pupil function ($v_{l,j}(\vec{\rho})$) [2]. For numerical reasons we used the chirp z transform [2, 4]. We considered a free-rotating dipole and hence all polarization terms contribute to the PSF equally Eq. 4.12. Monochromatic light was used for simulating and the wavelength is 680 nm. The NA of objective lens we used is 1.35. The refractive index of immersion media is 1.52 and the refractive index of sample medium is 1.33. The pixel size of the simulated images is 108.33 nm. We neglect supercritical angle fluorescence (SAF) effects because they are neglectable away from the coverslip.

$$P(\vec{\rho}) = A(\vec{\rho}) \exp\left(i \frac{2\pi W(\vec{\rho})}{\lambda} \right) \tag{3.S1}$$

where $\vec{\rho}$ is the normalized pupil function radius, $P(\vec{\rho})$ is the pupil function, $A(\vec{\rho})$ is the aplantic amplitude factor, $W(\vec{\rho})$ is the phase aberration, λ is the wavelength.

$$E_{l,j}(\vec{r}) = \int_{|\vec{\rho}|<1} d^2\rho \, P(\vec{\rho}) \, v_{l,j}(\vec{\rho}) \exp\left(-i\vec{k} \cdot \vec{r} \right) \tag{3.S2}$$

,where $E_{l,j}(\vec{r})$ is the electric field with l, j as the direction of polarization (j emitter polarization projects to l polarization on pupil plane), $v_{l,j}(\vec{\rho})$ is the vectorial factor [3], $\vec{k}$ is the wavevector.

$$PSF(\vec{r}) = \frac{1}{3} \sum_{l=x,y} \sum_{j=x,y,z} \left| E_{l,j}(\vec{r}) \right|^2 \tag{3.S3}$$

, where $PSF(\vec{r})$ is the point spread function function.

3

a

b
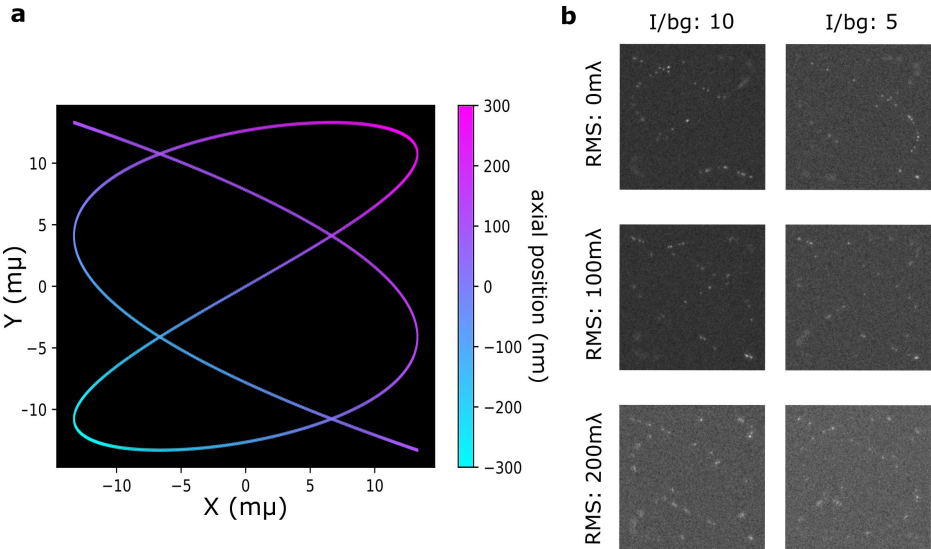
Figure 3.S1: Blinking image simulator. (a) Tubulin structure for blinking image simulation. (b) Aberrated blinking image under different RMS value and I/bg ratio.

3.S3. IMPACT OF AO CORRECTION ON THE LATERAL LOCALIZATION PRECISION FOR IN-SITU PSF ESTIMATION USING THE INSPR ALGORITHM

In this section, the impact on the lateral CRLB is investigated. In Fig. 3.3, we show that AO correction can improve the axial CRLB. In Fig. 3.S2 we found AO correction doesn't improve the lateral CRLB. In Fig. 3.8, it is also observed that AO correction has no significant improvement in lateral CRLB. Note that in Fig. 3.3, Fig. 3.8 AO correction did improve the axial CRLB.
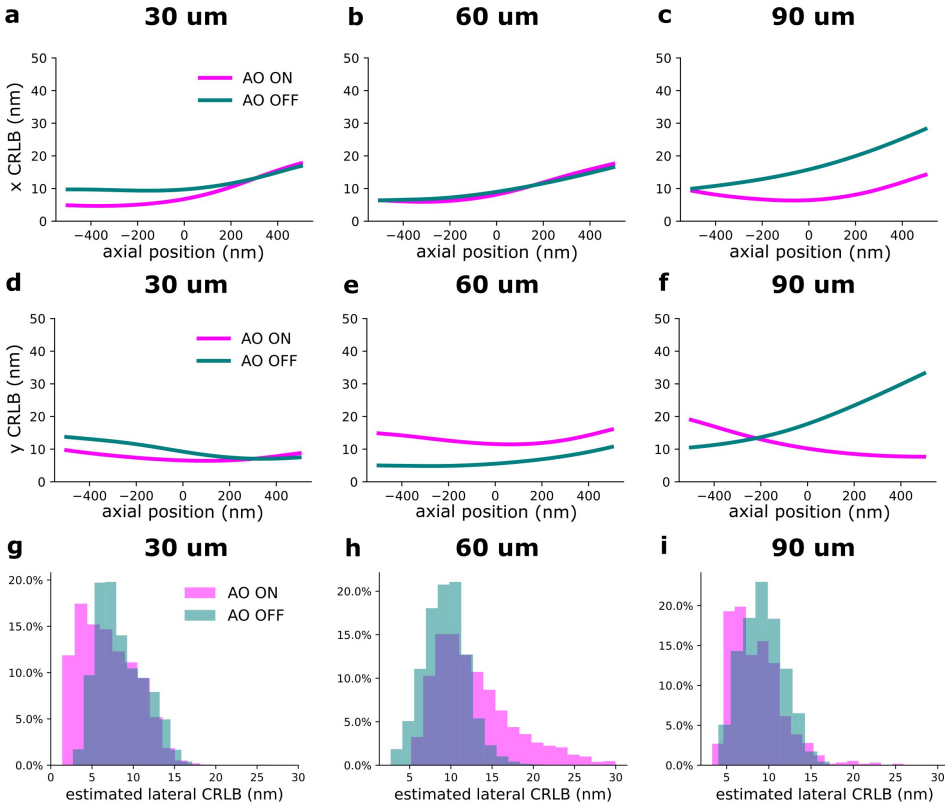
Figure 3.S2: Lateral CRLB of the INSPR model before and after AO correction at different imaging depth. (a-f) The theoretical x,y CRLB based on the INSPR PSF model from Fig. 3 (a-c) with 3000 photon of intensity and 50 photons/pixel of background. (g-i) The distribution of estimated lateral CRLB at different imaging depths.

3.S4. PREPARATION OF THE ARTIFICIALLY THICK CACO2-BBE SAMPLE

In this section, we show the flowchart on makig artificial thick Caco2-BBE sample. In Fig. 3.S3 (a), we show the the schematic figure of the artificial thick sample from three views (top view and side view1,2). Fig. 3.S3 (b) shows the material we used to make the artificially thick sample. Fig. 3.S3 (c) shows detailed steps to create the artificial sample and how to add dSTORM buffer into the sample.
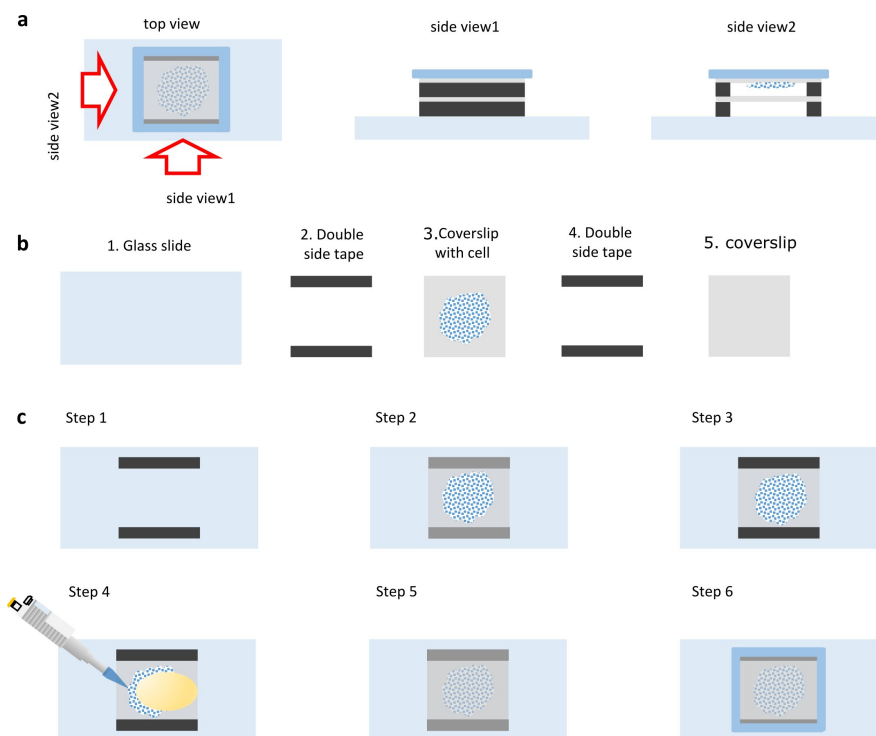
Figure 3.S3: (a) The figure of thick STORM buffer layer Caco2-BBE sample and the sideview. (b) Material to make thick STORM buffer layer Caco2-BBE sample in (a,c). (c) Protocol to make thick STORM buffer layer Caco2-BBE sample. Step 1: put double side tape on glass slides, Step 2: attach a coverslip on the double side tape, Step 3: attach double side tape on the coverslip in Step 2, Step 4: add STORM buffer (yellow ellipse) in the middle of double side tape with pipette , Step 5: cover the cell with another coverslip, Step 6: seal the edge of coverslip by Twinsil (Picodent, Wipperfürth).

3.S5. MEASURE THE THICKNESS OF DSTORM BUFFER LAYER

In the artificially thick Caco2-BBE sample, we added double sided tape as spacer between the cells and the coverslip to increase the thickness of the sample (Fig. 3.S3), which can introduce additional spherical aberration. The thickness of the spacer was measured by the optical setup in Fig. 3.S4 (a). A single mode coherent laser (640 nm) was launched from a reflected collimator and went through the 50:50 beam splitter focusing on the sample by an objective lens. The reflected light from the sample was acquired by the objective lens and went through the 50:50 beam splitter to the camera. When the incident light was focused on the interface between material, such as air-coverslip interface, the peak intensity of reflected light was much higher than the other situation. With this principle, we can identify the stage position from (b). The first interface the light can be focused on is the layer between air and the front side of the first coverslip, which is the P1 point in (b). The second interface can be focused is the back side of second coverslip, which is P2 point in (b). The third interface can be focused is the front side of second coverslip, which is the P3 point. The fourth interface can be focused is the back side of second coverslip. The distance between P2 and P3 is the distance of spacer we add in the sample, which is 64 μm.
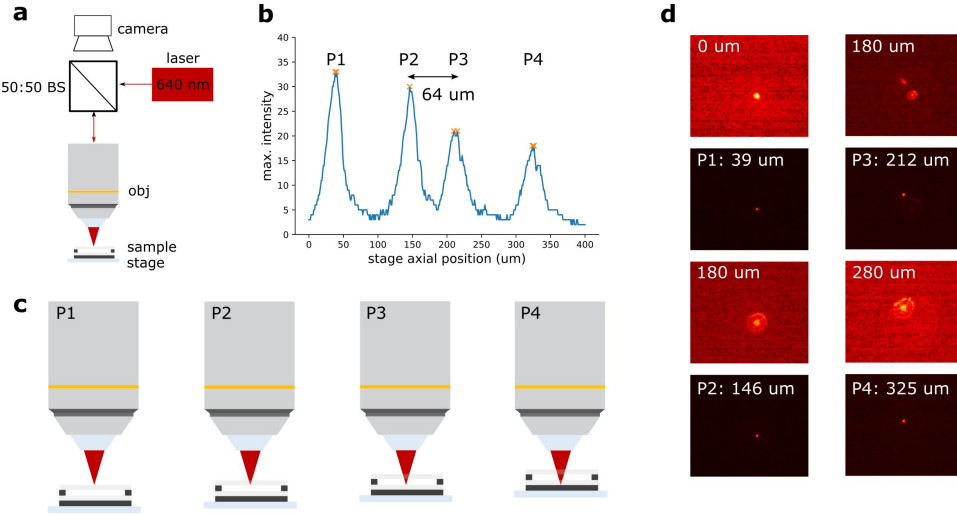
Figure 3.S4: Measurement of the thickness of artificial Caco2-BBE sample. (a) optical setup for sample thickness measurement. 50:50 BS: 50:50 beam splitter (BS013, Thorlabs); camera: CMOS camera (IDS UI3070CP-M-GL); obj: 10X objective lens (UMPlanFL N 10X NA:0.3, Olympus); sample: measured sample; stage: piezo stage (Smactact, x,y an SLC1730; z an SLC1720); laser: 640 nm single mode laser (HLS635, Thorlabs). (b) the maximum image value at different stage position. (c) Schematic of stage position corresponding to the peak of (b). P1: the first peak in (b), where is light is focused at the interface of the front side of first coverslip and air. P2: the second peak in (b), where the light is focused at the interface of the back side of first coverslip. P3: the third peak in (b), where the light is focused at the front side of second coverslip. P4: the fourth peak in (b), where the light is focused at the back side of second coverslip. (d) the raw camera image at different stage position.

3.S6. INFLUENCE OF SPHERICAL ABERRATION ON AXIAL CRLB

The spherical aberration can smooth the PSF along the axial dimension and this has an impact on the axial CRLB. To investigate the influence of spherical aberration on the axial CRLB, we simulated the the astigmatism and tetrapod PSF with additional spherical aberrations (Fig.3.S5 (a,c)) (Details of PSF simulation is in section 3.S2). In the Fig.3.S5 (b,d), we computed the CRLB with a intensity of 1000 photons and a background of 50 photons/pixel and found that the spherical aberration can significantly decrease the CRLB of engineered PSF.

In Fig.3.S5 (b), the CRLB curve with 90 mλ spherical aberration demonstrates a very bad CRLB, which means a bad localization precision. We think the reason is that the PSF change is very minor (see Fig.3.S5 (a) at 180 and 375 nm) and the gradient of PSF over the axial position is very small, resulting in a high CRLB. However, we want to note that the relationship between CRLB and PSF is not straightforward and it is hard to judge the CRLB only based on the shape of PSF.
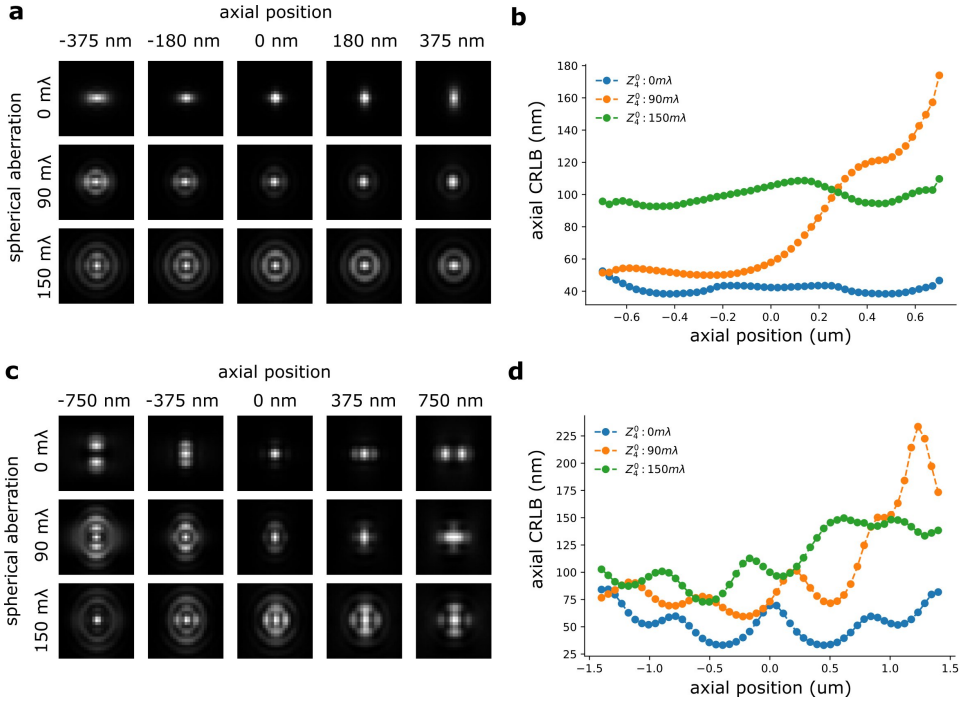
Figure 3.S5: Influence of spherical aberration on axial CRLB. (a) Simulated astigmatism PSF (100 mλZ_2^2) with the addition of different level of spherical aberration. (b) The axial theoretical CRLB of the astigmatism PSF with addition of different level of spherical aberration. The intensity used for simulation is 1000 photons and the background is 50 photons/pixel. (c) Simulated tetrapod PSF (100 mλZ_2^4) with the addition of different level of spherical aberration. (b) The axial theoretical CRLB of the tetrapod PSF with addition of different level of spherical aberration. The intensity used for simulation is 1000 photons and the background is 50 photons/pixel.

3.S7. INFLUENCE OF SPHERICAL ABERRATION ON THE 2D LO-CALIZATION PRECISION

To understand the influence of spherical aberration on the 2D localization of single-molecules, we simulated PSFs with different amounts of spherical aberration (details are in section 3.S2) and performed the localization by using Gaussian PSF model. We observed that the spherical aberration deteriorates the achievable localization (Fig. 3.S6 (a)). The reported localization precision is the standard deviation of estimated position from 100 times of localization and we repeated this for 10 times for the errorbar in Fig. 3.S6 (a). The spherical aberration can distort the PSF and the shape of the aberrated PSF doesn't match with a Gaussian function. The PSFs were simulated with the same intensity and background. However, the estimated intensity and background are biased in the presence of spherical aberration (Fig. 3.S6 (c,d)). In the meanwhile, the I/bg decreases (Fig. 3.S6 (e)). The reported CRLB and the estimation precision deteriorate by 40% as the spherical aberration (Z_4^0) increases to 120 mλ.
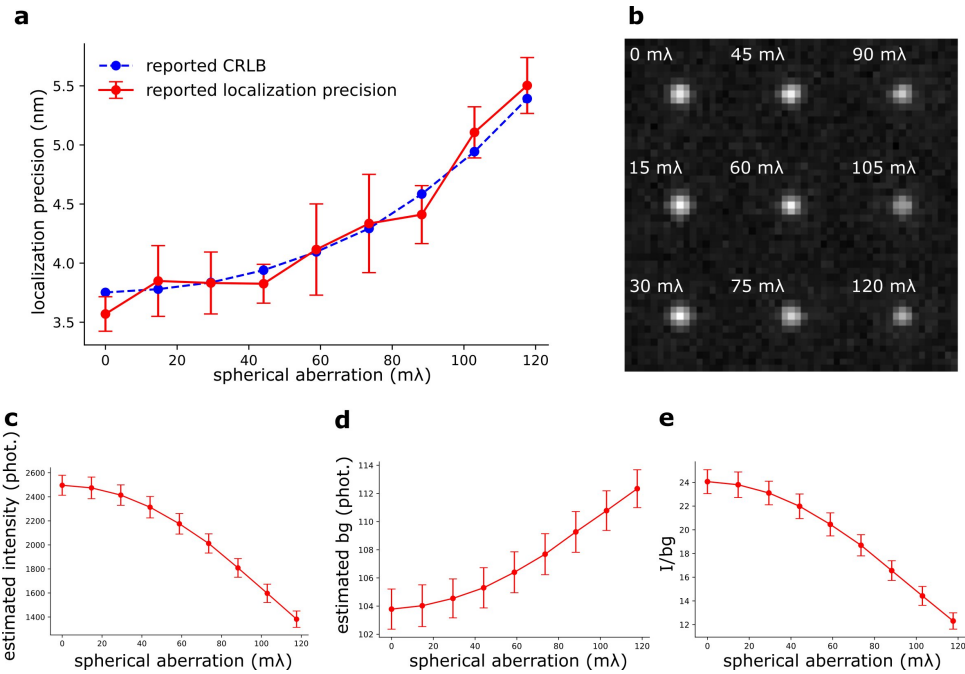
Figure 3.S6: Influence of spherical aberration on the 2D localization precision. (a) the CRLB, reported localization precision versus amplitude of spherical aberration. (b) the simulated PSF with different amplitude of spherical aberration. (c-e) the influence of spherical on estimated intensity (c), background (d), and SBR (e).

3.S8. CAMERA SETTING

In this research, we used Andor Zyla 4.2 SCMOS camera for imaging. For the dSTORM imaging, we used 501 pixels×501 pixels, which corresponds to 54 μm×54 μm FOV. The camera trigger was set to external trigger, which allows for external signal control from Arduino Micro-controller. In SOLEIL microscopy, the virtual confocal slit readout was achieved with a rolling shutter by activating the Andor SOLIS LightScan PLUS function in down sequential mode. The readout image is 16 bit format.

For initial aberration correction, the camera trigger mode was set to internal trigger and the camera was synchronized with DM through the customized Python script. The FOV was cropped to single PSF spot. The camera exposure time was 30 ms, which is 25 frames/second. The image readout was set to 16 bit mode.

For sensorless AO correction, the camera trigger mode was set to internal trigger and used customized Python script for controlling camera and DM. The camera readout is 16 bit. The FOV was cropped depend on the size of sample. In general, we ensured the FOV is larger than 30 μm×30 μm.

BIBLIOGRAPHY

1. Hung, S.-T. *et al.* SOLEIL: single-objective lens inclined light sheet localization microscopy. *Biomedical Optics Express* **13,** 3275–3294. https://opg.optica.org/boe/fulltext.cfm?uri=boe-13-6-3275&id=472719 (2022) (June 2022).

2. Siemons, M., Hulleman, C. N., Thorsen, R. Ø., Smith, C. S. & Stallinga, S. High precision wavefront control in point spread function engineering for single emitter localization. *Optics Express* **26,** 8397–8416. https://opg.optica.org/oe/fulltext.cfm?uri=oe-26-7-8397&id=383954 (Apr. 2018).

3. Stallinga, S. Effect of rotational diffusion in an orientational potential well on the point spread function of electric dipole emitters. *J. Opt. Soc. Am. A* **32,** 213–223. http://opg.optica.org/josaa/abstract.cfm?URI=josaa-32-2-213 (Feb. 2015).

4. Rabiner, L. R., Schafer, R. W. & Rader, C. M. The Chirp z-Transform Algorithm and Its Application. *Bell System Technical Journal* **48,** 1249–1292. (2022) (May 1969).

4

IMAGE SCANNING MICROSCOPY: A VECTORIAL PHYSICAL OPTICS ANALYSIS

Image Scanning Microscopy (ISM) achieves resolution beyond the diffraction limit by a factor of $\sqrt{2}$. However, prior ISM research predominantly employs scalar diffraction theory, neglecting critical physical effects such as polarization, aberrations, and Stokes shift. This paper presents a comprehensive vectorial ISM Point Spread Function (PSF) model that accounts for these phenomena. By considering the effect of polarization in emission and excitation paths, as well as aberrations and Stokes shift, our model provides a more accurate representation of ISM. We analyze the differences between scalar and vectorial theories in ISM and investigate the impact of pinhole size and aberration strength on resolution. At a numerical aperture of 1.2, the full width half maximum (FWHM) discrepancy between scalar and vectorial ISM PSFs can reach 45 nm, representing a 30% deviation from the vectorial model. Additionally, we explore multiphoton excitation in ISM and observe increased FWHM for 2-photon and 3-photon excitation compared to 1-photon excitation. The FWHM of the 2-photon excitation ISM PSF increases by 20% and the FWHM of the 3-photon excitation ISM PSF increases by 28% compared to the 1-photon excitation ISM. In addition, we found that the optimal sweep factor for 2-photon ISM is 1.22, and the optimal sweep factor of 3-photon ISM is 1.12 instead of the 2 predicted by the one-photon scalar ISM theory. Our work improves the understanding of ISM and contributes to its advancement as a high-resolution imaging technique.

4.1. INTRODUCTION

Fluorescence microscopy is a powerful tool for bioimaging, as fluorescent labeling enables high imaging specificity and contrast. However, the resolution of conventional fluorescence microscopy cannot surpass the diffraction limit [1]. To circumvent this limit, several super-resolution technologies have been developed. Stimulated emission depletion microscopy (STED) combines a confocal spot to create fluorescence with a donut to deplete the fluorescence at the edge of the confocal spot. This synergetic combination reduces the effective width of the confocal spot and thereby surpasses the diffraction limit[2, 3]. Single-molecule localization microscopy (SMLM) surpasses the diffraction limit by localizing sparsely activated single-molecules [4–6]. Structured illumination microscopy (SIM) adopts in-plane sinusoidal illumination to expand the effective bandwidth of spatial frequencies to enhance the resolution [7, 8].

SIM is the preferred super-resolution method for live-cell imaging because of the low illumination intensity, the flexibility in the choice of fluorophores or dyes, and the imaging speed. Although the original approaches relied on complex hardware and post-processing, in recent years we have seen a steady rise of less involved approaches that fundamentally make use of the same principles, such as image scanning microscopy[9]. ISM relies on the shifts between excitation and emission point spread function to create a sharper PSF with better imaging resolution. Several microscopes have been developed based on this principle[10–12]. The first implementation of ISM was based on confocal microscopy with a camera detector, where pixels were re-assigned in post-processing to create a super-resolution reconstruction [12]. Re-scan confocal microscopy performs this computation optically by adopting a second galvo mirror, which moves at a different speed to perform this shift operation [11]. Optical photon reassignment microscopy (OPRA) achieved ISM with only a single galvo mirror, which is used twice [10]. The speed of these ISM approaches is similar to confocal microscopy and multiplexing the number of illumination spots can increase the imaging speed [13, 14].

A robust theoretical foundation is essential for the evaluation and advancement of existing and innovative approaches in the field of illumination scanning microscopy (ISM). In the context of high-numerical aperture (NA) fluorescence microscopy, the Stokes shift of fluorescence represents a ubiquitous phenomenon across various fluorescent dyes. Furthermore, even cutting-edge optical setups are susceptible to aberrations, while the presence of polarization effects is inherent within the microscopy system. As such, these factors demand careful consideration when modeling the point spread function (PSF) [15]. Notably, the significance of polarization effects on PSF modeling is particularly pronounced in high-NA systems [16], and the precision of vectorial PSF modeling has been experimentally validated [15, 17]. While prior ISM researches have contributed to scalar aberration-free PSF modeling [11, 18], the Stokes shift effect [19], vectorial effects for PSF-engineered ISM [20], and multiphoton excitation ISM [21–24], a comprehensive vectorial ISM PSF modeling methodology, accounting for all the aforementioned effects, remains an unmet need. The availability of a reliable ISM PSF simulator offers a valuable reference for assessing the quality of ISM images and for selecting optimal optical elements and hardware parameters for ISM microscopy.

In this research, we develop this vectorial ISM PSF model considering the effects of polarization, Stoke shift, and aberrations. We investigate the predicted resolution im-

provement for single- and multiphoton excitation using the scalar and vectorial models. This is done by analyzing the differences of these models over the whole range of possible NA. We find that the highest resolution improvement can be achieved with 1-photon excitation and that the difference between the scalar and vectorial models increases with the NA. We investigate if the resolution improvement is robust against aberrations and how this can be mitigated. We find that aberrations decrease the resolution and that the effect of aberrations can be reduced by decreasing the size of the pinhole.

4.2. THEORY

4.2.1. SCALAR THEORY OF IMAGE SCANNING MICROSCOPY PSF

The scalar theory of ISM PSF was previously developed independently in two works [11, 18]. In this subsection, we expand upon the scalar theory of ISM from [11] by incorporating vectorial effects, Stokes shift, and aberrations. The ISM PSF equation can be described as follows [11]:

$$
\begin{aligned}
\mathrm{H_{ISM}}\left(\boldsymbol{u}_{\mathrm{c}}-\boldsymbol{u}_{\mathrm{o}},u_{\mathrm{z}}\right)=M^2 \int d^2 u_{\mathrm{s}}\, D\left(M\left(\boldsymbol{u}_{\mathrm{s}}-\boldsymbol{u}_{\mathrm{c}}\right)\right) \mathrm{H_{em}}\left(M\left(\boldsymbol{u}_{\mathrm{c}}-\boldsymbol{u}_{\mathrm{s}}\right)-\boldsymbol{u}_{\mathrm{s}}-\boldsymbol{u}_{\mathrm{o}},-u_{\mathrm{z}}\right) \\
\mathrm{H_{ex}}\left(\boldsymbol{u}_{\mathrm{o}}-\boldsymbol{u}_{\mathrm{s}},u_{\mathrm{z}}\right)
\end{aligned}
\tag{4.1}
$$

where $\mathrm{H_{ISM}}(\boldsymbol{u},u_z), \mathrm{H_{em}}(\boldsymbol{u},u_z), \mathrm{H_{ex}}(\boldsymbol{u},u_z)$ are the two-dimensional PSFs of an image scanning microscope, emission, and excitation of the widefield microscope, respectively. $D(\cdot)$ is the pinhole function which is defined as a two-dimensional binary circular mask function taking value 1 inside the circle and value 0 otherwise, and M is the sweep factor for ISM which represents the scaling of shift between excitation and emission PSF [11]. In ISM, the emission PSFs are effectively shifted from excitation PSFs to gain the image resolution, which can be realized by hardware and software [11, 25]. An effective PSF of ISM can be interpreted as the overlapped region of excitation PSF and shifted emission PSF. The main principle of the resolution enhancement of ISM is that the overlapped region is always narrower than the excitation or emission PSF. If the sweep factor is 1, it means no shift between excitation and emission PSF, which is a conventional confocal imaging, and gains no additional resolution enhancement. If the sweep factor is larger than 1, it means there is an additional shift between excitation and emission PSF, which can improve the imaging resolution. Furthermore, $\boldsymbol{u}_{\mathrm{c}}$ are two-dimensional coordinates in the camera plane, $\boldsymbol{u}_{\mathrm{s}}$ is the two-dimensional position of the confocal illumination position, $\boldsymbol{u}_{\mathrm{o}}$ are the two-dimensional coordinates in the object, and u_{z} is the distance from the focal plane in the objective plane.

Taking the Fourier transform of the ISM PSF, we obtain the optical transfer function (OTF) $\widehat{\mathrm{H}}_{\mathrm{ISM}}(\boldsymbol{q})$:

$$
\widehat{\mathrm{H}}_{\mathrm{ISM}}\left(\boldsymbol{q},u_{\mathrm{z}}\right)=\int d^2\boldsymbol{q}'\,\widehat{D}\left(\boldsymbol{q}'\right)\widehat{\mathrm{H}}_{\mathrm{em}}\left(-\frac{\boldsymbol{q}}{M}+\boldsymbol{q}',-u_{\mathrm{z}}\right)\widehat{\mathrm{H}}_{\mathrm{ex}}^*\left(\frac{(M-1)\,\boldsymbol{q}}{M}+\boldsymbol{q}',u_{\mathrm{z}}\right)
\tag{4.2}
$$

Note that this equation is different concerning earlier literature as [11] contains a mistake. Here, $\boldsymbol{q}=\left(\boldsymbol{q}_x,\boldsymbol{q}_y\right)$ are normalized optical coordinates such that $\|\boldsymbol{q}\|_2 \leqslant 1$, $\widehat{\mathrm{H}}_{\mathrm{em}}(\mathbf{q})$ is

the OTF of the emission PSF, $\widehat{H}_{ex}(\boldsymbol{q})$ is the OTF of the excitation PSF, and $\widehat{D}(\boldsymbol{q})$ is the OTF of the pinhole function.

THE EMISSION PSF AND OTF

In the scalar PSF model, the electric field (E_{em}) of the emission PSF (H_{em}) can be calculated using the following equation:

$$E_{em}(\boldsymbol{u}, u_z) = \frac{1}{\sqrt{2\pi}} \int d^2\boldsymbol{q}\, c_{em}(\boldsymbol{q}) \exp\left(-i\mathbf{k}_{em}(\mathbf{q}) \cdot \mathbf{u}\right) \exp\left(-ik_z(\boldsymbol{q}) u_z\right),$$

$$c_{em}(\boldsymbol{q}) = \begin{cases} A_{em}(\boldsymbol{q}) \exp\left(-i\frac{2\pi W_{em}(\boldsymbol{q})}{\lambda_{em}}\right) & \text{if } \|\boldsymbol{q}\|_2 \leqslant 1, \\ 0 & \text{otherwise.} \end{cases} \tag{4.3}$$

Here, $\mathbf{k}_{em}(\mathbf{q}) = \frac{2\pi NA}{\lambda_{em}}(\mathbf{q_x}, \mathbf{q_y})$, $k_z = \sqrt{n_{med}^2 - NA^2 |\boldsymbol{q}|^2}$, and λ_{em} is the wavelength of emission light. $A_{em}(\cdot)$ is the amplitude correction factor for the emission PSF (see [26]), which is expressed as:

$$A_{em}(\theta) = \sqrt{\frac{n_{imm} \cos\theta_{imm}}{n_{med} \cos\theta_{med}}} \frac{1}{\sqrt{n_{med} \cos\theta_{med}}}. \tag{4.4}$$

Here, n_{imm}, n_{med} are the respective refractive indices of the immersion and sample media, and $\theta_{imm}, \theta_{med}$ are the respective polar angle of light in the immersion and sample media. More details about the generalized Jones matrix are in the supplementary. $W_{em}(\boldsymbol{q})$ is the two-dimensional pupil phase function that models the aberrations in the emission path.

The emission PSF can be expressed as follows:

$$H_{em}(\boldsymbol{u}, u_z) = |E_{em}(\boldsymbol{u}, u_z)|^2. \tag{4.5}$$

The OTF of the emission is obtained as follows:

$$\widehat{H}_{em}(\boldsymbol{q}, u_z) = \int d^2 u\, H_{em}(\boldsymbol{u}, u_z) \exp(i\mathbf{k}_{em}(\boldsymbol{q}) \cdot \mathbf{u}). \tag{4.6}$$

THE EXCITATION PSF AND OTF

The electric field of scalar excitation PSF (H_{ex}) is modelled as follows:

$$E_{ex}(\boldsymbol{u}, u_z) = \frac{1}{\sqrt{2\pi}} \int d^2\boldsymbol{q}\, c_{ex}(\boldsymbol{q}) \exp\left(-i\mathbf{k}_{ex}(\mathbf{q}) \cdot \mathbf{u}\right) \exp\left(-ik_z(\boldsymbol{q}) u_z\right),$$

$$c_{ex}(\boldsymbol{q}) = \begin{cases} A_{ex}(\boldsymbol{q}) \exp\left(-i\frac{2\pi W_{ex}(\boldsymbol{q})}{\lambda_{ex}}\right) & \text{if } \|\boldsymbol{q}\|_2 \leqslant 1, \\ 0 & \text{otherwise.} \end{cases} \tag{4.7}$$

Here, $\mathbf{k}_{ex}(\mathbf{q}) = \frac{2\pi NA}{\lambda_{ex}}(\mathbf{q_x}, \mathbf{q_y})$ and λ_{ex} is the excitation wavelength. A_{ex} is the amplitude correction factor for the excitation PSF, which is defined as follows:

$$A_{ex}(\theta) = \sqrt{\frac{n_{med} \cos\theta_{med}}{n_{imm} \cos\theta_{imm}}} \frac{1}{\sqrt{n_{imm} \cos\theta_{imm}}}. \tag{4.8}$$

$W_{\text{ex}}(\boldsymbol{q})$ is the phase pupil function that models aberrations in the excitation path. The excitation PSF can be expressed as:

$$\text{H}_{\text{ex}}(\boldsymbol{u}, u_{\text{z}}) = |\text{E}_{\text{ex}}(\boldsymbol{u}, u_{\text{z}})|^2. \tag{4.9}$$

The OTF of the excitation is obtained as follows:

$$\widehat{\text{H}}_{\text{ex}}(\boldsymbol{q}, u_{\text{z}}) = \int d^2 u \, \text{H}_{\text{ex}}(\boldsymbol{u}, u_{\text{z}}) \exp(i \mathbf{k}_{\text{ex}}(\mathbf{q}) \cdot \mathbf{u}). \tag{4.10}$$

4.2.2. VECTORIAL THEORY OF IMAGE SCANNING MICROSCOPY PSF

Previous research successfully describes how resolution in ISM is achieved, but it neglects the vectorial effects and aberrations that arise with the use of high-NA objectives. To address this, we compute the vectorial PSFs taking into account Stokes shifts, aberrations, and polarization effects.

THE VECTORIAL EMISSION PSF

The emission light consists of three polarization directions (x, y, z), but only the light in the transversal direction (x, y) can propagate to the pupil plane. The electric field of the emission light, considering vectorial effects, can be expressed as follows:

$$\text{E}_{\text{em},lj}(\boldsymbol{u}, u_{\text{z}}) = \frac{1}{\sqrt{2\pi}} \int d^2\boldsymbol{q} \, c_{\text{em},lj}(\boldsymbol{q}) \exp\left(-\text{i}\mathbf{k}_{\text{em}}(\mathbf{q}) \cdot \mathbf{u}\right) \exp\left(-\text{i}k_{\text{z}} u_{\text{z}}\right)$$

$$c_{\text{em},lj}(\boldsymbol{q}) = \begin{cases} A_{\text{em}}(\boldsymbol{q}) \, \bar{\boldsymbol{M}}_{\text{em},lj}(\boldsymbol{q}) \exp\left(-\text{i}\frac{2\pi W_{\text{em}}(\boldsymbol{q})}{\lambda_{\text{em}}}\right) & , |\boldsymbol{q}| \leq 1 \\ 0 & , |\boldsymbol{q}| > 1 \end{cases} \tag{4.11}$$

, where $\text{E}_{\text{em},lj}(\boldsymbol{u}, u_{\text{z}})$ is the electric field with l, j as the direction of polarization (the emitter polarization of j projects to the polarization of l in the pupil plane), $W_{\text{em}}(\boldsymbol{q})$ is the two-dimensional pupil phase function and $\bar{\boldsymbol{M}}_{\text{em},lj}(\boldsymbol{q})$ is the element from the l's row and the j's column of the emission Jones matrix. The definition of $\bar{\boldsymbol{M}}_{\text{em},lj}(\boldsymbol{q})$ are in the supplementary section 4.S1. Compared with the Eq.4.3, the generalized Jones matrix ($\bar{\boldsymbol{M}}_{\text{em},lj}(\boldsymbol{q})$) extends the scalar emission PSF model to vectorial emission PSF model. The mathematics details about the generalized Jones matrix are in the supplementary section 4.S1. We considered the freely rotated emission dipole situation such that each polarization contributes to the PSF equally:

$$\text{H}_{\text{em}}(\boldsymbol{u}, u_{\text{z}}) = \frac{1}{3} \sum_{l=x,y} \sum_{j=x,y,z} \left|\text{E}_{\text{em},lj}(\boldsymbol{u}, u_{\text{z}})\right|^2. \tag{4.12}$$

THE VECTORIAL EXCITATION PSF

For the excitation path, the electric field should be described as:

$$E_{ex,lj}(\boldsymbol{u}, u_z) = \frac{1}{\sqrt{2\pi}} \int d^2\boldsymbol{q}\, c_{ex,lj}(\boldsymbol{q}) \exp\left(-i\mathbf{k}_{ex}(\mathbf{q}) \cdot \mathbf{u}\right) \exp\left(-ik_z u_z\right)$$

$$c_{ex,lj}(\boldsymbol{q}) = \begin{cases} A_{ex}(\boldsymbol{q})\, \bar{M}_{ex,lj}(\boldsymbol{q})\, \bar{I}_{ex,j} \exp\left(-i\frac{2\pi W_{ex}(\boldsymbol{q})}{\lambda_{ex}}\right) & ,|\boldsymbol{q}| \le 1 \\ 0 & ,|\boldsymbol{q}| > 1 \end{cases} \qquad (4.13)$$

With

$$\bar{I}_{ex} = \begin{bmatrix} I_x e^{i\delta_x} \\ I_y e^{i\delta_y} \end{bmatrix}, \qquad (4.14)$$

where $I_{x,y}$ standards for the amplitude of x, y polarization and $\delta_{x,y}$ standards for the phase delay of x, y polarization, which determines the chirality of excitation light. With this term, the polarization state of the excitation laser can be in any polarization state. $\bar{M}_{ex,lj}(\boldsymbol{q})$ is the element from the l's row and the j's column of the excitation Jones matrix, which is detailed defined in the supplementary. The excitation light incidents the pupil plane with two polarization directions (x, y), and after the refraction by the objective lens, the excitation light has the fraction on three polarization directions (x, y, z), $\bar{I}_{ex}$ stands for the polarization of excitation light source, and λ_{em} is the wavelength of excitation light.

The PSF of excitation ($H_{ex}(\cdot)$) can be described as

$$H_{ex}(\boldsymbol{u}, u_z) = \sum_{l=x,y,z} \sum_{j=x,y} \left|E_{ex,lj}(\boldsymbol{u}, u_z)\right|^2 \qquad (4.15)$$

4.2.3. VECTORIAL THEORY OF MULTI-PHOTON IMAGE SCANNING MICROSCOPY PSF

In the previous ISM theory, the excitation wavelength is considered the same as the emission wavelength, which limits the exploration of multi-photon ISM. To investigate multi-photon ISM, we start from Eq. 4.7, but the excitation wavelength for 2-photon and 3-photon excitation is twice and three times larger, respectively, than the 1-photon excitation wavelength. The electric field of the k-photon excitation PSF can be described as follows:

$$E_{ex,lj}(\boldsymbol{u}, u_z) = \frac{1}{\sqrt{2\pi}} \int d^2\boldsymbol{q}\, c_{ex,lj}(\boldsymbol{q}) \exp\left(-i\mathbf{k}_{ex}(\mathbf{q}) \cdot \mathbf{u}\right) \exp\left(-ik_z u_z\right)$$

$$c_{ex,lj}(\boldsymbol{q}) = \begin{cases} A(\boldsymbol{q})\left[\bar{M}_{lj}(\boldsymbol{q})\, \bar{I}_{ex,j}\right] \exp\left(-i\frac{2\pi W_{ex}(\boldsymbol{q})}{\lambda_{ex}}\right) & ,|\boldsymbol{q}| \le 1 \\ 0 & ,|\boldsymbol{q}| > 1 \end{cases} \qquad (4.16)$$

, where the subscription l stands for l-component of electric field, λ_{ex} is the excitation wavelength of multi-photon excitation. The multi-photon excitation PSF (H_{ex}) can be described as follows:

$$H_{ex}(\boldsymbol{u}, u_z) = \sum_{l=x,y,z} \sum_{j=x,y} \left|E_{ex,lj}(\boldsymbol{u}, u_z)\right|^2 \qquad (4.17)$$

Afterward, the effective multi-photon excitation PSF should consider the photon absorption possibility. The effective multi-photon [23] excitation PSF is:

$$H_{ex,k}(\boldsymbol{u}, u_z) = H_{ex}(\boldsymbol{u}, u_z)^k \tag{4.18}$$

where the subscript k stands for k-photons excitation. In the simulation of multi-photon ISM PSF, we used the effective multi-photon excitation PSF ($H_{ex,k}$) as the excitation PSF (H_{ex}).

4.2.4. COMPUTATION METHOD FOR THE SCALAR AND VECTORIAL ISM PSF

The method for simulating the ISM PSF involves evaluating the equations described in Sections 2.1 and 2.2. To obtain the optical transfer function (OTF) of the excitation and emission PSFs, the chirp z-transform method is used [27]. This method is commonly employed for fast and accurate computation of discrete Fourier transforms and is well-suited for simulating the PSFs in ISM.

In the simulation, the excitation and emission PSFs are evaluated using a pixel size of 5 nm and a simulation window size of 512 pixels. For simulating the vectorial excitation PSF, circular polarization is chosen as the simulation condition. The excitation wavelength is set to 640 nm for both 1-photon excitation, 1280 nm for 2-photon excitation, and 1920 nm for 2-photon excitation. The emission wavelength is fixed at 690 nm for all simulation scenarios.

The numerical aperture (NA) of the objective lens is specified as 1.35. The refractive index of the coverslip and immersion medium is set to 1.52, while the refractive index of the sample medium is 1.33.

The size of the simulation window at the Fourier plane is determined as 8NA/640 nm, and it is discretized with a total of 201 pixels in both the x and y directions. In the majority of simulations presented in this study, we select a sweep factor (M) of 2 for the ISM Point Spread Function to attain optimal resolution. Conversely, a sweep factor of 1 is employed for the Confocal PSF. It is important to note that in the case of the confocal PSF, we refer to the PSF acquired through a camera sensor, rather than a photon detector, as our equation does not involve the summation of photons over the detector area. For the simulation of multi-photon ISM, we vary the sweep factor to explore the optimal FWHM of the PSF.

By following these simulation conditions and using the chirp z-transform method, the scalar and vectorial ISM PSFs can be computed for various excitation scenarios, allowing for the investigation and analysis of multi-photon ISM.

4.3. RESULTS

4.3.1. EFFECTS OF STOKES SHIFT AND POLARIZATION ON IMAGE SCANNING MICROSCOPY PSF

In this section, we investigate the influence of Stokes shift and polarization on the excitation, emission, and point spread functions (PSFs). We compare these PSFs with their scalar counterparts to highlight the impact of vectorial effects in Fig. 4.1. We consider three scenarios: (1) "vectorial + Stokes shift" where both polarization and Stokes shift

are taken into account, (2) "vectorial + no Stokes shift" where only polarization is considered without Stokes shift, and (3) "scalar + no Stokes shift" where neither polarization nor Stokes shift are considered. The optical transfer function (OTF) and PSF are analyzed to compare these scenarios. Additionally, cross-section profiles are presented to visualize the differences between the PSFs.

In Fig. 4.1 (f-h), we show the OTF and PSF with and without the consideration of polarization and the Stokes effect. In Fig. 4.1 (j-l), we show the cross-section of them to visualize the difference. Comparing the cross-section curve from "vectorial + Stokes shift" and "vectorial + no Stokes shift" (Fig.4.1 (i-k)), we observe that the effect of polarization delivers more difference than Stokes shift. Besides, for a pinhole size of 1.0, the FWHM of the vectorial ISM PSF is 25% larger than the scalar ISM PSF (Fig.4.1 (k)).The observed phenomenon can be attributed to the interplay of various physical factors within the vectorial model. Notably, the pupil function undergoes additional modulation due to the influence of the Fresnel effect and the projection of the polarization field. These effects collectively introduce an amplitude term into the pupil function, which, in the spatial domain, can be likened to the operation of a Gaussian kernel, resulting in further blurring of the Point Spread Function (PSF). Consequently, this leads to the empirical observation of a broader PSF. A similar rationale has been proposed in prior research on vectorial PSF, as documented in Hanser's work [15].

4.3.2. COMPARISON OF SCALAR AND VECTORIAL ISM PSF FOR RESOLUTION IMPROVEMENT

In this section, we examine the impact of polarization on the image scanning microscopy point spread function and assess the resolution improvement achieved by ISM compared to widefield and confocal PSFs. For the widefield PSF, we utilize the emission PSF (H_{em}), while the confocal PSF is obtained by setting the sweep factor to $M = 1$. We refer to the PSF without considering polarization and Stokes shift as the scalar PSF, and the PSF considering polarization and Stokes shift as the vectorial PSF.

Fig. 4.2 (a) shows the FWHM of widefield, confocal, and ISM PSF. We found the consideration of the polarization can broaden the FWHM of the PSFs (Fig. 4.2 (a)). We observed that the minimum FWHM of vectorial image scanning PSF is 202 nm and scalar image scanning PSF is 150 nm. Besides, in many different pinhole sizes, the FWHM of vectorial ISM PSFs deviates significantly from scalar ISM PSF. In Fig. 4.2 (b), we show the improvement of ISM PSF over WF PSF. We find that the scalar PSF model underestimates the improvement and that it is slightly above the $\sqrt{2}$ for pinhole sizes between zero and two. The maximum improvement is achieved with a pinhole of 1.2 Airy unit (A.U.), which delivers an improvement of 1.46 assuming a scalar PSF and 1.48 assuming a vectorial PSF. In Fig. 4.2 (c), the maximum improvement of ISM PSF over confocal PSF is 1.45 in the vectorial PSF model and 1.46 in the scalar PSF model. In the large pinhole condition (pinhole size>2.0 A.U.), the improvement estimated by the scalar theory can be 1.36, but the one estimated by the vectorial theory is 1.40.

We assess the FWHM of both scalar and vectorial PSF as a function of the sweep factor. Fig. 4.2 (d-f) provides a visual representation of these evaluations. Fig. 4.2 (e) highlights the critical finding that the optimal sweep factor for the scalar PSF is precisely 2. In contrast, the vectorial PSF model yields an optimal sweep factor of 2.13, a result consistent
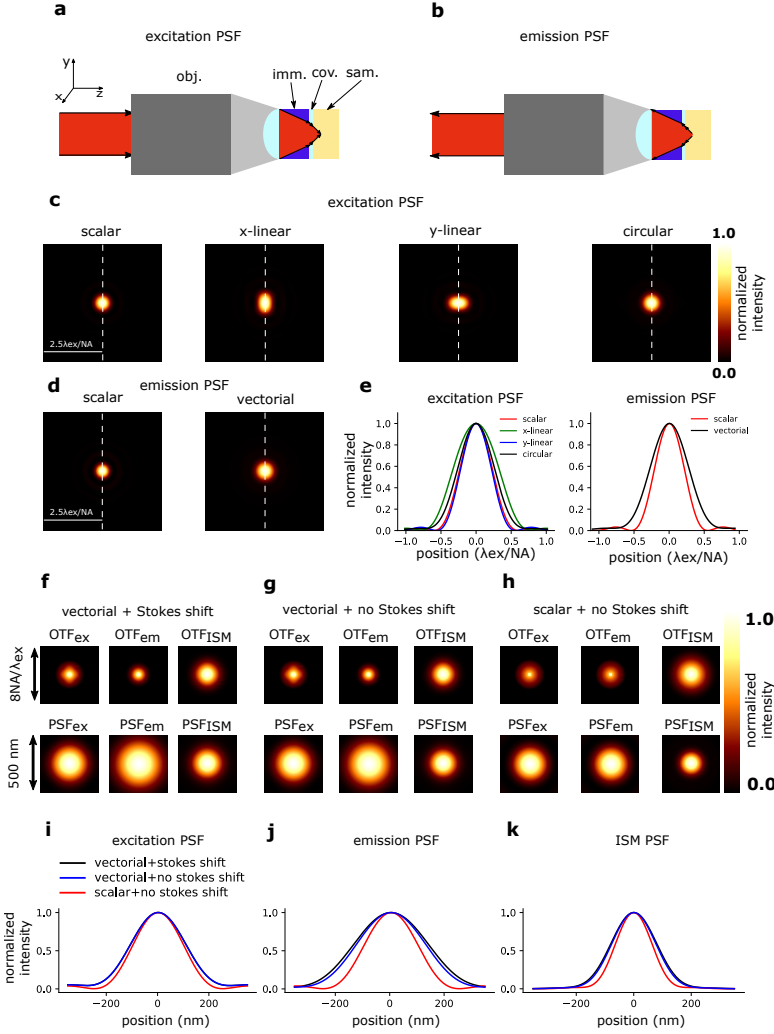
Figure 4.1: Demonstrate the difference between the vectorial and scalar PSF model. (a,b) In this paper, we consider the physical environment in that the light of excitation and emission PSF experiences the immersion media, coverslip, and sample media. The refractive index difference between different media refracts light which affects the polarization state. imm., cov., and sam. in panel stands for the immersion media, coverslip, and sample media respectively. The arrow direction identifies the propagation direction of light (c) The comparison between the scalar and the vectorial PSF. For several different excitation polarizations PSF (x-linear, y-linear, circular). (d) Scalar and vectorial emission PSF. (e) Cross-section of excitation and emission PSF.(f-h) OTF and PSF of excitation, emission, and image scanning with/without the consideration of polarization and Stokes shift. (i-k) Cross-section profile of excitation, emission, and image scanning PSF with and without the consideration of polarization and Stokes shift. vectorial+Stokes shift: with consideration of the effect of polarization and the excitation and emission wavelength are different. The polarization state for excitation is circular polarized. vectorial+no Stokes shift: considering the effect of polarization and the excitation and emission wavelength are the same. scalar+no Stokes shift: without considering the polarization and the excitation and emission wavelength are the same.

with the data presented in Fig. 4.2 (f). Expanding our investigation, Fig. 4.2 (g) illustrates the FWHM of the PSF across varying depths. Subsequently, Fig. 4.2 (h-i) reveals distinct behaviors in the improvement factors. Specifically, the improvement factor of the scalar PSF demonstrates a rapid decrease, while the vectorial PSF exhibits a relatively slower decline. These observations suggest intriguing nuances in the performance of the two PSF models.

4.3.3. COMPARISON OF SCALAR AND VECTORIAL PSF MODELS FOR DIFFERENT NA

The numerical aperture (NA) of a microscope plays a crucial role in determining the width of the point spread function. Increasing the NA leads to a decrease in the FWHM of the PSF, highlighting the wave and vectorial nature of light. In this section, we investigate the impact of NA on the ISM PSF by simulating it using both scalar and vectorial PSF models. We also evaluate the significance of considering the polarization effect for high NA ISM.

In Fig. 4.3 (a), we show the FWHM of ISM PSF calculated by scalar and vectorial PSF theory at different NA. To quantify the difference between scalar and vectorial ISM PSF, we defined the difference (ϵ) and difference ratio (R_ϵ) as follows:

$$\epsilon = r_v - r_s \tag{4.19}$$

$$R_\epsilon = \frac{\epsilon}{r_v} \tag{4.20}$$

where r_v is the FWHM of vectorial ISM PSF and r_s is the FWHM of scalar ISM PSF.

In Fig.4.3 (b), we show the difference ratio over different NA. We observe that with increasing NA, the difference ratio increases. When the NA is 1.2, the difference (ϵ) is 45 nm and the different ratio can raise to 30%, which means the size between scalar and vectorial ISM PSF can deviate by 30%. This result suggests that the relative difference increases for all ascending values of the NA. Secondly, the absolute difference also increases from NA>0.6 onwards. Therefore, not only does the difference between the models outlast the FWHM reduction for high NA, but the difference between models grows for high NA despite the total FWHM decreasing. The visualization of the PSFs for both scalar and vectorial ISM simulations is presented in Figure S2.

4.3.4. IMAGE SCANNING PSF WITH CONSIDERATION OF ABERRATIONS

In previous studies, the image scanning theory assumed a perfect, non-aberrated pupil function [11, 18], which is often not satisfied in practical experiments. Aberrations can occur in various parts of the imaging system, including the sample and lenses, and they can significantly affect the resolution of image scanning microscopy. In this section, we investigate the impact of aberrations on the ISM PSF.

To simulate the ISM PSF under the effect of aberrations, we consider aberrations that are simultaneously present in the excitation and emission PSFs, which means the aberration terms W_{ex}, W_{em} in Eq. 4.11 and 4.7 are equal.

We calculated the WF, confocal, and image scanning PSF under different amplitude of aberration (0 mλ, 36 mλ. 72 mλ). The amplitude of aberrations is defined based on the root mean square value of Zernike coefficients, which is computed as
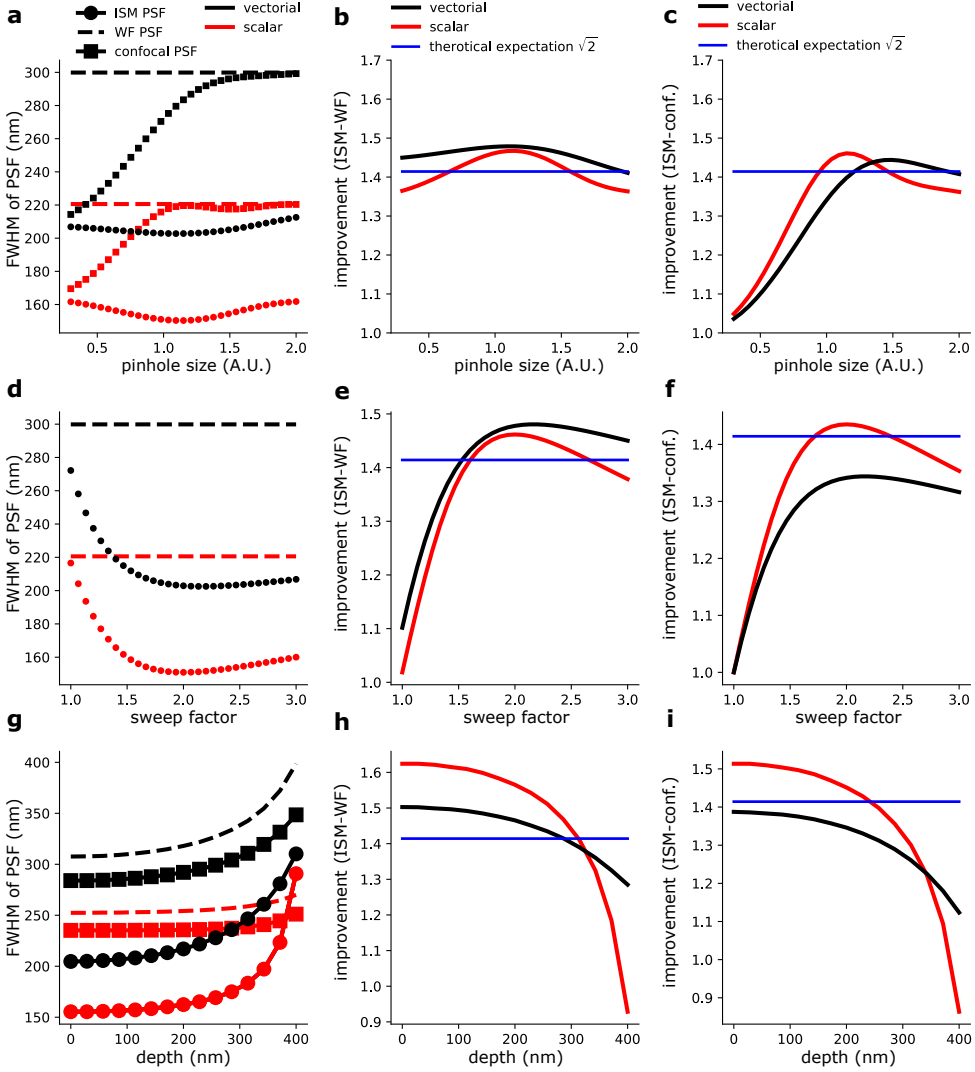
Figure 4.2: Comparison of the FWHM and improvement of confocal (conf.) PSF, and image scanning microscopy PSF over the different sizes of pinhole and widefield (WF) PSF. The pinhole does not affect the WF PSF and the FWHM of WF PSF is constant over the different sizes of a pinhole. (a) FWHM of WF, confocal, and ISM PSF with and without the consideration of polarization and Stokes shift. (b) The improvement between ISM and WF PSF with and without consideration of polarization and Stokes shift. (c) The improvement between ISM and confocal PSF with and without consideration of polarization and Stokes shift. (d) FWHM of the PSF for varying sweep factors. (e) Enhancement Factor comparing Image Scanning Microscopy (ISM) and Widefield (WF) PSFs across different sweep factors. (f) Enhancement Factor comparing ISM and Confocal PSFs under varying sweep factors. (g) FWHM of WF, Confocal, and ISM PSFs with and without considering polarization and Stokes shift effects. (h) Improvement Factor for Scalar and Vectorial ISM PSFs over Widefield PSFs at different depths.(i) Improvement Factor for Scalar and Vectorial ISM PSFs over Confocal PSFs at different depths. The sweep factor is set to 2 and the pinhole size is fixed at 1 A.U.

Figure 4.3: Benchmark of ISM PSF at different NA calculated by scalar and vectorial PSF theory. In the simulation, the pinhole size is chosen as 1 A.U. (a) The FWHM of PSF at different NA is calculated by scalar and vectorial PSF theory. (b) The difference ratio (R_ϵ) and the difference (ϵ) between scalar and vectorial PSF. The sub-figure shows the R_ϵ ratio at different NA.

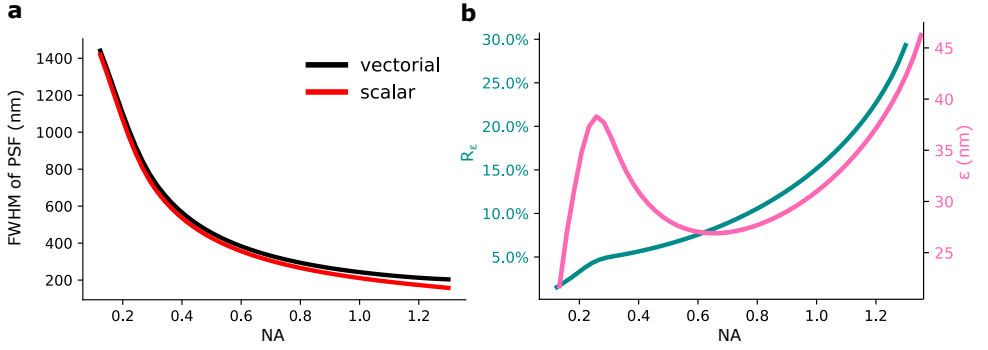$Z_{\mathrm{RMS}} = \sqrt{\sum_{i=1}^{24} C_i^2}$. The C_i stands for the Zernike coefficient of ith Zernike mode following Noll's indexing [28]. The aberrations terms ($W_{\mathrm{ex}}, W_{\mathrm{em}}$) are modelled as the summation of the first 24 Zernike modes after piston, tilt, tip, and defocus modes, since only the latter modes distort the PSF. We randomly assign an aberration to the first 24 Zernike modes. This is achieved by sampling each element from a uniform distribution and subsequently normalizing the vector to achieve the desired aberration strength. In Fig. 4.4 (a), we show the width of PSF at different pinhole sizes and aberrations. In the WF and ISM PSF, we observed that the FWHM of WF, confocal, and ISM PSFs increased as the aberrations increased. This observation aligns with the physical intuition because the aberrations can distort the PSF. However, the effect of aberrations on the confocal PSFs is not as significant as the one in ISM although both of them use pinhole in the emission path (Fig. 4.4 (a)). In Fig. 4.4 (b), we show the improvement of ISM PSF over WF PSF and over confocal PSF under different levels of aberrations. The maximum improvement happens around the 1 A.U. pinhole in all situations we have investigated. With small pinhole sizes (< 1 A.U.), the improvement of ISM over WF and confocal does not reduce a lot by the aberration. However, in large pinholes (> 1 A.U.), the improvement drops down significantly. With 72 mλ aberrations, the improvement between ISM and WF PSF is 1.44±0.033 when the pinhole size is 0.3 A.U. and the improvement is 1.34±0.044 when the pinhole size is 2.0 A.U. The pinhole size should be smaller than 1.5 A.U. and the improvement factor between ISM and confocal PSF can reach the theoretical expectation $\sqrt{2}$.

We conducted simulations of the Point Spread Function (PSF) for WF, confocal, and ISM under strong aberration conditions (Fig. 4.4 (c,d,e)). Under such challenging aberration conditions, the distribution of improvement factors exhibited a notably broader range. This posed a challenge when attempting to ascertain an average improvement in the ISM, particularly in the context of comparing it with the WF imaging. To address this issue, we shifted our focus to assessing whether ISM could still demonstrate improvement under these severe aberration conditions. We defined the possibility of achieving improvement as situations in which the improvement factor exceeded 1, as shown in

Fig. 4.4 (e). To ensure a fair and robust quantification of this possibility, we performed 60 simulations for each condition, considering different aberration amplitudes and pinhole sizes (1 A.U. and 2 A.U.).The results, depicted in Fig. 4.4 (e), revealed that when using a 1 A.U. pinhole, ISM consistently achieved improvement until an aberration amplitude of 216 mλ. In contrast, under the 2 A.U. pinhole condition, ISM maintained its ability to achieve improvement only up to an aberration amplitude of 144 mλ. These findings shed light on the impact of pinhole size and aberration amplitude on the ISM technique's capability to enhance imaging quality under challenging aberration conditions.

4.3.5. MULTI-PHOTON EXCITATION IN IMAGE SCANNING MICROSCOPY

When imaging thick samples, multi-photon excitation is commonly employed to minimize scattering induced by the sample. The longer wavelength used in multi-photon excitation reduces scattering effects, but it also increases the FWHM of the PSF. Additionally, the nonlinear absorbance of the light in multi-photon excitation virtually narrows the excitation PSF, resulting in what is known as the effective excitation PSF. In this section, we use the vectorial PSF theory to investigate 2-photon and 3-photon excitation in image scanning microscopy.

In Fig.4.5 (a), we show the excitation PSF (H_{ex}), effective excitation PSF ($H_{ex,eff}$), and ISM PSF (H_{ISM}) with 1,2,3-photon excitation. The excitation PSF of multiple photon excitation is wider as the excitation wavelength is longer. In ISM PSF simulation, we care more about the effective excitation PSF since that is the one we used for ISM PSF simulation. In Fig.4.5 (b), we show the cross-section of effective excitation PSF with 1,2,3-photon excitation. We observe that the FWHM of multiple photon effective excitation PSFs is larger. The physics behind this can be explained as follows. We can model the excitation PSF with a simple Gaussian function.

$$H_{ex} \sim e^{-\frac{r^2}{2\sigma^2}}, \tag{4.21}$$

where r is the distance from the center of PSF and σ is the standard deviation of the PSF. The standard deviation σ is proportional to the wavelength and NA through the diffraction limit:

$$\sigma \propto \frac{\lambda}{2NA} \tag{4.22}$$

For k-photon excitation, the excitation wavelength is k times larger than the one of 1-photon excitation wavelength, and hence the width of k-photon excitation PSF (σ_k) can be expressed as:

$$\sigma_k \propto \frac{\lambda_k}{2NA} = \frac{k\lambda_1}{2NA} \propto k\sigma_1 \tag{4.23}$$

, where σ_1 and σ_k is the width of 1-photon and k-photon excitation PSF and λ_1 and λ_k is the wavelength of 1-photon and k-photon excitation wavelength. The effective k-photon excitation PSF can be expressed as:

$$H_{ex,k}(r) \propto e^{-\frac{r^2}{2k\sigma_1^2}} \tag{4.24}$$
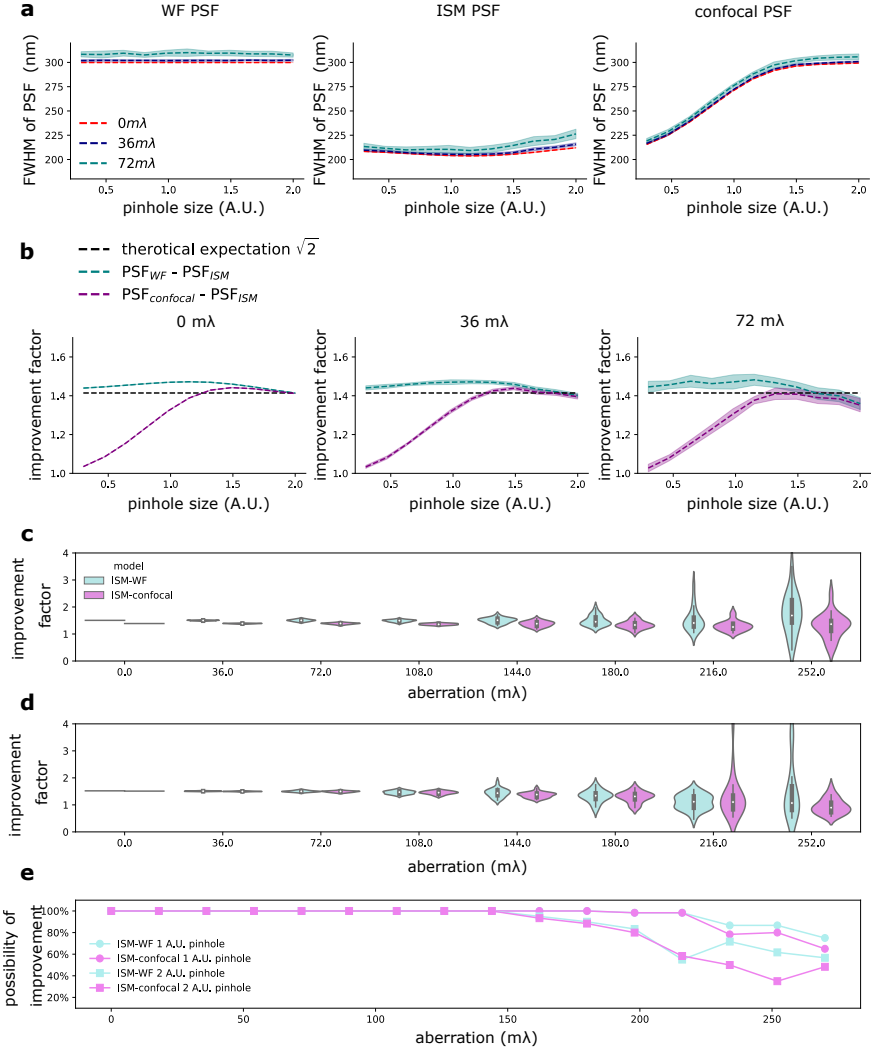
Figure 4.4: Benchmark the width of widefield (WF) PSF, image scanning microscopy PSF, and confocal PSF and the improvement. The PSFs in this simulation are all calculated by a vectorial model. (a) The FWHM of WF, ISM, and confocal PSF at a different level of aberration (0 mλ, 36 mλ, 72 mλ) and pinhole size. The aberration of WF, confocal, and image scanning PSF are randomly assigned to 24 Zernike modes. We measured the width of each PSF from 10 different random aberrations. The filled region in each sub-panel is the standard deviation from 20 measurements. (b) Benchmark the improvement of ISM PSF over WF PSF and ISM PSF over confocal PSF. The improvement is defined as $\frac{r_{\text{WF, confocal}}}{r_{\text{ISM}}}$, where $r_{\text{WF, confocal}}$ is the FWHM of widefield and confocal PSF respectively, and r_{ISM} is the FWHM of ISM PSF. (c) The improvement factor of ISM PSF over WF PSF and ISM PSF over confocal PSF in 1 A.U. of the pinhole. (d) The improvement factor of ISM PSF over WF PSF and ISM PSF over confocal PSF in 2 A.U. of pinhole. (e) Feasibility of achieving an improvement. We define 'achieving improvement' as the scenario where the improvement factor exceeds 1.

In Fig. 4.5(c), we present an analysis of the FWHM for the PSF of single/multi-photon excitation in ISM. Our findings reveal that a sweep factor of 2 may not always be the ideal choice for multiple-photon excitation ISM. Interestingly, we have identified distinct optimal sweep factors for different excitation modalities. Specifically, for 2-photon excitation ISM, the optimal sweep factor is determined to be 1.53, whereas for 3-photon excitation ISM, the optimal sweep factor is 1.4. Notably, a sweep factor of 2 is found to be optimal for one-photon excitation ISM (as illustrated in Figure 4.5(c)).

In Fig.4.5 (e), we show the FWHM of one-photon/multi-photon excitation ISM PSF with a sweep factor of 2 or with an optimal sweep factor. We found that the FWHM of the ISM PSF is larger for multi-photon excitation than 1-photon excitation. This is because the FWHM of the effective excitation PSF ($H_{k,ex}$) of multi-photon ISM is larger than the 1-photon excitation ISM, and this, in turn, broadens the multi-photon excitation ISM PSF. When the pinhole size is 1 A.U., the FWHM of 1-photon excitation ISM PSF is 189 nm, 2-photon excitation ISM PSF is 244 nm, and 3-photon excitation ISM PSF is 268 nm, which stands for a 20% increment of FWHM of 2-photon excitation ISM PSF and a 28% increment of FWHM of 3-photon excitation ISM PSF comparing with the 1-photon excitation ISM. In Fig.4.5 (d), we show the improvement of multi-photon ISM over widefield. With the multi-photon excitation, the improvement of ISM over WF decreases. Under the simulation we have investigated, the maximum improvement of 1-photon excitation ISM is 1.47, 2-photon excitation ISM is 1.22, and 3-photon excitation ISM is 1.12. In all calculated situations, the improvement of two and 3-photon excitation cannot be higher than the theoretical expectation $\sqrt{2}$. We also conducted simulations of the multi-photon ISM PSF using the optimal sweep factors, which were determined to be 1.53 for 2-photon ISM and 1.4 for 3-photon ISM. It is worth noting that the optimal sweep factor, as illustrated in Fig. 4.5(c), was identified under the specific condition of a 1 A.U. pinhole aperture. Importantly, our results consistently demonstrate that employing the optimal sweep factors consistently yields a narrower FWHM compared to using a sweep factor of 2 across various pinhole conditions. Under the specific condition of a 1 A.U. pinhole, our simulations revealed that the FWHM for 2-photon excitation ISM using the optimal sweep factor was 240 nm, whereas the FWHM for 2-photon excitation ISM with a sweep factor of 2 was slightly larger at 244 nm. In the case of 3-photon excitation ISM, the FWHM of the PSF with the optimal sweep factor was 257 nm, while the FWHM of the PSF with a sweep factor of 2 measured a larger value of 268 nm. These findings underscore the significance of the optimal sweep factor in achieving superior PSF performance in ISM applications.

4.4. CONCLUSION

In this paper, we have developed a vectorial theory of ISM by taking into account aberration, polarization, and Stokes shifts between excitation and emission. Previous ISM research predominantly relied on scalar theory, neglecting the high-NA effects that are present. To illustrate the disparity between scalar and vectorial ISM PSF models, we present the OTF and PSF in Fig. 4.1. The vectorial ISM PSF exhibits a FWHM that is 25% larger than the scalar ISM PSF, signifying a significant distinction. This disparity primarily arises from the effect of polarization rather than the Stokes shifts.

To further validate the advantages of employing vectorial theory in ISM PSF simula-

4
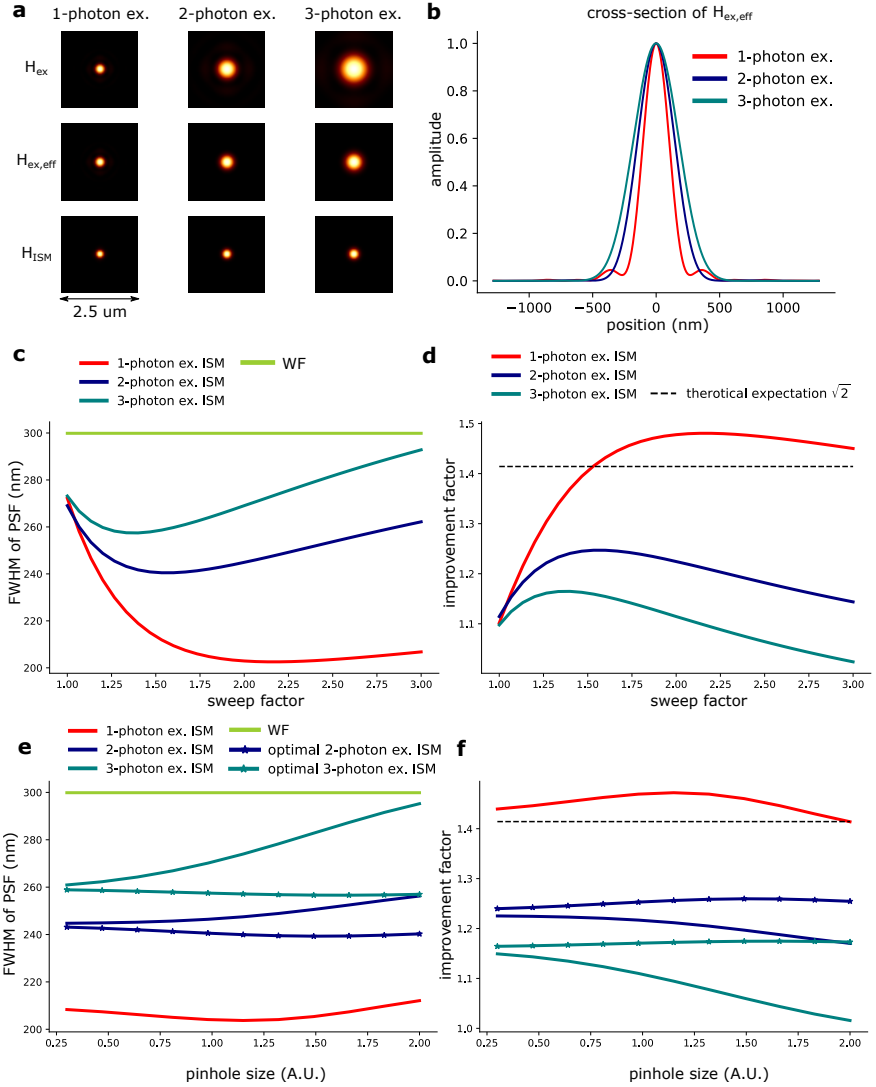
Figure 4.5: The width of multi-photon excitation ISM PSF and the improvement. (a) The excitation PSF (H_{ex}), effective excitation PSF ($H_{ex,eff}$), and ISM PSF under 1,2,3-photon excitation. The abbreviation ex. stands for excitation. The white dashed lines indicate the cross-section of the panel (b). (b) The cross-section profile of effective excitation PSF from 1,2,3-photon excitation. (c) The FWHM of 1,2,3-photon excitation ISM and widefield(WF) PSF under different sweep factors. The sweep factor does not affect widefield PSF. It is shown for reference. (d) Improvement of single and multi-photon ISM PSF over widefield PSF under different sweep factors. (e) The FWHM of PSF of multi-photon ISM under different pinhole sizes. The solid line stands for the ISM PSF simulated with a sweep factor of 2 and the dotted line stands for the ISM simulated with an optimal sweep factor searched by the data from sub-panel (c). In 2-photon excitation ISM PSF, the optimal sweep factor is 1.533 and in 3-photon excitation ISM PSF the optimal sweep factor is 1.4. (f) Improvement of single and multi-photon ISM PSF over widefield PSF under different pinhole sizes. For (c,d), the A.U. is defined as $\frac{1.22\lambda_{ex}}{NA}$, where λ_{ex} is 640 nm. (e)

tion, we conduct a benchmark by comparing the FWHM of the WF, confocal, and ISM PSF calculated based on both scalar and vectorial PSF theories. In our simulation, we observe that the FWHM of vectorial ISM PSFs is approximately 54 nm larger than those estimated by the scalar ISM PSF theory when the pinhole size is set to 1 A.U. (Fig. 4.2 (a)). Fig. 4.2 (b,c) suggests that the scalar theory and theoretical expectations slightly underestimate the resolution improvement offered by ISM in comparison to the estimates provided by the vectorial theory. In the benchmark between WF and ISM, the maximum improvement predicted by the vectorial ISM model can reach up to 1.48 when the pinhole size is set to 1.1 A.U. Similarly, in the benchmark between confocal and ISM, the improvement predicted by the vectorial ISM model can reach up to 1.46 when the pinhole size is set to 1.49 A.U. In addition, the scalar ISM PSF demonstrates an optimal sweep factor prediction of 2, while the vectorial ISM PSF predicts a slightly higher value of 2.13 (as depicted in Fig. 4.2 (e,f)). It is worth noting that the depth of imaging has a significant impact on the ISM PSF's performance, with the improvement factor diminishing as imaging depth increases (as shown in Fig. 4.2 (h,i)). Interestingly, the scalar ISM PSF exhibits a more pronounced decline in the improvement factor across various imaging depths compared to the vectorial ISM PSF (as illustrated in Fig. 4.2 (h,i)).

To further reinforce the rationale behind employing vectorial theory in ISM PSF simulation, we compare the ISM PSF calculated using scalar and vectorial theories at different NA (Fig. 4.3). The results indicate that the difference ratio (R_ϵ) between scalar and vectorial ISM PSF can increase up to 30% when NA is 1.3, while the difference ratio is only 5% when the NA is 0.1. This emphasizes the significance of considering polarization effects, particularly in high NA ISM PSF simulations. Based on the comparisons made between the scalar and vectorial ISM PSF models (Fig. 4.2, and Fig. 4.3), we conclude that both models can accurately predict the resolution improvement of ISM, but the scalar PSF model tends to underestimate the FWHM of the PSF when compared to the estimates provided by the vectorial PSF model.

The observed increase in the relative error (R_ϵ) as the NA increases aligns with the argument, highlighting the significance of vectorial effects in high NA scenarios. We believe the reason for the peak in the difference curve lies in the combined influence of two primary factors. Firstly, the width of the spectrum of the additional vectorial term in the vectorial PSF model plays a pivotal role. As elucidated in our main text, this additional vectorial term acts as an amplitude modifier on the pupil function, essentially behaving like a Gaussian kernel that affects the PSF's blurring. Consequently, the vectorial PSF model exhibits greater width compared to the scalar PSF model. With smaller NAs, the width of the vectorial term's spectrum decreases, resulting in a broader Gaussian blur kernel. The second factor at play is the NA itself. A larger NA intensifies the polarization effect. In low NA situations, the PSF's width is naturally large, but the impact of polarization is relatively minor. However, as the NA increases, the polarization effect becomes more pronounced, theoretically leading to a larger discrepancy between the scalar and vectorial PSF. Nonetheless, higher NAs also tend to reduce the absolute width of the PSF. Ultimately, the behavior of the difference curve depends on which of these effects predominates in shaping the PSF

Additionally, we investigate the influence of aberration and pinhole size on the ISM PSF. In Fig. 4.4, we demonstrate that aberration broadens the ISM PSF, leading to a de-

terioration in resolution and affecting the overall improvement. In the case of a 72 mλ situation, which is usually considered a diffraction limit condition, ISM with a 0.3 A.U. pinhole achieves an improvement of 1.45 ± 0.022, whereas using a 2.0 A.U. pinhole only yields an improvement of 1.35 ± 0.038. This qualitative outcome suggests that employing a smaller pinhole can counteract the deterioration of the PSF caused by aberrations when compared to using a larger pinhole. However, it's worth noting that a smaller pinhole rejects more emission signals, resulting in poorer imaging quality. In addition, we conducted simulations of WF, confocal, and ISM PSF under high aberration conditions, reaching up to 252 mλ. Our investigation revealed that reducing the pinhole size can significantly improve ISM's performance in the presence of high aberrations. Specifically, with a pinhole size of 1 A.U., ISM consistently exhibited improvements until the aberration reached 216 mλ. However, when using a 2 A.U. pinhole, ISM's performance started to deteriorate for aberrations exceeding 144 mλ. This observation is illustrated in Fig. 4.4.

Additionally, we explored the potential of leveraging multi-photon excitation in ISM and compared the ISM PSFs generated by 1-photon and multi-photon excitation. Our qualitative assessment indicated that multi-photon ISM PSFs are wider than their 1-photon counterparts, primarily due to the broader multi-photon excitation PSF. This broader excitation PSF ultimately results in a broader ISM PSF, as shown in Fig. 4.5 (a). Notably, the optimal sweep factor for multi-photon ISM is not 2 but rather 1.53 for 2-photon excitation ISM and 1.4 for 3-photon excitation ISM (Fig. 4.5 (c,d)), all of which were observed when using a 1 A.U. pinhole.

This trend in the optimal sweep factor can be attributed to the effective excitation PSF's width in multi-photon ISM, which is wider than in 1-photon excitation ISM. Furthermore, the OTF of the excitation PSF is narrower compared to that of the one-photon excitation PSF. According to Eq. 4.2, a narrower OTF constrains the range of usable sweep factors in ISM. Exceeding this range can shift the excitation OTF outside the emission OTF, resulting in an ineffective expansion of the effective OTF.

In the comparison between ISM and WF PSFs, our results consistently demonstrated that the optimal sweep factor always produced a narrower ISM PSF, regardless of the pinhole size (Fig. 4.5 (e)). However, multi-photon ISM fell short of achieving the theoretical expectation of $\sqrt{2}$ improvement, even with the optimal sweep factor. The maximum improvement we observed was 1.22 for 2-photon excitation ISM, 1.25 for 2-photon excitation ISM with the optimal sweep factor, 1.15 for 3-photon excitation ISM, and 1.17 for 3-photon excitation ISM with the optimal sweep factor (Fig. 4.5 (f)). Notably, the influence of the optimal sweep factor on ISM PSF was weaker when a smaller pinhole was employed, as indicated in Fig. 4.5 (e,f). This can be attributed to the fact that, when a near-zero pinhole is used in the ISM system, the ISM PSFs become independent of the sweep factor [11], and consequently, the effect of the sweep factor is diminished.

In summary, our findings suggest that optimizing the pinhole size and sweep factor is critical in enhancing ISM performance, particularly in the presence of high aberrations. Additionally, while multi-photon excitation widens the ISM PSF, the choice of optimal sweep factor remains crucial in obtaining the best achievable resolution.

CODE AND DATA AVAILABILITY

The code is freely available at the link below. https://github.com/qnano/ISM-PSF

DISCLOSURES

The authors declare no conflicts of interest.

4

BIBLIOGRAPHY

1. Born, M. & Wolf, E. *Principles of optics. Electromagnetic theory of propagation, interference and diffraction of light. 6.* (Pergamon Xxviii, 1993).

2. Willig, K. I., Harke, B., Medda, R. & Hell, S. W. STED microscopy with continuous wave beams. *Nature Methods* **4,** 915–918. (2022) (Oct. 2007).

3. Vicidomini, G., Bianchini, P. & Diaspro, A. STED super-resolved microscopy. *Nature Methods* **15,** 173–182 (Jan. 2018).

4. Rust, M. J., Bates, M. & Zhuang, X. Sub-diffraction-limit imaging by stochastic optical reconstruction microscopy (STORM). *Nature Methods* **3,** 793–796 (Aug. 2006).

5. Betzig, E. *et al.* Imaging Intracellular Fluorescent Proteins at Nanometer Resolution. *Science* **313,** 1642–1645. (2021) (Sept. 2006).

6. Hess, S. T., Girirajan, T. P. & Mason, M. D. Ultra-High Resolution Imaging by Fluorescence Photoactivation Localization Microscopy. *Biophysical Journal* **91,** 4258–4272. (2021) (Dec. 2006).

7. Gustafsson, M. G. L. Surpassing the lateral resolution limit by a factor of two using structured illumination microscopy. *Journal of Microscopy* **198,** 82–87. eprint: https://onlinelibrary.wiley.com/doi/pdf/10.1046/j.1365-2818.2000.00710.x. https://onlinelibrary.wiley.com/doi/abs/10.1046/j.1365-2818.2000.00710.x (2000).

8. Smith, C. S. *et al.* Structured illumination microscopy with noise-controlled image reconstructions. *Nature Methods* **18,** 821–828. (2022) (June 2021).

9. SHEPPARD, C. J. R. Super-resolution in confocal imaging. *Super-resolution in confocal imaging* **80,** 53–54. https://pascal-francis.inist.fr/vibad/index.php?action=getRecordDetail&idt=7325329 (2022) (1988).

10. Roth, S., Sheppard, C. J., Wicker, K. & Heintzmann, R. Optical photon reassignment microscopy (OPRA). *Optical Nanoscopy* **2,** 5. (2019) (2013).

11. Luca, G. M. D. *et al.* Re-scan confocal microscopy: scanning twice for better resolution. *Biomed. Opt. Express* **4,** 2644–2656. http://opg.optica.org/boe/abstract.cfm?URI=boe-4-11-2644 (Nov. 2013).

12. Müller, C. B. & Enderlein, J. Image Scanning Microscopy. *Physical Review Letters* **104** (May 2010).

13. Azuma, T. & Kei, T. Super-resolution spinning-disk confocal microscopy using optical photon reassignment. *Opt. Express* **23,** 15003–15011. http://opg.optica.org/oe/abstract.cfm?URI=oe-23-11-15003 (June 2015).

14. York, A. *et al.* Instant super-resolution imaging in live cells and embryos via analog image processing. *Nature Methods* **10,** 1122–1126. (2023) (Nov. 2013).

15. HANSER, B. M., GUSTAFSSON, M. G. L., AGARD, D. A. & SEDAT, J. W. Phase-retrieved pupil functions in wide-field fluorescence microscopy. *Journal of Microscopy* **216,** 32–48. eprint: https://onlinelibrary.wiley.com/doi/pdf/10.1111/j.0022-2720.2004.01393.x. https://onlinelibrary.wiley.com/doi/abs/10.1111/j.0022-2720.2004.01393.x (2004).

16. Braat, J. J., Dirksen, P., Janssen, A. J., van Haver, S. & van de Nes, A. S. Extended Nijboer–Zernike approach to aberration and birefringence retrieval in a high-numerical-aperture optical system. *J. Opt. Soc. Am. A* **22,** 2635–2650. https://opg.optica.org/josaa/abstract.cfm?URI=josaa-22-12-2635 (Dec. 2005).

17. Siemons, M., Hulleman, C. N., Thorsen, R. Ø., Smith, C. S. & Stallinga, S. High precision wavefront control in point spread function engineering for single emitter localization. *Opt. Express* **26,** 8397–8416. https://opg.optica.org/oe/abstract.cfm?URI=oe-26-7-8397 (Apr. 2018).

18. Schulz, O. *et al.* Resolution doubling in fluorescence microscopy with confocal spinning-disk image scanning microscopy. *Proceedings of the National Academy of Sciences* **110,** 21000–21005. (2020) (Dec. 2013).

19. Sheppard, C. J. R., Mehta, S. B. & Heintzmann, R. Superresolution by image scanning microscopy using pixel reassignment. *Opt. Lett.* **38,** 2889–2892. https://opg.optica.org/ol/abstract.cfm?URI=ol-38-15-2889 (Aug. 2013).

20. Wang, W. *et al.* Image scanning microscopy with a long depth of focus generated by an annular radially polarized beam. *Opt. Express* **28,** 39288–39298. https://opg.optica.org/oe/abstract.cfm?URI=oe-28-26-39288 (Dec. 2020).

21. Gregor, I. *et al.* Rapid nonlinear image scanning microscopy. *Nature Methods* **14,** 1087–1089. https://www.nature.com/articles/nmeth.4467 (Nov. 2017).

22. Tzang, O., Feldkhun, D., Agrawal, A., Jesacher, A. & Piestun, R. Two-photon PSF-engineered image scanning microscopy. *Optics Letters* **44,** 895. https://opg.optica.org/ol/abstract.cfm?uri=ol-44-4-895 (Feb. 2019).

23. Koho, S. V. *et al.* Two-photon image-scanning microscopy with SPAD array and blind image reconstruction. *Biomedical Optics Express* **11,** 2905. https://opg.optica.org/boe/fulltext.cfm?uri=boe-11-6-2905&id=431589 (May 2020).

24. Sheppard, C. J. R. *et al.* Image scanning microscopy with multiphoton excitation or Bessel beam illumination. *Journal of the Optical Society of America A* **37,** 1639. https://opg.optica.org/josaa/abstract.cfm?uri=josaa-37-10-1639 (Sept. 2020).

25. Müller, C. B. & Enderlein, J. Image Scanning Microscopy. *Physical Review Letters* **104.** https://journals.aps.org/prl/abstract/10.1103/PhysRevLett.104.198101 (May 2010).

26. Siemons, M. E., Kapitein, L. C. & Stallinga, S. Axial accuracy in localization microscopy with 3D point spread function engineering. *Opt. Express* **30,** 28290–28300. https://opg.optica.org/oe/abstract.cfm?URI=oe-30-16-28290 (Aug. 2022).

27. Rabiner, L. R., Schafer, R. W. & Rader, C. M. The Chirp z-Transform Algorithm and Its Application. *Bell System Technical Journal* **48,** 1249–1292. (2022) (May 1969).

28. Noll, R. J. Zernike polynomials and atmospheric turbulence∗. *J. Opt. Soc. Am.* **66,** 207–211. https://opg.optica.org/abstract.cfm?URI=josa-66-3-207 (Mar. 1976).

4

Supplemental information:

Image scanning microscopy: a vectorial physical optics analysis

4.S1. Vectorial model of excitation and emission PSF

In this paper, we model the PSF in the environment of immersion media, coverslip, and sample media. We follow the theory from the following citation [1–3]. We follow the Fourier optics method to model the PSF which means we start from the pupil function of PSF and compute the PSF by applying the Fourier transform on the pupil function. We fully consider the interaction between the polarization state of the electric field and the physical environment in the path from the pupil plane to the focal plane. In many procedures, the polarization state can be affected by the physical environment. We summarize four situations that can affect the polarization state of light in the PSF model into the following four Jones matrix.

$$
R_{\text{xyz}\to\text{msz}}(\phi) = \begin{bmatrix} \cos\phi & -\sin\phi & 0 \\ -\sin\phi & \cos\phi & 0 \\ 0 & 0 & 1 \end{bmatrix}
$$

$$
R_{\text{msz}\to\text{psz}}(\theta) = \begin{bmatrix} \cos\theta & 0 & -\sin\theta \\ 0 & 1 & 0 \\ \sin\theta & 0 & \cos\theta \end{bmatrix}
$$

$$
Re(\theta) = \begin{bmatrix} \cos\theta & 0 & \sin\theta \\ 0 & 1 & 0 \\ -\sin\theta & 0 & \cos\theta \end{bmatrix} \tag{4.S1}
$$

$$
F(\mathbf{q}) = \begin{bmatrix} F_P(\mathbf{q}) & 0 & 0 \\ 0 & F_S(\mathbf{q}) & 0 \\ 0 & 0 & 1 \end{bmatrix}
$$

$$
\theta(n,\mathbf{q}) = \arccos\sqrt{1 - \|\mathbf{q}\|^2} \cdot \frac{\text{NA}}{n}
$$

$$
\phi(\mathbf{q}) = \arctan\frac{q_{\text{y}}}{q_{\text{x}}}
$$

, where n in θ represents the refractive index of the environment(in immersion medium or sample medium). The definition of $R_{\text{xyz}\to\text{msz}}$, $R_{\text{msz}\to\text{psz}}$, $Re(\theta)$, and $F(\mathbf{q})$ are explained in Fig. 4.S1.

The whole polarization effect in the excitation and emission PSF modeling can be expressed as M matrix in the following:

$$
\bar{\mathbf{M}} = R_{\text{xyz}\to\text{msz}}^{-1}(\phi)\, R_{\text{msz}\to\text{psz}}(\theta_{med.})\, F(\mathbf{q})\, R_{\text{msz}\to\text{psz}}(-\theta_{imm.})\, Re(-\theta_{imm.})\, R_{\text{xyz}\to\text{msz}}(\phi) \tag{4.S2}
$$

, where $\theta_{imm.}$ stands for the polar angle of light in the immersion media and $\theta_{med.}$ stands for the polar angle of light in the sample media.

The resulting polarization state of light can be expressed as follows:

$$\mathbf{E}_{re} = \bar{\mathbf{M}}\mathbf{E}_{init.} \tag{4.S3}$$

,where $\mathbf{E}_{init.}$ is the initial state of polarization and $\mathbf{E}_{re}$ stands for the ultimate polarization state. To be clearer, in excitation PSF the $\mathbf{E}_{init.}$ is the polarization state of incident light in the pupil plane and the $\mathbf{E}_{re}$ is the polarization of light in the sample media. In emission PSF, the $\mathbf{E}_{init.}$ is the polarization state of the emission dipole and the $\mathbf{E}_{re}$ is the polarization state of light at the pupil plane.

Although the excitation and emission PSF share the same matrix to model the PSF, one point worth particularly identifying is how excitation and emission light experience $\bar{\mathbf{M}}$ differently. In excitation PSF, the z-component of $\mathbf{E}_{init.}$ is zero because the transferal wave has no z-component of the electric field and $\mathbf{E}_{re}$ has full vectorial components. On the other hand, the $\mathbf{E}_{init.}$ of the emission PSF has a full vectorial component because the emission dipole launches the fluorescence light isotropic in all solid angles and $\mathbf{E}_{re}$ has zero z-components because the z-component cannot propagate.
In addition, the excitation and emission PSF experience different Fresnel coefficients in the M matrix because they experience the same physical environment in different sequential order.

4.S2. BENCHMARK OF SCALAR AND VECTORIAL ISM PSF UNDER DIFFERENT NA

We show the simulation of the scalar and vectorial ISM PSF under different NA in Fig.4.S2.

a

$R_{xyz \to msz}$

pupil plane

b

Re

c

$R_{msz \to psz}$

d

$F(q)$
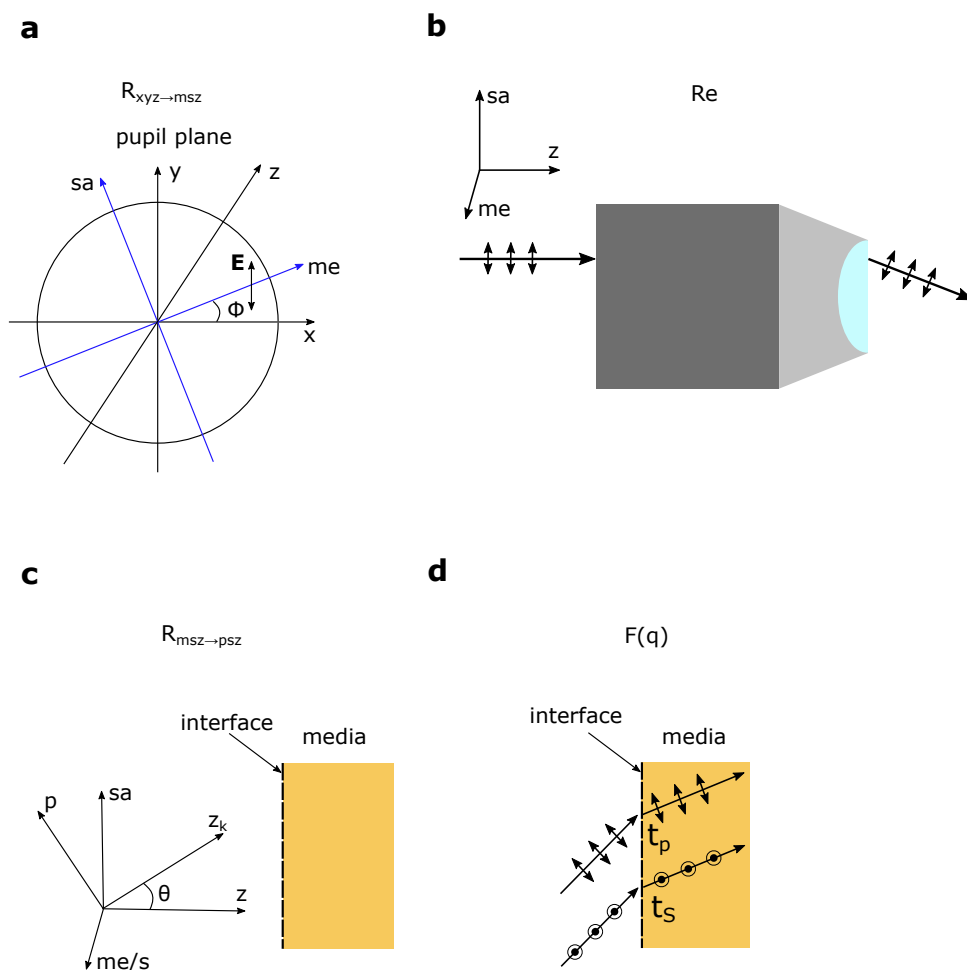
Figure 4.S1: Explanation of Jones matrix in the above equation. (a) The coordinate transforms from x/y/z co-ordinate to me/sa/z coordinate, where we denote meridional and sa denotes sagittal. (b) The polarization changes because of the refraction of the objective lens. (c) The transform from me/sa/z coordinate to $p/s/z_k$ coordinate, helps us correctly consider the p/s Fresnel coefficient at the interface. (d) the p/s Fresnel coefficients at the interface.
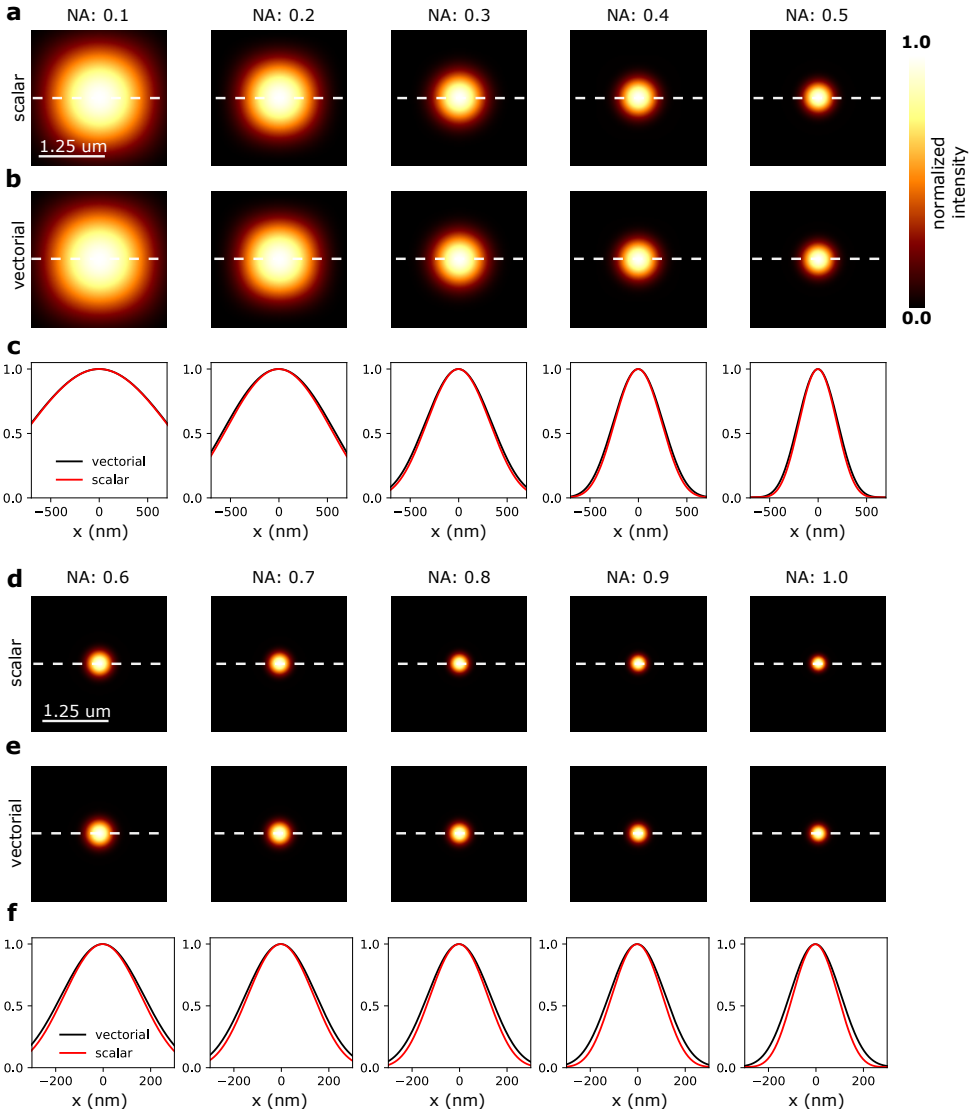
Figure 4.S2: Simulation of ISM PSF in different NA with scalar and vertorial PSF. (a) Simulated ISM PSF with scalar PSF model in different NA (NA:0.1 - 0.5). (b) Simulated ISM PSF with vectorial PSF model in different NA (NA:0.1 - 0.5). (c) Cross-section of scalar and vectorial ISM PSF. (d) Simulated ISM PSF with scalar PSF model in different NA (NA:0.6 - 1.0). (e) Simulated ISM PSF with vectorial PSF model in different NA (NA:0.6 - 1.0). (f) Cross-section of scalar and vectorial ISM PSF.

BIBLIOGRAPHY

1. Stallinga, S. Effect of rotational diffusion in an orientational potential well on the point spread function of electric dipole emitters. *J. Opt. Soc. Am. A* **32,** 213–223. https://opg.optica.org/josaa/abstract.cfm?URI=josaa-32-2-213 (Feb. 2015).

2. Siemons, M., Hulleman, C. N., Thorsen, R. Ø., Smith, C. S. & Stallinga, S. High precision wavefront control in point spread function engineering for single emitter localization. *Opt. Express* **26,** 8397–8416. https://opg.optica.org/oe/abstract.cfm?URI=oe-26-7-8397 (Apr. 2018).

3. Siemons, M. E., Kapitein, L. C. & Stallinga, S. Axial accuracy in localization microscopy with 3D point spread function engineering. *Opt. Express* **30,** 28290–28300. https://opg.optica.org/oe/abstract.cfm?URI=oe-30-16-28290 (Aug. 2022).

5

CONCLUSION AND OUTLOOK

5.1. CONCLUSION

This section concludes the results from chapters two to four. In the thesis motivation section, I introduce three issues that can deteriorate super-resolution imaging quality. Here, I conclude with the findings from Chapters 2 to 4 and explain how these results address the issues outlined in the thesis motivation section.

5.1.1. SOLEIL: SINGLE OBJECTIVE LENS LIGHTSHEET MICROSCOPY

In Chapter 2, I propose a solution to address the high background issue by lightsheet microscopy in SMLM imaging. I introduced the concept of Single Objective Lens Light-sheet Microscopy (SOLEIL), which is designed to offer a user-friendly solution. SOLEIL employs an inclined high Numerical Aperture (NA) lightsheet illumination method, resulting in a thin optical section. I discovered that achieving optimal optical sectioning involves a trade-off between the maximum inclined angle and excitation NA. A larger inclined angle yields a narrower optical section but relies on a smaller excitation NA, which can enhance optical sectioning.

To determine the optimal parameters for SOLEIL, I conducted simulations and found that an excitation NA of 0.66 and an inclined angle of 38° from the optical axis of the objective lens yielded the best results.

I demonstrated the effectiveness of SOLEIL in mitigating the high background issue in localization microscopy, leading to improved Cramer-Rao Lower Bound (CRLB) values compared to widefield and HILO microscopy. I repeated the benchmark with various cell samples, including COS-7 tubulin, HEK-293T tubulin, and Caco2-BBE ezrin samples. In all cases, SOLEIL outperformed widefield and HILO microscopy. In 2D Single Molecule Localization Microscopy (SMLM), SOLEIL's I/bg ratio was 3.5 to 8.5 times better than widefield microscopy, corresponding to a 54% to 72% improvement in CRLB and a 5 to 7 nm improvement in localization precision. In 3D SMLM, I used a deformable mirror to create an astigmatism Point Spread Function (PSF) and observed a 200% improvement in lateral and axial CRLB.

5.1.2. ADAPTIVE OPTICS SINGLE OBJECTIVE INCLINED LIGHT SHEET LO-CALIZATION MICROSCOPY

In Chapter 3, I introduced the AO-SOLEIL solution, which addresses sample-induced aberrations and high background issues in tissue imaging, enabling imaging of adult Drosophila brains. AO-SOLEIL combines a deformable mirror for sensorless aberration correction in SMLM imaging with the SOLEIL microscopy technique to address high background issues. Additionally, I employed in situ PSF calibration (INSPR) for precise PSF calibration to correct the remaining aberrations after AO correction.

I verified the robustness of the AO-SOLEIL solution through simulations and experiments. Simulation results indicated that employing a high number of steps (>7 steps) yielded a more stable sensorless AO algorithm, particularly in high-background situations (I/bg < 10). Additionally, the simulations showed that INSPR could not reliably calibrate the PSF model in the presence of strong spherical aberrations unless AO correction was performed.

In the experimental verification, I compared fluorescence bead images before and after AO correction and demonstrated that the axial CRLB of the INSPR PSF model improved significantly with AO correction, especially at greater imaging depths.

I demonstrated the effectiveness of AO-SOLEIL in various cell and tissue samples. In 2D imaging, AO correction improved PSF sharpness, resulting in a threefold improvement in single molecule detection efficiency in thick samples (65 μm). In thinner samples (17 μm), the improvement was 30%, indicating that AO correction's impact depends on sample thickness. In 3D SMLM, AO-SOLEIL was applied to imaging adult Drosophila brains, achieving a twofold improvement in axial CRLB compared to other experiments (SOLEIL without AO correction and widefield with AO correction).

5.1.3. IMAGE SCANNING MICROSCOPY: A VECTORIAL PHYSICAL OPTICS ANALYSIS

In Chapter 4, I introduced a comprehensive vectorial Point Spread Function (PSF) model for Image Scanning Microscopy (ISM). This model accounts for various factors, including polarization effects, aberrations, Stokes shifts, and Fresnel coefficients at media interfaces. Considering all these effects in the PSF model leads to increased precision.

In simulations, the Full Width at Half Maximum (FWHM) of the vectorial ISM PSF was 54 nm wider than that of the scalar ISM PSF. Moreover, the optimal sweep factor, as predicted by the vectorial ISM PSF model, was 2.13, contrasting with the value of 2 predicted by the scalar ISM PSF theory. Notably, when the pinhole size was set to 1.48 Airy units (A.U.), the optimal resolution improvement compared to widefield microscopy was 1.48. In the context of resolution improvement and imaging depth, the scalar ISM theory exhibited a rapid decrease, while the vectorial ISM theory showed a slower decline. Specifically, at an imaging depth of 400 nm, the scalar ISM theory suggested a resolution improvement over widefield microscopy of only 0.9, implying worse performance than widefield microscopy, whereas the vectorial ISM theory suggested an improvement of 1.3, indicating better performance.

Furthermore, I demonstrated the significance of adopting the vectorial ISM PSF model in high Numerical Aperture (NA) systems. With an NA of 1.3, the difference in FWHM between the vectorial and scalar ISM PSFs increased by up to 30%, whereas with

an NA of 0.1, the difference ratio was only 5%. Additionally, in simulations considering system aberrations, I found that even with a 72 mλ aberration, which corresponds to the diffraction limit level of aberration, the size of the pinhole significantly influenced the resolution improvement. In particular, using a 0.3 A.U. pinhole, the resolution improvement of ISM over widefield microscopy was 1.45, whereas with a 2.0 A.U. pinhole, the improvement was 1.35. In high aberration simulations, ISM with a 1 A.U. pinhole could achieve a resolution improvement of up to 216 mλ, while ISM with a 2 A.U. pinhole could only achieve a resolution improvement of up to 144 mλ. This underscores the importance of considering the pinhole size in the presence of system aberrations.

In terms of the scalar 1-photon ISM theory, it predicted an optimal sweep factor of 2. However, in multiple photon excitation ISM, simulations based on the proposed ISM PSF model suggested that the optimal sweep factor for 2-photon ISM was 1.53, and for 3-photon ISM, it was 1.4. The resulting optimal resolution improvements were 1.22 for 2-photon ISM and 1.17 for 3-photon ISM compared to widefield microscopy.

In summary, this chapter highlighted the distinctions between scalar and vectorial ISM PSF theories and explored how factors like aberrations, pinhole size, and Stokes shifts can impact the PSF model. These insights provide valuable guidance for individuals seeking to identify and optimize their ISM microscopy techniques and assess image quality.

5.2. OUTLOOK

In this section, I list possible solutions to further improve the super-resolution technology.

5.2.1. EXTENDED DEPTH OF FOCUS POINT SPREAD FUNCTION FOR SOLEIL

In the current SOLEIL system, I adopt the astigmatism PSF for 3D SMLM. However, the applicable axial range of astigmatism PSF is short (<1 μm), and it doesn't fully utilize the whole light sheet excitation. By using a longer PSF, it is possible to enlarge the FOV in each lightsheet excitation. In the current SOLEIL system, the full light sheet excitation range is 3.3 μm (Raylight length is 1.929 μm and inclined angle of SOLEIL is 30°, 3.3 μm= 1.929 μm×2× cos 30°), which means astigmatism doesn't effectively use the whole excitation range of SOLEIL. However, it is still unknown whether calibrating the long PSF is possible in INSPR.

There are some excellent works discussed about the long PSF in SMLM imaging. In DeepSTORM3D [1], they design a PSF with 4μm depth, which is realized by a phase plate. Or a tetrapod PSF is designed to achieve 6 μm imaging depth realized by a deformable mirror [2]. The above solutions make it possible to extend SOLEIL's imaging depth and use its full excitation range.

5.2.2. MULTI-COLOR SOLEIL

In SMLM imaging, multi-color imaging is an important tool to deliver biological information from images. A typical way to achieve color detection is to use a dichroic mirror in the emission path by which the different fluorescence dyes have different intensity ra-

tios for transmission and reflection channels [3]. However, the dichroic mirror can add aberration on the reflective channel, which differs the PSF of transmission from the PSF of the reflection channel. A possible solution is to use two deformable mirrors in transmission and reflection channels individually. However, this solution is not preferred as the cost and complexity of the system are very high. Thus, how to perform the AO correction for two-channel imaging with a single deformable deserves to be investigated. One possible solution is to correct the averaged aberration from two channels and make a trade-off from two-channel images, which means it corrects partial aberration in both channels. Then, it can build the PSF model individually from both channels by using the INSPR algorithm, which AO system addresses the CRLB decoration from aberration and the accurate PSF is acquired by INSPR.

5.2.3. Verify the vectorial ISM theory

The vectorial ISM theory is currently in the theoretical investigation phase and lacks experimental validation. A practical approach for verification involves imaging a small sample of fluorescent beads using re-scan confocal microscopy, as outlined in the study by reference [4]. In this experimental setup, the acquired images are convolved with the ISM Point Spread Function (PSF), allowing for the calculation of the width of the ISM PSF.

One of the advantages of using re-scan confocal microscopy for this verification is the flexibility of adjusting the sweep factor as a controllable parameter. This flexibility enables the exploration of optimal sweep factors, shedding light on how they affect the performance of ISM. Additionally, re-scan confocal microscopy performs ISM through purely optical means, eliminating potential errors introduced by algorithmic approaches.

To further investigate how the FWHM of the ISM PSF varies with different Numerical Aperture (NA) settings, an iris can be employed to adjust the excitation NA. Subsequently, re-scan microscopy can be utilized to image a small sample of fluorescent beads, facilitating a comprehensive analysis of how changing NA impacts the ISM PSF width.

5.2.4. Field dependent Point Spread Function in SIMFLUX and SOLEIL

The concept of SIMFLUX is to encode the molecule by intensity, which delivers additional information in the localization and enhances the localization precision. A further way to encode molecule position information is to create a spatial-variant PSF and encode the molecule position information in the shape of PSF as well [5]. In this way, an optimal solution to boost the SMLM localization precision is to combine the SIMFLUX with the spatial-variant PSF method. A possible hardware to realize this method is to add a relay lens system in the SIMFLUX system and add a waveplate in the relay system. In addition, this method can also be applied in SOLEIL to further improve the CRLB of localization. However, localizing the spatial variant PSF in high background situations is still unknown and needs to be investigated.

5.2.5. Large field of view SIMFLUX system

In the current SIMFLUX system, the fast switching between x,y patterns is realized by using digital micromirror device (DMD). However, DMD is an aberrated element as the front glass of the vacuum chamber of DMD can add additional aberration on the light. A strong aberration on the excitation path can distort the structural illumination pattern [6]. In the current system, we avoid this issue by using a small area on DMD, resulting in a small excitation area. It is possible to solve this issue by allocating a phase plate before DMD to correct the aberration from DMD front glass. A wavefront sensor could be used to measure the aberrations from the DMD front glass. With this correct, we can use a large excitation area on the SIMFLUX system without the concern of a distorted structural illumination pattern.

5

BIBLIOGRAPHY

1. Nehme, E. *et al.* DeepSTORM3D: dense 3D localization microscopy and PSF design by deep learning. *Nature Methods* **17,** 734–740. https://www.nature.com/articles/s41592-020-0853-5 (June 2020).

2. Fu, S. *et al.* Deformable mirror based optimal PSF engineering for 3D super-resolution imaging. *Opt. Lett.* **47,** 3031–3034. https://opg.optica.org/ol/abstract.cfm?URI=ol-47-12-3031 (June 2022).

3. Andronov, L., Genthial, R., Hentsch, D. & Klaholz, B. P. splitSMLM, a spectral demixing method for high-precision multi-color localization microscopy applied to nuclear pore complexes. *Communications Biology* **5,** 1–13. https://www.nature.com/articles/s42003-022-04040-1 (Oct. 2022).

4. Luca, G. M. D. *et al.* Re-scan confocal microscopy: scanning twice for better resolution. *Biomed. Opt. Express* **4,** 2644–2656. http://opg.optica.org/boe/abstract.cfm?URI=boe-4-11-2644 (Nov. 2013).

5. Fu, S. *et al.* Field-dependent deep learning enables high-throughput whole-cell 3D super-resolution imaging. *Nature Methods* **20,** 459–468. https://www.nature.com/articles/s41592-023-01775-5 (Mar. 2023).

6. Zheng, Y., Chen, J., Wu, C., Gong, W. & Si, K. Adaptive optics for structured illumination microscopy based on deep learning. *Cytometry Part A* **99,** 622–631. https://onlinelibrary.wiley.com/doi/full/10.1002/cyto.a.24319 (Feb. 2021).

ACKNOWLEDGEMENTS

Firstly, I would like to express my heartfelt appreciation to my colleagues and research collaborators for the invaluable support and knowledge they have provided me with over these past four years. Regardless of our individual relationships, I have gained tremendous insights from each and every one of you. Debugging Jelmer's code, for instance, has greatly honed my advanced programming skills. Daniel Fan's guidance has been instrumental in improving my communication and paper writing abilities, making our lab work an enjoyable experience. Additionally, Kristin and Ran's assistance with cell culturing proved indispensable in completing the SOLEIL paper. Your collective contributions have been instrumental in my academic journey.

Secondly, I want to extend my deepest gratitude to Michel, without whom I could not have successfully completed my PhD research. Your guidance and support have been pivotal to my growth as a researcher. I also wish to acknowledge Carlas for his patience and mentorship, which have not only enhanced my scientific knowledge but have also fostered a mature mindset for problem-solving. I eagerly look forward to the opportunity to continue working with you in my upcoming postdoctoral research endeavors.

CURRICULUM VITÆ

Shih-Te HUNG

19-06-1995   Born in Tainan, Taiwan.

EDUCATION

2013–2017   BSc. Physics, National Taiwan normal university
                 Taipei, Taiwan

2017–2019   M.Sc. Photonics, Fridrich-Schiller University
                 Jena, Germany

2020-2024   PhD. ,Delft University of Technology
                 Delft, The Netherlands
                 Thesis: SUPER-RESOLUTION MICROSCOPY IN TISSUE
                                 THROUGH ILLUMINATION ENGINEERING AND
                                 ABERRATION CORRECTION
                 Promotor: Prof. dr. Michel Verhaegen, Prof. dr. Carlas Smith

LIST OF PUBLICATIONS

- Shih-Te Hung, Dylan Kalisvaart, and Carlas Smith, "Image scanning microscopy: a vectorial physical optics analysis," Opt. Express 32, 2024

- Shih-Te Hung, Jelmer Cnossen, etc., "SOLEIL: single-objective lens inclined light sheet localization microscopy," Biomed. Opt. Express 13, 2022

- Shih-Te Hung, Arnau Llobet Rosell, etc., "Adaptive optics in single objective inclined light sheet microscopy enables three-dimensional localization microscopy in adult Drosophila brains," Front. Neurosci. 16, 2022

- Daniel Fan, Jelmer Cnossen, Shih-Te Hung, etc., "Three-dimensional localization microscopy with increased axial precision through TIRF angle modulation," Optics Communications 542, 2023

- Nagaraj Nagalingam, Aswin Raghunathan, Vikram Korede, Edwin F.J. Overmars, Shih-Te Hung, etc. ,"Low-cost fluorescence microscope with microfluidic device fabrication for optofluidic applications,", HardwareX 14, 2023

- Dylan Kalisvaart, Jelmer Cnossen, Shih-Te Hung, etc.,"Precision in iterative modulation enhanced single-molecule localization microscopy," Biophysical Journal 121, 2022

- Rui Shi, Zongzhao Wang, Shih-Te Hung, etc., "Numerical analysis of tiny-focal-spot generation by focusing linearly, circularly, and radially polarized beams through a micro/nanoparticle," Opt. Express 29, 2021

- Quint Houwink, Dylan Kalisvaart, Shih-Te Hung, etc. , "Theoretical minimum uncertainty of single-molecule localizations using a single-photon avalanche diode array," Opt. Express 29, 2021